IV. APPLIED BATTERY RESEARCH FOR TRANSPORTATION

Materials Research

Modeling, Diagnostics, and Performance Studies

Abuse Diagnostics & Mitigation

Applied Research Facilities

IV Applied Battery Research for Transportation

IV.A Introduction

The Applied Battery Research (ABR) for transportation program is focused on materials and cell couples for high energy batteries for use in PHEV40 (PHEVs with a 40 mile all-electric range) light-duty vehicles. The key barriers associated with PHEV batteries are:

- High cost

- Insufficient energy density to meet the 40-mile all-electric range,

- Limited calendar and cycle life,

- Insufficient tolerance to abusive conditions, and

- Operation between -30ºC and +52ºC.

The program is seeking to develop higher energy materials, higher voltage electrolytes, combined into more optimal cell chemistries that are more stable and long-lived in the cell environment; as well as possessing cost advantages over current materials. The program is also focused on understanding and enhancing the abuse tolerance of the individual materials, components, and cell chemistries, which will help reduce the level of complexity of the electronic control system and thereby realize cost savings.

One of the unique characteristics of the ABR program is the full design of experiment approach to identifying, diagnosing, and addressing issues with high-energy, high power cells. ABR investigators work to apply iterative, multi-mode applied R&D processes that move from materials and advanced chemistry through design, fabrication, performance testing, and diagnostics. Successful outcomes will lead to new, improved technical knowledge for the ABR program, but more importantly, they will collectively provide a forum to directly address scientific and engineering barriers to the commercialization of electric drive vehicle (EDV) electrochemical energy storage systems.

Seven DOE national laboratories and two external laboratories are collaborating in the program. Argonne National Laboratory (ANL) provides coordination of the program activities for DOE. The other participating DOE laboratories are Brookhaven National Laboratory (BNL), Idaho National Laboratory (INL), Lawrence Berkeley National Laboratory (LBNL), Oak Ridge National Laboratory (ORNL), the National Renewable energy Laboratory (NREL), and Sandia National Laboratories (SNL). The two additional laboratories contributing to the program are the Army Research Laboratory and the Jet Propulsion Laboratory. As part of this program, ANL researchers maintain close communications and collaborations with a large number of international material supply companies, through which they gain access to the latest advanced electrode and electrolyte materials for evaluation.

Research and development within the ABR program can be characterized by two major features: what are the technologies under study and what is the common approach to all ABR scientific investigations. ABR projects all must deal with technological development with a near-term societal benefit—battery chemistries are selected for optimization and development that are expected to be in EDVs, commercially available, within a window of four to eight years. The common philosophy among all ABR projects is a problem-centric focus. This strongly complements the discovery-based research activities within the VTP-BATT program and those supported by the DOE Office of Basic Research.

The year 2011–2012 was a transitional year for the program, with major supporting facilities becoming operational. ANL has installed and is bringing into full operation three new facilities: a materials scale up facility, a cell fabrication facility, and a cell tear down and diagnostics facility. These three operations will be critical to the future success of this program as they will enable full investigation and characterization of new material and cell variations in commercially relevant cells (18650s and 1Ah pouch cells).

Central to the mission of ABR is the ability to test and study the most promising new cell materials as complete cells with cells and components fabricated as functional battery components. The service facilities established under the Recovery Act and completed last year make this possible. The three service facilities at Argonne National Laboratory provide cell materials (the Battery Materials Scale-Up Research program within Argonne's Materials Engineering Research Facility (MERF)), fabricated electrodes and full cells (the Cell Fabrication Facility), and post-test breakdown and diagnostics (the Post-Test Facility.) These services are available to all participants in ABR, as well as other DOE programs. Over 150 square meters of electrodes have been supplied to DOE researchers across eight different national labs to serve their testing needs. The scale-up work in electrolyte and electrolyte additives at MERF has produced four additives/components all being evaluated for use in next-generation Li-ion batteries. Three more components are in the

manufacturing scale-up process right now. The post-test facility has provided spectroscopic, microscopic, and electrochemical characterization of hundreds of samples, the majority coming from materials fabricated into Li-ion batteries.

In fiscal year 2012, several projects were either started or re-aligned with the overall objective of providing a more detailed understanding of various critical materials and component processing functions. These processing R&D projects included work at Oak Ridge National Laboratory directed at on-line characterization and quality control during electrode fabrication and at utilizing aqueous slurry technology in electrode preparation, moving away from the cost and safety issues of a flammable, toxic manufacturing solvent. At Argonne National Laboratory, in addition to work in optimizing electrode composition and fabrication conditions in the Cell Fabrication Facility, researchers who had previously focused on developing new active cathode materials (ACMs), moved their efforts onto improving the understanding of the role precursor compounds played in synthesizing ACMs. The National Renewable Energy Laboratory in Denver, CO joined the ABR teram in 2012 to begin work on applying state-of-the-art atomic layer deposition (ALD) coating technologies to treating electrode materials and electrodes with the aim of extending life, and improving performance and safety.

The remainder of this section provides technical highlights and progress on the Applied Battery Research program for FY 2012. The information provided is representative only and detailed information is available from publications cited in each project overview.

IV.B Materials Research

IV.B.1 ABR Project: Mitigation of Voltage Fade in Lithium-Manganese-rich Oxide Cathode Materials (ANL)

Anthony Burrell

Argonne National Laboratory
9700 South Cass Avenue
Argonne, IL 60439-4837
Phone: (630) 252-2629
E-mail: Burrell@anl.gov

Collaborators:
Ali Abouimrane, Daniel Abraham, Khalil Amine, Mahalingam Balasubramanian, Javier Bareno Garcia-Ontiveros, Ilias Belharouak, Roy Benedek, Ira Bloom, Zonghai Chen, Dennis Dees, Kevin Gallagher, Hakim Iddir, Brian Ingram, Christopher Johnson, Wenquan Lu, Nenad Markovic, Dean Miller, Yan Qin, Yang Ren, Michael Thackeray, Lynn Trahey, and John Vaughey all from Argonne National Laboratory

Start Date: March 2012
Projected End Date: September 2014

Objectives

- Define voltage fade. September 2012, (complete)
- Establish test protocols. September 2012, (complete)
- Benchmark materials properties using different synthesis techniques. September 2012 (complete)
- Initiate detailed structural analyses of composite electrode structures at the Advanced Photon Source (APS) by X-ray diffraction, X-ray absorption and pair-distribution function (pdf) analyses. September 2012, (complete)
- Initiate measurement of entropy changes in standard composite cathode material. September 2012, (complete)

Technical Barriers

The objective of the work is to enable the Argonne high energy composite layered cathode $xLi_2MnO_3 \cdot (1-x)LiMO_2$ (M = Ni, Mn, Co), also referred to as lithium and manganese rich NMC material (LMR-NMC), for the 40-mile PHEV (PHEV-40) application. This class of materials offers the potential for capacities exceeding 250mAh/g, excellent cycle and calendar life, and outstanding abuse tolerance. This material currently possesses a voltage fade issue (and other related issues) that effects its long-term cycle life and this issue needs to be resolved.

Technical Targets

- Develop a cell to meet the 10-mile PHEV goal.
- Obtain a positive-electrode material that can operate in the high-potential range (4V – 5V vs. Li/Li+) while still achieving approximately 130 mAh/g of capacity.
- Develop and utilize a high-potential, stable electrolyte system that can operate in the temperature range of -30°C to 55°C.

Accomplishments

- Established performance metrics for the LMR-NMC materials.
- Established voltage fade test protocols.
- Established data presentation format for voltage fade.
- Established a database for all voltage fade data.
- Initiated compositional analysis of Li, Mn, Ni, and Co for database.
- Produced single particle mounted samples for *in situ* analysis.
- Design and fabrication of an *in situ* cell-mount was successfully carried out which allowed easy acquisition of reliable electrochemical and X-ray diffraction data.
- Two composite cathode materials were prepared with different compositions and synthesis conditions and tested against the Toda HE5050 baseline material under various cycling protocols. *In situ* and *ex situ* X-ray absorption and diffraction data were also collected and analyzed.
- Initiated atomic scale modeling to develop and evaluate hypothesis for fade mechanisms.
- A purchase order was finalized for a 300 MHz (7.02 Tesla) Solid State NMR dedicated magnet and spectrometer with high spinning speed capability. A static probe is also included to initiate additional *in situ* studies. Bruker Inc. estimates Spring 2013 delivery.
- Synthesis of lithium-6 and deuterium enriched electrolyte and cathode materials.

- ^{6}Li MAS NMR experiments on pristine and cycled Li_2MnO_3 and TODA HE5050 cathode materials.

- ^{2}H MAS NMR experiments on pure electrolyte and pristine/charged and discharged electrodes.

- The electrochemical properties of lithium-nickel-manganese-oxide composite electrode structures in three-component 'layered-layered-spinel' systems, prepared by lowering the lithium content of 'layered-layered' $Li_2MnO_3 \bullet LiMO_2$ materials (M=Mn, Ni), were evaluated.

- The effects of Mg substitution and AlF_3 coatings on 'layered-layered-spinel' electrode materials were studied.

- A baseline system, $xLi_2MnO_3 \bullet (1-x)LiCoO_2$, was used to initiate in-depth studies at the Advanced Photon Source to determine structural features that would shed light on, and provide clues to counter, the voltage decay phenomenon in 'layered-layered' electrodes.

- Established an electrochemical quartz crystal microbalance in an inert atmosphere for the measurement of cathode SEI mass change.

- Submitted request for synchrotron time to perform fluorescence-overlaid-tomography of single, cycled LMR-NMC cathode particles.

<div align="center">✧   ✧   ✧   ✧   ✧</div>

Introduction

$xLi_2MnO_3 \bullet LiMO_2$ (M = Ni, Co, Mn) composite cathode materials currently receive world-wide attention as promising candidates for the next generation of high-capacity lithium-ion batteries. This class of materials is capable of delivering 250 mAh/g or more over extended cycling. However, in order to access such capacities, these materials must first be 'activated' to high voltages (>4.5 V) to access lithium associated with Li_2MnO_3-like domains. During the activation process oxygen loss and transition metal (TM) migration and rearrangement have both been reported; after which, a continuous decay of the average voltage with cycling is observed. In addition, a large hysteresis in voltage is observed when cycling over the extended windows (~4.6 – 2.0 V) needed to obtain the desired capacities. Therefore, the decrease in energy output with cycling is accompanied by an overall energy-inefficiency. To date, no work, to our knowledge, has been directly aimed at understanding hysteresis in lithium-excess materials. This work begins an initial investigation into the hysteresis phenomenon in order to better understand the structural and chemical properties of composite materials as a function of lithium content and to explore possible correlations, if any, related to voltage fade.

We propose an integrated approach to solving this critical issue which involves a coordinated set of characterization and synthesis experiments designed to both understand the causes of voltage fade and then eliminate the problem. To do this, we have formed a team of researchers that can maximize the ANL capacities in theory, materials development, characterization, cell level modeling, testing, scale-up and characterization.

Approach

Bring together a diverse technical team that will share data and expertise to "fix" voltage fade in the LMR-NMC cathode materials. This will be a single team effort (i.e. not multiple PI's working independently on the same problem).

- Definition of the problem and limitations of the composite cathode materials.

- Data collection and review of compositional variety available using combinatorial methods.

- Modeling and Theory.

- Fundamental characterization of the composite cathode materials.

- Understand the connections between electrochemistry and structure.

- Synthesis.

- Post treatment/system level fixes.

Results

Underpinning data collection and methodology.

Baseline materials selection.

While there cannot be a "perfect" baseline material in the LMR-NMC class due to the breath of potential materials compositions and almost infinite processing variations we selected a commercial batch of HE5050 ($0.5Li_2MnO_3 \bullet 0.5LiMn_{0.375}Ni_{0.375}Co_{0.25}O_2$,) as our initial reference point. We have 10kg of well characterized material which has been validated in our Materials Validation Facility and electrodes prepared in the Cell Fabrication Facility (CFF). The Toda HE5050 electrodes have also been sent to ARL, JPL, LBNL, BNL, ORNL, NREL and INL and as such present the most well characterized sample of an LMR-NMC material known. This baseline material will be used to validate any post formation modifications (coating for example).

Materials and experimental details.

The LMR-NMC, $0.5Li_2MnO_3 \bullet 0.5LiMn_{0.375}Ni_{0.375}Co_{0.25}O_2$, is supplied by Toda according to specifications provided by Argonne. It is commonly referred to as "TodaHE5050". The other two oxides are $LiNi_{0.8}Co_{0.15}Al_{0.05}O_2$, also known as NCA, and $Li_{1.05}(Ni_{1/3}Co_{1/3}Mn_{1/3})_{0.95}O_2$, also known as NCM333. Note, that the NCA does not contain any Mn and Li

concentration is stoichiometric; the NCM contains 31.3% Mn and is slightly Li-rich.

Table IV - 1 summarizes chemistries and electrode formulations of the positive electrodes tested. Galvanostatic cycling is conducted in 2032-type coin cells (1.6 cm^2 area electrodes) with Li-metal counter electrodes. They are assembled in an Ar-atmosphere glove box (O$_2$ < 10 ppm, H$_2$O < 1 ppm) and cycled at exactly 30°C. A standard cycling protocol is used to allow all future work to be directly comparable. This protocol uses moderate charge and discharge rates of <C/10 to reduce electrode polarization. Electrochemical cycling is carried out over a 2.0 and 4.7 V vs. Li$^+$/Li voltage window. The protocol also measures cell resistances via a current interrupt technique at various cell voltages during charging and discharging. The current is stopped for 10 minutes and voltages are recorded before and after the stopping period to estimate the cell resistance. This value is then used to estimate the near equilibrium voltage, also referred to as resistance corrected voltage.

Table IV - 1: Chemistry and Formulation of Positive Electrodes Tested for Voltage Fade

Desciption	TodaHE5050 baseline	NCA	NCM333
Active material	86 wt.% Li$_{1.2}$Ni$_{0.15}$Mn$_{0.55}$Co$_{0.1}$O$_2$ (Toda HE5050)	84 wt% LiNi$_{0.8}$Co$_{0.15}$Al$_{0.05}$O$_2$ (Fuji CA1505)	84 wt% Li$_{1.05}$(Ni$_{1/3}$Co$_{1/3}$Mn$_{1/3}$)$_{0.95}$O$_2$ (Enerland)
Binder	8 wt.% PVdF (Solvay 5130)	8 wt% PVdF binder (Kureha KF-1100)	8 wt% PVdF binder (KF7208)
Additives	4 wt.% SFG-6 graphite (Timcal) 2 wt.% SuperP (Timcal)	4 wt% SFG-6 graphite (Timical) 4 wt% carbon black (Chevron)	8 wt% SuperP carbons
Current collector	Al, 15 μm	Al, 30 μm	Al, 20 μm
Electrolyte	1.2 M LiPF$_6$ in ethylene carbonate : ethyl methyl carbonate (3:7 by wt.)		
Separator	25 μm thick (Celgard 2325)		
Active loading density	6.64 mg-cm^{-2}	8.0 mg-cm^{-2}	10.24 mg-cm^{-2}
Electrode porosity	37%	29.3%	
Laminate thickness	35 μm	35 μm	58 μm

LMR-NMC baseline performance.

Figure IV - 1 shows charge and discharge voltage profiles of the first 20 cycles. Some capacity loss is apparent. Most of this occurs during and after the activation cycle (0th cycle). This is well known, and is mostly due to loss of oxygen from the active oxide, but also due to additional electrolyte reduction/oxidation processes. A gradual capacity loss from then on is related to a variety of degradation processes, including surface structural changes of the oxide particles, transition-metal ion dissolution from them, particle isolation, as well as cell resistance increase (apparent at the end of charging). Electrochemical cycling and impedance spectroscopy of three-electrode cells show that cell resistance predominantly originates from the positive side, and is related to surface film formation between the active oxide and electrolyte which impedes Li-ion motion, as well as a degrading electronic network.
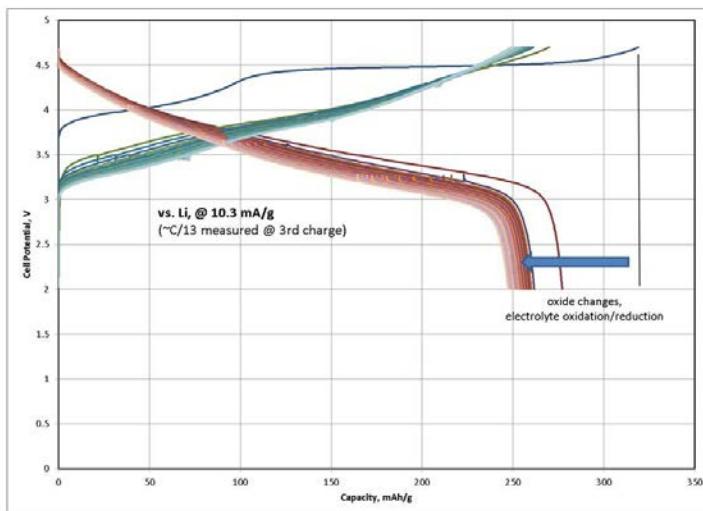

Figure IV - 1: Charge and discharge voltage profiles of the LMR-NMC 0.5Li$_2$MnO$_3$•0.5LiMn$_{0.375}$Ni$_{0.375}$Co$_{0.25}$O$_2$ cycled against metallic Li for 20 cycles. Various mechanisms have been identified to cause the apparent capacity fade**.**

To identify voltage fade, capacity loss and increasing cell resistance need to be factored out first. One way of doing this is to show capacity-normalized voltage profiles. This is done in Figure IV - 2. If the normalized *charge*

profiles drop in voltage, despite an increase in cell resistance, the oxide material experiences severe voltage fade. Figure IV - 2 also shows normalized profiles during discharging. Here, however a drop in voltage can also be partly related to increasing cell resistance. Nevertheless, it is clear that cell potentials drop over a wide range of charge states and discharge depths throughout cycling.
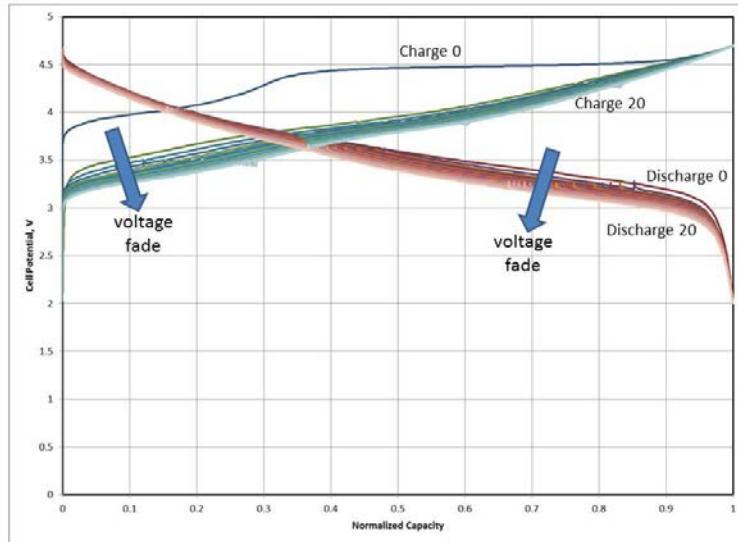

Figure IV - 2: LMR-NMC voltage profiles during charge and discharge versus normalized capacity. Voltage fade is clearly evident**.**

Another way of demonstrating voltage fade is to calculate average charge and discharge voltages and plot them versus cycle number. This is done in Figure IV - 3 in which *resistance-corrected* average voltages are shown. Voltage fade is clearly evident: The average *charge* voltage decreases from 3.95 V to 3.77 V (~0.24% or 10 mV per cycle, excluding 0th and 1st cycles); and the average *discharge* voltage decreases from 3.65 V to 3.53 V (~0.17% per cycle) after 20 cycles. Note that the biggest drop in average voltage within one cycle occurs after the initial activation charge, clearly evident in Figure IV - 1 and Figure IV - 2. Note also that the average charge potential drops faster than the average discharge potential. Extended cycling up to 80 cycles (data not shown) reveals that the average voltage continues to decay steadily at a rate of 1.5 mV per cycle from the 50th cycle onward.
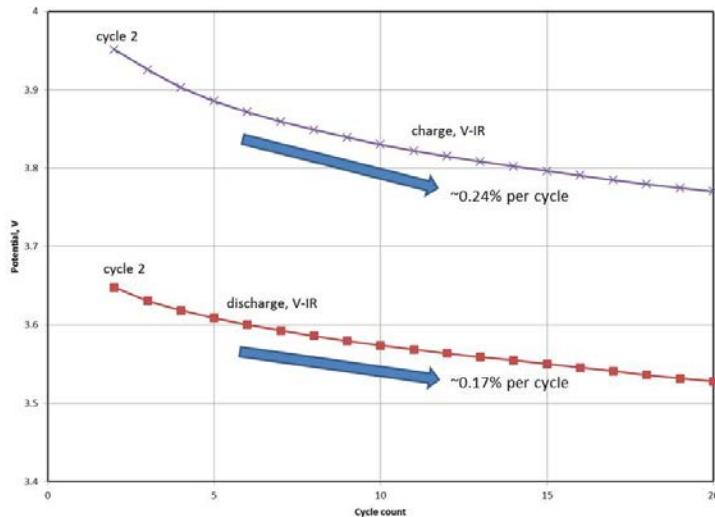

Figure IV - 3: Resistance-corrected average cell potentials plotted versus cycle number. A continuous drop in average potential exceeding 0.1V is apparent during charging and discharging. The drop in average charge potential is larger than the drop in the average discharge potential. The average potential is calculated by dividing the measured total energy (current x time x voltage) by the measured cell capacity (current x time)**.**

Comparison of the LMR-NMC baseline to NCA and NCM oxides.

Capacity-normalized voltage profiles for the NCA and the NCM333 materials are shown in Figure IV - 4 and Figure IV - 5, respectively. Voltage windows and cycling conditions are comparable to those of the baseline material. Note, that the cycling window of 2.0 to 4.7 V vs. Li$^+$/Li is relatively wide for these oxides; it is however of technical interest to investigate performance over a wide voltage range to maximize the cell's deliverable energy, and simply to also allow direct comparison to the baseline material.

A closer look at NCA and NCM materials in Figure IV - 4 and Figure IV - 5 shows that voltage fade is not unique to Li- and Mn-rich materials. However, the voltage fade of the LMR-NMC appears to be unparalleled. Only moderate voltage fade is apparent for the NCA and NCM oxides. While the NCA shows signs of fade only when above 4.2 V (i.e. at high state-of-charge), the NCM shows signs of fade across all charge states and discharge depths.
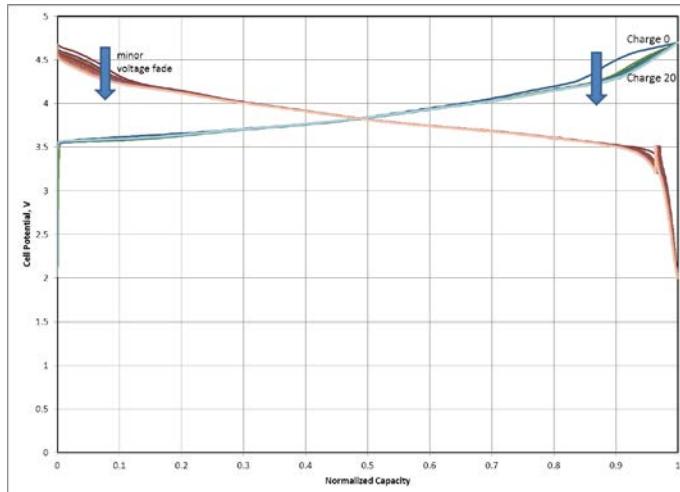
Figure IV - 4: Capacity-normalized voltage profiles for NCA. Some minor voltage fade is apparent at the end of charge and beginning of discharge.
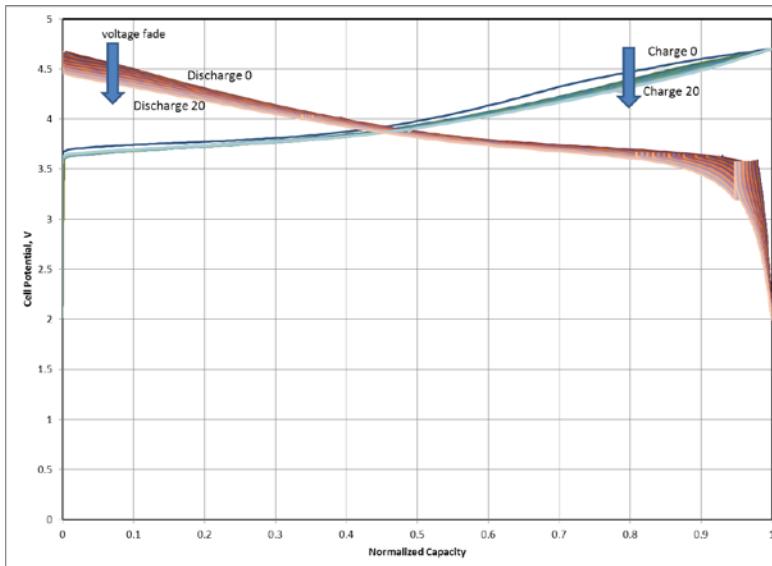

Figure IV - 5: Capacity-normalized voltage profiles for NCM333. Some voltage fade is apparent over all charge states and discharge depths.
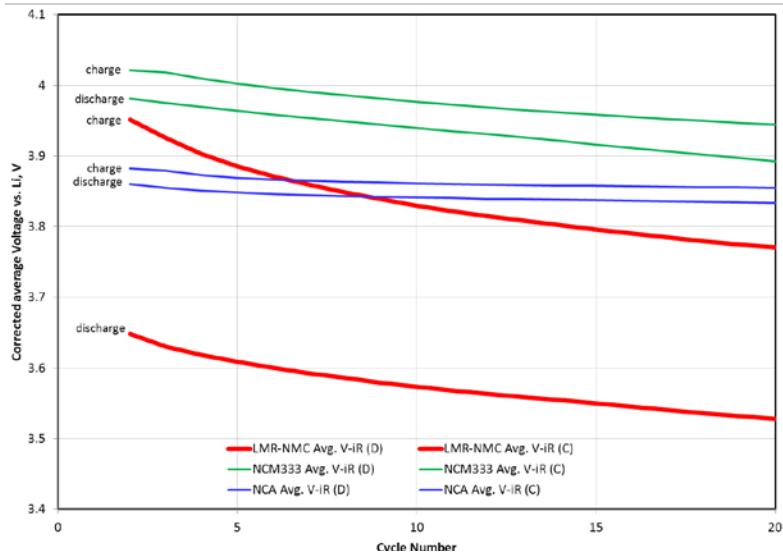
Figure IV - 6: Resistance corrected average charge and discharge voltages for the LMR-NMC, NCA and the NCM333 oxides. All three materials show voltage fade, however fade is strongest for the baseline material**.**

Figure IV - 6 contrasts these three materials in terms of their resistance-corrected average charge and discharge voltages and confirms the observations just described. While only minor voltage fade is observed for the NCA oxide (~1 mV per cycle), more fade is experienced by the NCM oxide (~5 mV per cycle) during charge and discharge. Noteworthy is also that all materials fade primarily during the initial cycles. However, voltage fade of the NCA appears to slow down and its average voltage approaches a constant value of 3.85V. The NCM and LMR-NMC continue to show voltage fade over 20 cycles - with no sign of approaching a constant average voltage. After 20 cycles, the average discharge voltages of both drop below 3.90V and 3.55V. Figure IV - 6 also displays the hysteresis (difference between charge and discharge voltage) of the three materials. Note that the baseline's hysteresis is exceptionally large and close to 250mV

(NCA: ~30mV; NCM: ~60mV). These initial data suggest that voltage fade is a phenomenon experienced by at least some, if not all, layered oxide materials. Future work will investigate exactly this phenomenon in greater detail.

Voltage fade, along with capacity losses and resistance increases result in decreasing energy densities. Loss of deliverable energy for the three oxide electrodes is shown in Figure IV - 7. Here, it is apparent that the LMR-NMC material, when compared to NCA and NCM, is indeed a high-energy material, despite the observed voltage fade. However, future work will need to investigate whether voltage fade eventually leads to inferior energy densities after 100+ cycles. The gravimetric energy density of the LMR-NMC drops by approximately 0.7% per cycle with energy efficiencies around 91% for the first 20 cycles. All oxides show capacity fade on cycling, which contribute to the energy loss on cycling is also shown.
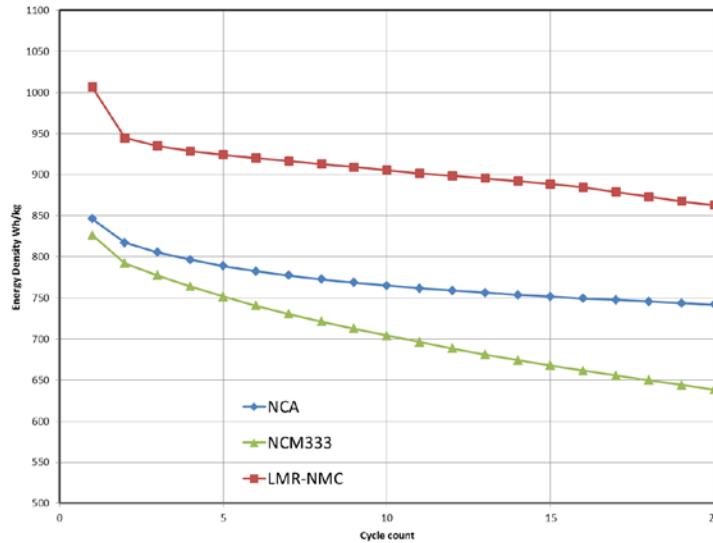
Figure IV - 7: Gravimetric energy densities during discharge plotted versus cycle number for LMR-NMC, NCA, and NCM. Voltage fade, along with capacity loss and cell resistance increase, lead to an overall loss in deliverable energy for a given amount of active oxide.

Metrics.

An initial set of performance targets have been created using the Battery Performance and Cost model (BatPaC is available from www.cse.anl.gov/batpac). The most significant value of the LMR-NMC cathodes is realized when they are paired with an advanced Li-ion anode. Thus, we used data from a modified graphite-silicon composite electrode (GrSi) to understand the relationship between cathode performance and pack level cost. The assumed properties of the advanced Li-ion anode electrode are as follows:

- 1,300 mAh g^{-1} and 1,040 mAh cm^{-3}
- 85% 1st cycle efficiency
- 50% electrolyte porosity in the discharge state
- 80:10:10 active:binder:carbon

Two benchmarks are used to set the performance targets for the LMR-NMC cathode. The first comparison is to the next best cathode option. *The LMR-NMC material must result in a lower cost, higher performance battery than the other options or it will not be utilized.* A high performance, low cobalt NMC material is selected as the next best cathode option for Li-ion batteries. This cathode has a specific capacity of 175 mAh g^{-1} at the C/3 rate and an average open-circuit voltage (OCV) of 3.85 V vs Li when operated up to 4.4 V. The second comparison is against the DOE/USABC PHEV40 cost targets. Batteries were designed for both PHEV40 (17 kWh, 65 kW, 360 V) and EV150 (40 kWh, 100 kW, 360 V) applications. Figure IV - 8 displays the result of these calculations against the benchmarks.
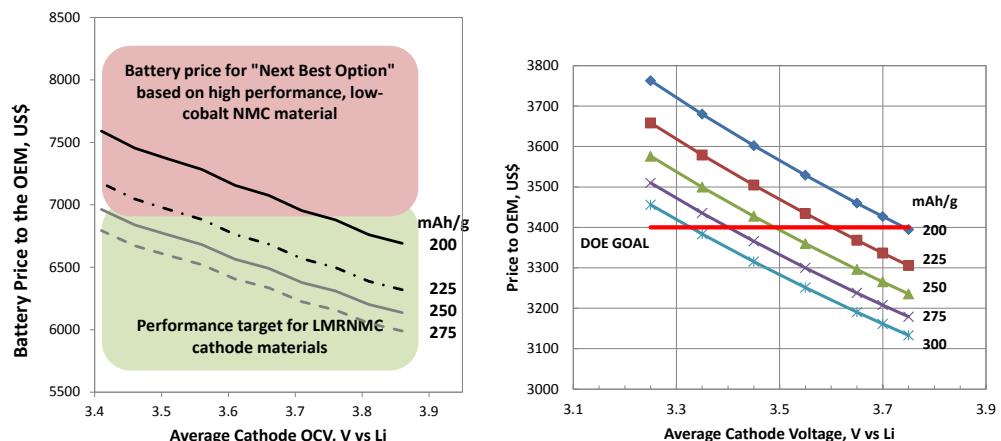

Figure IV - 8: Battery Price to OEM for an advanced Li-ion anode with LMR-NMC cathodes with varying capacities as a function of cathode OCV for (left) an EV150 compared against the next best Li-ion cathode option and (right) a PHEV40 compared against DOE goals.

Analysis of these two figures leads to similar requirements for the LMR-NMC material. As the capacity of the electrode increases, a slightly lower average voltage is allowable to still beat the benchmarks. An increase of 25 mAh g^{-1} is roughly equivalent to a 10 mV increase in voltage. The minimum average OCV for the following capacities (C/3 rate) are below. Since uncertainty exists in the input prices, advanced anode material, and other areas, these values below should be considered estimates of the minimum performance necessary.

It remains to be seen if higher valued OCVs (+20 mV) than those listed below are necessary for the implementation of LMR-NMC in commercial cells.

LMR-NMC minimum performance target (capacities at C/3 rate)

- 225 mAh/g and U_{avg} > 3.60 V vs Li

- 250 mAh/g and U_{avg} > 3.50 V vs Li

- 275 mAh/g and U_{avg} > 3.40 V vs Li

As an aside, a current area of intense development by OEMs and battery manufacturers is the design of a powertrain that makes the most efficient use of cell chemistries that operate over a wide voltage window such as LMR-NMC, particularly LMR-NMC/GrSi. Success in this industrial effort is necessary for the use of the LMR-NMC cathode materials in vehicle applications.

Testing Protocols.

Based upon our understanding of the baseline material and the use of the economic model we selected, a standardized test protocol has been established to reliably measure the average OCV for all investigators in the ABR program. The protocol was written to correct for ohmic losses and maximize the fraction of Li-ions accessed within the LMR-NMC material. Initial testing is completed at room temperature to expand the range of accessible test stations. If voltage fade is minimal, accelerated testing is then completed at 55 °C. Ira Bloom (ANL) has created an Excel Macro that automatically processes the cycling data for average voltage, ohmic loss correction, and plots various figures of interest.

The initial test protocols are:

Electrode fabrication (laminate preparation)

The cathode material should be prepared with a specific capacity near 1.5-1.75 mAh/cm^2. This translates to a specific active mass loading of 6 to 7 mg/cm^2 for a cathode material with 250 mAh/g of reversible capacity. This loading was chosen as it will likely balance to premade graphite negative electrodes (e.g. Saft made A12 graphite electrode). Further assessment of first cycle capacity and other measurements is necessary to assure a well-balanced cell.

The electrode is also recommended to be made with the standard electrode composition of 84 wt% active

material, 8 wt% PVDF binder, 8 wt% Super P Li carbon black. Alternate compositions may be used as the tester sees fit, but the change should of course be reported.

Cycling protocol

- 1st Electrochemical Evaluation

- Cell configuration: Lithium metal as negative

- Temperature: room temperature

- First cycle: as the tester desires; 2-4.7V 10 mA/g recommended. Cycling procedure: 20 mA/g and 2 V to 4.7 V; Current interrupts will be implemented at (charge) 3.5V, 3.9V, 4.3V and (discharge) 4.7V, 4.0V, 3.6V, 3.2V, and 2.0V each with a 10 minute rest to measure a quasi-OCV. Further testing protocols at 55C are implemented for any material that passes this initial testing.

- Number of cycles: >20

- Total test time: >20 days

Confirmation on the effectiveness of the test protocols an evaluation of the effect that both initial charge voltage and cycling voltages have on voltage fade in HE5050 (0.49Li$_2$MnO$_3$ • 0.51LiNi$_{0.37}$Co$_{0.24}$Mn$_{0.39}$O$_2$, Toda) was carried out. Figure IV - 9 shows the 1st and 6th discharge capacity for a range of cells charged to different voltages and then cycled to different maximum voltages. It is apparent that the discharge capacity increases with increasing the high cut-off voltage. In addition, the discharge capacity on the 6th cycle is largely independent of the charging voltage. It appears that the only factor that limits capacity in this study is the high voltage cut-off. Finally, the capacity seems increasing linearly with cut-off voltage until 4.7V cut-off voltage, there is not significant advantage in cycling to greater than 4.7V regardless of charging voltage.
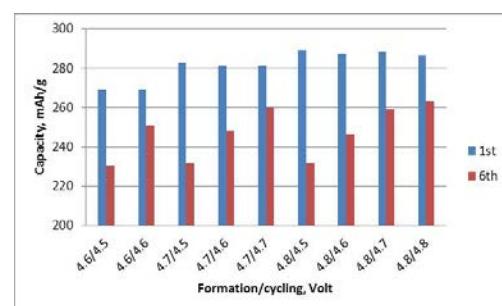

Figure IV - 9: Discharge capacity after 1st and 6th cycles under various testing conditions.

Moreover there is a perception that voltage fade does not occur at lower cycling voltages. This is not the case and using the normalized capacity then plotting average voltage vs cycle voltage, as shown in Figure IV - 10, fade is observed at all voltages.
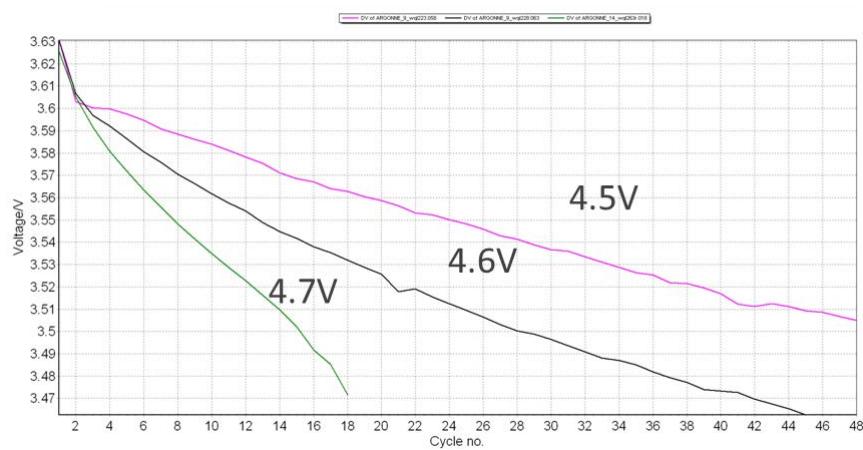
Figure IV - 10: Voltage fade observed after a 4.7V formation with various cycling voltages.

Database.

We have developed a database (see Figure IV - 11), where all data generated in this project will be stored, which is in the process of being populated. Data that is collected using the standard protocols will be included and directly comparable. Other data will be added as it becomes relevant. Once there is sufficient data available mining other factors and correlations will begin.
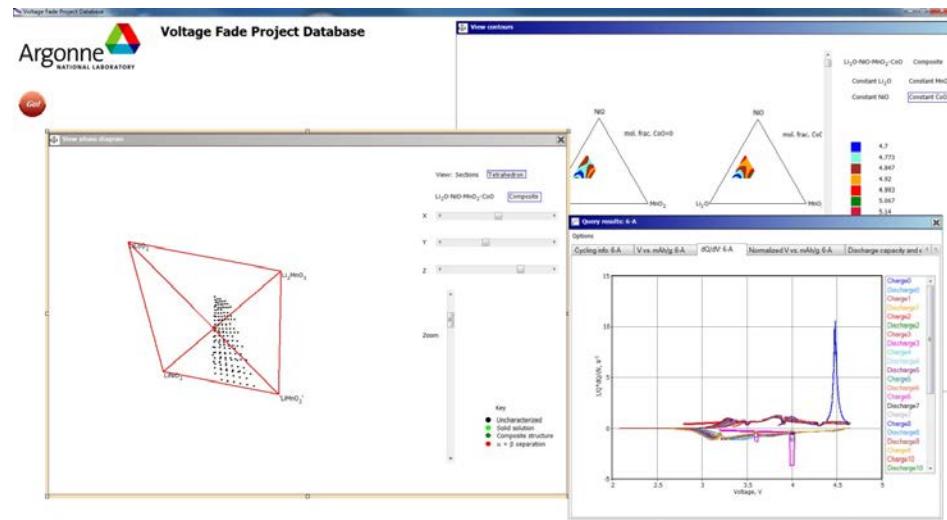

Figure IV - 11: Data base established for all voltage fade materials.

Materials characterization.

While many different compositions for LMR-NMC have been described no systematic study of how chemical composition affects voltage fade has been undertaken. We have taken advantage of the combinatorial equipment newly available at ANL to synthesize 147 different samples to explore wide range of composition of LMR-NMC material. We expect to get an overview of how the chemical composition, such as Li, Ni, Mn and/or Co concentration affects the voltage fade. There are many synthetic methods available for the formation of cathode materials we selected sol-gel as the most convenient and as the focus of this study is only comparing chemical composition effects and the internal consistency of the synthesis will provide the data required. The precursors have been prepared and composition we are systematically assessing the effect composition has on voltage fade all data is being entered into the database.

Atomic-scale models of voltage-fade materials.

Atomic-scale simulation is one of the diagnostic tools being applied at ANL to gain insight into characteristic atomic arrangements and transformations that occur in materials that exhibit voltage fade. During the first reporting period (03-2012 to 06-2012), first principles

DFT calculations at the GGA+U level were performed, with the VASP code, for a set of lithium-excess materials. We have focused initially on the pseudo-binary system $xLi_2MnO_3.(1-x)LiCoO_2$. The enthalpy of formation has been calculated as a function of x, for Li_2MnO_3 domains with different shapes within the $LiCoO_2$ matrix. The calculations employed 192-atom supercells, with each layer containing 6x8 ions. 15 different domain sizes were considered, in addition to the endpoints x=0, and x=1. The preliminary calculations allowed us to extract few heuristic rules with respect to the atomic arrangements within the materials. The formation energy (relative to phase separated Li_2MnO_3 and $LiCoO_2$) is found positive for all domain sizes, which indicates that phase separation is favored. Furthermore, no critical nucleus size exists below which energy increases with increasing domain size, so that agglomeration is favored for all domain sizes.

A positive surface energy exists between domains (of any size and shape) and the matrix, which is proportional to the under-coordination of the Li ions at the periphery of the domains. Ribbon-shaped domains are lower in energy, for given composition x, than compact domains, owing to their smaller Li under-coordination. Although phase separation and large domains are thermodynamically favored, real cathode materials are expected to contain a distribution of domains that span the full range of sizes; the actual domain size distribution reflects the temperature at which defect mobility and transition-metal atomic transport become negligible upon cooling, following the annealing step employed in most synthesis routes. Preliminary calculations for domains in $Li(Mn_{0.5}Ni_{0.5})O_2$ and $Li(Mn_{1/3}Ni_{1/3}Co_{1/3})O_2$, along similar lines to those for $LiCoO_2$, suggest similar behavior, with slightly lower domain formation energies than in $xLi_2MnO_3.(1-x)LiCoO_2$, owing to shielding of the Li at domain peripheries by Mn. Finally, simulations were performed of the initial delithiation of $xLi_2MnO_3.(1-x)LiCoO_2$. It was found that the thermodynamically favorable sites for removing Li and creating Co(4+) lie at the periphery of the Li_2MnO_3 domains, which enables the Co(4+) to shield the domain Li ions (see Figure IV - 12).

Example of ribbon Li_2MnO_3 domain within $LiCoO_2$ matrix

Calculated formation enthalpy vs. domain size for $xLi_2MnO_3.(1-x)LiCoO_2$
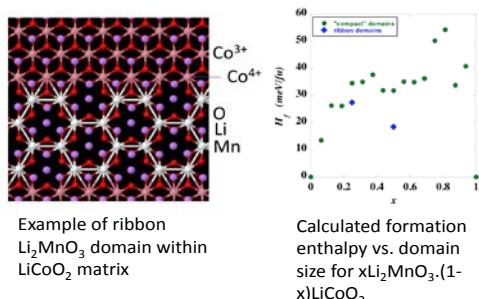
Figure IV - 12: Example Li_2MnO_3 Domain within $LiCoO_2$ Matrix.

Mixing enthalpy of $xLi(Li_{1/3}Mn_{2/3})O_2.(1-x)LiMO_2$.
First principles calculations were performed, at the GGA+U level, as a function of x, of the mixing enthalpy of

Li_2MnO_3 with a layered system $LiMO_2$. The periodic computational cell included 48 formula units and 192 atoms, and employed the R-3m structure. Each Li_2MnO_3 domain in the M layer consisted in a compact cluster of $LiMn_2$ trimers, arranged to maximize the number of Mn neighbors for each domain Li. Most effort was given to the model system M=Co (the subject of extensive experimental work at ANL) with some results also obtained for $M=Mn_{1/2}Ni_{1/2}$. Positive enthalpies were found for all x and all domain sizes considered. Ribbon domains have lower energy than compact domains, for a given domain size. Results are consistent with a phase diagram in which solid solubility, with SRO, exists for all x at high temperatures, and a miscibility gap, unobserved because of slow kinetics, occurs at low temperatures. Further tests of this picture would be valuable, however, since experiment indicates that for $M=Mn_{1/2}Ni_{1/2}$ and x=0.6, $LiMO_2$ is dissolved in C2/m (rather than R-3m) $Li(Li_{1/3}Mn_{2/3})O_2$.

NMC cluster expansion (collaboration with J. Bhattacharya, C. Wolverton, NU).

A DFT database is being generated for $M=Ni_{1/3}Mn_{1/3}Co_{1/3}$, to be employed in fitting ECI parameters for a cluster expansion. Calculations for thirty low energy configurations of a twelve formula unit cell were performed (see Figure IV - 13). The cluster expansion will enable Monte Carlo simulations of thermally equilibrated structures at elevated temperatures at which synthesis and annealing are performed.
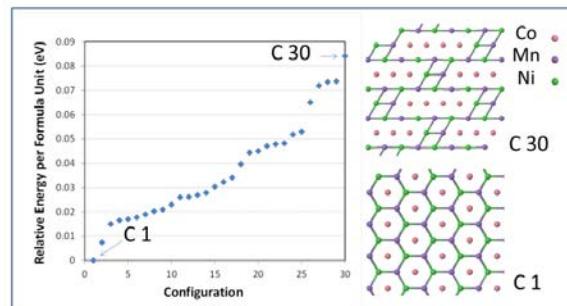

Figure IV - 13: DFT results for relative energies of thirty configurations of $Li(Ni_{1/3}Mn_{1/3}Co_{1/3})O_2$. The lowest energy configuration is the ordered arrangement C1. The partially segregated arrangement of C30, with NiMn zigzags interrupted by lines of Co, is still low enough in energy to be present at elevated temperatures.

Thermodynamic easements.

Thermodynamically, the voltage of LMR-NMC is directly related to the entropy change of the composite cathode material. Investigation on thermodynamics of composite electrode should shed a light on the root cause of its voltage fade during cycling. In addition, lithium ion diffusion and electronic conductivity of LMR-NCM will be studied to better understand the thermodynamics and kinetics role in voltage fade.

HE5050 electrode was then chosen for *in situ* heat generation measurement using 2032 coin type cells. The cell was charged and discharge at C/10 rate. Both

voltage profile and heat flow rate during charge and discharge were recorded and 3rd formation cycle is shown in Figure IV - 14. The blue curve is voltage and the red curve is for heat flow rate. The heat feature during discharge is found different to that during charge, which indicates the different process is taking place. This is consistent with the electrochemical analysis which shows significant hysteresis (Figure IV - 15) where relaxation is extremely slow, potentially indicating a high barrier phase change.
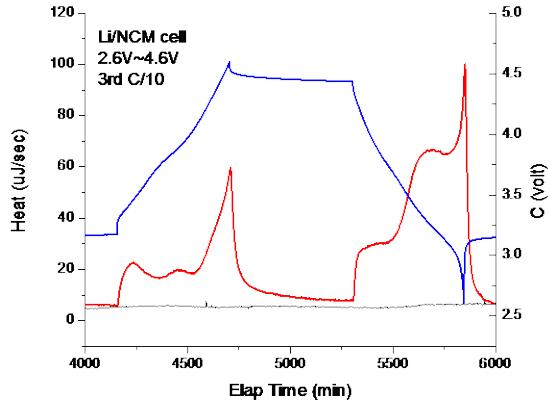

Figure IV - 14: Voltage and heat profile of HE5050 during charge and discharge.

Galvanostatic intermittent titration technique (GITT). Figure IV - 15 (a - d) display the potential and path dependence of the hysteresis for $Li_{1.25}Ni_{0.33}Mg_{0.02}Mn_{0.65}O_y$ synthesized via traditional precipitation methods. Starting from a discharged state, Figure IV - 15 (a), removing lithium from the structure follows the high potential boundary curve, or charging curve. Alternatively, starting from the charged state, Figure IV - 15 (b), lithiation of the structure follows the lower potential boundary curve or discharge curve. These scanning curves demonstrate critical states of lithiation where the measured OCV moves from one boundary curve to the other. The measurements show a jump from lower to upper boundary curves near a lithium content of 0.3 in $Li_{1-y}M_{0.8}O_z$ and a jump from upper to lower near 0.7. Examination of the corresponding dQ/dV plots, Figure IV - 15 (c) and (d), reveal a striking relationship between the upper and lower boundary curves. Figure IV - 15 (c), showing increasing apex potential scanning curves, suggests that the lithium sites emptied above 4.3 V are not filled again until 3.2 V on discharge; after which, charging again follows the upper boundary curve. A change in potential of 1 V is a dramatic hysteresis in site energy. The fraction of lithium content associated is estimated at 12% from electrochemical data.
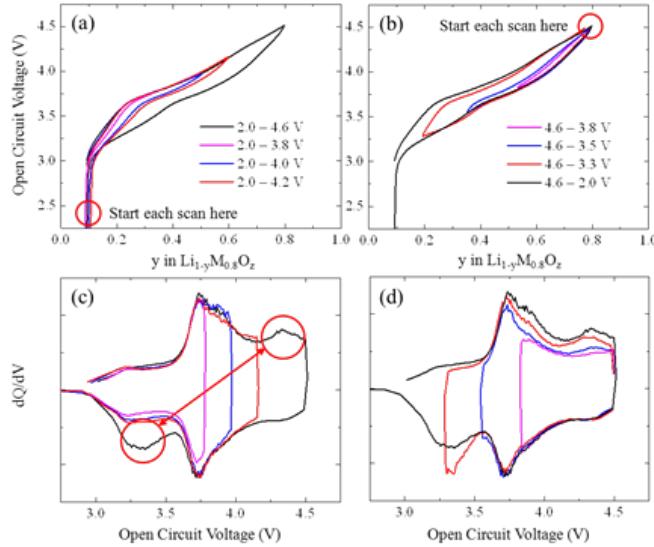

Figure IV - 15: Measured Open Circuit Voltages (a) and (b), and the corresponding dQ/dV (c) and (d) for $Li_{1.25}Ni_{0.33}Mg_{0.02}Mn_{0.65}O_y$.

The stability of the hysteretic loop is examined in Figure IV - 16. In this experiment, two cells are cycled through the activation process and then fully discharged to 2 V at 10 mA/g. The first cell is then charged to 3.7 V at 10 mA/g and potentiostated at this potential for 7 days. The second cell is charged to 4.6 V, discharged to 3.7 V at 10 mA/g, and potentiostated at this potential for 7 days.

Both cells were then discharged at 10 mA/g to 2 V to measure the accessible capacity of the material after the week long potentiostatic hold. As shown in Figure IV - 16, the hysteresis loop is not closed even after 7 days. Clearly, the hysteresis is stable on the timescales of interest to battery developers.
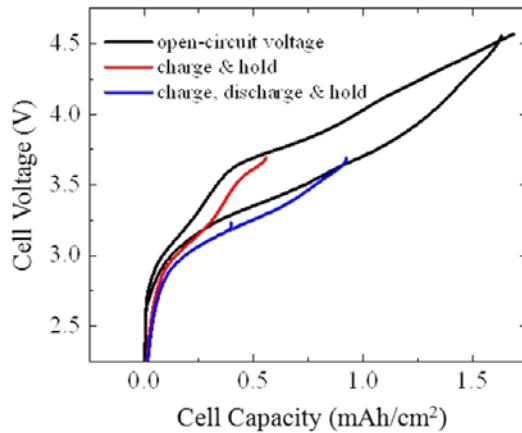
Figure IV - 16: Measured open circuit voltages at 3.7V on charge (red) and discharge (blue) after a 7 day potentiostatic hold for Li$_{1.25}$Ni$_{0.33}$Mg$_{0.02}$Mn$_{0.65}$O$_y$.

Figure IV - 17 shows the electrochemical and *in situ* diffraction results from a Li$_{1.2}$Mn$_{0.6}$Ni$_{0.2}$O$_2$ composite made by ion-exchange from a Li$_2$MnO$_3$ precursor. The samples had been cycled 9 times prior to measurements between 4.6 – 2.0 V to activate and establish a 'stable' structure. XRD data along the voltage curve (a) and the corresponding dQ/dV (b) were extracted from the *in situ* XRD data; 500 scan of which are shown from the (003) region in Figure IV - 17(c).


Figure IV - 17: (a) Voltage profile of cycle #10 during *in situ* XRD measurements and (b) the corresponding dQ/dV plot. (c) Raw XRD data during the charge/discharge process.

Figure IV - 18 (a) and (b) show the results of refinements for the sample shown in Figure IV - 16 and similar experiments conducted *ex situ* for the baseline Toda HE5050 composite (Li$_{1.2}$Ni$_{0.15}$Mn$_{0.55}$Co$_{0.10}$O$_2$). As can be seen from the data, the same general trend is observed for each composite despite the different compositions and *ex situ* versus *in situ* conditions. That is, a smoothly varying a lattice parameter and a more dynamic behavior along the c axis.
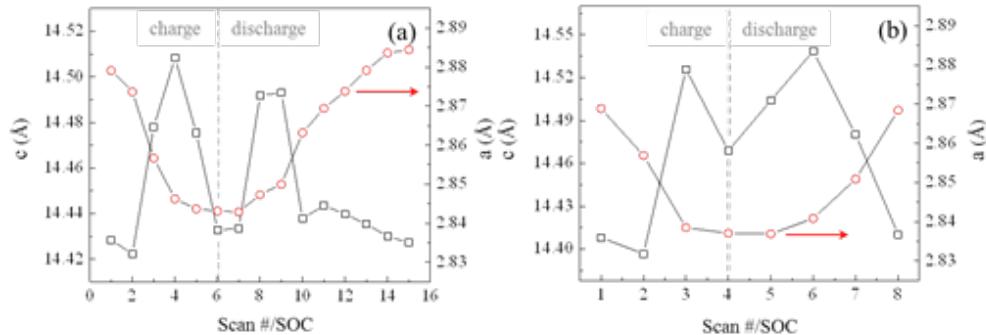

Figure IV - 18: Refined lattice parameters as a function of charge and discharge for Li$_{1.2}$Mn$_{0.6}$Ni$_{0.2}$O$_2$ (a) and the Toda HE5050 (b).

Figure IV - 19 shows *ex situ*, Ni K-edge X-ray absorption near edge spectroscopy (XANES) data for the Toda HE5050 at various states of charge and discharge. Comparing the edge at 4.2 V on charge (red) and discharge (purple) we observe similar edge energies (oxidation), however, there is almost a 15% difference in the SOC between these points. Similarly, comparing the same SOCs, i.e. ~75%, on charge (red) and discharge (orange), we observe clearly different edge energies (oxidation) between the two. Therefore, the same amount of lithium in the structure does not lead to the same voltage or oxidation of TMs on charge and discharge.
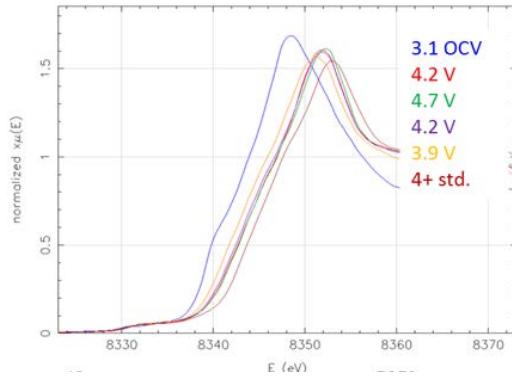
Figure IV - 19: Ni K XANES data for the Toda HE5050 comparing edge energies at different SOCs on charge and discharge.

The *In situ* and *ex situ* X-ray and electrochemical studies reveal that regardless of composition, synthesis method, or cycling protocol, 'activated' lithium-excess composite materials undergo hysteresis accompanied by similar lattice dynamics. The hysteresis in the composite materials is not due to kinetics, but rather, is a stable and persistent phenomenon. In addition the GITT studies show that lithium extracted above ~4.2 V cannot be re-accommodated on discharge until much lower voltages; revealing a ~1 V hysteresis in site energies. This voltage also corresponds to the limit to which 'activated' composite materials can typically be cycled without the onset of voltage fade. The XANES data reveal that similar

lithium contents (SOC) on charge an discharge lead to differing edge energies (oxidation) corroborating the GITT results that lithium does not have access to the same set of sites on discharge as on charge.

Material characterization during charge discharge.

High-resolution synchrotron x-ray diffraction.

The HE5050 standard material shows the typical superlattice reflections in the diffraction pattern due to the ordering of Li and transition metals (TMs) in the TM layers. The main features of the XRD pattern can be well described by a layered structure with the R-3m symmetry. The composition can be written as HE5050 = $\{Li_{1-x}Ni_x\}^{3a}[\{Li_{0.2+x}Ni_{0.15-x}Mn_{0.55}Co_{0.1}\}^{3b}]O^{6c}$, with *1.0(1)%* of Li/Ni exchange between Li in the Li layers and Ni in the TM layers. The lattice parameters are $a_h=b_h=2.85518(2)$ Å, $c_h=14.2479(2)$ Å, and $V_h=100.589(2)$ Å^3. If the monoclinic structure (C2/m) is used for profile fits (Figure IV - 20, left), one gets lattice parameters $a_m=4.94610(8)$ Å, $b_m=8.56459(9)$ Å, $c_m=5.02830(6)$ Å and $\beta_m=109.178(3)$ deg, $V_m=201.184(3)$ Å^3 (in comparison with $a_m=4.937(1)$ Å, $b_m=8.532(1)$ Å, $c_m=5.030(2)$ Å and $\beta_m=109.46(3)$ deg, $V=201.137(1)$ Å^3 from single crystal study by Strobel et al.). Note that $b_m/a_m=1.732=$sqrt(3). One can see the relationship between the two symmetries: $b_m\sim$sqrt(3)* $a_m\sim3* a_h$, and $c_m*cos(\beta_m-90)\sim c_h/3$.
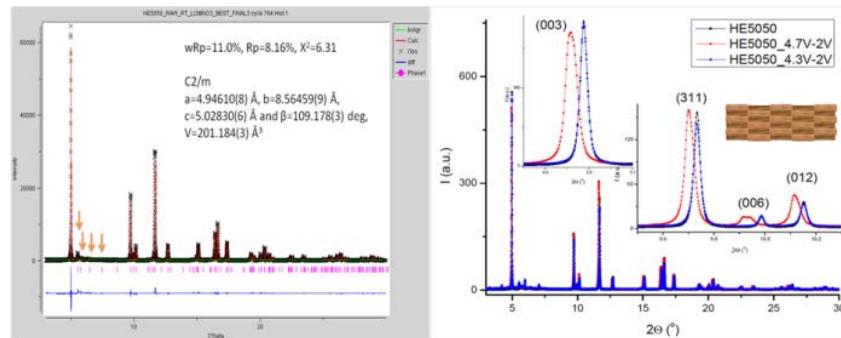

Figure IV - 20: (left) HR-SXRD pattern of HE5050 shows the super-reflections (020), (110), (11-1), (021), etc. due to the presence of Li/M ordering and associated monoclinic phase (C2/m). (right) HR-SXRD patterns of HE5050. HE5050_4.3V-2V_1 cycle, and HE5050_4.7V-2V_1cycle. The inset drawing shows a possible interconnected layered structure for the heterogeneous structure after the activation.

The HE5050 cathode was charged to 4.3 V and 4.7 V, respectively, and then discharged to 2.0 V. The diffraction patterns of the two cathode materials after first cycle were plotted together with the original HE5050 in Figure IV - 20 (right). The material that was charged to 4.3 V and discharged to 2.0 V (HE5050_4.3V-2V) showed almost identical XRD pattern to the HE5050, except slightly broadened peaks. But the materials that was charged to 4.7 V and discharged to 2.0 V (HE5050_4.7V-2V) has a pattern quite different from the raw HE5050, indicating a clear irreversible structural change. At first glance, the XRD can be well fitted using the layered structure with

lattice parameters of $a_h=b_h=2.86370(2)$ Å, $c_h=14.3315(2)$ Å, and $V_h=101.784(2)$ Å^3. There is *3.2(1)%* of Li/Ni exchange between Li in the Li layers and Ni in the TM layers, indicating a slightly more Ni moved to the Li layers after the activation. The activated HE5050 (4.7V-2V) has a lattice expansion of 0.30% along a, and 0.59% along c and a volume expansion of 1.19%, in comparison to the raw HE5050.

However, close inspections revealed that all peaks become broad and, especially, (00l) peaks are split. This indicated that after the activation (charged above 4.5V), the materials become structurally heterogeneous, or phase

separated. One possibility for the phase separation could be that two similar layered structures interconnected (the inset drawing in Figure IV - 20 (right)), but with a misfit (lattice strain) of 0.26% along the c axis (perpendicular to the layers) and 0.16% within the layers. But there might be other possibilities for the structural inhomogeneity.

With electrochemical cycling, the cathode particles undergo structural changes. We studied samples harvested from a coin cell that had been cycled 1,500 times. Transformations to spinel or "spinel-like" phases are commonly reported and were the dominant transformation observed in this work. However, a transformation to a rock-salt-related structure was also observed. Examples of each of the structures observed are shown in Figure IV - 21, for which Li_2TMO_3 and the layered phases were recorded from the as-prepared material and the spinel and rock-salt structures were recorded from cycled material.
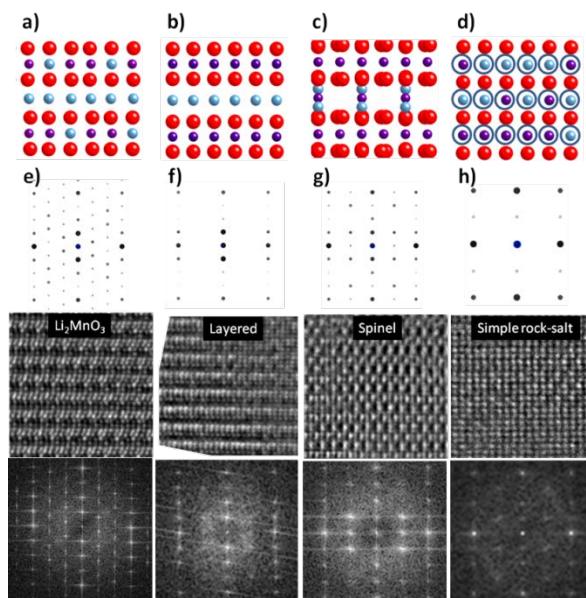

Figure IV - 21: Crystal structure models for Li_xTMO_2 phases; (a) Li2TMO3 (110 plane), (b) layered (1-100), (c) spinel (112) and (d) simple rock-salt (112). Oxygen is drawn as red, TM as purple, and Li as blue. The atom columns with circles represent randomly mixed Li/TM columns. The corresponding experimental selctron diffraction patterns, high resolution images, and Fourier Transform patterns from the high resolution images are shown under each crystal model (e-h).

The spinel-like phase is the dominant transformation product observed. This is illustrated in Figure IV - 22, which shows representative electron diffraction and high-resolution images for fresh, as-prepared oxide (Figure IV - 22 a,c) and for oxide harvested from the coin cell after 1500 cycles (Figure IV - 22 b,d).
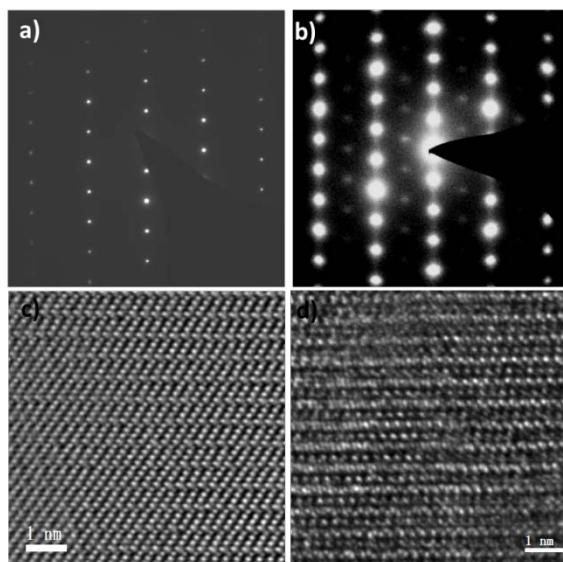

Figure IV - 22: Electron diffraction patterns from (a) fresh and (b) 1500 times cycled $Li_{1.2}Ni_{0.15}Mn_{0.55}CO_{0.1}O_2$ showing the transformation from layered to spinel-like structure. Corresponding high resolution images are presented in (c) and (d).

Figure IV - 23 shows a region of cycled material that reveals the rather uniform transformation to spinel-like phase over a larger region. With respect to the ideal layered phase, the transformation to spinel-like involves reordering of both lithium and TM (with a corresponding relaxation of oxygen) as can be seen by comparing Figure IV - 21b and Figure IV - 21c. The relaxation of TM to "Li positions" likely takes place during lithium extraction, induced by local structural distortions as Li moves out of the structure. This leaves TM-vacancy planes within the crystal in the delithiated state. However, it is important to note that the as-prepared oxide includes domains of both the layered $Li(Mn,TM)O_2$ phase and $Li_2(Mn,TM)O_3$, the latter already incorporating mixed layers containing both Li and TM (Figure IV - 21a). The presence of these pre-existing mixed layers is important – extraction of Li from these layers also leaves TM-vacancy layers. Thus, when Li is reintroduced, it faces an array of planes that begin to look more and more alike. In essence, the "pure" Li planes are lost and the structure tends towards a more uniform distribution of mixed TM-Li planes. From Figure IV - 21d, one can see that in the limit the rock salt structure may be a natural terminal phase.
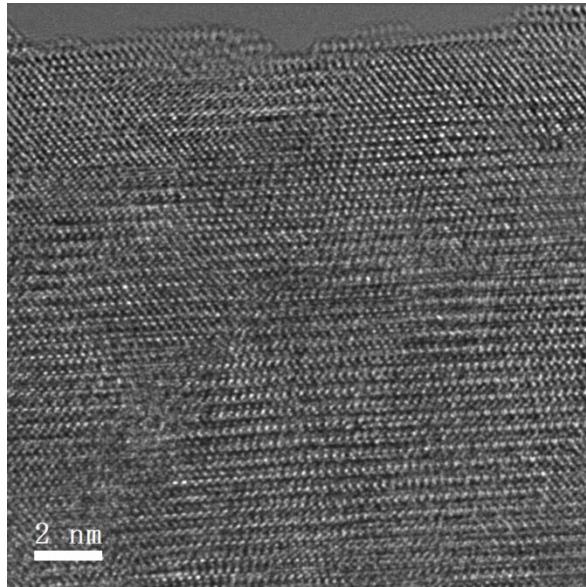
Figure IV - 23: High resolution image of $Li_{1.2}Ni_{0.15}Mn_{0.55}CO_{0.1}O_2$ after cycling (1500x) showing the uniform transformation to spinel-like phase.

While our observations show this reordering of TM, comparing the degree of cation mixing observed experimentally with structural models suggests that the reordering on the cation positions generally is not going as far as a mixing on every second or every cation position mixing (which would yield simple rock salt) even for many cycles, but it is moving in that direction. Rock salt is indeed one of the phases we observe in highly cycled material although only as a minority phase.

Clearly over a large number of cycles there are significant changes observed in the cathode material. The major issue is discovering how fast these changes occur and how much they are related to voltage fade. A major challenge in establishing the correlation between structural changes and voltage fade is that, even for small coin cells, the cathode consists of millions of individual particles. Thus, analyses on local regions that provide great detail about atomic-level structure and chemistry are difficult, if not impossible, to correlate with electrochemical behavior measured globally. Our approach to address this challenge is to carry out electrochemical measurements on single $Li_{1+x}(Mn,TM)O_2$ oxide particles so that the electrochemical and structural characterization can be carried out on the same region of material.

In order to carry out electrochemical measurements and microstructural characterization on the same material, we developed a microscale battery that uses a single oxide particle as the active cathode. An oxide particle attached to a probe serves as the cathode and the cell is completed by partially immersing the particle in a liquid electrolyte covering an anode/counter-electrode (Li for our current studies). The entire set-up can be implemented in a scanning electron microscope so that SEM imaging can be carried out while the cell is cycled, either live during cycling or by interrupting cycling to capture images at

specific points in the process. An example of the experimental set-up is shown in Figure IV - 24.
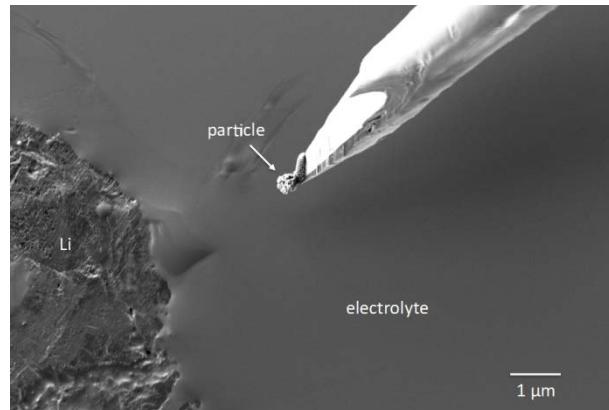
Figure IV - 24: Scanning electron microscope image of our microscale battery set up. A single $Li_{1+x}(Mn,TM)O_2$ particle is attached to a probe tip which serves as one electrode and is used to place the particle in the electrolyte covering the anode (Li metal in this case). In this image, the particle is just above the electrolyte.

One of the first and most important tasks required for this work was to perfect this measurement approach and establish that our localized electrochemical measurements truly provide a measure of voltage fade. Due to the size of individual particles and the challenges associated with the small currents required, the measurements we have carried out to date have been at about a 1C rate (corresponding to a $\approx$ 20 pA current). Although this rate is higher than that used in the standard coin cell testing protocol for voltage fade, we can achieve reliable electrochemical data even from a single $Li_{1+x}(Mn,TM)O_2$ particle, as shown in Figure IV - 25. These data are reasonably consistent with those obtained in real-world systems (coin cells) and clearly show the voltage fade effect in this single particle. However, much more work is required to confirm the electrochemistry at this scale.
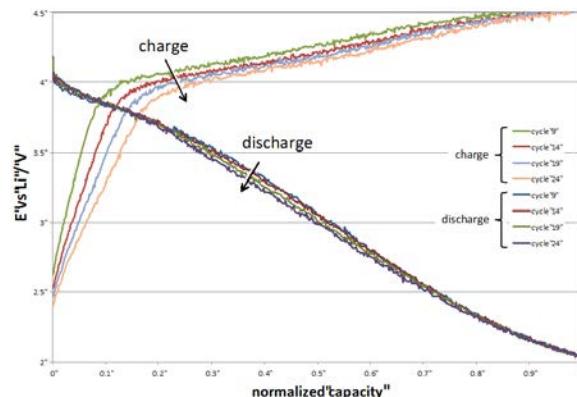
**Figure IV - 25:** Electrochemistry cycling data from a single $Li_{1+x}(Mn,TM)O_2$ particle collected using the setup shown in the previous figure.

With the capability to carry out single particle electrochemistry, the next challenge is to correlate those

measurements with structure. Our microscale approach provides the capability for scanning electron microscopy in concert with cycling, and an example of this is shown in Figure IV - 26 for the same particle for which cycling data is shown in Figure IV - 25. In this case, the post-cycling microscopy reveals a structure that is not significantly different from that typically observed in as-prepared material. This SEM-level observation is important. In other Li battery materials (such as $Li(Ni,Co,Al)O_2$), dramatic changes in structure can occur even in just one charge cycle, but no such phenomena are observed here. A subtle but important aspect of this particular observation is that we know the electrochemical response of this specific particle and that it did indeed exhibit voltage fade as seen in Figure IV - 25. In post-test characterization of particles harvested from coin cells, we have no reliable way of ensuring that any specific particle reflects the global electrochemical performance due to variations from particle to particle. It is this aspect of our localized measurement approach that will be even more important in the next phases as we move to more detailed characterization approaches such as transmission electron microscopy.

In future work, we will use this approach to further assess voltage fade in single particles and incorporate more comprehensive characterization approaches to complement electrochemical measurements. Firstly, by electrochemical cycling of single particles, we will learn if there are variations in the evolution and degree in voltage fade from particle to particle. This information can provide clues to the origin of voltage fade. Secondly, with the development of this single particle approach, we can now apply a variety of characterization approaches to a single particle, including tomographic and spectroscopic analysis. One of our major thrusts will be to apply comprehensive electron microscopy and spectroscopy, which provides atomic-level information regarding structure and chemistry. Correlated with baseline structural characterization that we have reported previously, these studies will provide more incisive insight into the role of local structure on voltage fade.
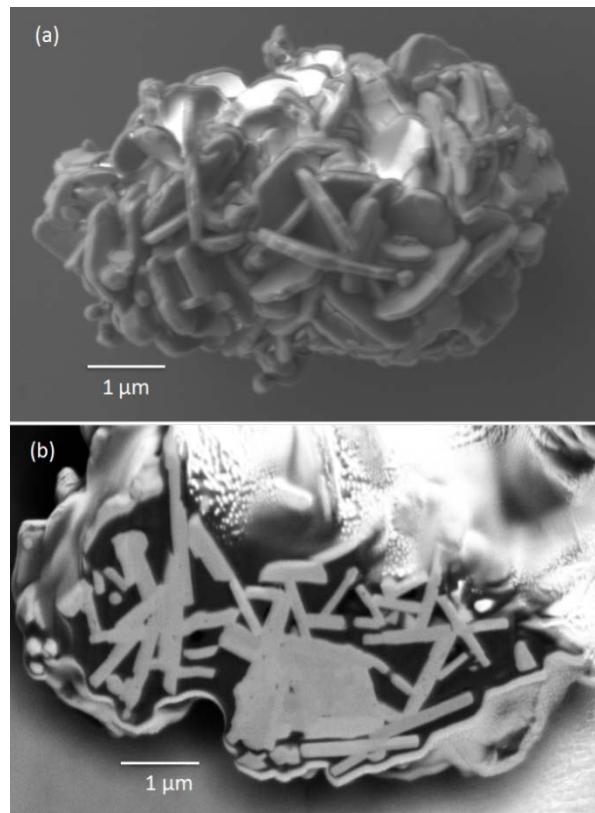

Figure IV - 26: Scanning electron micrographs of the $Li_{1+x}(Mn,TM)O_2$ particle from the previous figure (a) in the pristine condition before cycling and (b) after 26 complete charge/discharge cycles.

Solid State NMR. Solid State NMR is a quantitative local structure probe and can be used to determine which species are removed on charging the battery and how the local structure changed on extended cycling and how these changes effect the electrochemical performance. The local structure of the high energy materials and the changes upon activation and subsequent cycling are closely associated with electrochemical processes such as voltage fade and performance of the materials.

Synthesis and preparation. Prior to the installation of low field (7.02) high resolution NMR, preliminary experiments have been performed with the high field (11.7 T) system in place at ANL. Electrode materials were prepared using lithium-6 enriched precursors and a sol gel based high temperature synthetic method. Electrochemical evaluation was done using a lithium-6 enriched electrolyte. The electrolyte salt was synthesized via a precipitation reaction using ^6LiCl and $AgPF_6$ to obtain $^6LiPF_6$. The cell enrichment is completed using lithium-6 metal as anode.

In addition to following the movement and re-distribution of lithium cations, several models for voltage fade have invoked proton insertion (from electrolyte decomposition) as a component of the phenomena. Samples for detecting the presence of inserted protons into cathode lattice were prepared by using electrolyte prepared with deuterated solvents.

Preliminary NMR results. The ^{6}Li MAS NMR spectrum of the industry standard TODA HE5050 material is shown in Figure IV - 27 and reported for the 1st time for Li-rich NMC type materials. Two groups of resonances were observed for the Li species present in the lattice; Li in Li layers around 480-707 ppm and Li in transition metal layers around 1330-1430 ppm. For the lithium in Li layers, three resonances (480, 550 and 707 ppm) were observed indicating, presumably, the different local ordering/domains originating from Fermi-contact shifts of neighboring Ni, Co and Mn. Additionally, a large buildup of diamagnetic lithium species (-3 ppm) is detected upon cycling which requires further characterization.
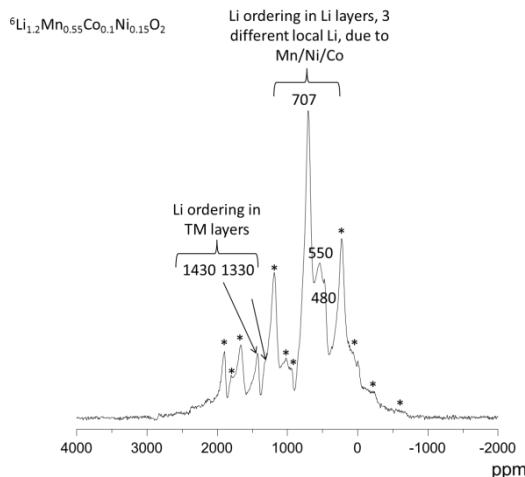

Figure IV - 27: ^{6}Li MAS NMR of pristine TODA HE5050 material at a spinning speed of 35 kHz at 11.7 Tesla magnetic field. * indicates spinning side bands.

For the lithium in transition metal layers, two resonances, at 1,330 and 1,430 ppm, were observed. These resonances are tentatively assigned to Li within 1Ni/5Mn and 6Mn type arrangements, respectively. However the true origin of all the resonances listed above and the corresponding Fermi-contact shifts are not clear and collaboration within ANL, with computational groups is currently in progress to aid in this regard. This study is going to focus on generating a rule set to calculate NMR chemical shifts and perform peak fitting from domain models.

Another relevant model material is Li_2MnO_3 which pre-activation constitutes the lattice stabilizing inactive component in the composite. However, during the activation, the role and electrochemical activity of this component is still unclear. A set of cycling experiments were performed with low temperature synthesized (450°C, electrochemically active) Li_2MnO_3 and the spectra are shown in Figure IV - 28. The resonances at 595 and 1240 are due to Li in Li layers and Li in transition metal layers respectively, for pristine Li_2MnO_3. Then the material is fully charged (delivering more than 300mAhg^{-1}) more than 90% of the Li in the lattice has been removed (see Figure IV - 28, Li_2MnO_3 full charge). The mechanism of such

extensive Li removal and its balance with lattice oxygen loss is unknown since previous studies indicated the Mn oxidation state remains at Mn(IV). Subsequent discharge results in intercalation of approximately 40% Li into the lattice, filling both Li sites in Li layers and transition metal layers. It must be noted that all the spectra are normalized for Li quantification. The mechanism for reintercalation in the activated material and post-activation structural re-arrangements is currently being investigated.
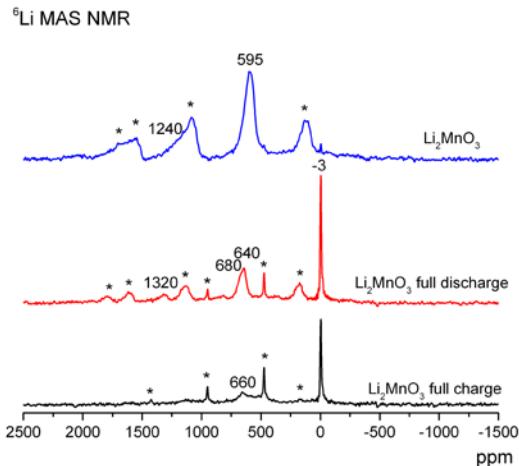

Figure IV - 28: ^{6}Li MAS NMR of cycled Li_2MnO_3 material at a spinning speed of 35 kHz at 11.7 Tesla magnetic field. * indicates spinning side bands.

NMR characterization studies on the possibility of proton insertion into the lattice were performed on industry standard TODA HE5050 material. Samples were cycled with deuterated electrolyte and characterized with ^{2}H MAS NMR after one and ten cycles. The resonance observed at 4.7 ppm (1 cycle) is due to diamagnetic deuteron species; presumably as a result of SEI build up (more concentrated after 10 cycles) and residual electrolyte (see Figure IV - 29). However, any intercalation deuterons were expected to have Fermi-contact shifts due to the presence of paramagnetic transition cations. This phenomenon should have manifested possible resonances in the range of 200 to 400 ppm which was not detected at the end of the 10th cycle. The effect of further cycling is currently being studied.
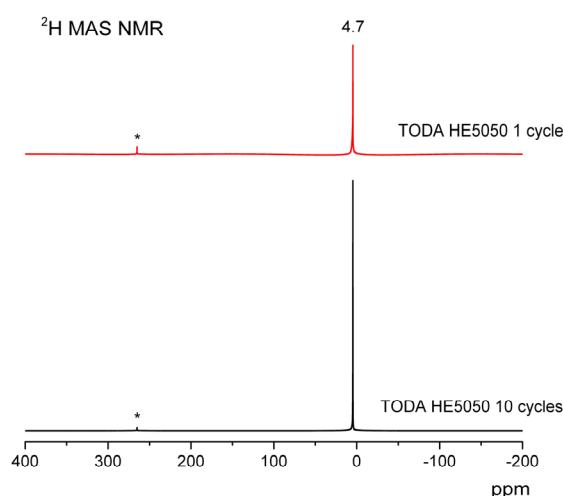
Figure IV - 29: ^{2}H MAS NMR of cycled TODA HE5050 material at a spinning speed of 20 kHz at 11.7 Tesla magnetic field. * indicates spinning side bands.

Synthetic approaches and materials modification.

'Layered-Layered-Spinel' Electrodes. Using knowledge gained from previous work and recognizing the potential of using a $LiMn_{1.5}Ni_{0.5}O_4$ spinel component to stabilize high capacity 'layered-layered' $0.5Li_2MnO_3 \cdot 0.5LiMn_{0.5}Ni_{0.5}O_2$ electrodes and to counter voltage decay, and given the tendency for manganese-rich layered electrode structures to convert readily to spinel, as shown above, studies of 'layered-layered-spinel' materials were continued by exploring electrode compositions with a lower manganese content. Focus was placed specifically on the '$Li_xMn_{0.65}Ni_{0.35}O_y$' system, for which the end members are $0.3Li_2MnO_3 \cdot 0.7LiMn_{0.5}Ni_{0.5}O_2$ (x=1.3; y=2.3), in which the average manganese and nickel oxidation states are 4+ and 2+, respectively, and $LiMn_{1.3}Ni_{0.7}O_4$ (x=0.5; y=2) in which the corresponding average oxidation states are expected to lie between 4+ and 3.77+ for Mn, and 2.57+ and 3+ for Ni. This system is highlighted by the dotted tie-line between $0.3Li_2MnO_3 \cdot 0.7LiMO_2$ and LiM'_2O_4 (M and M' = Mn, Ni) in Figure IV - 30. In particular, compounds with a lithium content of x=1.3, i.e., the parent 'layered-layered' composition, and x=1.25 were selected for detailed evaluation, the latter value corresponding to a targeted spinel content of 6%. The beneficial effects of 1) using Mg^{2+} as a dopant ion and 2) treating the electrode particle surface with an acidic solution of AlF_3 to enhance cycling stability, reduce first-cycle capacity loss, and to slow voltage decay on cycling were also studied.
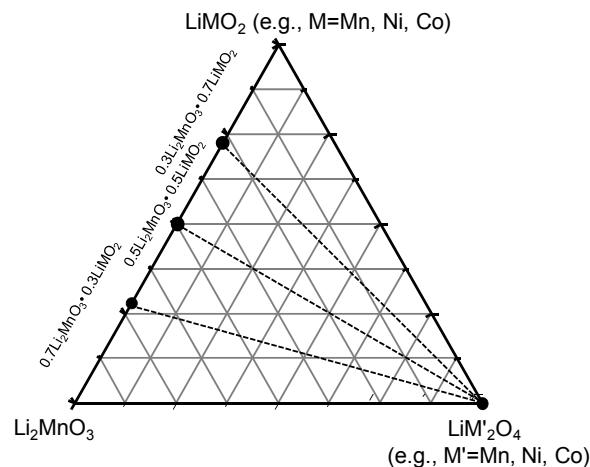

Figure IV - 30: A compositional phase diagram of a 'layered-layered-spinel' system with $Li_2MnO_3 \cdot (1-x)LiMO_2$ ('layered-layered') and LiM'_2O_4 (spinel) components.

Based on the hypothesis that small amounts of spinel are more likely to be effective in stabilizing high capacity 'layered-layered' composite electrode structures without impacting their rate capability, initial electrochemical experiments were conducted on $Li_xMn_{0.65}Ni_{0.35}O_y$ compounds in which the targeted values of x and y fell within the range $1.10 \leq x \leq 1.30$ and $2.22 \leq y \leq 2.30$, respectively, corresponding to compounds with a spinel content between 0 and 25%. The maximum discharge capacity and first-cycle efficiency, plotted as a function of the lithium content, x, for these five samples are shown in Figure IV - 31. The data clearly show that for higher spinel content (i.e., lower values of x) the first cycle efficiency is high because the spinel component can accommodate the oversupply of lithium released from the electrode during the activation of the Li_2MnO_3 component on the initial charge; for lower spinel content, the first-cycle efficiency decreases, reaching about 78% when no spinel is present (x=1.3). Conversely, when targeting a high spinel content, e.g., 25% (x=1.10) and 19% (x=1.15), the capacity delivered by the composite 'layered-layered-spinel' electrode is relatively low (92 and 140 mAh/g, respectively). Figure IV - 31 therefore demonstrates that optimum capacity and first-cycle efficiency are likely to be obtained when x lies between 1.20 and 1.25, i.e., from electrodes containing between about 6 and 12% spinel.
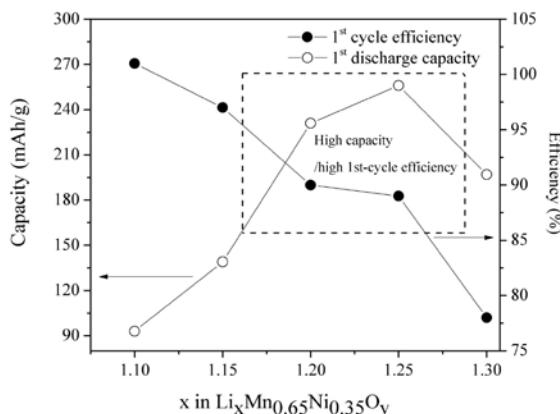
Figure IV - 31: Variation in capacity (mAh/g) and first-cycle efficiency (%) as a function of x in $Li_xMn_{0.65}Ni_{0.35}O_y$ electrodes.

The X-ray powder diffractions of various products are provided in Figure IV - 32, which include (a) a baseline 'layered-layered' $Li_{1.3}Mn_{0.65}Ni_{0.35}O_{2.3}$ (equivalent to $0.3Li_2MnO_3\bullet0.7LiNi_{0.5}Mn_{0.5}O_2$); (b) a Mg-substituted product of (a), $Li_{1.3}Mn_{0.65}Ni_{0.33}Mg_{0.02}O_{2.3}$; (c) a 'layered-layered-spinel' product with targeted composition $Li_{1.25}Mn_{0.65}Ni_{0.35}O_{2.28}$ equivalent to $0.94\{0.3Li_2MnO_3\bullet0.7LiNi_{0.5}Mn_{0.5}O_2\}\bullet0.06LiMn_{0.65}Ni_{0.35}O_2$) with 6% spinel; (d) a Mg-substituted equivalent of (c), $Li_{1.25}Mn_{0.65}Ni_{0.33}Mg_{0.02}O_{2.28}$; and (e) an AlF_3-treated equivalent of (d). The X-ray diffraction patterns are consistent with those expected for composite Li_2MnO_3-based 'layered-layered' or 'layered-layered-spinel' structures.


Figure IV - 32: XRD patterns of various materials derived from the 'layered-layered-spinel' $Li_xMn_{0.65}Ni_{0.35}O_y$ system.

Given the close similarity that can exist in the XRD patterns of cubic-close-packed layered and spinel lithium metal oxides, it is not surprising that the low spinel content (6%) in the layered-layered-spinel' products, $Li_{1.25}Mn_{0.65}Ni_{0.33}O_{2.28}$ and Mg-substituted $Li_{1.25}Mn_{0.65}Ni_{0.33}Mg_{0.02}O_{2.28}$, made it difficult to distinguish the layered- and spinel components from one another

(Figure IV - 32c and Figure IV - 32d). Nevertheless, the asymmetric broadening of the peaks at approximately 37, 44 and 64 º2θ, indicative of spinel formation, was clearly evident in the XRD pattern of the latter sample, as highlighted by the arrows in Figure IV - 32d. These two spinel peaks were unquestionably visible in the AlF_3-treated sample (Figure IV - 32e); in this case, the slight increase in peak magnitude and improved peak resolution is attributed to the AlF_3 surface treatment that increases the spinel content through Li removal (by acid leaching) and subsequent drying and annealing, consistent with the compositional analysis of this compound. It was therefore concluded that an advantage of AlF_3 surface treatment using acidic conditions is that it provides a technique to simultaneously stabilize the surface and tailor the amount of stabilizing spinel in the bulk of composite 'layered-layered-spinel' electrode structures.

An experiment was conducted to assess the feasibility of activating a 'layered-layered-spinel' $Li_{1.25}Mn_{0.65}Ni_{0.33}Mg_{0.02}O_{2.28}$ electrode at 4.95 V for 2 cycles to access the high capacity of the electrode, and then to lower the upper cut-off voltage to 4.6 V to a) minimize side reactions with the electrolyte solvent and b) provide greater cycling stability (Figure IV - 33a-c). Figure IV - 33a shows the voltage profiles of the first two cycles of a $Li/Li_{1.25}Mn_{0.65}Ni_{0.33}Mg_{0.02}O_{2.28}$ cell obtained between 4.95 and 2.5 V, and the subsequent 11th and 51st cycles between 4.6 and 2.5 V. This procedure yielded a discharge capacity of almost 200 mAh/g. Of particular interest are the dQ/dV plots of lithium cells with (i) an untreated $Li_{1.25}Mn_{0.65}Ni_{0.33}Mg_{0.02}O_{2.28}$ 'layered-layered-spinel' cathode for the 1st, 2nd, 11th and 50th cycles between 4.6 and 2.5 V (Figure IV - 33b), and (ii) a corresponding AlF_3-treated cathode that was subjected

Figure IV - 34: a) XRD patterns and b) PDF spectra of $xLi_2MnO_3 \bullet (1-x)LiCoO_2$, for x=0.1, 0.3, 0.7, and 0.9 annealed at 850°C.

Figure IV - 33: Effect of activation voltage on the performance of 'layered-layered-spinel' $Li_{1.25}Mn_{0.65}Ni_{0.33}Mg_{0.02}O_{2.28}$ and AlF_3-treated electrodes: a) typical voltage profile of an uncoated electrode; b) and c) dQ/dV plots of lithium cells with uncoated and AlF_3-coated electrodes, respectively. The cells in a) and c) were subjected to two activation cycles between 4.95 and 2.5 V, before being cycled between 4.6 and 2.5 V, whereas the cell in b) was cycled only between 4.6 and 2.0 V followed by an additional 49 cycles between 4.6 and 2.5 V (c). These data indicate that the untreated $Li_{1.25}Mn_{0.65}Ni_{0.33}Mg_{0.02}O_{2.28}$ cathode suffers from continuous voltage fade, which is apparent in two dominant reduction peaks (indicated by arrows in Fig. 32b), when cycled over a 4.6 to 2.5 V range. The chemistry of the AlF_3 electrode has changed significantly from the untreated version and further work is needed to determine the cause of this change.

To obtain a deeper understanding of the voltage decay exhibited by 'layered-layered' lithium-metal-oxide structures, high-resolution X-ray diffraction (XRD) and pair-distribution function measurements (PDF) have been initiated at the Advanced Photon Source. As a baseline, $xLi_2MnO_3 \bullet (1-x)LiCoO_2$ samples with x=0.1, 0.3, 0.7, and 0.9 were prepared and annealed at 850°C. XRD and PDF plots are shown in Figure IV - 34a and b. These preliminary data suggest the formation of a complex structure, exhibiting solid-solution behavior within a composite "Li_2MnO_3" and "$LiCoO_2$" matrix.

Another approach to correcting voltage fade is to change the synthesis method. In this study, the ammonia effect on tuning the precipitate morphology was initiated. Although ammonia was widely used in precipitation reactions and its importance has been emphasized in the previous reports a systematic investigation was needed to correlate the ammonia concentration in the coprecipitation medium to the crystal and agglomeration growth. This research shows that ammonia is not only a chelating agent and pH buffer during the precipitation reaction, but also plays a significant role in tailoring the morphology of the primary and secondary particle and the particle size distributions.

Ammonia concentration has direct impact on the secondary particle growth rate and the way in which the primary particles pack. Evolutions of four selected experimental conditions were compared in Figure IV - 35. Neither the low M_S/M_A (M_S/M_A=0.667, red line in Figure IV - 35), nor the high M_S/M_A (M_S/M_A=4, black line in Figure IV - 35) can benefit the secondary particle growth. After 10 hours of reaction, the D50 were still under 10 μm for these two conditions. A compromised ratio M_S/M_A=1.8 (olive line in Figure IV - 35), however, can lead to faster growth of D50, which stabilized between 10 and 11 μm after 5 hours. Further decrease of M_S/M_A to 1.5 significantly boosted the growth rate (blue line in Figure IV - 35): D50 quickly reached 23 μm from the initial 8 μm in the first 4 hours, with an average growth rate of 4.28 μm/hr, after which, D50 slowly shrunk to 9

µm and became stabilized at this size. One hypothesis is when the agglomerates approach a critical size, the shear stress exerted on the agglomerates by the hydrodynamic motion becomes larger than the cohesive force among primary particles, and then the agglomerates break down to smaller fragments, resulting in smaller D50.
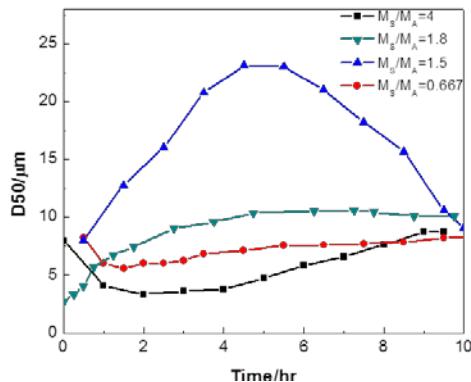

Figure IV - 35: Average particle size evolution of $Ni_{0.25}Mn_{0.75}(OH)_2$ precursors as a function of reaction time.

The M_S/M_A effect on the agglomerate morphology is shown in Figure IV - 36. Both low M_S/M_A (0.667) and high M_S/M_A (4) led to loosely packed secondary particles with irregular morphology (Figure IV - 36a and Figure IV - 36f). When the M_S/M_A is 1.5, the agglomerates became spherical with a very narrow particle size distribution (Figure IV - 36b), which has led to the higher tap density of the precursor.
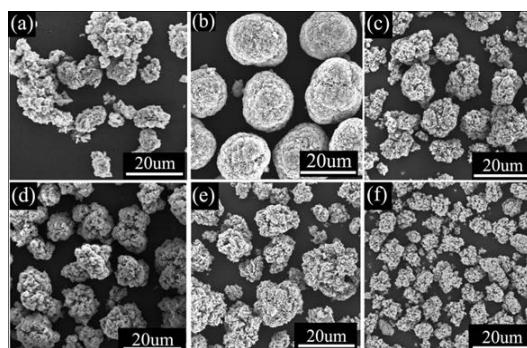

Figure IV - 36: SEM images of $Ni_{0.25}Mn_{0.75}(OH)_2$ secondary particles synthesized with different M_S/M_A in the base solutions (a) 0.667, (b) 1.5, (c) 1.8, (d) 2, (e) 2.5, (f) 4.

The various agglomerate morphologies are a result of diverse packing behaviors of the primary particles synthesized with different M_S/M_A. SEM images in Figure IV - 37 showed the ammonia effect on the primary particle morphology. In general, all of the precursors are lamellar with a lateral dimension around 500 nm. When the ammonia concentration is low, the primary particles are multi-layered plates with rough edges (Figure IV - 37 a and Figure IV - 37 b). With the increase of M_S/M_A from 0.667 to 1.5, the thickness of the nanoplates had an increase from ~50nm to >100nm, which directly lead to the mass increase of the agglomerates, adding the chance

of effective collisions that can trim the agglomerate to be spherical. Further increase in M_S/M_A led to single layer plates with smooth basal surfaces (Figure IV - 37 c to Figure IV - 37 e). Their irregular edges are results of particle disruption created by strong fluid shear forces in the CSTR reactor. When M_S/M_A was increased to 4, primary particles became regular hexagonal plates (Figure IV - 37 f), which may relate to the anisotropic growth of the six fold symmetry of the crystallites.
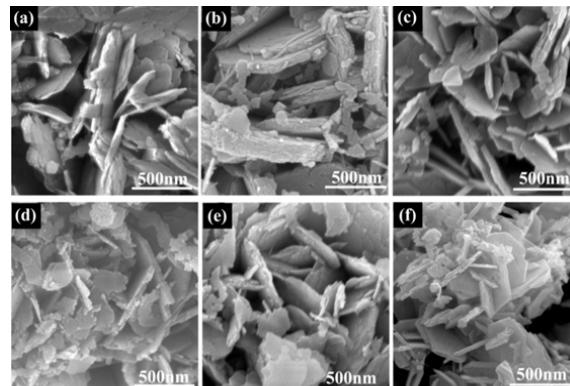
Figure IV - 37: SEM images of $Ni_{0.25}Mn_{0.75}(OH)_2$ primary particles synthesized with different MS/MA in the base solutions (a) 0.667, (b) 1.5, (c) 1.8, (d) 2, (e) 2.5, (f) 4.

Analysis of the electrochemical performance of these materials indicates that there is no significant change in the voltage fade performance.

Conclusions and Future Directions

The complex nature of these materials requires rigorous understanding of the experimental conditions and comprehensive baseline comparisons to ensure that "improvements" are not simply the result of unexpected changes in the material but are infect due to the experimental variable. The establishment of a single testing and data presentation procedure as well as rigorous scientific approached to data is essential to the success of this project. To this end we have test procedure and standard samples which enable real comparisons of data. It is our strong believe that we need to understand the mechanism of the voltage fade phenomena if we are to limit or fix this process. Over the next year, we will determine if protons are present in the lattice and contribute to fade, we will determine if coatings have a positive effect on voltage fade and most importantly we will determine the origin of the enhanced capacity in the LMR-NMC materials.

FY 2012 Publications/Presentations

Publications

1.   D. Kim, G. Sandi, J. R. Croy, K. G. Gallagher, S.-H. Kang, E. Lee, M. D. Slater, C. S. Johnson, and M. M. Thackeray, Composite 'Layered-Layered-Spinel'

Cathode Structures for Lithium-ion Batteries, J. Electrochem. Soc., (2012). In press.

Patent Applications

1. D. Kim, J. R. Croy, and M. M. Thackeray, Electrode Structures and Surfaces for Li Batteries. Submitted for filing, September 2012.

Presentations

1. M. M. Thackeray, Development of High-Capacity, Cathode Materials with Integrated Structures, Presentation at the Annual Merit Review Meeting, DOE Vehicle Technologies Program, Arlington VA, 14-18 May, 2012.
2. K. Burrell, Voltage Fade in the LMR-NMR high capacity materials, Presentation at the Annual Merit Review Meeting, DOE Vehicle Technologies Program, Arlington VA, 14-18 May, 2012.
3. M. M. Thackeray, J. R. Croy, D. Kim, G. Sandi-Tapia, K. G. Gallagher and M. Balasubramanian High Capacity Li- and Mn-rich Metal Oxide Electrodes: Challenges and Opportunities, IMLB 16, Jeju Korea, June 2012.

.

IV.B.2 Electrode Composition and Processing

IV.B.2.1 Scale-up and Testing of Advanced Materials from the BATT Program (LBNL)

Frank McLarnon (Program Manager)

Vincent Battaglia (Principal Investigator)
1 Cyclotron Road
Berkeley, CA 94960
Phone: (510) 486-7172; Fax: (510) 486-4260
E-mail: vsbattaglia@lbl.gov

Start Date: October 2010
Projected End Date: September 2014

Objectives

- Identify, procure, and test promising materials developed in the BATT Program.
- Establish performance, compare to the baseline, and communicate advances and limitations back to BATT PI.

Technical Barriers

High energy density and specific energy are critical performance characteristics for batteries for PHEVs and EVs. Li-ion technology currently is the technology that comes closest to meeting the targets developed by DOE and the USABC. The cost of electricity storage is expensive and Li-ion batteries are no exception. New materials capable of higher energy are needed to address these barriers. They must also demonstrate thousands of deep discharge cycles and a calendar life of 10 to 15 years.

Technical Targets

- Energy density (PHEV) 207 Wh/l
- Energy density (EV) 300 Wh/l
- Cost (PHEV) 207 S/kWh (40 miles)
- Cost (EV) 150 $/kWh (150 miles)

Accomplishments

- Evaluated a high-voltage electrolyte additive recommended by Brett Lucht. (Prof. Lucht indicates he was made aware of the HFiP additive through a collaboration with ARL.)
- Evaluated Ni-spinel materials from MIT, UT, and two commercial material suppliers.

- A flame-retardant additive developed at CWRU was demonstrated to show that it has no negative impacts on cell cycleability.

✧　　✧　　✧　　✧　　✧

Introduction

Batteries are very expensive when compared to other means of storing energy, but essential if the US is to move to a transportation infrastructure based on electricity. Thus, it is critical to find new materials that operate and are stable at high and low voltages. The BATT Program has several investigators developing such materials. These investigators have gone through a rigorous solicitation process to join the BATT program and are experts in the field of materials development - their labs are dedicated to making new electrolytes or active materials.

The Office of Vehicle Technologies sees the need to independently test these new materials and provide a reference to the tests by comparing the results to a baseline cell chemistry. In our BATT project, a baseline chemistry is identified and a full evaluation performed. Once the limitations of the baseline are identified, they are shared with the other BATT PIs, who in turn develop new chemistries. However, their labs may not be set-up for making electrodes and cells of the required quality; our labs are.

Our group is continuously improving its electrode preparation methods and cell fixtures. It also develops methodologies for assessing cell failures, all through BATT Program support. However, it is the ABR Program that supports the comparison testing of BATT materials.

In a meeting with the ABR management, it was decided that this year's effort would focus primarily on materials developed for the BATT Ni-spinel Focus Group. Argonne would also test Ni-spinel materials that it received from industry and share the results with LBNL. Argonne would also test other advanced materials from industry and report the results at the AMR.

Approach

Every two years, investigators developing cathodes, anodes, or electrolytes are encouraged to send to LBNL samples of their material. To test appropriately, 10 g of active material or 1 ml of electrolyte is required. If the investigator would rather focus their resources on

developing materials rather than scaling them up, then one our group members visits their laboratory and learns the processing procedures.

This year materials were received from Brett Lucht, URI; Dan Scherson, CWRU; Ram Manthiram, UT; and Gerd Ceder, MIT. For comparison, next generation materials from NEI and Nippon Denko were also tested.

Results

High-voltage Electrolyte Additive. Figure IV - 38 shows the performance of the baseline chemistry for a Focus Group of the BATT Program: $LiNi_{0.5}Mn_{1.5}O_4$ with 1 M $LiPF_6$ in EC:DEC1:2. One sees that the first charge requires several milliamphours before reaching the cut-off voltage of 4.9 V. Once it reaches the cutoff voltage, it begins its first discharge, achieving a first-cycle efficiency of just 0.04%. After this unusually poor cycle, the cell cycles normally with a cycling efficiency *ca*. 91%. Figure IV - 39 shows the same half-cell chemistry but with the addition of 1% hexafluoroisopropanol (HFiP) as recommended by Prof. Lucht. Here one sees that the long first charge is suppressed with a first cycle efficiency of 92%. After the first cycle, the cell cycles normally with an efficiency of 94%. We postulate that gas formed in the cell during the first charge acts as a chemical shuttle between the cathode and lithium metal counter electrode. The addition of HFiP is believed to form a protective film on the cathode much more quickly than without it. The film in turn greatly limits the rate at which the shuttle is oxidized.
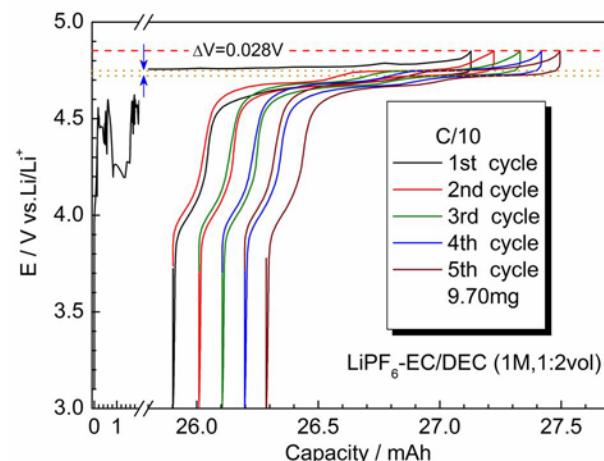
Figure IV - 38: First 5 cycles of a half cell of $LiNi_{0.5}Mn_{1.5}Mn_4$ with 1 M $LiPF_6$ in EC:DEC 1:2.
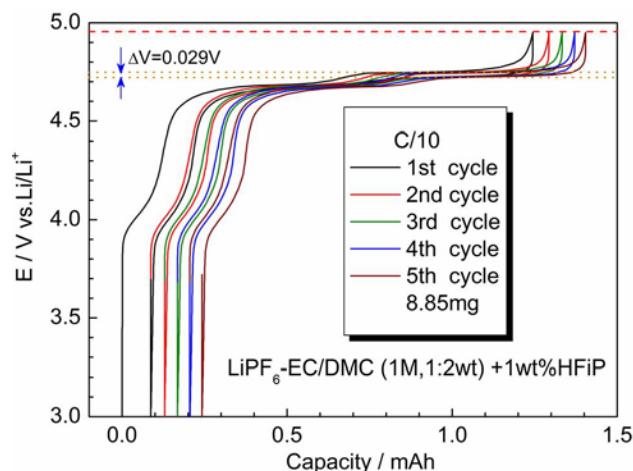
Figure IV - 39: First 5 cycles of a half cell of $LiNi_{0.5}Mn_{1.5}Mn_4$ with 1 M $LiPF_6$ in EC:DEC 1:2 with 1% HFiP.

In a full cell, where graphite forms a compact film during the first charge, this as-formed SEI is sufficient to limit the shuttle and allow the cell to charge to 5.25 V before reaching the oxidation limit of the liquid electrolyte.

Ni-spinel Cathodes. Figure IV - 40 shows the half-cell rate performance of cathode materials from NEI, Nippon Denko, University of Texas, and the Massachusetts Institute of Technology. Only one of these materials is doped: the one labeled LNMFO from UT is doped with Fe. In addition, all of the materials but the one from MIT has a disordered structure. Close inspection of the data indicates that the materials generally have the same capacity between 3.5 and 4.9 V, and that all of the materials show the same rate capability to C/2, except the MIT material. The poor rate capability of ordered material was predicted by the DFT calculation performed in the BATT Program.
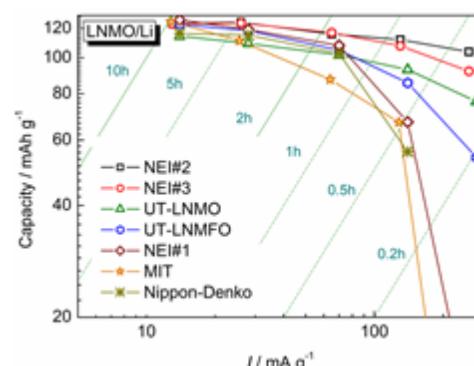
Figure IV - 40: Rate performance of $LiNi_{1/2}Mn_{3/2}O_4$ materials.

These same cathode materials were also tested in full cells against a graphite anode. Tests against graphite showed large capacity fade at high rates. In fact, all of the materials demonstrated approximately half of their capacity at C/2, except the MIT material. This material showed the same decrease in rate capability when tested against graphite as it did when tested against Li. This

results in the MIT material in a full cell to have the highest capacity at C/2 among all chemistries. It is believed that this is a result of the ordered material showing less Mn dissolution, where the Mn deposits on the graphite creating a high-impedance film.

High-voltage Electrolytes. Four electrolyte additives were evaluated in half cells, as shown in Figure IV - 41. Two were recommended by Prof. Lucht, LiBOB and HFiP, and two are well known electrolyte additives, FEC and VC. For reference, a cell without an additive performs like the cells with LiBOB and HFiP. If the loss of capacity of the full-cell data as compared to the half-cell data as described in the previous sub-section, then these additives, which are intended to improve high-voltage cell performance, appear to have little effect on the anode. Furthermore, FEC, which is known to improve the anode performance, also appears to have a positive influence in this high voltage cell. This further supports the theory that the deterioration of the full-cell performance arises from the anode. Finally, VC, which is known to improve both cathodes at 4.2 V and anodes, shows very poor performance in our tests. However, VC also showed poor performance in the half cell, indicating that the VC is not stable to 4.9 V and causes major inefficiencies in the cell.
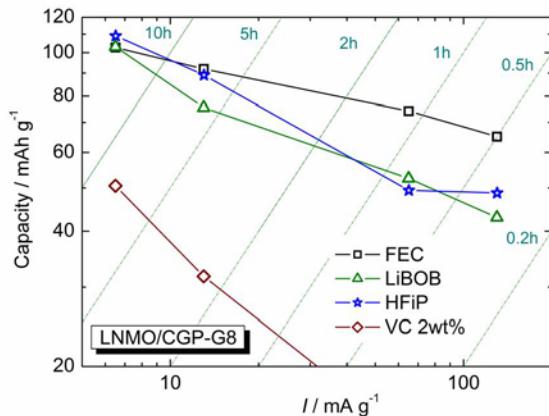
Figure IV - 41: The effect of electrolyte additives on full-cell rate performance.

Flame-Retardant Electrolyte Additive. Dan Scherson has been working on FRIONs (flame retardant ions) in the BATT Program for three years. He has made some progress and demonstrated that some of his latest additives can reduce the flammability of electrolytes with just 0.5 % added. He sent a sample of his salt to LBNL to test its cycleability. Some previous work with Novolyte indicated that the electrolyte was further improved by the addition of VC. Thus, we made an electrolyte formulation of 1M LiPF6 in EC:DEC plus 1.5 % VC and 0.5 % CWRU salt. Full cells with NCM cathode and graphite anode were made with and without the additive.

Figure IV - 42 shows two plots, Figure IV - 42.a is without the FRION and Figure IV - 42.b is with the FRION. Clearly, the cell with the electrolyte with the

additives is cycling at least as well as the cell without the additive. Scherson has already demonstrated that the electrolyte is nonflammable, and this effort was intended to if it had any impact on cell durability. The next step is be to make a sufficient amount of flame-retardant electrolyte to put in 18650s and test them tested for abuse tolerance at SNL.

Conclusions and Future Directions

This project has always been considered the bridge between the applied research program (ABR) and the directed fundamental research program (BATT). This year we received several materials for evaluation, most of them for the Ni-spinel system. These materials are already well characterized for the physical characteristics before they arrive at our lab. They are then incorporated into well-made half and full cells and evaluated for rate and cycling performance. Combining the known characteristics of the materials with the performance allows us to identify factors critical for cycling and rate.
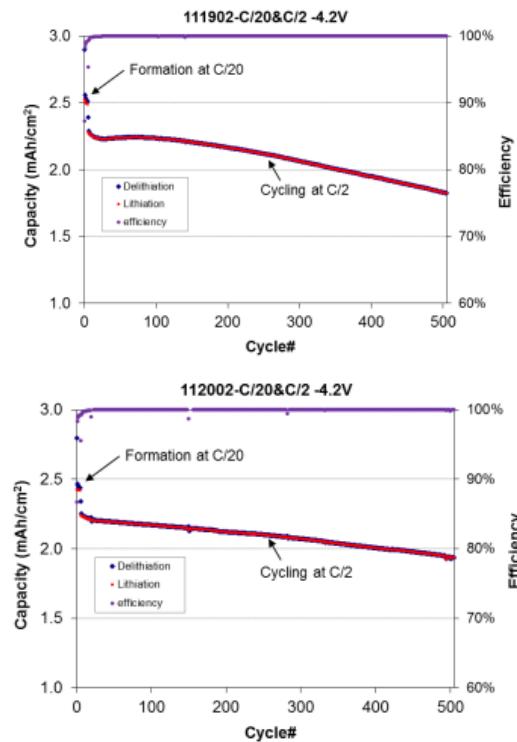
Figure IV - 42: a.) Graphite/NCM without additive, b.) Graphite/NCM with VC and FRION.

This year, it was determined that additives designed for high-voltage electrolytes were able to stop excessive side reactions in half cells but had little effect preventing the loss of rate performance found in full cells. It was also determined that the additive VC, thought to improve cell performance on both the anode and cathode sides in cells cycled to 4.2 V, could not withstand the voltages seen in a Ni-spinel cell. On the contrary, FEC, which is known for

improving anode performance in full cells, was also effective in the Ni-spinel high voltage cell.

It was also found that Ni-spinel materials all behave similarly, independent of morphology or processing except for a material specifically made with low transition-metal disorder. This material showed low inherent rate capability but may have had the highest stability against Mn dissolution.

Finally, a material additive designed to reduce the flammability of electrolytes appears to have no negative impacts on cycleability. This investigator will be encouraged to test his material in larger cells.

In the future, there will be new Focus Groups identified in the BATT Program. Materials from industry will have to be baselined and BATT materials evaluated against the baseline. Other materials developed in the program outside of the Focus Groups will also be evaluated against the standard BATT Baseline (Graphite/NCM).

FY 2012 Publications/Presentations

1. 2012 DOE Annual Merit Review Meeting Presentation.

IV.B.2.2 Cathode Processing Comparison (ANL)

Ilias Belharouak

Argonne National Laboratory
9700 South Cass Avenue
Argonne, IL 60439-4837
Phone: (630) 252-4450; Fax: (630) 972-4544
E-mail: belharouak@anl.gov

Collaborators:
Dapeng Wang, Argonne National Laboratory
G. Koenig, Argonne National Laboratory
Xiaofeng Zhang, Argonne National Laboratory
Khalil Amine, Argonne National Laboratory
Greg Krumdick, Argonne National Laboratory
G. Zhou, Binghamton University
R. Axelbaum Washington University in Saint Louis
C. Wang. Pacific Northwestern National Laboratory

Start Date: January 2011
Projected End Date: September 2014
Rolled into Voltage Fade in the LMR-NMC Materials
for FY13

Objectives

- We aim to correlate the electrochemical properties of materials (ANL-composite cathodes) to their structural, morphological, and physical properties by coordinating the science of synthesis with the science of function, in order to enable the use of these compounds in vehicle technologies:
- Develop a comparative study at the level of precursors.
- Investigate the origin of voltage fade observed in LMR-NMC cathode materials using a material synthesis approach.
- Compare the electrochemical performance of LMR-NMC type cathodes made through different synthetic routes; carbonate, hydroxide, and oxalate.
- Assist the materials screening and cell fabrication efforts through the sampling of LMR-NMC cathodes.
- Assist the material scale up effort at Argonne.

Technical Barriers

The challenges is the development of a safe cost-effective PHEV battery with a 40 mile all electric range that meets or exceeds all performance goals.

- Develop cost effective synthetic methods for the scale up of transition metal precursors.

- Synthesize high capacity materials with high packing density, spherical morphology, and suitable porosity.
- Comprehend the inconsistencies and fluctuations of the electrochemical results in LMR-NMC type cathodes.
- Comprehend the voltage fade phenomenon encountered in these materials.

Technical Targets

- Design of CSTR reactor and cooprecipitation reaction to produce Ni/Co/Mn carbonates and hydroxides.
- Characterize and understand (correlation approach) both the precursors and their lithiated materials using structural, physical, chemical, and electrochemical tools.
- Investigate the origin of voltage fade observed in Li- and Mn-rich cathode materials using a material synthesis approach.

Accomplishments

- Design of continuous stirred tank reactor and coprecipitation reactions for the production of 1Kg Precursor materials.
- For the carbonate process:
  - Systematic investigations including morphological, structural, compositional, and electrochemical characterizations were conducted on cathode materials prepared using co-precipitated carbonate precursors in a CSTR reactor.
  - Continuous particle growth has been observed for carbonate precursors regardless of chemical compositions.
  - The cathode samples were found to contain secondary particles composed of highly crystalline polyhedral primary particles whose sizes depend upon lithium contents.
  - The particles larger than 20 μm developed concentric ring layers within their cores, which compromised the overall electrochemical performance in terms of capacity and rate capability due to the sequential void that separates the inner layers.
  - Ball milling improved the electrochemical performance; however, it also accelerated side reactions between the electrode and electrolyte at high operating voltage, leading to gradual capacity loss with cycling.
- For the hydroxide process:

- o Variety of morphologies were obtained using CSTR-hydroxide process.
- o Secondary particles (10 µm size) comprising nano-plate primary particles were found to deliver over 200 mAh/g capacity at the 1C rate. However, the packing density was below 1 g/cm^3.
- o $Ni_{0.25}Mn_{0.75}(OH)_2$ precursor having spherical particles (15 µm) and high packing density (1.6 g/cm^3) has been obtained by tuning the experimental and engineering conditions during CTRS co-precipitation.

✧   ✧   ✧   ✧   ✧

Introduction

Key to the development of low-cost and high-energy/power electrochemical couples for lithium batteries is the cathode. Lithium-rich composite cathode materials have been extensively investigated since 2001. Nowadays, there is a consensus among researchers that these materials are composites comprising two layered components with an overall composition of $xLi_2MnO_3 \cdot (1-x)LiMO_2$ (M is a transition metal). Nuclear magnetic resonance and transmission electron microscopy studies have corroborated the existence of Li_2MnO_3-like domains (space group C2/m) within a predominant $LiMO_2$ layered phase (space group, R-3m). The major benefit of the composite structure is that upon charge to a high potential (>4.3 V), where conventional cathodes are unstable, the material remains intact through the activation of Li_2MnO_3; hence, capacities in the range of 250 mAh/g have been achieved. However, the composite delivers modest capacity when it is charged at high rates. Reducing the particle size to nano-scale levels has been suggested as a means to improve the rate performance by shortening the lithium diffusion pathways. However, nanoparticles have low packing densities and high surface area and, thus, promote side reactions. Also, they are not economical because of the added synthesis cost. Nano-architecture materials have the potential to overcome these problems without jeopardizing the advantages conferred by the nanotechnology.

Approach

Within a general approach consisting of coordinating the science of synthesis with the science of function, three synthetic routes, hydroxide, carbonate and oxalate processes, were developed to prepare the precursors that will serve to produce LMR-NMC cathode materials. A comparative study using the three routes will be made at the levels of the materials morphology, physical characteristics, and electrochemical properties. Blending between materials made through the carbonate or hydroxide precursors and the same compositions made

through the oxalate will be done in order to get the most use of the high packing density for high energy density and high porosity for high rate capability. A close examination of voltage fade behavior in these materials was initiated since the project rolled into voltage fade in the LMR-NMC Materials for FY13.

Results

This report will focus on the carbonate process. Carbonate co-precipitation by the CSTR method was employed to prepare precursor materials that can be used to produce large quantities of cathode materials for lithium-ion batteries. Because of the continuous stirring in this method, the carbonate precursor particles formed and trapped within the reactor walls can undergo significant growth, as outlined in our previous work. In our experimental setup, the precursor $Ni_{0.25}Mn_{0.75}CO_3$ was continuously collected for 7 hours after the solution reached steady state.

The XRD pattern of the collected precursor $Ni_{0.25}Mn_{0.75}CO_3$ is shown in Figure IV - 43. The material was a single phase and could be indexed based on the space group (R3c) of $MnCO_3$.
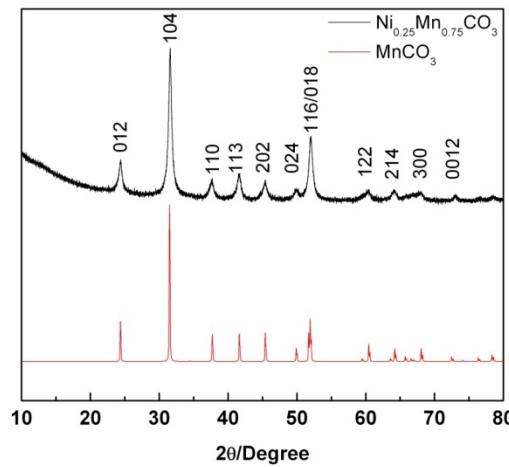
Figure IV - 43: X-ray diffraction pattern of the synthesized carbonate precursor.

The morphology and particle size distribution of $(Ni_{0.25}Mn_{0.75})CO_3$ are shown in Figure IV - 44. The particles, in general, seemed to be dense and spherical with smooth surfaces. They had sizes however, ranging from 15 to 50 µm. The particle size distribution measured by laser diffraction primarily exhibited a broad and symmetric peak centered at 30 µm (inset in Figure IV - 44). We anticipate that the particles above 20 µm would neither be suitable for electrode fabrication nor yield high electrochemical performance. The surface area of the particles determined by the BET method was 150 m^2/g, indicating that the particles had a high porosity despite the dense appearance. This finding confirmed that the particles were porous secondary agglomerates made of nanosize primary particles.
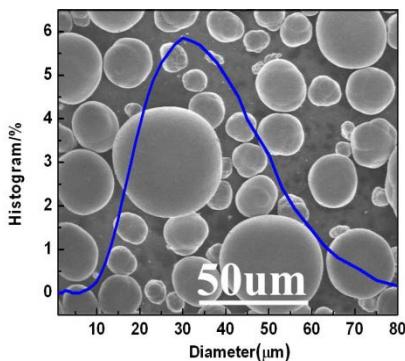
Figure IV - 44: Particle size distribution superimposed on SEM image of synthesized carbonate precursor.

Next, we mixed $Ni_{0.25}Mn_{0.75}CO_3$ with carbonate and calcined the mixture at 900^oC to prepare $Li_{1.42}Ni_{0.25}Mn_{0.75}O_{2+\gamma}$. Unlike a previous report, the as-prepared material had a low specific capacity of only 155 mAh/g, which could be due to the wide particle size distribution that the material preserved from the precursor (Figure IV - 45a and Figure IV - 45e). To investigate this matter, we classified the $Li_{1.42}Ni_{0.25}Mn_{0.75}O_{2+\gamma}$ secondary particles into three size groups by sieving the as-prepared material: below 20 µm, between 20 µm and 38 µm, and above 38 µm. The morphology and particle size distributions of the $Li_{1.42}Ni_{0.25}Mn_{0.75}O_{2+\gamma}$ before and after sieving are shown in Figure IV - 45. Before sieving, the cathode material had a wide particle size distribution, with a peak centered at 30 µm (Figure IV - 45e), similar to $Ni_{0.25}Mn_{0.75}CO_3$. Figure IV - 45f plots the three particle size distributions, which are centered at 15 µm (red solid line), 25 µm (blue solid line), and 40 µm (green solid line), respectively.
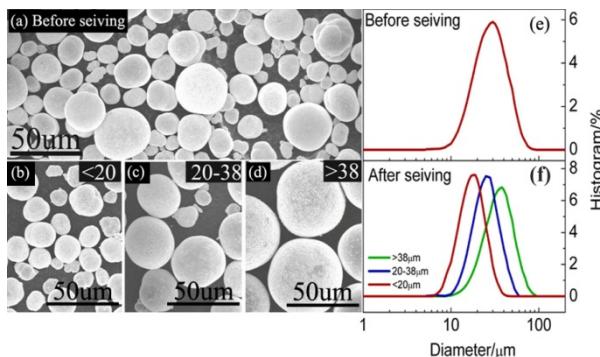

Figure IV - 45: Cathode morphologies and particle size distributions before and after sieving.

Thereafter, EDXS (Figure IV - 46) was performed on cross-sectioned particles of $Ni_{0.25}Mn_{0.75}CO_3$ and $Li_{1.42}Ni_{0.25}Mn_{0.75}O_{2+\gamma}$ along the diameters of the samples sieved below 20 µm (Figure IV - 46a), between 20 µm and 38 µm (Figure IV - 46b), and above 38 µm (Figure IV - 46c). This experiment was conducted primarily to check the manganese and nickel compositions across the secondary particle of both the precursor and lithiated compounds

after sieving. Nickel and manganese atomic percentages are shown as green and red lines, respectively, in Figure IV - 46. For all samples, we observed small fluctuations around the nominal atomic percentages (25% Ni and 75% Mn).

This finding indicates that the chemical composition was relatively homogeneous for the precursors and cathode materials within the composition analysis limits of EDXS. One of the interesting observations was a "core-shell" type morphology in both the precursor and cathode materials, which was manifested as concentric circular rings for larger particles (Figure IV - 46). The interfaces between these layers can be distinguished by darker contrasts in the case of the precursors, whereas, in the case of cathode samples, the interfaces evolved into clear voids separating the nearby layers. The number of concentric rings increased with the increase in secondary particle size. Indeed, for particles below 20 µm, only one interface could be observed separating a core of about 15 µm and a thinner shell. For the particles larger than 38 µm, up to 10 rings could be found. The solid core and subsequent rings of the $Li_{1.42}Ni_{0.25}Mn_{0.75}O_{2+\gamma}$ cathode sample are clearly visible in the high-magnification SEM image in Figure IV - 47. The cohesion between the adjacent dense rings is ensured through the continuity between the dendritic particles grown on each side of the rings. The high porosities observed between the dense rings could be useful for electrolyte impregnation across the layers. However, because the dense character of the rings could lead to the blockage of electrolyte, lithium diffusion between the outer and inner rings and the core of the particles could be inhibited.
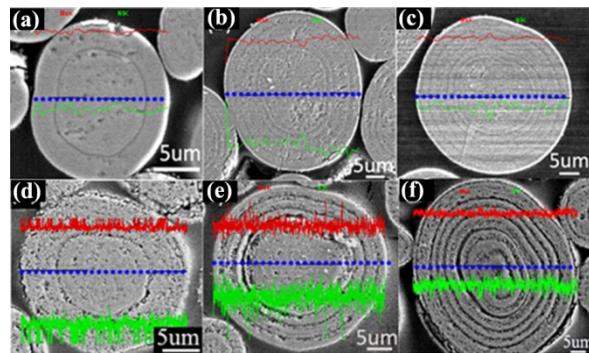

Figure IV - 46: EDXS curves superimposed on SEM images of bisected precursors with particle sizes of (a) <20 µm (b) 20-38 µm, and (c) 38-75 µm and cathode materials with particle sizes of (d) <20 µm (e) 20-38 µm, and (f) 38-75 µm.
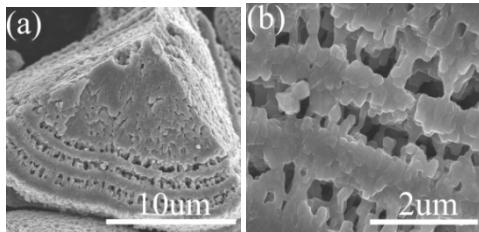
Figure IV - 47: SEM images of cathode materials with core-shell like features: (a) low magnification image and (b) higher magnification image of local area.

Because of the secondary particles with different sizes, we suspected that, during calcination with lithium carbonate, the cathode sample particles may have different degrees of lithiation, depending upon their sizes. To investigate this hypothesis, high-energy XRD and ICP were used to characterize the structure and chemical composition of the lithiated samples after sieving. The XRD patterns of all samples are shown in Figure IV - 48.
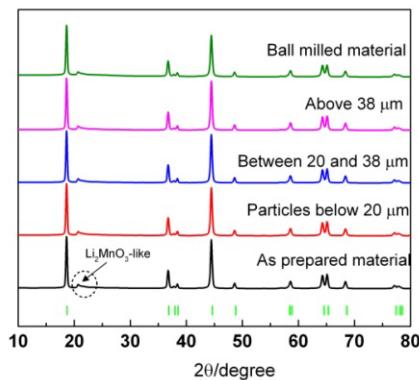

Figure IV - 48: High-energy XRD patterns for cathodes with different particle sizes.

All of the cathodes with different particle sizes can be mainly indexed to the R$\bar{3}$m space group, and matched well with the diffraction pattern of LiNi$_{0.5}$Mn$_{0.5}$O$_2$ reference material. The small additional peaks between 20 and 23° (2θ) are usually assigned to Li$^+$ and Mn^{4+} order in the manganese layer of the Li$_2$MnO$_3$ component in this material. Essentially, we did not notice a measurable difference between the diffraction patterns for the samples sieved below 20 μm, between 20 μm and 38 μm, and above 38 μm. In fact, the calculated cell parameters obtained using Rietveld refinements were found to be similar for the different samples (Table IV - 2). Furthermore, the ICP results do not reveal any significant deviation in the Mn/Ni atomic ratio among the samples (Table IV - 3). However, the compositions in all samples were slightly lean in nickel, possibly due to the incomplete precipitation of nickel during the co-precipitation process.

Table IV - 2: Cell parameters after GSAS refinement**.**

Sample	a (Å)	b (Å)	c (Å)	Cell Volume (Å³)	c/a
Pristine	2.862(8)	2.862(8)	14.267(2)	101.266(7)	4.98(3)
>38um	2.862(7)	2.862(7)	14.266(9)	101.259(6)	4.98(3)
20-38um	2.862(9)	2.862(9)	14.268(2)	101.279(7)	4.98(3)
<20um	2.862(7)	2.862(7)	14.268(8)	101.274(4)	4.98(4)

Table IV - 3: ICP result of cathode materials with different particle sizes**.**

Sample	Mn (atomic %)	Ni(atomic%)	Mn/Ni(atomic)	Li/(Mn+Ni) (atomic)
<20um	75.6±5.3	24.380±1.7	3.10±0.22	1.49±0.11
20-38um	75.9±5.4	24.111±1.7	3.14±0.22	1.52±0.11
>38um	75.9±5.4	24.065±1.7	3.15±0.22	1.50±0.11

The charge-discharge profiles and capacities of lithium cells made of size-selected Li$_{1.42}$Ni$_{0.25}$Mn$_{0.75}$O$_{2+\gamma}$ electrodes are compared to those of the as-prepared Li$_{1.42}$Ni$_{0.25}$Mn$_{0.75}$O$_{2+\gamma}$ in Figure IV - 49. The current density was 20 mA/g, which is equivalent to C/10 assuming that 200 mA/g is achieved at the 1C rate. The cell was initially charged to 4.8 V, discharged to 2 V, and then cycled between 2 and 4.6 V in the subsequent cycles. The charge capacity of the as-prepared sample containing a broad range of particles sizes (Figure IV - 49a) was quite similar to that of all size-selected samples (Figure IV - 49b, Figure IV - 49c, and Figure IV - 49d), which was around 250 mAh/g. The first discharge capacities were 176 mAh/g (particles below 20 μm), 170 mAh/g (between 20 and 38 μm), and 162 mAh/g (above 38 μm). These results indicate that the smaller the particles, the higher the discharge capacity. The as-prepared material, which had a wide particle size distribution, delivered a discharge capacity of 164 mAh/g, close to that of the material composed of the largest particles (above 38 μm).
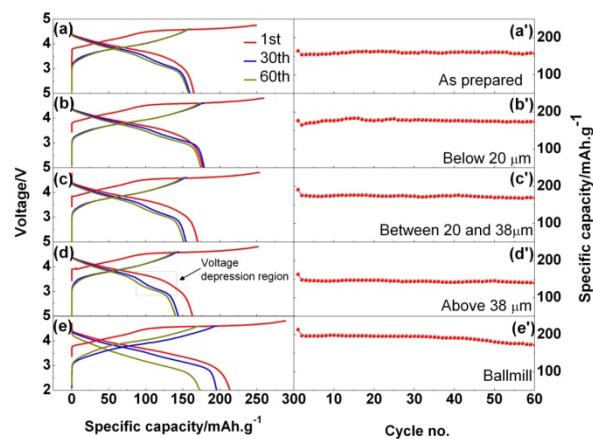
Figure IV - 49: Electrochemical performance of cells prepared with cathodes with different particle sizes: left, voltage-capacity profile; right, cycling performance.

Starting from the second cycle, the cells with electrodes composed of size-selected particles and as-prepared material (Figure IV - 49a to Figure IV - 49d) showed good capacity retention over 60 cycles. The cells made of the smaller particle electrodes showed the lowest

capacity fade. The low capacity observed for the large particle electrode may have been due to the texture of the concentric rings within the particles. As mentioned above, effective lithium diffusion would be difficult from a massive ring to a subsequent one because of the voids that exist between these rings, which can increase the interfacial resistance within the larger particles. Therefore, the core of such particles may not be fully activated, and thus lower capacities are to be expected. We also believe that these particles could be vulnerable to mechanical stress, which could result in pulverization during calendaring. To verify this hypothesis, we used low-energy ball milling to break down the secondary particles so that larger material surfaces would be electrochemically activated. The cathode sample was ball-milled for 1 hour in a planetary ball miller. The ball-milled sample exhibited spherical fragments. After the ball milling, the particle size distribution of the sample became narrower compared to the as-prepared sample, and the surface area became larger, 6 m^2/g (ball-milled sample) vs. 1 m^2/g (as-prepared sample). Subsequently, lithium cells were made of the ball-milled sample and cycled under the same conditions mentioned above (Figure IV - 49e). As expected, the cell exhibited a drastic increase in the initial charge and discharge capacities, 290 and 215 mAh/g, respectively, as compared with 250 and 176 mAh/g for the electrodes whose particles were below 20 μm (Figure IV - 49e and Figure IV - 49b). However, because of the larger surface area, which usually promotes side reactions, the capacity gradually faded upon consecutive cycling to 4.6 V. The voltage profile during the discharge of the ball-milled electrode did not show the voltage depression in the 3-V region compared to the electrodes prepared from samples before ball milling, despite the occurrence of an overall voltage drop. Furthermore, the 3-V voltage depression region seemed to be more pronounced for the electrodes with larger particle sizes compared to those with smaller sizes. The reason for this difference is still under investigation, although the main factors that exacerbated the voltage depression seemed to be linked to particle size and surface area of the material.

The rate performances of all samples are shown in Figure IV - 50. The cells were initially cycled between 2 and 4.8 V for 1 cycle under a C/10 rate to activate the electrode material, and then cycled between 2 and 4.6 V at C/10, C/4, C/2, and 1C for 10 cycles per step. In general, the capacity retention of all samples declined with the rate increase (Figure IV - 50). However, higher capacities were achieved for the samples composed with smaller particle sizes. For example, at the 1C rate the specific capacities were 152 mAh/g (ball-milled sample), 115 mAh/g (samples below 20 μm and 20-38 μm), 97 mAh/g (as-prepared sample), and 67 mAh/g (sample above 38 μm). The results clearly show that the rate capability is strongly dependent upon the particle size of the samples. Also, the inner ring texture by which the large particles are

constructed could have contributed to the worsening of the lithium diffusion and kinetics.
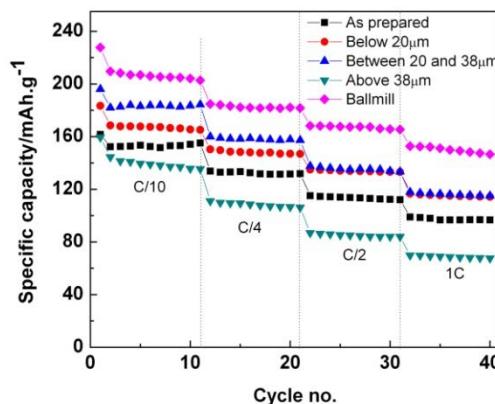
Figure IV - 50: Rate performance of half cells prepared with cathodes of different secondary particle sizes.

Conclusions and Future Directions

Systematic investigations including morphological, structural, compositional, and electrochemical characterizations were conducted on the cathode material $Li_{1.42}Ni_{0.25}Mn_{0.75}O_{2+\gamma}$ with three ranges of secondary particle size. These samples were prepared from co-precipitated carbonate precursors in a CSTR. The cathode samples were found to contain secondary particles composed of highly crystalline polyhedral primary particles, with average size around 100 nm, regardless of the secondary particle size. The particles larger than 20 μm developed concentric ring layers within their cores, which compromised the overall electrochemical performance in terms of capacity and rate capability due to the sequential void that separates the inner layers. Ball milling improved the electrochemical performance; however, it also accelerated side reactions between the electrode and electrolyte at high operating voltage, leading to gradual capacity loss with cycling. Note that we used the milling method for the purpose of proof of concept only, because it cannot ensure long-term cathode functionality due to the occurrence of side reactions. The following methods should be investigated for obtaining high capacity and stable materials via the carbonate co-precipitation method: (1) prevent growth of the precursor particles above 20 μm during co-precipitation; (2) optimize the Li/transition metal ratio because the particles have Ni-hydroxide enriched cores and are sensitive to moisture; and (3) determine the proper balance between porosity and surface area of particles because the former is suited for improving the capacity and rate capability and the latter is unsuited for long life due to parasitic side reactions.

The summary conclusions are the following:

Carbonate process:

- Systematic investigations including morphological, structural, compositional, and electrochemical

characterizations were conducted on cathode materials prepared using co-precipitated carbonate precursors in a CSTR reactor.

- Continuous particle growth has been observed for carbonate precursors regardless of chemical compositions.

- The cathode samples were found to contain secondary particles composed of highly crystalline polyhedral primary particles whose sizes depend upon lithium contents.

- The particles larger than 20 µm developed concentric ring layers within their cores, which compromised the overall electrochemical performance in terms of capacity and rate capability due to the sequential void that separates the inner layers.

- Ball milling improved the electrochemical performance; however, it also accelerated side reactions between the electrode and electrolyte at high operating voltage, leading to gradual capacity loss with cycling.

Hydroxide process:

- Variety of morphologies was obtained using CSTR-hydroxide process.

- Secondary particles (10 µm size) comprising nano-plate primary particles were found to deliver over 200 mAh/g capacity at the 1C rate. However, the packing density was below 1 g/cm^3.

- $Ni_{0.25}Mn_{0.75}(OH)_2$ precursor having spherical particles (15 µm) and high packing density (1.6 g/cm^3) has been obtained by tuning the experimental and engineering conditions during CTRS co-precipitation.

FY 2012 Publications/Presentations

Papers

1. Growth mechanism of Ni0.3Mn0.7CO3 Precursor for high capacity Li-ion battery cathodes, D.P. Wang, I. Belharouak, G. Koenig Jr., G.W. Zhou and K. Amine. Journal of Materials Chemistry, 21 (2011) 9290-9295.
2. Chemistry and electrochemistry of concentric ring materials for lithium batteries, D.P. Wang, I. Belharouak, G.W. Zhou and K. Amine. J. Mater. Chem., 2012,22, 12039-12045.
3. Nano-architectured multi-structural cathode materials for high capacity lithium batteries, Dapeng Wang, Ilias Belharouak, Guangwen Zhou, and Khalil Amine, Advanced Functional Materials, Adv. Funct. Mater., 2012, 10.1002/adfm.201200536.

Presentations

1. Advanced high capacity materials for energy storage applications, I. Belharouak, International Conference on Materials for Advanced Technologies ICMAT-2011, Singapore, June 26-July 1, 2011.
2. Growth mechanism of $Ni_{0.3}Mn_{0.7}CO_3$ precursor with continuous stirred tank reactor (CSTR) for high capacity cathodes, D. Wang, I. Belharouak, G.W. Zhou, K. Amine, 220th ECS meeting, Boston, MA, October 9-14, 2011.
3. Cation effect on lithium- manganese- rich composite cathode materials, D. Wang, I. Belharouak, G.W. Zhou, K. Amine, MRS Fall Meeting & Exhibit, Boston, MA, November 28 - December 2, 2011.

Posters

1. High rate capacity $Li_{1.2}Ni_{0.2}Mn_{0.6}O_2$ cathode material synthesized by continuous stirred tank reactor (CSTR), D. Wang, I. Belharouak, G.W. Zhou, K. Amine, 7th International Symposium Inorganic Phosphate Materials, Argonne, Illinois, November 8-11, 2011.
2. Growth mechanism of $Ni_{0.3}Mn_{0.7}CO_3$ precursor with continuous stirred tank reactor (CSTR) for high capacity cathodes, D. Wang, I. Belharouak, G.W. Zhou, K. Amine, 5th International Conference on Polymer Batteries and Fuel Cells, Argonne, Illinois, August 1-5, 2011.

IV.B.2.3 Optimization of Li-ion Battery Electrodes (ANL)

Wenquan Lu

Argonne National Laboratory
9700 South Cass Avenue
Argonne, IL 60439-4837
Phone: (630) 252-3704; Fax: (630) 972-4414
E-mail: luw@anl.gov

Collaborators:
Sun-Ho Kang (ANL)
Dennis Dees (ANL)
Qingliu Wu (ANL)
Khadija Yassin-Lakhsassi (ANL)
Miguel Miranda (ANL)
Nathan Liu (ANL)
Thomas K. Honaker-Schroeder (ANL)
Gary Henriksen (ANL)
Electron Microscopy Center (ANL)

Subcontractor:
Illinois Institute of Technology, Chicago, IL

Start Date: October 2008
End Date: September 2012 (completed)

Objectives

To establish the scientific basis needed to streamline the optimization of lithium-ion electrode processing.

- To identify and characterize the physical properties relevant to the electrode performance at the particle level.
- To quantify the impact of fundamental phenomena associated with electrode formulation and fabrication (process) on lithium ion electrode performance.

Technical Barriers

Develop a cost-effective and abuse tolerant lithium-ion battery for a PHEV with a 40 mile all electric range that meets or exceeds all performance goals.

- Establish the interdependence of lithium-ion electrode performance and the specifics of the electrode fabrication process.
- Reduce the complexity of the optimization process caused by the broad range of active materials, additives, and binders.
- Quantify the impact of fundamental phenomena on electrode performance.

Technical Targets

- Correlate the electronic conductivity with the electrochemical performance of the electrode.
- Develop a model to quantify the impact of electronic conductivity on cell performance.

Accomplishments

- Particle conductivity was measured using both nano probe SEM and in-house developed power conductivity apparatus.
- Carbon coated $LiNi_{1/3}Co_{1/3}Mn_{1/3}O_2$ samples were characterized. The electrode conductivity was investigated using 4 point probe modeling. The cells made of NCM powder with and without carbon coating were also studied in terms of their electrochemical and physical properties.
- Electrode optimization studies were carried out on $LiFePO_4$ electrodes using a COMSOL electrochemical modeling software package. The studies focused on establishing an optimum composition zone to achieve the desired electrochemical performance.

✧   ✧   ✧   ✧   ✧

Introduction

In general, the performance of a lithium-ion electrode is highly dependent on the specifics of the fabrication process. Furthermore, the broad range of active materials for both positive and negative electrodes (e.g. oxides, phosphates, graphites, carbons, and alloys), as well as polymer binders and conductive additives, compounds the complexity of the optimization process. The literally hundreds of variables associated with the fabrication of new active material electrodes generally require lengthy development efforts to be fully optimized. This sometimes causes promising materials to be discarded prematurely. Quantifying the impact on performance of the fundamental phenomena involved in electrode formulation and fabrication should greatly shorten the optimization process for new electrode active materials. The goal of this work is to establish the scientific basis needed to streamline the lithium-ion electrode optimization process for new materials.

Approach

The conventional approach is to optimize the electrode by varying the amounts of conductive additive and binder to overcome the percolation threshold at the

laminate level. New electrode materials are generally judged on their electrochemical properties. This method, generally adopted by industry, requires lengthy development efforts to fully optimize a single material and sometimes causes promising materials to be discarded. Our new approach in this project attempts to establish the scientific basis at the particle level. The focus is on the chemical and physical properties (e.g. primary particle size, secondary particle size and extent of agglomeration, as well as the surface characteristics, see Figure IV - 51), which, in most cases, can dictate the overall performance of the electrode.

Based on modeling work by Dennis Dees, it was established that the electronic conductivity does not impact on electrode impedance when the electronic conductivity is much larger than the ionic conductivity (>0.01 S/cm). Therefore, it will be very helpful to optimize the electronic conductivity of the electrode to meet the energy and power requirement for the lithium ion batteries. The factors affecting the distribution of binder and conductive additives throughout the composite matrix is being systematically investigated at the particle level, as well as their effect on overall electrode performance. Modeling work is being conducted to help quantify the impact of fundamental phenomena on electrode performance.
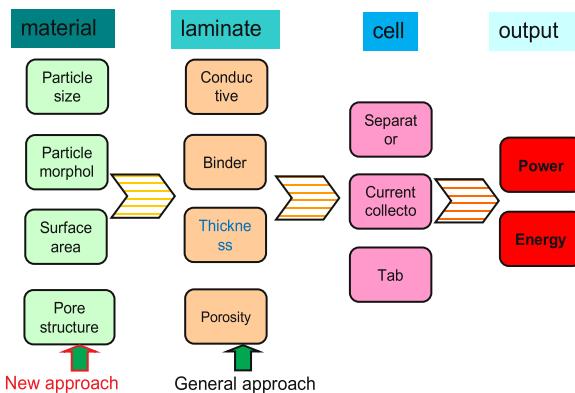

Figure IV - 51: Schematic diagram of streamlining the optimization of electrode.

Results

Relationship between active material, conductive additive, and binder: The 4 probe measurement on a single particle, $LiNi_{0.8}Co_{0.15}Al_{0.05}O_2$ (NCA), was carried out using Omicron UHV Nanoprobe (Germany) at Center for Nanoscale Materials (ANL), as shown in Figure IV - 52. The calculated conductivity was higher than that reported in literature. Therefore, we speculate that the interface resistance makes great contribution to the powder conductivity.
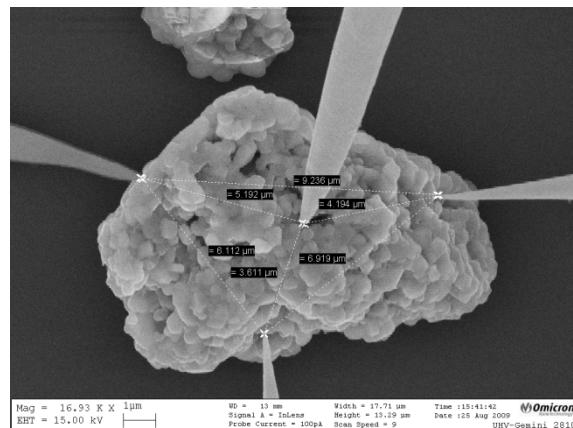
Figure IV - 52: Conductivity measurement using nano probe SEM.

Conductive carbon additive effect on $LiFePO_4$ was then investigated using an in-house developed apparatus and the results are shown in Figure IV - 53. Apparently, the electronic conductivity of the physical mixture increases with increasing the conductive additive, especially at low additive composition. It can be seen from this figure that as low as 5 wt.% carbon additive can improve the powder conductivity of non-carbon coated $LiFePO_4$ significantly from ~10^{-7} to ~10^{-3} S/cm. The result indicates that the percolation threshold is less than 5wt.% even for this extremely poor conductive electrode materials, which suggests that less conductive carbon additive is possible to make good conductive composite electrode.

The effect of PVDF binder on the particle conductivity was also investigated using nanoprobe SEM. The resistance of the graphite with PVDF film was found extremely high due to the poor conductivity of PVDF binder.

The investigation above demonstrated that the interfacial resistance of electrode particles is a significant contributor to electrode resistance with fixed electrode materials. It is rational to expect that the conductive coating on active materials can improve the electrode conductivity.
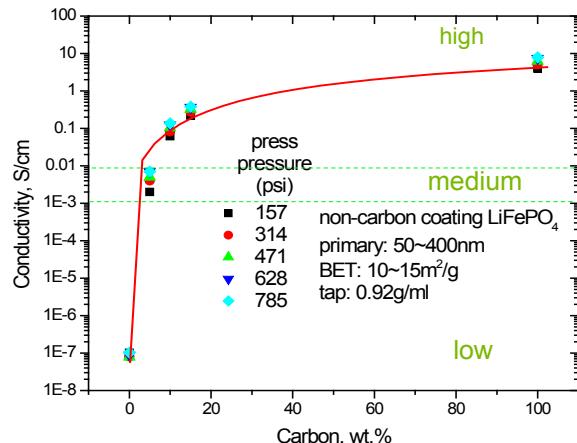
Figure IV - 53: Carbon Additive Effect on Conductivity of LiFePO$_4$/Carbon Blend.

Novel carbon coating on LiNi$_{1/3}$Co$_{1/3}$Mn$_{1/3}$O$_2$ (NCM). The carbon coating of NCM particles was engineered by Hosaka, using a novel carbon coating technology without reducing the metal oxide. Two different carbon coated NCM samples (1wt.% and 3wt.%) were prepared. SEM and TGA results confirmed the desired amount of carbon was coated on the surface of particles.

The conductivity of electrodes made with both uncoated and coated NCM particles were also investigated using the 4-point probe method. The coated carbon on the particle was taken into consideration when preparing the electrode slurry. For instance, only 2wt% additional carbon was added into composite when 5wt% carbon additive is the target for 3wt% carbon coated NCM particles. The subtrates for the electrodes are either conductive aluminum foil or insulating polyester.

SEM was carried out on electrodes employing both particles with and without carbon coatings (see Figure IV - 54). It can be clearly seen from images that less carbon additive is present in the matrix of the electrode made of NCM with 3wt% carbon coating. For this sample, the target carbon additive was 5wt%. Only 2wt% additional carbon was added into composite since there was 3wt% coated carbon on the particle. Therefore, there was less carbon to form the conductive matrix in the composite, leading to higher electrode sheet resistance, which is confirmed by the 4 point probe measurement on the electrode over the insulating polyester substrate. However, the electrode resistance with aluminum substrate from four point probe measurement was lower. We speculate that the interface resistance is different for these two electrodes and was further investigated using the following model.
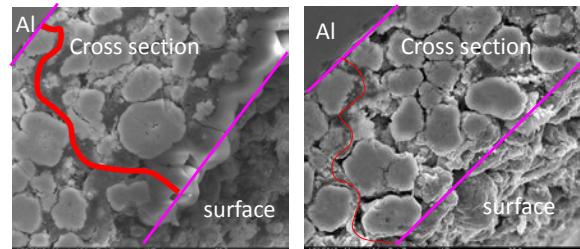
Figure IV - 54: SEM images of electrode with no carbon coating (left) and with 3% carbon coating on the particles.

The model adopted a three-layer geometry (Figure IV - 55). The top layer is the coating of electrode materials including active material, carbon additive, and PVDF binder. The bottom layer is the substrate (either metal foil or insulating substrate). Finally, the middle layer is the interface between coating and substrate. The conductivity of coating was assumed isotropic. The electrode conductivity was calculated using the model by varying the probe contact resistance and interfacial resistance for electrode coating on either aluminum or polyester.
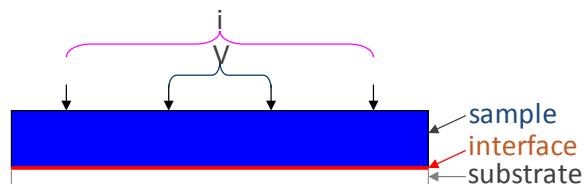
Figure IV - 55: Four point probe electrode conductivity geometry.

The calculated conductivity is shown in Figure IV - 56. The calculated conductivity from modeling fits very well with the 4 probe measurement. The probe contact resistance was also obtained from this model, which was used, along with the conductivity, to calculate the interfacial resistance between electrode coating and aluminum substrate. It was determined that the interfacial resistance was 0.2 ohm-cm^2, which is much higher than the electrode resistance (less than 0.05 ohm). The modeling results suggest that the interfacial resistance between the coating and substrate plays a significant role to the total electrode conductivity, which can in turn affect the cell power performance for automobile applications.
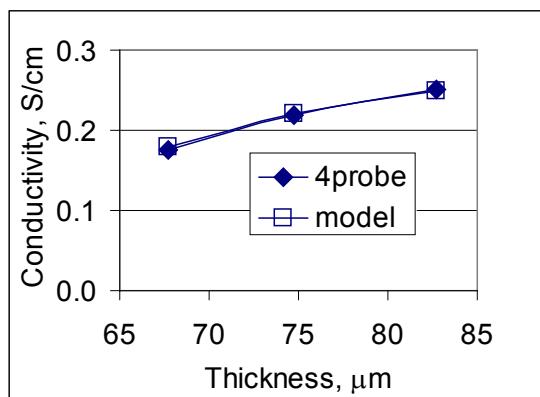
Figure IV - 56: Electrode conductivity of coating using polyester as substrate.

The hybrid pulse power characterization (HPPC) was carried out on the half cells containing NCM powders with and without carbon coating. The calculated area specific impedances (ASI) at the same depth of discharge (DOD) are shown in Figure IV - 57. The impedance of both electrodes is relatively constant with porosity. The left plot of the ASI results for the electrode without carbon coating as a function of electrode porosity is less constant with the impedance decreasing with more calendering. As for electrode with 3% carbon coating, the overall impedance is reduced from around 40 ohm-cm^2 to 30 ohm-cm^2. The test results demonstrated that the carbon coating on NCM powder did significantly improve the power performance at the cell level.
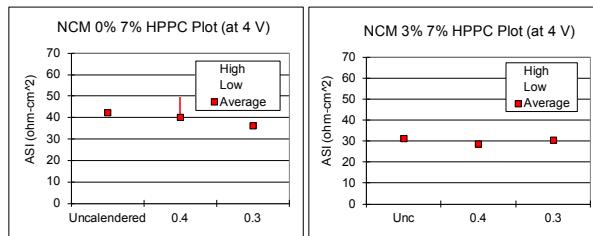
Figure IV - 57: ASI of NCM electrode with and without carbon coating.

Modeling on the optimum composition zone: The objective of this modeling work is to determine the optimum electrode composition that will provide high energy and high power with minimum carbon and binder loadings. In this porous electrode modeling study, the physical parameters such as electrical conductivity and electrode porosity were used for a variety of compositions to predict the corresponding electrochemical performance. The porous electrode model along with cell design parameters such as cathode thickness, electrode delamination, and brittle nature of the electrode were also used to screen the optimum composition zone for high energy and high power. Thereafter, coin cells were fabricated for the same range of electrode compositions and the corresponding electrochemical performances of the cells were measured. The results of the optimization

studies of LiFePO$_4$ are presented in the Figure IV - 58 below.
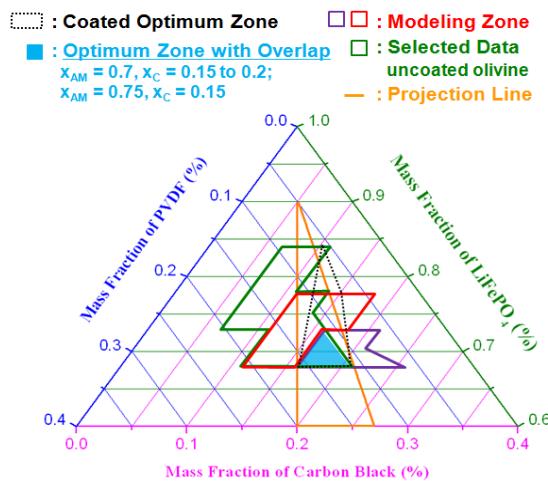
Figure IV - 58: ASI of NCM electrode with and without carbon coating.

Modeling results indicate that porosity is a more dominating factor than electronic conductivity to decide electrode performance. Higher carbon content in the mixture improves capacity, but very large carbon content leads to thicker cathode leading to voltage loss and hence lowers energy. The optimum composition for high rate performance is, 15% < Carbon < 20%; 70% < AM < 75%. This optimum composition is not affected significantly by nature of carbon coating on olivine material. Based on this approach (model+experiment), we will attempt to search the optimum zone for any given cathode material and nature of binder/carbon materials.

Conclusions and Future Directions

In the past four years, we investigated the interactions among active material, conductive additive, and binder. It was found that percolation threshold is low even for extremely poor conductive electrode materials, such as LiFePO$_4$, which suggests that less conductive carbon additive is possible to make good conductive composite electrode.

Then, the novel carbon coating effect on NCM was studied using 4 point probe method. The interfacial conductivity between the electrode coating and substrate turns out to be very critical to the overall conductivity of electrode.

Finally, a porous electrode model work was used to determine the optimum electrode composition. The modeling results indicate the optimum composition zone for LiFePO4. A similar study will be attempted for lithium manganese rich nickel cobalt oxide.

This fiscal year is the last year for "optimization of lithium ion battery electrode". Through four years study, the effect of each component of lithium ion battery electrode was better understood. We also successfully discovered that the interficacial resistance between

electrode and current collector is important factor to affect the electrode's overall conductivity. This finding will help us to prepare better electrodes for high energy and high power lithium ion batteries. Under this project, we started the modeling work to determine the optimum composition of the electrode for given electrode design. More effort is needed to complete this study in the future.

FY 2012 Publications/Presentations

1. Streamlining the Optimization of Li-Ion Battery Electrodes, W. Lu, 2012 DOE Annual Peer Review Meeting Presentation, May 14th-18th 2012, Washington DC.
2. Electronic Conductivity Optimization of Lithium-Ion Battery Electrode, W. Lu, N. Liu, and D. Dees, 220th ECS Meeting & Electrochemical Energy Summit in Boston, Massachusetts (October 9-14, 2011).
3. Electrode Optimization for High Performance Li-Ion Cells, A. Benmayza, V. Ramani, J. Prakash, and W. Lu, 220th ECS Meeting & Electrochemical Energy Summit in Boston, Massachusetts (October 9-14, 2011).
4. Olivine electrode engineering impact on the electrochemical performance of lithium-ion batteries, Wenquan Lu, Andrew Jansen, Dennis Dees, and Gary Henriksen, J. Material Research, 25 (8) 2010, 1656-1660.

IV.B.2.4 Development of Industrially Viable Battery Electrode Coatings (NREL)

Robert Tenent

National Renewable Energy Laboratory
16253 Denver West Parkway
Golden, CO 80401
Phone: (303) 384-6775
E-mail: robert.tenent@nrel.gov

Collaborators:
Anne Dillon (NREL)
Chunmei Ban (NREL)
Bryant Polzin (ANL)
Andy Jansen (ANL)
Chris Orendorff (SNL)

Subcontractor:
University of Colorado at Boulder

Start Date: January 2012
Projected End Date: September 2015

Objectives

- To develop a deposition system for thin protective electrode coatings using a novel "in-line" atmospheric pressure atomic layer deposition (AP-ALD) reactor design that can be integrated into manufacturing to address needs for improvement in rate capability, cycle life, and abuse tolerance in a cost effective manner.

Technical Barriers

Thin electrode coatings produced by Atomic Layer Deposition (ALD) have been shown to lead to significant improvements in lithium ion battery performance. At present, ALD is not likely suitable for large format coating of deposited electrodes. This work seeks to develop new equipment for ALD that allows in-line deposition of coatings at room temperature.

Technical Targets

- Limited calendar and cycle life
- Abuse tolerance
- High cost.

Accomplishments

- Demonstration of improved performance for an ALD alumina coated commercial electrode material.
- Demonstration of ALD alumina coatings on up to 6" by 6" substrates.
- Demonstration of atmospheric pressure ALD deposition on a moving substrate.
- Design of a new in-line ALD system for deposition on porous substrates.

✧   ✧   ✧   ✧   ✧

Introduction

Recent work conducted between NREL and the University of Colorado at Boulder has demonstrated improved performance for both anode and cathode materials following deposition of thin protective Al_2O_3 (alumina) coatings using Atomic Layer Deposition (ALD). These protective ALD coatings have been shown to improve durability, rate capability, operation at a higher potential vs Li/Li^+ and may possibly improve cell safety.

As an example, Figure IV - 59 shows improved cycling performance for $LiCoO_2$ before and after ALD coatings. It is important to note that these samples were cycled from 3.3V to 4.5V which is considered an abusive condition for $LiCoO_2$; however the ALD coating appears to stabilize the electrode.
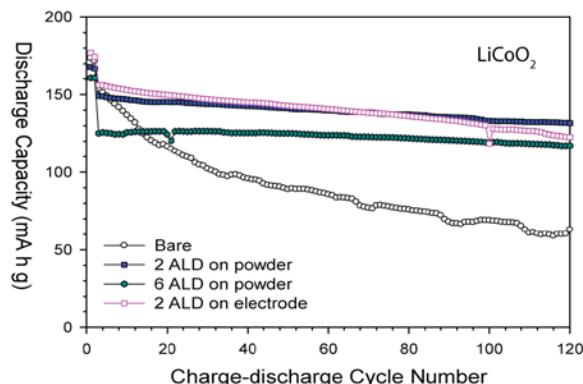

Figure IV - 59: Cycling performance for ALD alumina coated samples of $LiCoO_2$ cycled between 3.3V and 4.5V.

ALD is performed using sequential, *and separate*, exposures of two (or more) reacting species to a stationary substrate at temperature and under a moderate vacuum (100 mTorr). Extensive purging is required between

precursor exposure steps in order to eliminate the possibility of cross reaction in the gas phase. ALD is not likely compatible with present battery manufacturing processes based on the need for vacuum as well as sequential static exposures of precursor materials and subsequent purging steps. NREL is developing a new reactor design that will enable ALD to be performed not only at increased pressures, but also on moving substrates.

Approach

As discussed above, ALD methods are conducted by sequential and separate exposure of a sample substrate surface to gas phase precursors which react to form a film. Deposition is typically performed in a closed reactor system at mild vacuum as is shown in Figure IV - 60. Precursor exposure steps are conducted in a single chamber and are separated *in time*. In a typical exposure "cycle" a sample is exposed to one precursor and the chamber is then purged with inert gas prior to exposure to the second precursor completing the coating reaction. The "cycle" ends with another extensive inert gas purging step before the process can be started again. Film growth takes place by repeating this cycling precursor exposure process multiple times. The sequential and separate exposures are keys to achieving the excellent conformal film deposition on highly textured substrates for which the ALD technique is known.
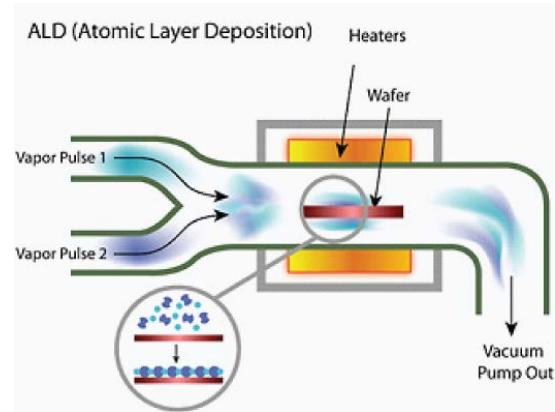

Figure IV - 60: A typical ALD chamber with sequentially separated precursor exposure which draws out overall processing time.

As an alternative to the temporal separation of precursor exposure in the same reaction chamber, our work proposes a *spatial* separation of precursor exposure steps that is more consistent with "in-line" processing techniques. Figure IV - 61 shows a simplified conceptual schematic of our proposed apparatus.

Our "spatial" ALD approach employs a multichannel gas manifold deposition "head" that performs sequential exposure of precursor materials as an electrode foil translates beneath it. It is important to note that similarly designed deposition heads are currently employed by glass manufacturers for production of a variety of coated glass products using high-volume, in-line atmospheric pressure chemical vapor deposition (AP-

CVD). Our approach leverages this existing knowledge base as well as our ALD expertise in order to enable in-line ALD coating that will allow the transfer of our previously demonstrated ALD-based performance improvements to larger format devices.
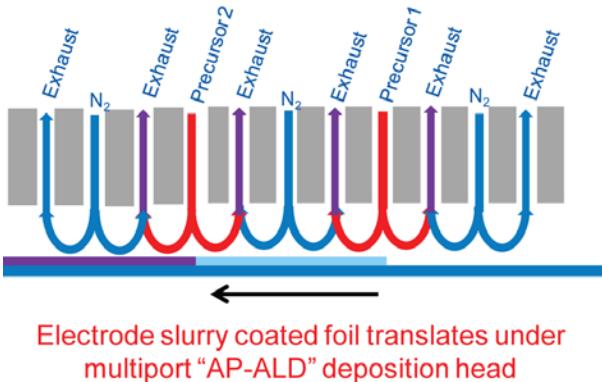
Figure IV - 61: A simplified schematic demonstrating the in-line spatial ALD concept.

Results

Our initial project focus has included two main thrusts. The first involves studies of the effect of ALD alumina coatings on a variety of commercial cathode materials. The second thrust is focused on scaling of the ALD process. We have demonstrated ALD coatings on electrode foils up to a size of 6" by 6" and also conducted work on an improved design for in-line ALD on porous electrode substrates. All of these areas will be discussed in more detail below.

Development of In-Line ALD. Leveraging and building upon previous work by our collaborators at the University of Colorado at Boulder, we have recently completed a preliminary design for an in-line ALD system specific for deposition on porous substrates. The majority of our previous work was focused on the deposition of aluminum oxide via the reaction of trimethyl aluminum with water vapor. More recent work performed by Professor Steven George's group at the University of Colorado at Boulder (CU-Boulder) showed that aluminum oxide could be deposited onto flat silicon substrates using an in-line atmospheric pressure ALD (AP-ALD) format.

Figure IV - 62 shows the design for the initial in-line AP-ALD demonstration from our collaborators at CU-Boulder. The deposition system consists of a multichannel gas manifold that creates separated exposure zones for both trimethyl aluminum and water. A silicon wafer was placed on a heated substrate which was translated underneath the gas flow head. The wafer substrate was moved back and forth below the deposition head to drive two full ALD alumina deposition cycles per translation. All deposition was performed at atmospheric pressure. An example of an alumina film deposited on a silicon wafer using in-line AP-ALD is shown in Figure IV - 63.
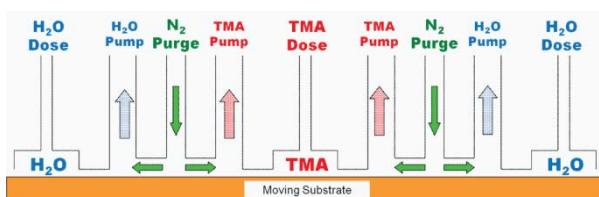
Figure IV - 62: A preliminary design from the George Group for demonstration of in-line AP-ALD.
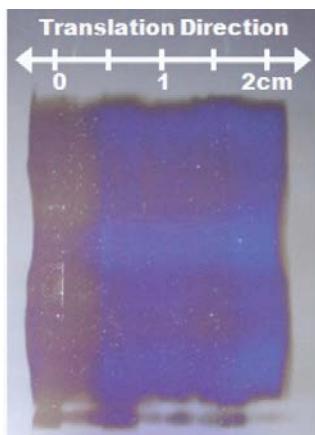
Figure IV - 63: Demonstration of in-line deposition of aluminum oxide onto a silicon wafer at atmospheric pressure.

Design of In-Line AP-ALD for Porous Substrates.
While the above work has demonstrated the feasibility of in-line AP-ALD, a crucial factor for successful coating of battery electrodes using this technique is the ability to coat *porous* substrates. Coating of a porous substrate presents a specific technical challenge as precursor materials must be able to fully penetrate as well as be removed from the porous film as rapidly as possible. This requires that the porous film be exposed to alternating high and low gas pressure regimes. Under viscous flow (high pressure) conditions, a high number of gas phase collisions drives penetration of precursor gases into the film, while molecular flow conditions (low pressure) allow rapid removal of unreacted precursor prior to the next precursor exposure step. Figure IV - 64 shows a recently completed improved design that will allow in-line deposition to be performed with alternating pressure regimes.

As shown in this new design, the coated electrode foil translates underneath multiple gas source heads which would be similar to the gas head designs shown previously, but these gas deposition heads would also be contained in a larger chamber that would be at a lowered pressure to facilitate removal of unreacted precursor. We are currently in the process hiring a post-doctoral researcher who will construct and test the initial prototype for this new reactor.
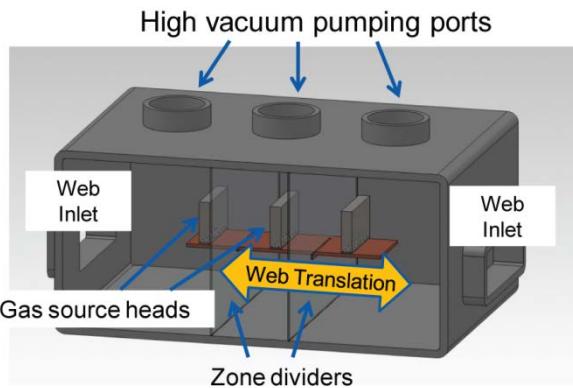
Figure IV - 64: Initial design of an in-line ALD reactor for deposition on porous substrates.

Deposition on Large Format Samples. In addition to our work related to in-line AP-ALD, NREL has also recently acquired a larger format ALD system. This system allows ALD to be performed on electrode foils up to 6" by 6". This system will be used to facilitate larger format pouch cell testing while the in-line depositions systems are completed. Figure IV - 65 shows a 6" by 6" foil of Toda HE5050 provided by the Argonne Cell Fabrication facility that has been coated with 5 cycles of ALD alumina. Cells fabricated from this sample are currently under test and larger format cells will be provided to external parties for testing once initial efficacy of the coating method is established.

Initial Screening of Commercial Electrode Materials. NREL has obtained a variety of electrodes and electrode materials (powders) from collaborators at Argonne NL (Bryant Polzin and Andy Jansen) as well as Sandia NL (Chris Orendorff) to enable preliminary investigation of the effects of ALD coatings. Table IV - 4 lists the materials received.

Figure IV - 65: A 6" by 6" foil of TodaHE5050 following coating with 5 cycles of ALD alumina.

Table IV - 4: ABR Electrode Materials Received for Coating with ALD Alumina.

A12 Graphite
Toda HE5050 NMC
Toda NCA
AML Made LiNiMnO
Toda NMC111
Toda NMC 523

All materials have been under extensive evaluation initially on a coin cell format level at NREL prior to coating with aluminum oxide using ALD. At present, ALD alumina depositions have been performed on formed electrodes of Toda NMC111 from Sandia as well as Toda HE5050 from Argonne and samples are currently under test.

Toda NMC111. In collaboration with Sandia, NREL performed ALD alumina coating on electrode foils of Toda NMC111 and CP A10 graphite. These foils were used for fabrication of 18650 cells and subsequent thermal analysis to determine the effect of ALD coatings on suppression of high temperature thermal runaway. Figure IV - 66 shows coated foils and 18650 cells fabricated at Sandia. These electrode foils were coated by rolling the foils up and placing them in a standard ALD deposition system. Upon return to Sandia, 18650 cells were fabricated and tested. Cells were formed with coated anode or coated cathodes paired with uncoated electrodes in order to ease determination of the effect of ALD coating on either electrode. Upon initial testing, it was found that several cells failed and the cause was attributed to damage due to the electrode rolling process that was used to enable deposition in the existing (not in-line) ALD systems. Cell failures were found to predominate with the coated cathode cells; however, several coated anode cells were functional and subjected to accelerated rate calorimetry (ARC) testing at Sandia to examine the effect of ALD coatings on thermal runaway. Figure IV - 67 shows ARC data from Sandia for one of the coated anode cells. Comparison of measurements made for an identical cell fabricated without any ALD coating appears to show an approximately 20°C increase in the onset temperature for high rate thermal runaway. This likely indicates that the ALD coatings stabilize the anode and suppress high temperature decomposition.
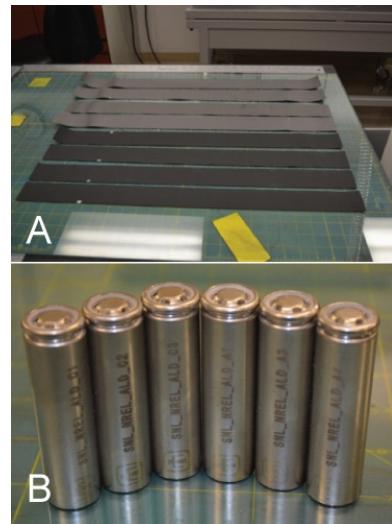
Figure IV - 66: (A) Samples of NMC 111 and A10 Graphite provided by Sandia NL and coated with ALD alumina by NREL/CU (B) 18650 cells fabricated from coated ALD foils for testing at Sandia.
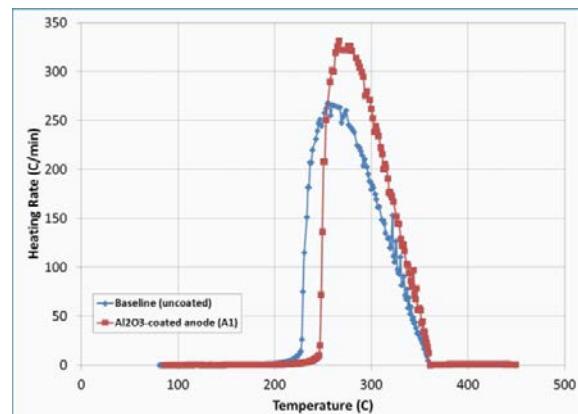
Figure IV - 67: Accelerated Rate Calorimetry Data for Cells with and without an ALD alumina coated anode.

While this data is suggestive that ALD coatings may improve safety, significant further work is needed and planned to assess this. In order to avoid the earlier issues with damage to electrode foils, NREL is currently developing coating processes for powders of NMC 111 and 523 that can be used for further studies.

Toda HE5050. In addition to testing of the NMC 111 material, NREL has also begun work on characterizing the performance of ALD coatings on Toda HE5050 using already formed electrodes provided by the Argonne Cell Fabrication Facility (Bryant Polzin). Work in this area has been conducted to date using standard, single chamber, ALD systems to perform initial screening experiments. The HE5050 material was chosen for further experimentation due to interest in understanding how ALD coatings may impact the voltage fade phenomenon observed for this material. Figure IV - 68 shows initial cycling capacity data for HE5050 electrodes tested in a half cell format under a variety of conditions with and without ALD alumina coatings.
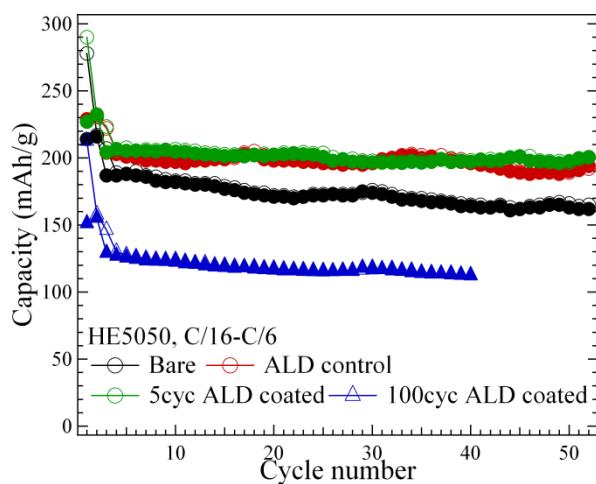
Figure IV - 68: Cycling capacity performance for a variety of HE5050 samples with and without ALD coatings. Condition details are given in the text.

The samples for the data shown in Figure IV - 68 consisted of an untreated sample that was tested as received (bare) and two samples that were coated with either 5 or 100 cycles of ALD alumina. In addition to these coated samples another control sample was placed in the ALD reactor and exposed to an identical process temperature profile, but without *deliberate* precursor exposure. The data in Figure IV - 68 appears to show that the ALD coated and ALD control samples give better cycling durability than the uncoated sample. It is interesting to note that the ALD control sample that was only exposed to heating does appear to give a similar response to the 5 ALD cycle sample. Also, we note that similar experiments with 10 and 20 cycles of ALD alumina showed nearly identical behavior to the 5 cycle sample. This result is inconsistent with multiple previous observations that increasing number of ALD cycles leads to a decrease in initial capacity. In an attempt to further understand the situation, coating experiments were performed with 100 cycles of ALD alumina on an HE5050 electrode. The 100 cycle sample does show the initial capacity loss as well as apparently improved cycling durability as compared to a bare sample. Based on the current data, our hypothesis is that while it is certainly possible that the thermal treatment of the HE5050 sample in the ALD chamber may well play a role in improving performance, the absence of the expected capacity decreases with the 10 and 20 cycle samples, likely indicates incomplete coverage of the electrode at low cycle number under the deposition conditions used. Issues with nucleation of ALD films are not uncommon and NREL is currently conducting further experiments based on modifying deposition conditions as well as "post mortem" analysis of existing samples to understand these issues. At this time the observed behavior is not clearly understood.

Conclusions and Future Directions

Significant progress has been made this year on the development of an in-line ALD coating system compatible with coating on formed electrodes. By leveraging existing expertise with our collaborators in the George group at CU-Boulder, we have been able to significantly reduce the amount of time required to demonstrate in-line atmospheric pressure ALD and have been able to move toward design refinement specific to battery materials. We have completed an initial design for a new battery specific in-line reactor and are currently completing a post-doctoral hire to begin work on prototype system construction and demonstration. We anticipate work on this new system to initiate in early CY13.

NREL will continue to work with other ABR PIs not only to supply ALD coated materials (both powders and electrodes), but also to further understand the role that these materials can play in a variety of systems.

FY 2012 Publications/Presentations

1. 2012 DOE Annual Peer Review Meeting Presentation.

IV.B.2.5 Evaluate the Impact of ALD Coating on Li/Mn-rich Cathodes (NREL)

Shriram Santhanagopalan and Ahmad Pesaran

National Renewable Energy Laboratory
15013 Denver West Parkway
Golden, CO 80401
Phone: (303) 275-3944
E-mail: Shriram.Santhanagopalan@nrel.gov

Collaborators:
Chunmei Ban, National Renewable Energy Laboratory
Mohamed Alamgir, LG Chem Power, Inc., Troy MI
David King, ALD Nanosolutions, Broomfield CO
Karen Buechler, ALD Nanosolutions, Broomfield CO

Start Date: June 2012
Projected End Date: Projected September 2013

Objectives

- To assess the technical viability of the Atomic Layer Deposition (ALD) technique on commercial battery active material such and Li/Mn-rich cathode materials.
- To mitigate durability and abuse tolerance issues associated with high capacity Li manganese-rich cathodes.

Technical Barriers

- Rapid fade in capacity of the high voltage Li - manganese rich cathode, particularly at high temperatures (45°C).
- Lack of uniformity data from large batches of commercial active material treated with the atomic layer deposition (ALD) technique to overcome durability issues.
- Ineffectiveness in coating sheets of electrodes directly with ALD to achieve results similar to coating powders of active material.

Technical Targets

- Demonstrate capacity loss of less than 20% at C/2 rate over 500 cycles at 45°C for the high-voltage manganese-rich cathode.
- Demonstrate scalability of the ALD process by coating batches up to 500g, of the manganese-rich cathodes with alumina, to reproduce cell level performance observed at the lab-scale.

- Build capabilities to directly coat electrode sheets up to 6" x 6" in size.

Accomplishments

- Collaborated with LG Chem Power Inc. (LGCPI) and obtained commercial samples of Li manganese-rich cathode materials.
- Collaborated with ALD NanoSolutions, a leading company for coating ALD on battery materials to scale-up ALD coating using alumina on high capacity Mn-rich cathode material.
- Initial evaluation of the coated powders show little to no reduction in cell capacity over 50 cycles.
- Modification of reactor to coat electrode sheets was initiated.
- Initial results indicated that 2-3 cycle ALD coatings with Al_2O_3 could decrease the Li/Mn-rich fade rate.

✧   ✧   ✧   ✧   ✧

Introduction

Extending the driving range of PHEVs requires the use of high-voltage cathodes that offer consistent performance over 5000 cycles, 15 years of battery life without compromising safety. The Mn-rich cathode is an excellent choice of material for these specifications and has been shown to have the potential to be stable over a wide voltage window between 4.5 and 2.7 V. Preliminary work at the lab-scale, between NREL and LG Chem Power Inc. (LGCPI) indicated that while ALD coating of the cathode improved its cycling performance, no enhancements were observed on coating carbon-based anodes. In the current effort initiated in June of 2012, we demonstrate the scalability of the ALD process and re-affirm findings from the preliminary study, using large format pouch cells. In addition to this, we will also explore the viability of coating sheets of electrodes directly.

Approach

Powders

- Coat 200-500g batches of Mn-rich cathode powders in pilot-scale reactors at a sub-contractor's facility.
- Optimize the coating conditions to minimize rate-capability losses, if any, by building cells using several batches of ALD-coated cathode material and testing them at NREL.

- Evaluate optimized coatings by building and testing pouch cells at LGCPI.

Electrodes

- Modify ALD-reactors to hold sheet-electrodes.
- Develop a process to coat electrodes uniformly across the thickness of the sample.
- Characterize and test samples at NREL and LGCPI.
- Refine coating process based on initial evaluation results.

Results

In FY12, the focus was on scaling up the ALD coating of powder samples. Two different samples of cathode powders were provided by LGCPI. Each of these samples was subjected to two different ALD coating profiles (Run 1 and Run 2) to assess the uniformity of the coating and the resistance as a function of the number of cycles. The profiles were chosen based on the preliminary investigation of these cathode materials carried out earlier at NREL.

ALD Coating. The pre-processing step included drying at overnight. No unusual off-gassing or decomposition reactions were observed. The coating process involved the following steps:

i) loading the bed of powders into the fluidized bed reactor (shown in Figure IV - 69),

ii) fluidizing the powders at the coating temperature and pressure

iii) introducing the ALD precursors sequentially. Each cycle comprised of the routine A-purge-B-purge – and the process was repeated for the desired number of cycles.

Figure IV - 69: Fluidized Bed Reactor to coat powders with ALD cycles: the existing reactor at ALD Nanosolutions can process up to 8L of powder per batch.

The coating was carried out at the vendor ALD Nanosolutions' facility in Broomfield, CO. ALD Nanosolutions has been doing ALD coating of battery materials and has the capability to process multiple batch

sizes from tens of grams to tens of kilograms. The samples were fluidized at 10 cm^3 per minute after the initial drying. The coating time per batch was about 2.5 hours. The initial trials focused on alumina coatings, since we had demonstrated the proof-of-concept with alumina on the Mn-rich cathode material.

Characterization. The baseline sample consisted of spherical particles with a D_{50} of 11 and 12 μm for the two batches (Sample 1 and Sample 2). The SEM images before and after coating are shown in Figure IV - 70. A uniform coating is observed for both the cycle profiles. Upon coating, the alumina content after Run 1 and Run 2 are shown in Table IV - 5. Run 1 employed fewer cycles to form a thin ALD coating and Run 2 involved a thicker coating.

Sample 1 (Baseline)　　　　Sample 1 (Coated)

Sample 2 (Baseline)　　　　Sample 2 (Coated)
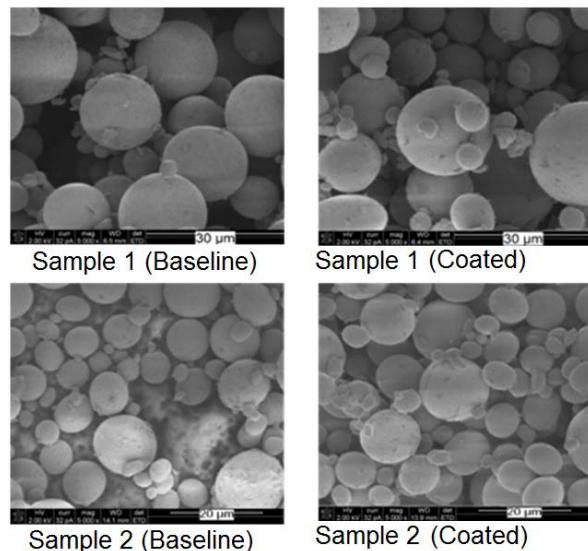
Figure IV - 70: SEM images of two different batches of Mn-rich cathode powders coated with alumina: the coatings are uniform and conformal over a range of baseline particle sizes.

Table IV - 5: Composition of Alumina on different batches of Mn-rich cathode material coated with Al_2O_3 using ALD.

Sample ID	Run 1	Run 2
1	0.98%	1.86%
2	1.12%	1.91%

Physical observations showed that the alumina on Sample 2 tends to flake off readily (perhaps due to a different surface treatment on the baseline particles). Neither sample showed any degradation or discoloration when stored in the electrolyte at 60^oC over two weeks.

Cell-Evaluation. The coated material was evaluated using coin cells at NREL and pouch cells at LGCPI. The sample coated in Run 1 showed good cyclability and low IR-drop during the 1C discharge pulses (Figure IV - 71). The cells which were fabricated with the samples coated in Run 1, showed almost no degradation after 50 cycles at 100% Depth of Discharge (DOD), when cycled at 25^oC at

the C/2 rate. As shown in Figure IV - 72, the baseline samples showed a detectable loss in cell capacity under identical conditions.
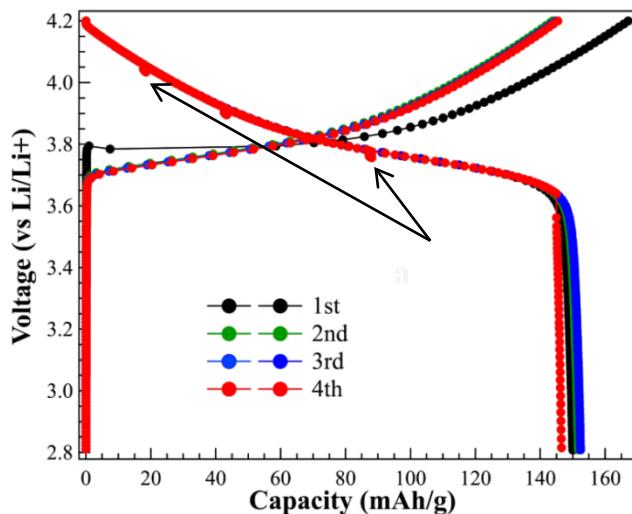
Figure IV - 71: Initial evaluation of Sample 2 coated with Al_2O_3 in Run 1 using coin cells at NREL: Charge and Discharge at C/5 (25°C) with 1C-discharge pulses for 20s after every 10% discharge.
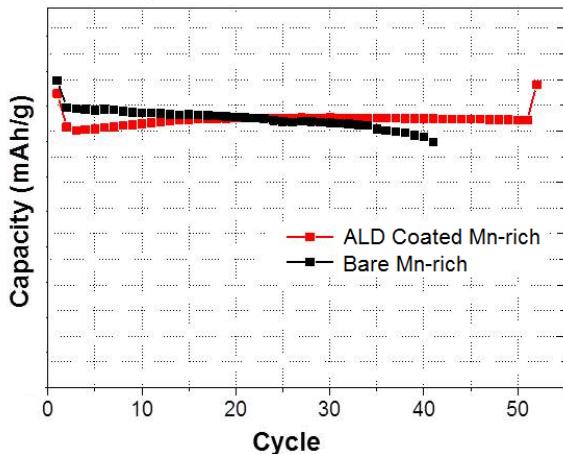
Figure IV - 72: Cycling performance of pouch cells at 25°C subjected to 100% DOD cycles at the C/2-rate.

The samples coated in Run 2 showed higher resistance versus the baseline material as confirmed by electrochemical impedance measurements (Figure IV - 73) possibly because the coating thickness is higher.
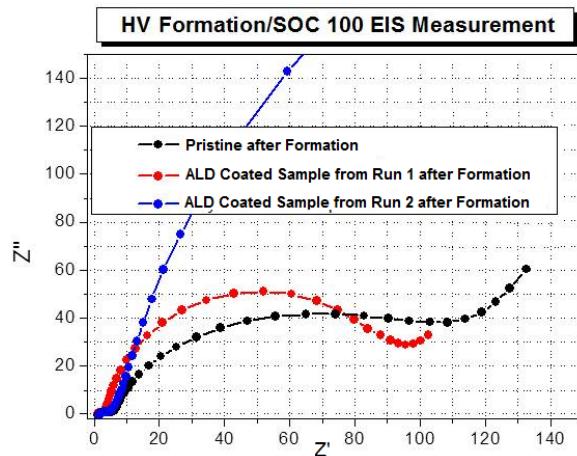
Figure IV - 73: EIS measurements on Mn-rich cathode material coated with different ALD layers of Al_2O_3: the powders coated in Run 2 show larger impedance build up compared to the baseline.

Conclusions and Future Directions

The initial results indicate that the ALD technique is quite scalable with the cathode powders. A semi-continuous production option has also been validated for large scale manufacturing that will facilitate industry adoption. Initial results indicated that 2-3 cycle ALD coatings with Al_2O_3 could decrease the Li/Mn-rich fade rate. The initial cycles of the baseline particles coated Al_2O_3, shows a gradual increase in the cell capacity. This is indicative of the need for optimizing the coatings and the cathode properties, to enhance mutual compatibility, and maximize the cell performance. A predictive roadmap is an integral feature to expedite the commercialization of the technology. Future runs will focus on such optimization based on these initial results.

The second part of the project focuses on coating electrode sheets directly with ALD cycles. Towards this end, modification of the reactors to coat electrodes is underway. NREL has been working with ALD Nanosolutions, to install electrode-racks to facilitate coating of electrodes as large as 6" x 6". Future work will include coating of sheets of electrodes.

FY 2012 Publications/Presentations

1. Shriram Santhanagopalan, Mohamed Alamgir, Karen Buechler, David King and Ahmad Pesaran, "Evaluate ALD Coatings of LGCPI Cathode Materials or Electrodes", Milestone Report # 55894, Submitted September 2012.

IV.B.2.6 Overcoming Processing Cost Barriers of High-Performance Lithium-Ion Battery Electrodes (ORNL)

Peter Faguy (ABR Program Manager)

David L. Wood, III
One Bethel Valley Road
P.O. Box 2008, MS-6134
Oak Ridge, TN 37831
Phone: (865) 574-1157; Fax: (865) 241 4034
E-mail: wooddl@ornl.gov

Collaborators: Andy Jansen (ANL), Chris Orendorff (SNL)

Start Date: October 1, 2011
Projected End Date: September 30, 2014

Objectives

- Eliminate costly, toxic, and flammable solvents.
- Improve aqueous electrode suspensions via dispersant addition.
- Improve wetting of aqueous electrode suspensions to current collector.
- Reduce cost of manufacturing composite electrodes.
- Validate processing achievements on baseline materials

Technical Barriers

The major problems with aqueous electrode dispersions are: 1) excessive agglomeration of active phase particles and conductive carbon additive; 2) poor wetting of the dispersion to the current collector substrate; and 3) cracking of the electrode coating during drying. N-methylpyrrolidone (NMP) based processing has the inherent disadvantages of high solvent cost and toxicity and the requirement that the solvent be recovered or recycled.

Technical Targets

- Selection of an appropriate dispersant for dispersing electrode suspensions.
- Control of rheological properties and agglomerate size in electrode suspensions.
- Improvement of wetting of aqueous cathode suspensions on Al foil.
- Achieving desirable cathode performance with cathodes manufactured through aqueous processing.

Accomplishments

- Confirmation of effectiveness of polyethyleneimine (PEI) as the dispersant for $LiFePO_4$, $LiNi_{0.5}Mn_{0.3}Co_{0.2}O_2$ (NCM 523) and A12 graphite.
- Improvement of wetting of aqueous $LiFePO_4$ suspensions on Al foil via corona plasma treatment.
- Successful manufacturing of $LiFePO_4$ composite cathodes through aqueous processing.
- Successful manufacturing of NCM 523 cathode and ConocoPhillips (CP) A12 graphite anode.

✧   ✧   ✧   ✧   ✧

Introduction

For conventional lithium-ion batteries, the manufacturing process for $LiFePO_4$ cathodes involves a slurry processing in which $LiFePO_4$ is mixed with other additives in a solvent with polyvinylidene fluoride (PVDF) and N-methyl-2-pyrrolidone (NMP) as the typical binder and solvent, respectively. If the composite cathodes could be processed by an aqueous method, in which the expensive NMP is replaced with deionized water, the cost would be significantly reduced, and the process for recovery and treatment of NMP would be eliminated. Based on a recent Oak Ridge National Laboratory (ORNL) processing cost study, this approach has a potential to save up to 70% in the electrode processing steps translating to a 12% reduction of the overall battery pack cost. However, replacing NMP with water also creates some problems, such as particle agglomeration and inferior wetting of aqueous suspensions on current collector.

We have proposed to control particle agglomeration using an appropriate dispersant(s). The addition of the dispersant increases the charge on particle surfaces, and, consequently, the repulsive potential. As a result, the particles will repel each other when dispersed. Inferior wetting of aqueous suspensions on the current collector may be improved by increasing the surface energy of current collector via corona plasma treatment. With the appropriate dispersant and surface energy of current collector substrate, $LiFePO_4$ cathodes were manufactured through aqueous processing with excellent performance. This is a significant step towards low-cost manufacturing of composite electrodes for lithium-ion batteries.

Approach

Fabrication of composite electrodes via organic (baseline) and aqueous suspensions was completed. A focus was placed on the effect of processing parameters and agglomerate size on the aqueous-route cell performance and microstructure of the composite electrode. Several active anode graphite and cathode (NMC, LiFePO$_4$, etc.) materials were selected with various water-soluble binders. The conductive carbon additive was held constant. Rheological (viscosity) and colloidal (zeta potential) properties of the suspensions with and without dispersant were measured with a focus on minimization of agglomerate size. These measurements have shown the effects of agglomerate size and mixing methodology on suspension rheology and have helped determine the stability (i.e. ion exchange processes across the surfaces of various crystal structures) of active materials in the presence of water. Composite electrodes were made by tape casting and slot-die coating, and electrochemical performance of electrode coatings was characterized in half-cells.

Improved cell performance with reduced processing and raw material cost will be demonstrated using pilot-scale coatings. Half-cells were tested and evaluated for irreversible capacity loss, AC impedance, capacity vs. charge and discharge rates. Ultimately, long-term performance through at least 500 charge-discharge cycles will be obtained in coin cells and pouch cells. The coin cells will be used for screening and coarse evaluation of different suspension chemistries and coating methodologies. A fine tuning of these research areas will be completed using ORNL pouch cells and large format cells with ORNL's industrial partners. Electrode coatings will be produced on the ORNL slot-die coater and supplied in roll form to Argonne National Laboratory (ANL), Sandia National Laboratories (SNL), and other industrial partners for assembly into full coin and large-format cells.

Electrode morphology will be characterized by scanning electron microscopy (SEM) and TEM. The bulk structure and surface of the active materials will be characterized using XRD and XPS, respectively.

Results

During the first half of the year, research focused on LiFePO$_4$ cathodes as this project transitioned from the Advanced Manufacturing Office (AMO) to the Vehicle Technologies Program (VTP). During the second half of the year, efforts were concentrated on the VTP Applied Battery Research (ABR) baseline active materials of Toda LiNi$_{0.5}$Co$_{0.2}$Mn$_{0.3}$O$_2$ (NCM 523) cathode and CP A12 graphite anode in collaboration with ANL and SNL. Round robin testing of these baseline electrodes (made by ORNL, ANL, and SNL) is being conducted by ANL and will be completed by December 2012.

Figure IV - 74 shows the surface energy data for a LiFePO$_4$ cathode dispersion with poly(ethyleneimine) (PEI), which is added to reduce agglomeration of the active and conductive additive particles, and for various Al foil surfaces with and without corona treatment. It is seen that the surface energy of the electrode dispersion is well above that of the untreated Al foil (62.9 vs. 47.9 mJ/m^2). This situation results in poor wetting of the dispersion to the current collector foil, but the data in Figure IV - 74 shows that corona treatment conditions of ≥0.4 J/cm^2 raise the surface energy of the foil above the surface energy of the dispersion, which is the condition required for good wetting. Corresponding half cell performance data is shown in Figure IV - 75 for the different surface treatment energy densities. An optimum energy density of 0.4 J/cm^2 was found, and cells with corona treatment (regardless of energy density) significantly outperformed the cell with no corona treatment. It is thought that the optimum value of 0.4 J/cm^2 results from sufficiently cleaning the surface of adsorbed hydrocarbons and subsequent hydroxylation, but falls short of possible restructuring of the surface at much higher energy densities. This restructuring could result in significant roughening and formation of pits and voids, which would lower the adhesion energy and raise the interfacial tension of the electrode coating and result in increased half cell high-frequency impedance.
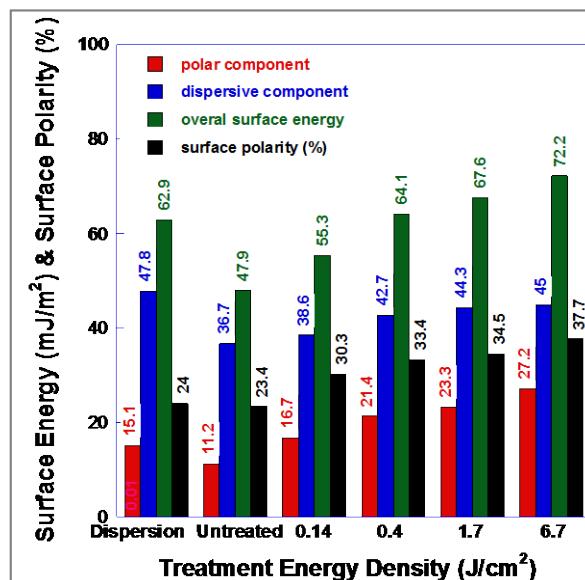

Figure IV - 74: Surface energy of treated and untreated Al foils and LiFePO$_4$ aqueous dispersion; the surface energy and polarity of Al foils increased with increasing corona treatment energy density.
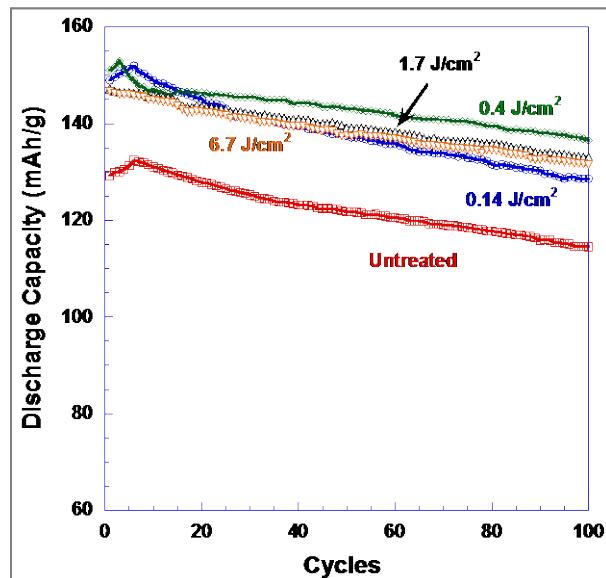
Figure IV - 75: Cycling of LiFePO$_4$ cathodes at 0.5C/-0.5C (0.34 mA/cm^2) confirming 0.4 J/cm^2 as the best corona treatment energy density for long term performance.

ABR Baseline Coatings. A NCM 523 dispersion consisting of 50.7 wt% and 49.3 wt% NMP was prepared by first mixing NCM 523 with Solvay 5130 PVDF in NMP solution, followed by dispersing the Denka carbon black. An A12 graphite dispersion was prepared composed of 45 wt% solids and 55 wt% NMP. Super P Li carbon was first dispersed in the Kureha 9300 PVDF and NMP solution. Then A12 was mixed into the resulting dispersion with a planetary mixer. The dispersions were coated using the ORNL slot-die coater, and the wet electrodes were pre-dried using seven convective heating zones with temperatures ranging from 150°F to 270°F.

Figure IV - 76 shows a roll of NCM 523 cathode and A12 graphite anode with 6" width. The electrodes demonstrate excellent quality free of defects. Desired solid loadings were obtained for the round robin testing, and Table IV - 6 lists the electrode properties. The electrode balance between anode and cathode was 1.1 n/p.
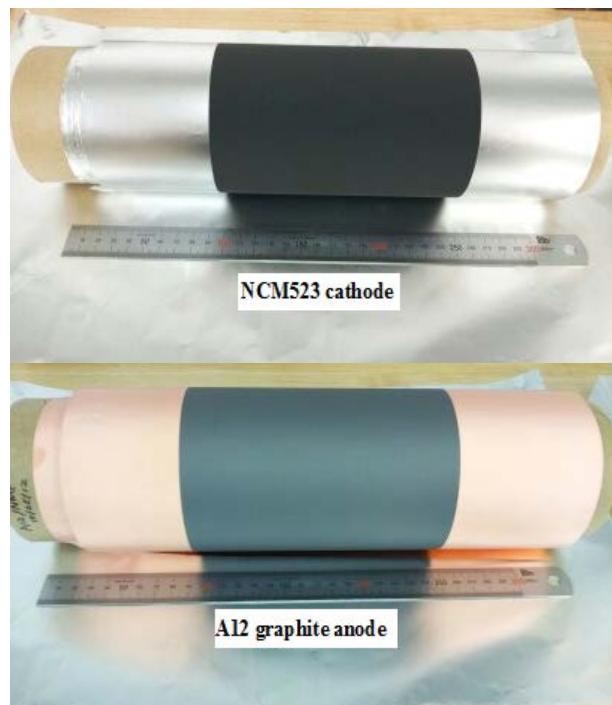
Figure IV - 76: A roll of NCM523 cathode and A12 graphite anode from baseline coating.

Table IV - 6: Properties of ABR baseline electrode coatings.

Electrode	Composition	Solid loading (mg/cm^2)	Capacity (mAh/g)	Electrode balance
NCM 523	NCM 523 / Denka carbon black / Solvay 5130 PVDF = 90/5/5 wt fraction	12.92	160	Anode / cathode = 1.1
A12	A12 / Super P Li / Kureha 9300 PVDF = 92/2/6 wt fraction	6.93	320	

NCM 523 cells were evaluated by charging and discharging at C/5 for 25 cycles, and rate performance was investigated by charging at C/5 and varying the discharge rates. C-rate was calculated based on a theoretical capacity of 160 mAh/g for NCM 523. As shown in Figure IV - 77a, NCM 523 demonstrated excellent first charge and discharge capacity of 172.1 and 170.0 mAh/g, respectively, with 2.1 mAh/g irreversible capacity loss (ICL). The discharge capacity after 25 cycles was 165.7 mAh/g, with retention of 97.5%. C-rate dependence is shown in Figure IV - 77b, and excellent capacity at C/10 and C/5 was obtained – higher than 165 mAh/g. The capacity dropped from ~165 mAh/g to ~140 mAh/g when the C-rate was increased from C/5 to 1C. This rate behavior indicates a well-produced electrode.
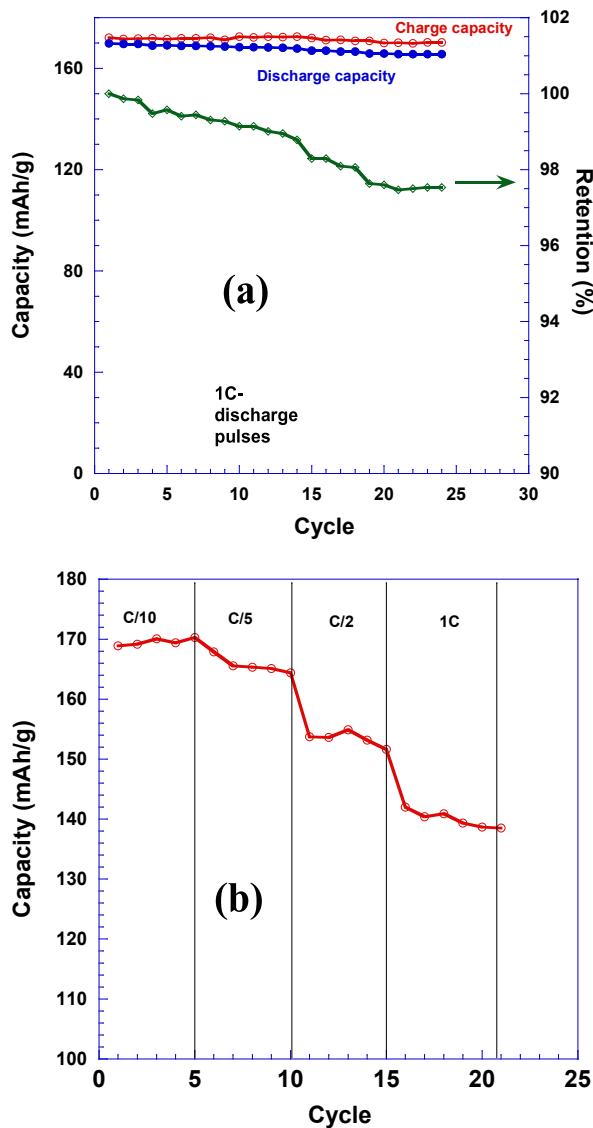
Figure IV - 77: Initial performance of NCM 523 cathodes; a) 25 cycles discharged at C/5 and b) rate performance.

Zeta potential of NCM 523 and A12 graphite. Zeta potential was measured for dispersant selection for both NCM 523 and A12 graphite using a ZetaPALS instrument (Brookhaven Instrument Corporation). Carboxymethyl cellulose (CMC) has been reported to be an effective dispersant for graphite and was selected for this work as a starting point. According to the zeta potential results in Figure IV - 78, the isoelectric point (IEP) of A12 graphite was pH≈3. The addition of 1 wt% CMC (Fisher Scientific, MW = 250,000 g/mol, DS = 0.7) shifted the IEP to lower pH. More importantly, the zeta potential range of A12 with 1 wt% CMC was more negative compared to that of A12 and close to -30 mV at the natural pH of the A12 dispersion (pH≈6). Generally, dispersed particles with a surface charge more positive than 30 mV or more negative than -30 mV are considered to be stably dispersed. Thus,

the stability of the A12 graphite dispersion with 1 wt% CMC was improved over that without CMC addition.
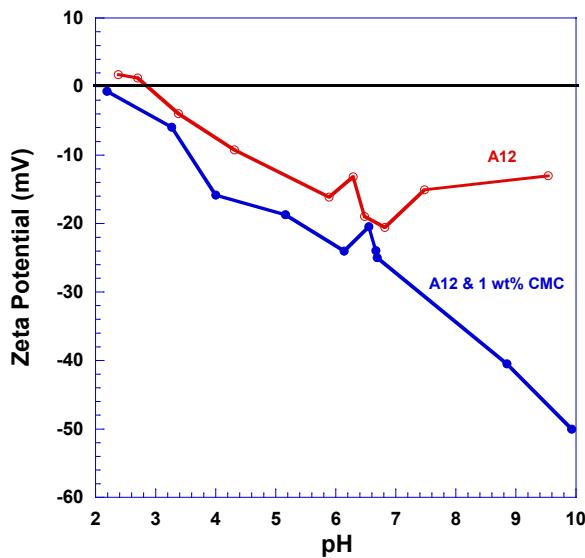
Figure IV - 78: Zeta potential of A12 graphite with and without CMC; the addition of 1 wt% CMC resulted in a more negative charge on the A12 surface.

Similarly, zeta potentials of NCM 523 with and without CMC were also investigated (see Figure IV - 79). The addition of 1 wt% CMC shifted the IEP to pH<2, and the zeta potential with CMC was more negative than -30 mV at the natural pH of NCM 523 (pH≈7.2). Therefore, CMC was also effective in improving the stability of the NCM 523 aqueous dispersion.
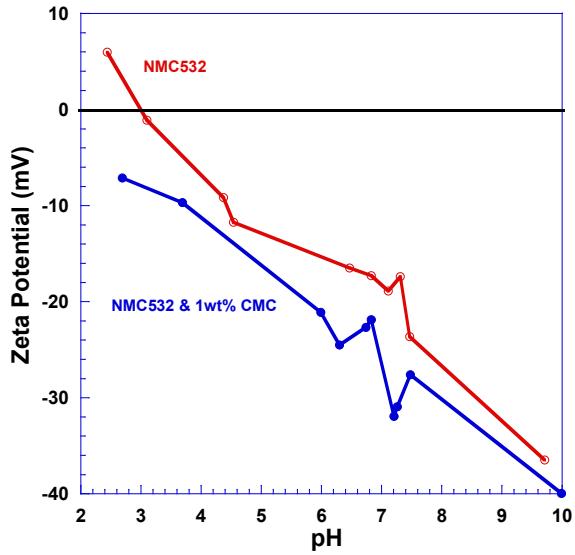
Figure IV - 79: Zeta potential of NCM 523 with and without CMC; the addition of 1 wt% CMC resulted in a more negative charge on the NCM 523 surface.

Rheological properties of aqueous NCM 523. Aqueous NCM 523 (Toda America) suspensions with various CMC (Fisher Scientific, M.W.=250,000 g/mol,

DS=0.7) concentrations were prepared by mixing CMC solution in water for 10 min followed by dispersing NCM 523 in the resulting solution for 10 min. The mixing process was carried out by a high-shear mixer (model 50, Netzsch). The CMC concentration was based on NCM 523 mass, and the NCM 523 to water ratio was 1:2.5.

Rheological properties of aqueous NCM 523 with various CMC concentrations were investigated using a controlled stress Rheometer (AR-G2, TA Instruments) and shown in Figure IV - 80. The NCM 523 suspensions exhibited shear thickening behavior with CMC concentration below 0.5 wt%. The rheological behavior switched to Bingham plastic/Newtonian behavior and shear thinning at shear rate below 1000 s^{-1} with 1.0 wt%
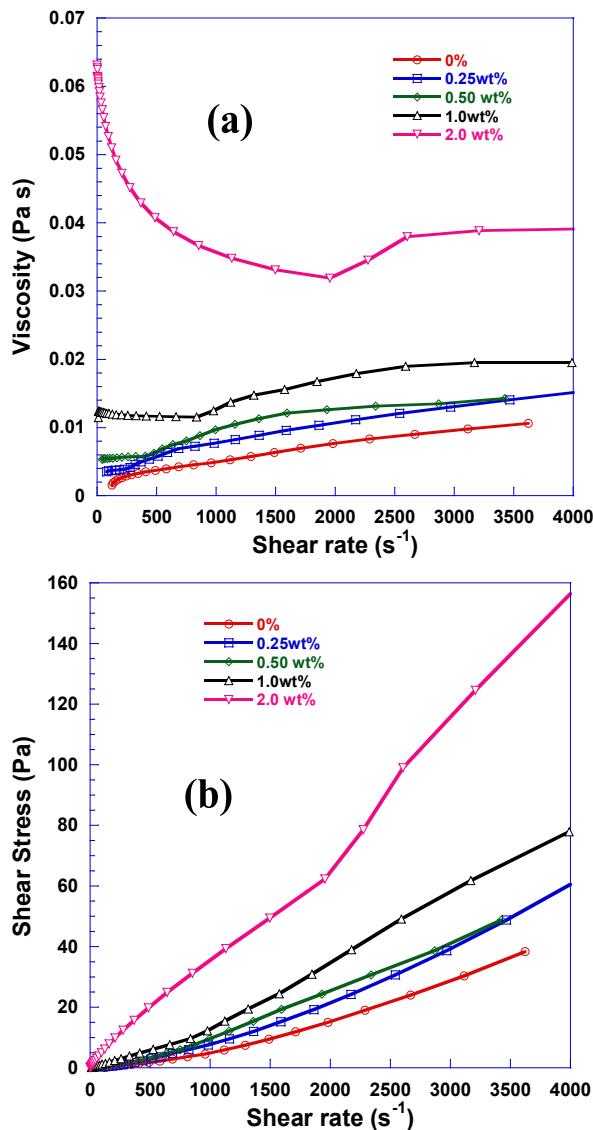

Figure IV - 80: Rheologic properties of aqueous NCM 523 suspensions with various CMC concentrations a) viscosity vs shear rate and b) shear stress vs shear rate.

and 2.0 wt% CMC, respectively. The critical shear rate (>1000 s^{-1}) was relatively high, which was above the

operating window of most common coating methods. For instance, coating using a doctor blade with 200 μm gap and a shear rate of 750 s^{-1} translates to coating speed of 12 m min^{-1}, which is higher than the industrial coating speed (~20 ft min^{-1}) in manufacturing lithium-ion battery electrodes. Therefore, the low shear rate region is more interesting and will be focused in the following discussion. The rheological behavior change was further evidenced by the shear stress and shear rate plot as shown in Figure IV - 80b, which could be fitted with Herschel−Bulkley (H−B) model. The fitting power-law indices are listed in Table IV - 7.

Table IV - 7: Parameters from H-B model for the NCM523 suspensions.

CMC concentration	0.0 wt%	0.25 wt%	0.50 wt%	1.00 wt%	2.00 wt%
Power-law index, n	1.57	1.51	1.64	1.05	0.83

The H−B equation is one of the most employed models for situations where a nonlinear dependence exists of shear stress on shear rate. It is described by the power law equation and is stated as the following:

$$\tau = \tau_0 + K\dot{\gamma}^n \quad \begin{cases} \text{if } \tau > \tau_0 \\ \text{if } \tau \leq \tau_0 \end{cases}$$
$$\dot{\gamma}=0 \qquad\qquad\qquad\qquad (1)$$

where τ, τ_0, K, $\dot{\gamma}$ and n are the shear stress, yield stress (stress needed to initiate the flow), consistency index, shear rate and power-law index, respectively. If n = 1, this function reduces to the classical Bingham plastic equation. If $\tau_0 = 0$ and n = 1, this function describes Newtonian behavior.

The power-law index was 1.05 with 1.0 wt% CMC, demonstrating the best suspension stability. In addition, NCM 523 suspension exhibited higher viscosity with increasing CMC concentration. This suggested that CMC not only acted as a dispersant in aqueous NCM 523 suspension but also a binder.

Median agglomerate size, D_{50}, of the aqueous NCM 523 suspension was measured by laser diffraction (Partica LA-950 V2, Horiba Scientific) and is shown in Figure IV - 81. D_{50} was approximately constant and not dependent on CMC concentration, which could be attributed to the spherical structure of NCM 523 secondary particles with large particle size and high density. Although the effect of CMC on the agglomerate size of NCM 523 is not pronounced, the addition of CMC significantly affects the rheological properties of NCM 523 suspensions.
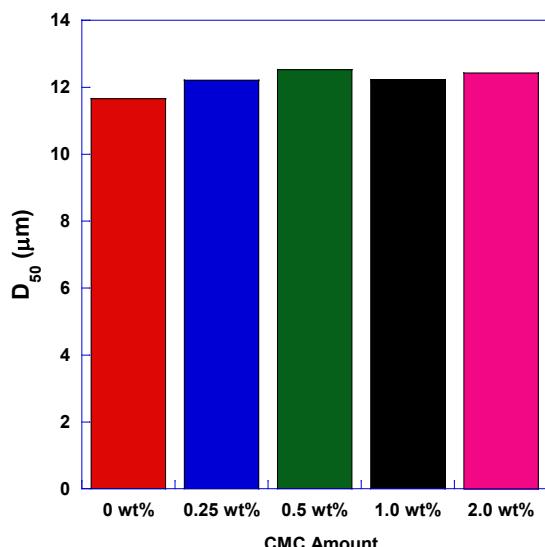
Figure IV - 81: Agglomerate size of aqueous NCM523 suspension with various CMC concentrations.

Conclusions and Future Directions

PEI has been shown to be an effective dispersant for aqueous processing of $LiFePO_4$. The wetting of aqueous $LiFePO_4$ on the Al foil was significantly improved via corona plasma treatment, and the electrode performance improved as well. High quality NCM 523 and A12 graphite electrodes were successfully manufactured as baseline coatings for round robin testing between ORNL, ANL, and SNL.

The addition of CMC shifts the surface charge of NCM 523 cathode and A12 graphite anode to more negative values and improves the dispersion of the two materials. An NCM 523 suspension with 1 wt% CMC demonstrates Bingham plastic behavior indicating a stable dispersion.

ORNL will continue supporting the round robin electrode testing and electrode processing standardization activities led by ANL. ORNL will also optimize the processing conditions to manufacture NCM 523 cathodes and A12 graphite anodes through aqueous processing with emphasis on the formulation, dispersion chemistry, mixing protocol, coating method, and drying protocol. Testing in half-cells, full coin cells, and full-active-area pouch cells will be carried out, and the cell performance from aqueous processing will be compared to that of the ABR baseline coatings.

FY 2012 Publications, Reports, Presentations, Intellectual Property, and Patent Applications

1. J. Li, B.L. Armstrong, J. Kiggans, C. Daniel, and D.L. Wood, "Optimization of $LiFePO_4$ Nanoparticle Suspensions with Polyethyleneimine for Aqueous Processing," *Langmuir*, 28 (2012) 3783-3790.

2. J. Li, C. Rulison, J. Kiggans, C. Daniel, and D.L. Wood, "Superior Performance of $LiFePO_4$ Aqueous Dispersions via Corona Treatment and Surface Energy Optimization," *Journal of The Electrochemical Society*, **159**, A1152–A1157 (2012).

3. J. Li, B. Armstrong, J. Kiggans, C. Daniel, and D. Wood, "Dispersant and Mixing Sequence Effects in $LiFePO_4$ Processing," 221st Meeting of The Electrochemical Society, Seattle, Washington, Abstract No. 164, May 6-11, 2012.

4. J. Li, B. Armstrong, J. Kiggans, C. Daniel, and D. Wood, "Lithium Ion Cell Performance Enhancement Using Aqueous $LiFePO_4$ Cathode Dispersions and Polyethyleneimine Dispersant", *Journal of the Electrochemical Society,* Under Review.

5. D. Wood, J. Li, D. Mohanty, S. Kalnaus, B. Armstrong, and C. Daniel, "Advanced Materials Processing for Lithium-Ion Batteries", 222nd Meeting of the Electrochemical Society, Honolulu, HI, October 7-12, 2012.

6. B.L. Armstrong, C. Daniel, D.L. Wood, and J. Li, "Aqueous Processing of Composite Lithium Ion Electrode Material," Filed October 12th, 2012, U.S. Patent Application No. 13/651,270 (UT-Battelle, LLC).

IV.B.2.7 Roll-to-Roll Electrode Processing and Materials NDE for Advanced Lithium Secondary Batteries (ORNL)

Peter Faguy (ABR Program Manager)

David L. Wood, III
One Bethel Valley Road
P.O. Box 2008, MS-6134
Oak Ridge, TN 37831
Phone: (865) 574-1157; Fax: (865) 241 4034
E-mail: wooddl@ornl.gov

Collaborators: Dan Abraham, Andy Jansen (ANL), Chris Orendorff (SNL), Athena Safa-Sefat (ORNL); Keyence America, FLIR Systems, Inc., Solar Metrology, Ceres Technologies, Inc.

Start Date: October 1, 2011
Projected End Date: September 30, 2014

Objectives

- Raise the production yield of lithium secondary battery electrodes from 80-90% to 99% and utilize *in situ* and *ex situ* diagnostic tools for electrode structural characterization to improve the performance.
- Reduce associated cost by implementing in-line XRF, laser sensing, and IR thermography as non-destructive evaluation (NDE) and quality control (QC) tools.
- Correlation of *in situ* XRD with TEM, SQUID (magnetic susceptibility), and neutron scattering diagnostics for understanding the microstructure of electrodes in order to increase the performance, safety, and calendar life.

Technical Barriers

- Material processing cost and electrode quality control.
- Cell calendar and cycle life and performance.
- Electrode stability at high voltage.

Technical Targets

- Implementation of critical QC methods to reduce scrap rate by an order of magnitude (to meet $300/kWh VTP storage goal for PHEVs).
- Correlation of cathode microstructural parameters with performance to meet calendar and cycle life and long-term performance needs.

- Integrate material diagnostics findings with electrode NDE development pathway to advance lithium secondary battery manufacturing science.

Accomplishments

- In-line IR imaging demonstrated the ability to identify the defects and inhomogeneity in the electrodes.
- In-line laser thickness measurement shows benefits of tracking electrode coating thickness; uniformity results of ± 2-3% have been obtained.
- Preliminary off-line XRF results have been obtained for slot-die coated electrodes showing excellent transition metal composition and areal loading uniformity.
- *In situ* XRD allowed for investigation and monitoring of the voltage fading mechanism in Toda HE5050 Li-rich cathode by identifying the spinel phase during low voltage discharge after subsequent cycles.
- Magnetic susceptibility measurement (SQUID) provided information on the redox mechanism by demonstrating the change in average transition metal ion oxidation states in Toda HE5050 cathode during high-voltage (4.5 V *vs.* Li/Li$^+$) hold.
- Both TEM and SQUID results were correlated to provide detailed insights to structural degradation pathways in Toda HE5050 during high-voltage (4.5 V *vs.* Li/Li$^+$) hold and show oxygen loss followed by migration of transition metal ions to the lithium layer during prolonged voltage hold.

✧　　✧　　✧　　✧　　✧

Introduction

Due to high scrap rates associated with lithium secondary cell production, new methods of quality control (QC), which have been successful in other industries, must be implemented. The flaws in the electrodes are not detected unit the formation cycling when the entire manufacturing steps have been completed, and the associated scrap rates drive the cost of lithium secondary cells to an unacceptable level. If the electrode flaws and contaminants could be detected in line near the particular processing steps that generate them, then the electrode material could be marked as unusable and the processing equipment could be adjusted to eliminate the defects more quickly. ORNL is considering in line nondestructive evaluation such as X-ray fluorescence spectroscopy (XRF), IR thermography for electrode uniformity, flaws,

blisters as well as metal particle detection and laser thickness sensing of the electrode wet thickness measurement.

In addition, ORNL is providing off-line diagnostic capabilities and expertise to address the materials issue with ABR developed electrode. Currently, we are concentrating on a Li-rich high voltage cathode, Toda HE5050 ($0.5Li_2MnO_3$- $.5LiNi_{0.375}Co_{0.25}Mn_{0.375}O_2$). This lithium rich cathode oxide delivers promising discharge capacities between 200-250 mAhg-1between the voltage window of 2.0-4.7 V (vs. Li^+). However, these materials suffer issues such as voltage fade, low efficiency in first cycle, and an unexpected impedance rise during high voltage hold. Our diagnostics are focusing on those unresolved issues and are establishing the microstructural features of cathode materials that contribute to the degradation of their electrochemical properties. We will subsequently propose solutions to overcome these degradation mechanisms. Materials are obtained from ANL in collaboration with Dan Abraham.

ORNL is currently addressing the following questions on ABR developed electrodes (Li-rich Toda HE5050).

1. Why does voltage of the battery containing Li rich Toda HE5050 cathode drop after subsequent cycles?

2. What is the cause behind the impedance rise during high voltage hold?

3. Why is the first cycle efficiency less at high voltage cycling?

4. How does $LiMnO_3$ activation process relate to the delithiation/lithiation in Li-rich Toda HE5050 composite oxide cathodes?

Approach

1. In line diagnostics.

1.1 Determining the feasibility of in-line XRF with equipment supplier. Solar Metrology has been identified as a top manufacturer of in line XRF instruments for roll-to-roll applications and has a great deal of experience with other industries. ORNL is working closely with them to establish this technology for the lithium secondary battery industry. ORNL is producing tape casted and slot-die coated electrode rolls (anodes and cathodes) to test the appropriateness of the method and determine any required equipment modifications to the standard model. All key process parameters, such as line speed, coating thickness range, elemental homogeneity, etc., will be examined. In-line XRF data will also be correlated with *ex situ* X-ray Computed Tomography (XCT) data to gain a complete chemical and structural picture of the electrode as it is coated and dried.

1.2 Determining the feasibility of in-line laser with equipment supplier. Keyence has been selected as the partner for developing a set of laser thickness sensors for lithium secondary battery electrode production. ORNL has purchased the sensors from Keyence and integrated them directly into ORNL's slot-die coating line for the proof-of-concept experiments.

1.3 Correlation of wet and dry thickness measurement. The output data from wet layer thickness measurement using laser sensors will be correlated with the thickness measurement capability by marking the regions that are out of specification during coating process. The coated electrode rolls with markings will be fed into the in line XRF equipment to determine if the wet regions out of specification match with the dry regions that are determined to be out of specification. A feedback mechanism will be determined that considers whether the wet and dry thickness is a better input for adjusting the dispersion flow rate into the slot-die coater. The IR imaging QC will be correlated with the thickness variation data to determine any further systematic flaw formation mechanism.

2. Offline diagnostics.

2.1 Determining the microstructural changes in ABR developed cathodes during cycling by combined magnetic susceptibility and diffraction tools. ORNL will utilize its expertise in material diagnostic tools such as magnetic susceptibility, *in situ* XRD, TEM and neutron diffraction to investigate the issues related to the ABR developed cathodes. The pristine and cycled materials will be investigated and the structure-electrochemical property correlation will be furnished. The mechanism of voltage/capacity fade in those cathodes will be reported and the method to overcome this barrier will be proposed.

Results

1. In line diagnostics.

1.1 In line laser caliper set-up on slot-die coater system. A Keyence laser caliper system was successfully mounted on our slot-die coater, which is shown in Figure IV - 82. To obtain baseline noise from the thickness measurement (Figure IV - 83), a calibration shim was used. Throughout the 30 minutes of data acquisition, the data were clustered at 92 microns. Variation of ± 1 μm from this average was observed, which validates this approach for measuring electrode thickness.
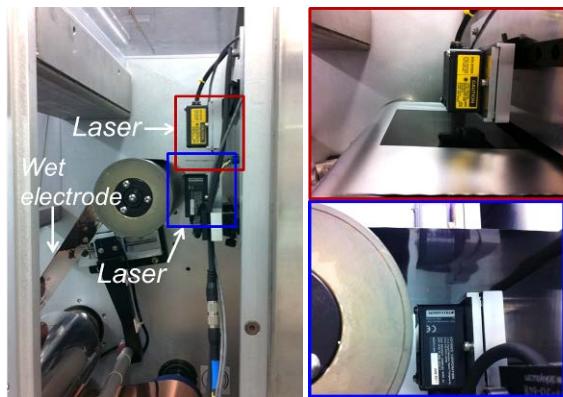
Figure IV - 82: In-line laser caliper set-up inside slot-die coater for wet thickness measurement.
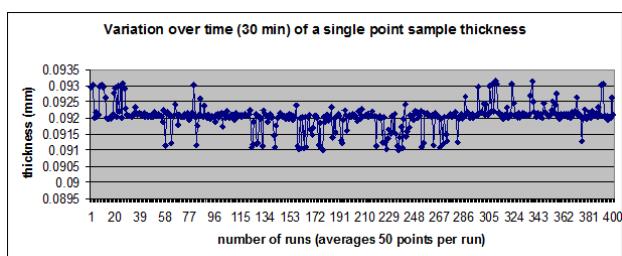
Figure IV - 83: Baseline noise determination from using calibration shim.

Initial laser thickness tests were performed on patch-coated $LiFePO_4$ electrodes on Al foil using a coating speed of 1 ft/min and the results are shown in Figure IV - 84. The average $LiFePO_4$ thickness was found to be 41.3 micron with Al current collector thickness as 18.5 ± 4 micron. These values were close to the expected values. To verify the approach during a larger scale coating trial, these measurements were performed while coating a $LiNi_{0.5}Co_{0.2}Mn_{0.3}O_2$ (NCM 523) electrode (also at 1 ft/min). The thickness measurements of two different regions A and B are shown in Figure IV - 85, and the average coating thickness was found to be 112.26 ± 5.86 micron for region A. However, the average coating thickness was found to be 126.98 ± 2.98 micron in region B. Hence, the non-uniformity of the coating thickness can be precisely and effectively tracked by this laser caliper thickness measurement system. In region A the standard deviation was higher compared to the region B, which indicates the coating in region A was less uniform.

Figure IV - 84: Thickness measurement of $LiFePO_4$ electrode on Al foil.
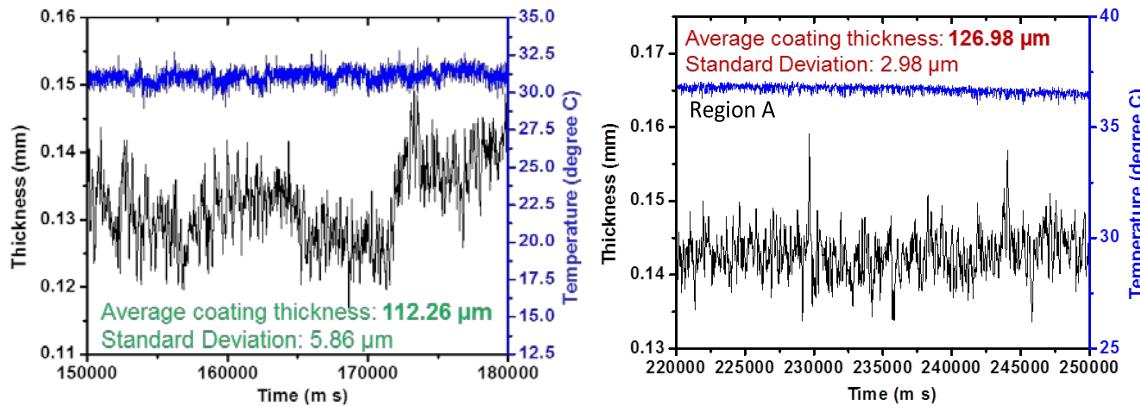
Figure IV - 85: In line thickness measurement of LiNi$_{0.5}$Co$_{0.2}$Mn$_{0.3}$O$_2$ (NCM 523) electrode at different regions; the y-axis represents the temperature at which data were collected.

1.2 In-line IR set-up on slot-die coater. In order to check the homogeneity of dried electrode coatings, IR thermography was utilized outside the slot-die coater. One example from a LiFePO$_4$ electrode is given in Figure IV - 86. Visual inspection revealed little information about the quality of the coating (Figure IV - 86a). However, during IR flashing, very thin spots and several thin lines across the electrode surface were revealed (Figure IV - 86b), which indicates defects associated with the electrode. The temperature profile of the electrode (Figure IV - 86c) shows the thinner (orange and red) and thicker (green) areas indicating thickness variation across the electrode. To complement this result, the high power quartz lamp is viewed through the electrode, and the image (Figure IV - 86d) shows bright and dark spots (thinner and thicker spots, respectively).
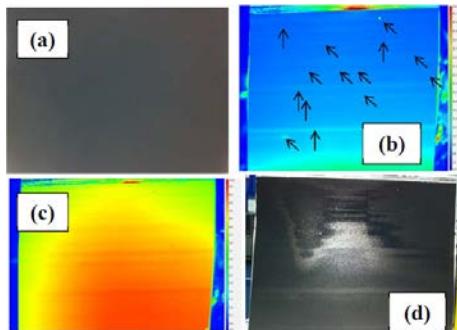
Figure IV - 86: Homogeneity and defect analysis of LiFePO$_4$ electrode coating: visual digital image (a), IR image (b), temperature profile (c), and image taken when quartz lamp is viewed through the electrode (d).

This off-line measurement verified IR thermography as an effective method for QC purposes. Therefore, in-line IR thermography was performed on the dried NCM 523 electrode exiting the heating zone of the slot-die coater, and the experimental set-up is shown in Figure IV - 87. IR images were taken continuously (one image every 5 s) while the dried NCM 523 electrode was exiting the heating zone of slot-die coater at 1 ft/min. The images were subsequently processed to check the homogeneity and quality of the coating. Two representative images are

shown in Figure IV - 88a-b. The temperature profile correlates with the flaws (blisters, pinholes, large agglomerates, etc.) on the coated electrode (Figure IV - 88a), which cannot be detected from digital images. In addition, two line scans were performed in another area of the coating (Figure IV - 88b), which also show the difference in temperature (confirming the presence of defects in the coating).

Figure IV - 87: In line IR imaging set-up on a slot-die coater.
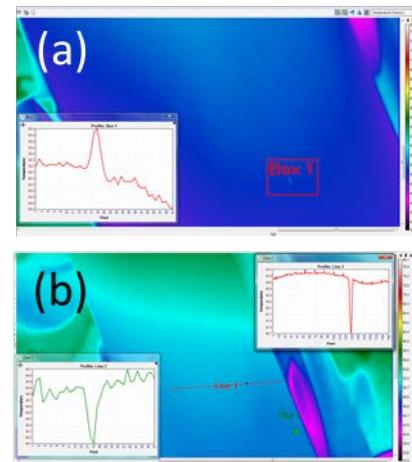
Figure IV - 88: Processed in-line IR imaging data at different regions of a LiNi$_{0.5}$Co$_{0.2}$Mn$_{0.3}$O$_2$ (NCM 523) cathode coating.

1.3 Analyzing stoichiometry and thickness uniformity of electrode samples by XRF. The compositional homogeneity and thickness uniformity of a NCM 523 cathode was also verified by XRF and initial results are given in Figure IV - 89. The composition of the electrode at two different locations was measured, and the ratio of Ni:Co:Mn was found to be close to the nominal composition of the material (0.5:0.2:0.3 Ni:Co:Mn). Excellent thickness uniformity was also obtained (1-2% variation).
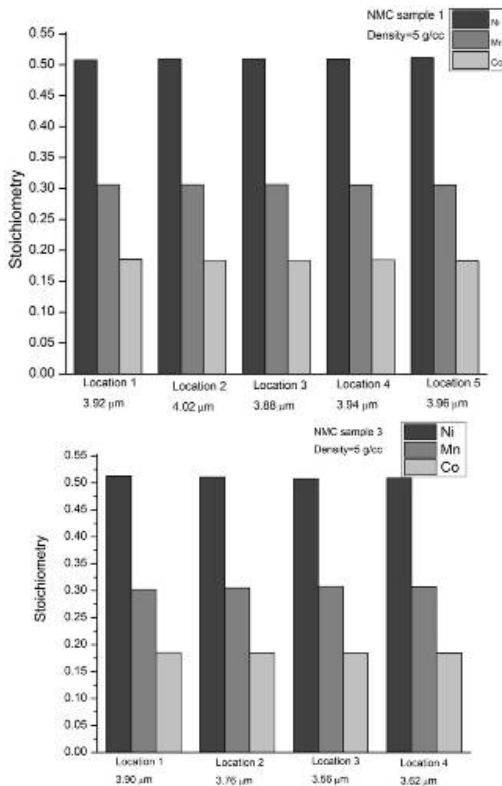
Figure IV - 89: Stoichiometry and thickness uniformity of Ni, Co, and Mn at different locations of a NCM 523 electrode coating.

2. Off-line materials diagnostic on Toda HE5050.

2.1 *In situ* XRD studies during electrochemical cycling to address the voltage fade issue in Toda HE5050 cathode materials. *In situ* XRD experiments were performed on Toda HE5050 lithium rich cathode with composition $0.5Li_2MnO3$-$0.5LiNi_{0.375}Co_{0.25}Mn_{0.375}O_2$. The Toda HE5050 contains two phases, a Li_2MnO_3 monoclinic phase (*C2/m* space group) and $LiNi_{0.375}Co_{0.25}Mn_{0.375}O_2$ layered trigonal phase (*R-3m* space group). The electrochemical cycling was performed in a half-cell configuration with lithium metal as a counter electrode. A specially designed cell for *in situ* XRD with large (9.8 mm in diameter) Kapton window was used. 2032 coin cell hardware was used with 1.2M LiPF6 in ethylene carbonate / dimethyl carbonate (EC/DMC 3:7 per volume) mixture as the electrolyte (Purolyte®, Novolyte) and Celgard 2500 as the separator. The electrodes had the following composition: 86%wt Toda

HE5050 – 8%wt PVDF binder – 4%wt Timcal SFG-6 Graphite – 2%wt Timcal Super P. *In situ* experiments were performed for a freshly prepared electrode (first cycle) and after 16 and 36 cycles. The electrochemical experiments were done at the rate of 10mA/g (C/32 rate calculated based on therorical capacity). The electrochemical voltage vs. capacity curves are presented in Figure IV - 90. The suppression of the discharge profile is clearly visible (refer to arrow mark) after subsequent cycles, which was investigated by *in situ* XRD. The *in situ* XRD patterns from the freshly prepared and cycled (16 and 36 cycles) electrodes were collected, and the lattice parameters were derived by least squares refinement. Figure IV - 91, the calculated lattice parameters during charge and discharge cycle for the freshly prepared electrode and after 36 cycles are shown. In this curve, the increase (decrease) in *c (a)* lattice parameter during early charging (≤ 4.4 V) confirms the lithium ion extraction from the lithium layer. During this process, when lithium ions are being extracted from the lithium layer, the vacancies are created and due to the electrostatic repulsion among cubic-closed-packed oxygen layer, the unit-cell expands.
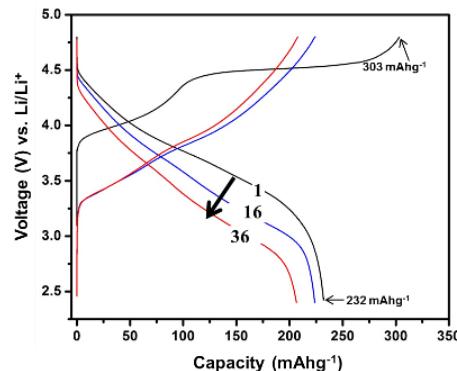
Figure IV - 90: Galvanostatic charge/discharge profiles of Toda HE5050 cathode showing voltage fade after subsequent cycling.
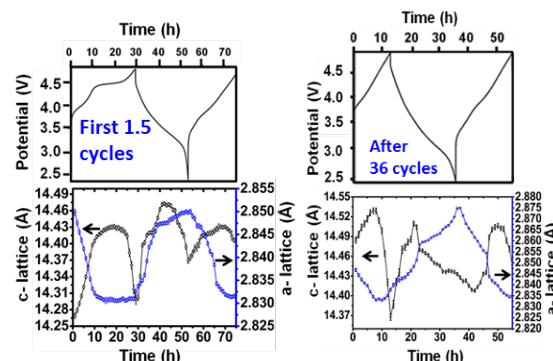
Figure IV - 91: Change in lattice parameter (with error bars) in Toda HE5050 cathode material at different points in the electrochemical charge/discharge profile; these plots were collected from the freshly prepared cell (first 1.5 cycles) and after 36 cycles.

The decrease in *a*- lattice parameter is due to the introduction of ions having smaller ionic radii, Ni^{+4} and Co^{+4}, that are formed due to oxidation of Ni^{+2} and Co^{+3}

during lithium extraction charge compensation. For the fresh cell the *a*- lattice parameter remains constant in the plateau region (4.4 V-4.6 V), which indicates that the extraction of lithium ions, along with the oxygen (Li_2O) due to activation of monoclinic Li_2MnO_3 phase and lithium ions, are being extracted from the transition metal layer. This was not observed after 16 and 36 cycles, which clearly demonstrates that the monoclinic phase percentage decreases after repeated charge/discharge cycles. Interestingly, new peaks were detected during the discharge process (highlighted in circles in Figure IV - 92) of the cells that were cycled for 16 and 36 times. These new peaks were assigned to characteristic (440) planes from spinel phase (ICDD PDF# 00-018-0736) and possibly the $LiMn_2O_4$ phase. The percentage of phase was 64% trigonal and 36% monoclinic after 16 cycles and 72% trigonal and 28% monoclinic after 36 cycles, as compared to 46% trigonal and 54% monoclinic phase for the fresh electrode, which confirms a decrease in monoclinic phase after subsequent cycles. It is also speculated that the layer to spinel phase transformation may suppress the voltage profile and cause the voltage fade in Toda HE5050 lithium-rich cathodes.
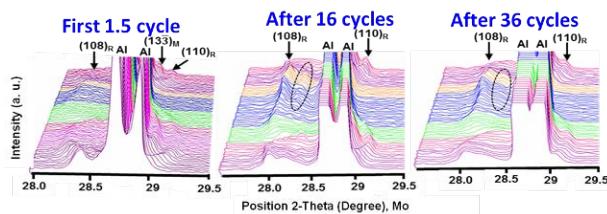
Figure IV - 92: (108), (110), (13) reflection during first 1.5 cycles, after 16 cycles, and after 36 cycles. The R and M subscripts designate the rhombohedral (trigonal) phase and monoclinic phase, respectively. The color stacks represents the different charge/discharge voltages. The appearance of new peaks is highlighted in the dotted regions.

2.2 Magnetic susceptibility and transmission electron microscopy studies during high-voltage hold.

We are currently investigating the stability of Toda HE5050 cathode while holding the cell as constant voltage (4.5 V). Cells containing Toda HE5050 cathode and a Li metal anode were first charged to 4.6 V and discharged to 3.0 V followed by a second cycle charge up to 4.5 V at a rate of 20 mA/g (at a rate of C/16). A separate cell was built for each experiment and electrochemical reactions were stopped at the particular time of interest: after completion of the second charge before high-voltage hold (named as BH), after 60h (AH60), after 70h (AH 70), and after 90 h (AH 90) of holding at 4.5V (see Figure IV - 93). High-resolution transmission electron microscopy (TEM) and selected area electron diffraction (SAED) were collected using a Hitachi HF3300 TEM at 300 kV. DC magnetization was measured as a function of temperature using a Quantum Design Magnetic Property Measurement System. Each sample was first cooled to 5 K in zero field (ZFC) followed by an applied field of 100 Oe, and the data

were collected from 5 K to 320 K. The sample was also cooled in the applied field (FC) from 320 K down to 5 K, while measuring magnetization. Field-dependent magnetization measurements, M(H), were measured at 5 K up to ~7 Tesla. The variation of magnetic susceptibility data with temperature for the pristine material is presented in Figure IV - 94. The pristine sample shows the paramagnetic behavior obeying the Curie-Weiss law at high temperature above 100 K, and the magnetic moment increases in the low temperature region ($\leq$ 75 K). The FC and ZFC curves bifurcate at 50 K indicating a transition from paramagnetic to ferro/antiferromagnetic ordering in the lattice. The presence of lithium ions in the TM layers in Li-rich composite $Li_{1+x}MO_2$ (M=Co, Mn, Ni) structure generates Li_2MnO_3 type ordering and eventually lead to magnetic transition at low temperature. The magnetic interlayer exchange in Li_2MnO_3 is antiferromagnetic (AF), and the compound undergoes AF ordering transition at 50 K. The oxidation state of Co, Ni, and Mn ions in pristine $Li_{1.2}Co_{0.1}Mn_{0.55}Ni_{0.15}O_2$ was determined from a comparison of the experimentally measured effective magnetic moments with the calculated theoretical magnetic moments by considering the magnetic moments of Ni^{2+}, Mn^{4+}/Mn^{3+}, Co^{3+}/Co^{4+} with high spin (HS) and low spin (LS) configurations in octahedra (MO_6) environment. The effective magnetic moments calculated from the plot of inverse molar magnetic susceptibility *vs.* temperature between 100 K and 320 K using the equation $\chi_m = C_m/(T-\theta)$. Here, χ_m is the molar magnetic susceptibility, C_m is the Curie constant, and θ is the Weiss temperature. The experimental effective magnetic moment for pristine Li-rich NMC compound was found to be 3.06 μ_B and is best explained by a combination of 0.15 moles of Ni^{2+} (HS; S= 1), 0.55 moles of Mn^{4+} (HS; S=3/2) and 0.1 moles of Co^{3+} (HS; S=0), which corresponds to a theoretical effective magnetic moment of 3.07μ_B. Hence, the composition of pristine material can be written as $Li_{1.2}Ni^{2+}(HS/LS)_{0.15}Mn^{4+}(HS/LS)_{0.55}Co^{3+}(LS)_{0.1}O_2$.
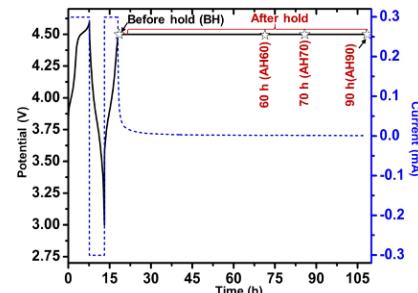

Figure IV - 93: Electrochemical voltage profile showing the desired point of interest for analysis (before hold and after holding for 60h, 70h, and 90h).
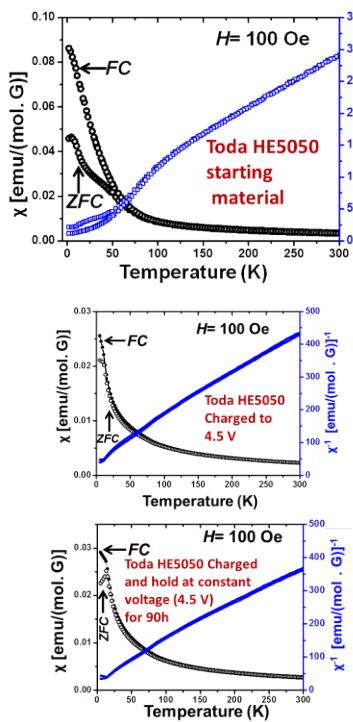
Figure IV - 94: Magnetic susceptibility data for pristine Toda HE5050 after charging to 4.5 V and after holding for 90h.

The magnetic susceptibility curves for BH, AH60, AH70, and AH90 confirm the absence of magnetic ordering at the low temperature region, and the associated effective magnetic moments were calculated and are shown in Table IV - 8. The effective magnetic moment after charging to 4.5 V (BH) is lower than the pristine material, which is due to oxidation of Ni^{+2} and Co^{+3} to Ni^{+4} and Co^{+4} ions, respectively, during lithium ion extraction. The Ni^{+4} has spin value equal to zero (S=0) and decreases the effective magnetic moment. Comparing experimental and theoretical effective magnetic moment models taking different oxidation states of transition metal ions, some fraction of Mn^{+3} ions were found to be present in BH material (see Table IV - 8). During long term holding, the effective magnetic moment was found to increase. When the voltage is constant, it is expected that no net lithium ion diffusion occurs across the electrode. The effective magnetic moment, which is directly related to oxidation states of TM ions, should not change if no lithium ions are extracted/inserted from/into cathode structure. However, the increase in effective magnetic moment during prolonged hold duration illustrates that the charge compensation must have been followed by release of oxygen. This observation is also supported by *ex situ* XRD data where the *c*- lattice parameter of Toda HE5050 cathode was found to decrease after the longer term hold. In the high voltage (delithiated) state, lithium deficient $Li_{1.2-y}Co_{0.1}Mn_{0.55}Ni_{0.15}O_2$ is not stable since the Fermi level is situated within the oxygen valence band by dropping the Fermi energy into the top of the O^{2-}:2p band, which may lead to release of oxygen from $Li_{TM}O_6$ and/or $TM_{TM}O_6$.

This release of oxygen from $Li_{TM}O_6$ may 1) drive the Li_{TM} to migrate from TM layers to the lithium layer filling the octahedra vacancy and/or 2) drive some of the TM ions to lithium layer to fill the vacancy in the lithium layer.

Table IV - 8: Experimental and theoretical effective magnetic moment and magnetic saturation values for pristine, before (BH), and after (AH60, AH70, and AH90) high-voltage hold at 4.5 V. The oxidation states of TM ions which are in agreement with experimental and theoretical effective magnetic moments are also shown.

Material	μ_{exp} (BM)	Model	μ_{theo} (BM)	M_s (emu mol^{-1})
Pristine	3.06 ± 01	0.15Ni^{+2}(HS/LS) 0.55Mn^{+4}(HS/LS),0.1Co^{+3}(LS)	3.07	510
BH	2.70 ± 03	0.15Ni^{+4} (LS) 0.40Mn^{+4}(HS/LS), 0.15Mn^{+3} (LS), 0.01Co^{+4} (LS)	2.78	275
AH60	2.79 ± 01	0.12 Ni^{+4} (LS), 0.03Ni^{+2} (HS/LS) 0.40Mn^{+4}(HS/LS), 0.15Mn^{+3} (LS) 0.1Co^{+4} (LS)	2.83	350
AH70	2.82 ± 01	0.08 Ni^{+4} (LS), 0.07Ni^{+2} (HS/LS) 0.40Mn^{+4}(HS/LS), 0.15Mn^{+3} (LS) 0.1Co^{+4} (LS)	2.88	445
AH90	2.89 ± 02	0.06 Ni^{+4} (LS), 0.09Ni^{+2} (HS/LS) 0.40Mn^{+4}(HS/LS), 0.15Mn^{+3} (LS) 0.1Co^{+4} (LS)	2.91	300

Oxygen loss and filling of the vacancy in the lithium layer by foreign ions could reduce the electrostatic repulsion between *ccp* oxygen layers causing the contraction of the unit cell along the *c*-axis. Due to similar ionic radii of Ni^{+2} and Li^{+}, Ni^{+2} is believed to migrate to lithium layer, which was further confirmed by SAED analysis where a forbidden ($10\bar{1}0$) reflection was observed in the crystals from a cathode that was held at steady voltage for 70h (Figure IV - 95). The particle exhibits a two phase region in the TEM image, which was further confirmed by its FFT taken from two regions (layered and spinel phase was observed).
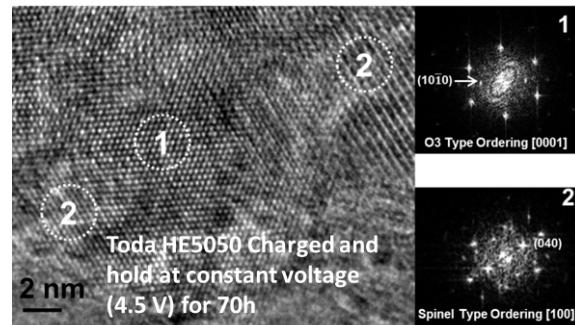
Figure IV - 95: High-resolution TEM showing both the O3 and spinel type lattice fringe in agreement with the corresponding FFT; the particle was analysed from AH70 sample.

The Ni^{+2} in the lithium layer can create a 180 degree antiferromagnetic exchange via Ni^{+2}(lithium layer)-O-Ni^{+2}(TM layer) and/or ferromagnetic exchange interaction via Ni^{+2}(lithium layer)-O-Mn^{+4} (TM layer) (see the model in Figure IV - 96a). In order to investigate this hypothesis, the magnetization curves M(H) at T=5 K was collected and presented in Figure IV - 96b. From this information, magnetic saturation (M_s), which determines the strength of ferromagnetic interaction, can be estimated from the

linear extrapolation to magnetic field (H) → 0. It is evident that the M_s value increases for the AH60 and AH70 materials, which indicates a prominent ferromagnetic interaction. However, for AH90, the M_s value decreases, which indicates that antiferromagnetic exchange is dominant over the ferromagnetic interaction. This antiferromagnetic interaction was also supported by high-resolution TEM data where cubic spinel phase was observed (See Figure IV - 97). The SAED data from that particle also shows the crystal orienting along cubic [100] zone axis.
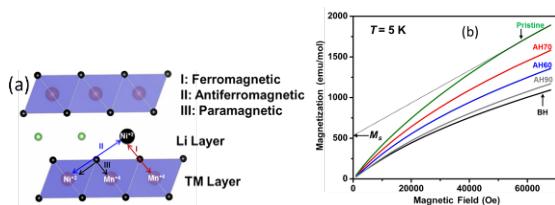
Figure IV - 96: Magnetic model showing the different exchange interaction (a) and the M(H) curves at 5K (b); the linier extrapolation was done to calculate the magnetic saturation values.
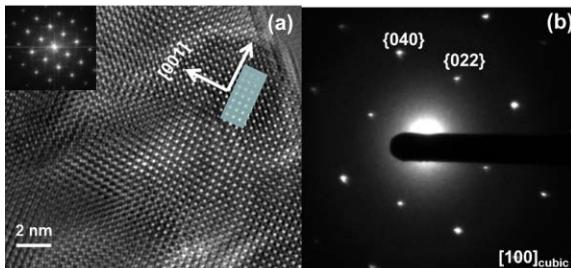
Figure IV - 97: High-resolution TEM image from the AH90 particle showing spinel like lattice fringes (see the simulated image of cubic spinel phase along [100] direction; the FFT and SAED shows spinel phase reflections.

Conclusions and Future Directions

Laser sensors were successfully mounted on the ORNL slot-die coater and calibrated for thickness measurement experiments. The method was validated during coating trials up to 70-80 ft at 1 ft/min line speeds. Thickness was measured on both continuous and patch coated electrodes, and excellent thickness uniformity was observed (2-3% variation). The next steps for this measurement technique is to convert from point scanning to line scanning to obtain thickness variation across the web, and to obtain measurements at higher coating speeds (5-10 ft/min).

IR thermography was implemented on dried electrode coatings produced on the ORNL slot-die coater, and analysis of the processed data verified the ability to detect small defects (pinholes, blisters, and large agglomerates) by the temperature line scans. Next steps include purchasing equipment to determine dried thickness of

electrode coatings exiting the dryer. Initial XRF measurement of tape casted electrodes was completed, and the results showed homogeneous distribution of transition metals across the coating width, as well as excellent thickness uniformity. The next steps involve integrating a desktop XRF unit from Solar Metrology with the ORNL tape caster to obtain in-line measurements of compositional uniformity and thickness (areal weight). These results will be correlated with the IR thermography thickness measurements.

Material diagnostics on Toda HE5050 was also completed using *in situ* XRD, which showed the layered to spinel phase transformation and revealed the presence of (440) spinel peaks after subsequent cycles (to 4.8 V *vs.* Li^+). This phase transformation is believed to cause the observed voltage fade during long-term cycling. Magnetic susceptibility data showed a change in average TM oxidation states during a hold at 4.5 V *vs.* Li^+. Detailed analysis was correlated with TEM results and revealed oxygen release followed by migration of Ni^{+2} to the lithium layer, which eventually causes the shrinkage of unit cell along *c*- axis. Detailed investigation of this voltage fade mechanism in Li-rich cathodes will be continued and a method to overcome this characteristic will be proposed.

FY 2012 Publications/Presentations

1. D. Mohanty, S. Kalnaus, R. Meisner, K. J Rhodes, E. A Payzant, D.L Wood, C. Daniel, "Structural Transformation of a Lithium-Rich $Li_{1.2}Co_{0.1}Mn_{0.55}Ni_{0.15}O_2$ Cathode During High Voltage Cycling Resolved by *In situ* X-Ray Diffraction", *Journal of Power Sources*, Under Review (2012).
2. D. Mohanty, S. Kalnaus, R. Meisner, A. S. Sefat, J. Li, K.J Rhodes, E. A Payzant, D.L Wood, C. Daniel, "Structural Transformation in a $Li_{1.2}Co_{0.1}Mn_{0.55}Ni_{0.15}O_2$ Lithium-Ion Battery Cathode During High-Voltage Hold", *RSC Advances*, Under Review (2012).
3. D. Mohanty, S. Kalnaus, R. Meisner, A. S. Sefat, J. Li, D.L Wood, C. Daniel, "Structural Evolution in Lithium-rich $0.5Li_2MnO_3 \cdot 0.5LiNi_{0.375}Co_{0.25}Mn_{0.375}O_2$ Cathode during High Voltage Cycling; an *in situ* X-Ray Diffraction Investigation" MRS 2012, Boston, MA, November 25, 2012.
4. D. Mohanty, A.S. Sefat, J. Li, S. Kalnaus, R. Meisner, D.L Wood, C. Daniel, "Investigating Phase Transformation Pathways in Lithium-rich $Li_{1.2}Co_{0.1}Mn_{0.55}Ni_{0.15}O_2$ Cathode Material during High Voltage Cycling by Magnetic and Diffraction Studies", MRS 2012, Boston, MA, November 25, 2012.

IV.B.3 Applied Battery Research on Anodes

IV.B.3.1 Developing a New High Capacity Anode with Long Life (ANL)

Ali Abouimrane & Khalil Amine

Argonne National Laboratory
9700 South Cass Avenue
Argonne, IL 60439-4837
Phone: (630) 252-3729 or 3838; Fax: (630) 972-4520
E-mail: abouimrane@anl.gov; amine@anl.gov

Collaborators:
B. Liu, (CSE/ANL).
P. Y. Ren Advanced Photon Source, (APS/ANL).
Z. Fang (University of Utah).
FMC, Northwestern University,

Start Date: October 2008
Projected End Date: September 2012

Objectives

New high capacity anode materials based on the mixture of M_aO_b oxides (M: Si, Sn, Mo, Ge) and Sn_xCo/Fe_yC_z alloys will be prepared and tested in full cell configuration for lithium batteries applications.

Technical Barriers

The primary technical barrier is the development of a safe cost-effective PHEV battery (40 mile) that meets or exceeds all DOE performance goals. The actual technical barriers are:

- Cell energy density (by volume or/and by weight) limitations
- Battery cycle life and high temperature performance.

Technical Targets

When this new chemistry is combined with NMC the following result can be achieved:

- Preparation of a scalable anode material (~250 grams),
- A Cell with nominal voltage of 3.5 V;
- A Cell with energy density of 450Wh/kg;
- An improvement in the cell energy density per volume.

Accomplishments

We use iron instead of cobalt to reduce the cost and toxicity. We try to find out the best combination of SiO-$Sn_xFe_yC_z$ in term of voltage output, cycling performance, and deliverable capacity:

1. Prepare a scalable amount of anode material using ball milling method.
2. Screen out the best combination
3. Study on the structure of as-milled samples and shed light on the way to modify this anode material

✧   ✧   ✧   ✧   ✧

Introduction

State-of-the-art lithium ion battery technology is being developed for large scale applications such as electric vehicles (EVs) and hybrid electric vehicles (HEVs). For this purpose, lithium ion batteries must have long term cycling performance with high capacity. The graphite which is currently used as an anode material has a capacity of about 372 mAh/g where lithium forms graphite intercalation compounds LiC_6 with excellent reversibility. Ongoing research efforts have focused on utilizing various materials (oxides, alloys, tin, silicon) to increase battery capacity, cycle life, and charge-discharge rates. Attention has been recently given to the potential of metal oxide anodes for lithium-ion batteries because of their low price and their high theoretical capacities (more than 600 mAh/g). However, these anode materials suffer from their poor cycleability due to the volume expansion of the lithiated material. Other interesting anode materials are tin based alloys which have been investigated for use in electronic devices and introduced into the market by Sony. For these anodes a practical capacity of about 400-500 mAh/g can be achieved and an increase of the capacity per volume of the full cell battery by 30% was obtained comparatively to the use of the graphite anode. As tin based alloys contain a huge amount of the inactive, expensive and toxic cobalt that prevent the volume expansion during the cycling. Our objective for new anodes is to use iron instead of cobalt, increase the capacity to 600-800 mAh/g with a tap density higher than 1.9g/cc which is 65% higher than that of graphite (1.1~1.2g/cc). New materials based on various compositions of oxide and alloys SiO-$Sn_xFe_yC_z$ system are

prepared and tested as anodes for lithium batteries. The lithium insertion in these anode materials is studied and a mechanism is proposed.

Approach

In order to be cost competitive to the graphite anode we are using iron instead of cobalt, which has many advantages of low cost and toxicity. Different compositions of anode materials based on $SiO-Sn_xFe_yC_z$ system have been investigated. Sn-Fe-(C) anode materials have been studied in some literatures. But due to the low capacity or bad cycle performance, it cannot meet the requirement for applications. SiO has attracts much attention due to its high specific capacity (over 1400 mAh/g). However, this material suffers from its poor cycleability due to the volume expansion of the lithiated material. Sn-Fe-C can exhibit higher volumetric energy density than the conventional graphite anode and has a good cycleability with less volume expansion by tuning the composition. In the SiO- $Sn_xFe_yC_z$ composite, SnFeC will play the role of buffer for SiO anode and improve its cyleability and SiO will provide more capacity.

Results

The Figure IV - 98a shows the discharge/charge specific capacity versus cycle number of 50wt.%SiO-50wt.%$Sn_{30}Fe_{30}C_{40}$ composite electrode, along with its coulombic efficiency. It delivers a specific capacity of 900 mAh/g and 700 mAh/g at the rate of 300 mA/g and 800 mA/g, respectively. The coulombic efficiency is 67% of 1st cycle. The capacity loss of 1st cycle may be attributed to more Li+ ions trapped in electrode particles and consumed on SEI formation. After the initial cycles, the coulombic efficiency rapidly increases to near 100%, then remaining stable throughout the cycles, indicating that the formed passivating film on electrode remained intact and showed excellent reversible cycling. The initial capacity loss mainly comes from SiO (1st cycle efficiency: 50~55%). Ball-milled Sn30Fe30C40 not only works on prolonging cycle life, but also improving 1st cycle efficiency. The various current densities were loaded on the composite electrode shown in Figure IV - 98b. The composite electrode maintains 600 mAh/g upon a high current density (1200 mA/g). It exhibits excellent recoverable performance after switching back to a low current density (100 mA/g).

Different compositions based on $SiO-Sn_xFe_yC_z$ material are prepared by the same way. Figure IV - 99 shows cycle performance of six different compositions. The amount of SiO is fixed on 50 weight percent for sustaining high capacity. We try to obtain the good balance between capacity and cycle life by tuning the amount of carbon and iron separately.
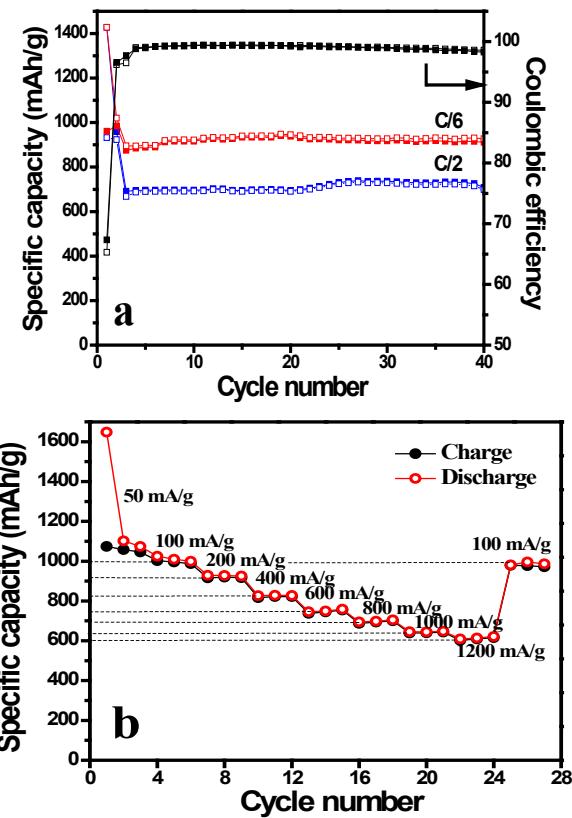
Figure IV - 98: Cycle performance and rate capability of 50wt.%SiO-50wt.%$Sn_{30}Fe_{30}C_{40}$ prepared by spex-milling.

According to the result, it can be seen that cycle performance is improved by increasing the amount of carbon. Accordingly, the initial delivered capacity drops down. That means carbon can absorb the volume expansion of lithiated tin based alloys and silicon. Therefore, carbon can help the capacity retention. Then, we fix the amount of carbon and change the amount of iron. It can be seen that $SiO-SnFe_4C$ exhibits the superior performance.

XRD pattern of ball-milled $SiO-Sn_{30}Fe_{30}C_{40}$ is given in Figure IV - 100. It indicates clearly that Bragg peaks at low angle become slightly broad. Crystal alloys tend to be highly distorted after mechanical alloying. Graphite peaks are not observed. Compared to Fe and Sn alloys, carbon suffers from weak scatter property. So carbon is not detected after milling by X-ray diffraction. Metal oxides peaks are not detectable, which implies that milling occurred without large amount of oxidation. Or they exist in amorphous state. Due to the trend of amorphourization of as-milled samples, lab X-ray diffraction apparatus is limited by low energy and low resolution to index peaks accurately. Therefore, high energy X-ray diffraction was carried out. Commercial SiO is known to be an amorphous phase.
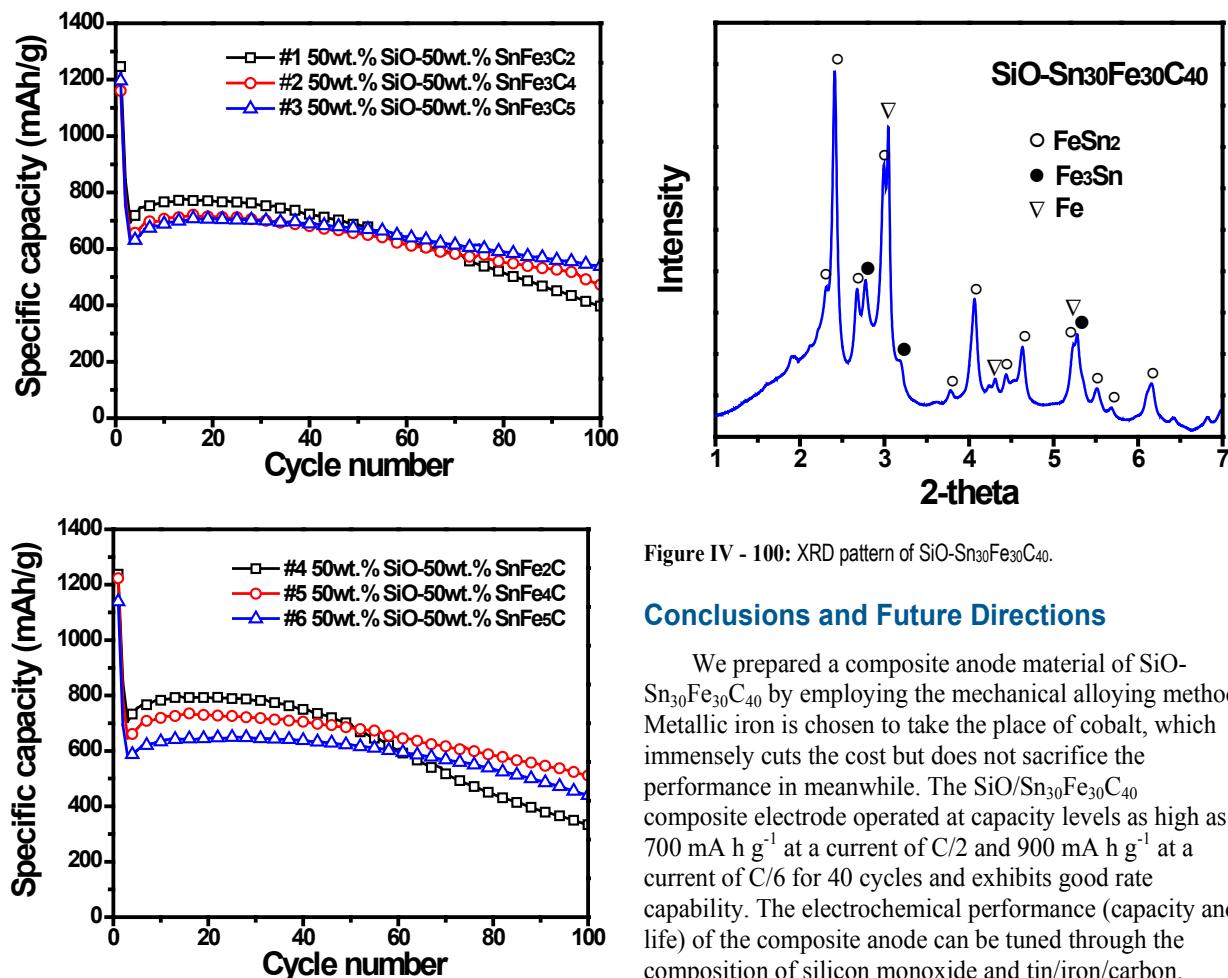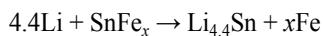
Figure IV - 99: Cycle performance of different compositions.

The structure of SiO consists of nanoparticles of Si distributed in a matrix of amorphous SiO_2. Three phases, $FeSn_2$, Fe_3Sn and Fe can be observed in the high resolution XRD pattern. The lithium intercalation process for Fe-Sn alloys ($FeSn_2$, FeSn and Fe_3Sn_2) was reported earlier. $FeSn_2$ and $CoSn_2$ have the same structure (tetragonal), which belongs to space group $I4/mcm$ with Sn atoms occupying 8h sites and Fe/Co atoms in 4a sites. FeSn/CoSn is hexagonal, space group $P6/mmm$ with Sn in 1a and 2d and Fe/Co in 3f. The charge process is expected based on the following reaction,

$$4.4Li + SnFe_x \rightarrow Li_{4.4}Sn + xFe$$

Iron serves as "matrix-glue" that holds the structure and restrains the pulverization. The structures of the intermetallic compounds affect the electrochemical reaction of the phases with Li.

Therefore, $FeSn_2$ exhibits a larger capacity but poorer cycleability, while FeSn presents the better cycle performance but has lower capacity.

Figure IV - 100: XRD pattern of $SiO-Sn_{30}Fe_{30}C_{40}$.

Conclusions and Future Directions

We prepared a composite anode material of $SiO-Sn_{30}Fe_{30}C_{40}$ by employing the mechanical alloying method. Metallic iron is chosen to take the place of cobalt, which immensely cuts the cost but does not sacrifice the performance in meanwhile. The $SiO/Sn_{30}Fe_{30}C_{40}$ composite electrode operated at capacity levels as high as 700 mA h g^{-1} at a current of C/2 and 900 mA h g^{-1} at a current of C/6 for 40 cycles and exhibits good rate capability. The electrochemical performance (capacity and life) of the composite anode can be tuned through the composition of silicon monoxide and tin/iron/carbon. Further work using a mixture of this anode material with small amount of carbon coated lithium from FMC is envisaged.

FY 2012 Publications/Presentations

1. Abouimrane, B. Liu, Y. Ren, Z. Zak Fang and K. Amine, "Developing a New High Capacity Anode with Long Life" DOE Merit Review, Washington D.C. USA, May 14 – May 18, 2012.

2. Abouimrane, B. Liu, Y. Ren, D. Wang, Z. Zak Fang and K. Amine Ultra high energy ball milling study of SiO-SnCoC material as anode for lithium batteries The Materials Challenges in Alternative & Renewable Energy (MCARE), US, Feb. 21 Mar. 1 (2012).

3. Abouimrane, D. Dambournet, K. W. Chapman, P.J. Chupas, H. Eltayeb, B. Liu and K. Amine Investigation of new anode materials based on oxides and alloys for rechargeable lithium batteries International Battery-Association Pacific Power Source Symposium Joint Meeting, Waikoloa, Hawaii, US, January 9-13 (2012).

IV.B.3.2 Spherical Carbon Anodes Fabricated by Autogenic Reactions (ANL)

Vilas G. Pol

Argonne National Laboratory
9700 South Cass Avenue
Argonne, IL 60439-4837
Phone: (630) 252-8127; Fax: (630) 972-4176
E-mail: pol@anl.gov

Collaborators:
Michael Thackeray, Argonne National Laboratory
Zhenhua Mao, ConocoPhillips
Mark Ewen, ConocoPhillips

Start Date: October 2010
Projected End Date: September 2012

Objectives

- Synthesize novel spherical carbon anode materials and to collaborate with industry to evaluate their electrochemical performance relative to commercially available materials.

- Devise techniques to effectively combine carbon spheres and industrial carbons with lithium-alloying elements to increase their electrochemical capacity for use in PHEVs and EVS.

- Compare the chemical, physical, structural, and morphological properties of spherical carbon-composite electrode materials with conventional carbon-composite materials.

- Complete the final summary report.

Technical Barriers

Graphitic carbon, although widely used as the predominant anode in lithium-ion batteries, accommodates lithium close to the potential of metallic lithium which makes it an intrinsically unsafe material - particularly when used in conjunction with flammable electrolyte solvents and metal oxide cathodes at high potentials. The safety concerns of graphite can be somewhat mitigated by using meso-carbon micro beads (MCMB) with rounded edges. However, MCMB products are synthesized at or above 2,800 °C, making it an expensive form of graphite. Therefore, there is an incentive to prepare inexpensive spherical carbon particles and to enhance their electrochemical properties and abuse tolerance.

Technical Targets

- Consolidate industrial collaborations for this project.

- Prepare carbon samples for industrial partner for heat-treatment to 2,400-2,800 °C; prepare carbon-composite samples using Argonne's carbon spheres and industrial carbon products.

- Evaluate and optimize the electrochemical properties of carbon-composite samples in lithium cells.

- Determine the chemical, physical and electrochemical properties of Argonne's carbon-composite anodes relative to commercially available carbon-composite materials.

Accomplishments

- Several batches of carbon sphere samples were autogenically synthesized at 700 °C and dispatched to an industrial collaborator, ConocoPhillips, for high temperature heat treatment. After receiving the heat-treated products (2,400°C, 2,800°C), their composition, structure, morphology and electrochemical properties were evaluated relative to as-prepared (700 °C) carbon spheres.

- Heat-treated carbon sphere samples were sonochemically coated with ~10 wt.% Sn or ~11 wt.% SnO_2-Sb nanoparticles (<10nm diameter) and their electrochemical properties determined.

- The compositional, structural, morphological and electrochemical properties of composite carbon sphere electrodes, sonochemically coated with lithium alloying elements, were compared with sonochemically-coated industrial carbon products.

✧   ✧   ✧   ✧   ✧

Introduction

Carbon is an extremely versatile material that exists in numerous forms with diverse physical, chemical, electrical and electrochemical properties. From an electrochemical standpoint, graphite negative electrodes and carbonaceous current collecting agents are workhorse materials in the lithium battery industry. Graphite is an intercalation electrode; it accommodates one lithium atom per C_6 unit a few tens of millivolts above the potential of metallic lithium, generating a theoretical electrochemical capacity of 372 mAh/g. Meso-carbon micro beads (MCMB) with rounded edges are a synthetic, but expensive, form of graphite used by the lithium battery industry, can minimize heat-generating side reactions during overcharge. Furthermore, hard carbons, comprised of disordered graphitic planes, can yield a higher electrochemical capacity than graphite but at higher potentials (vs. metallic lithium) thereby offering enhanced safety. In this project, an autogenic process to synthesize hard carbon spheres

was exploited. The carbon spheres can be heated to increase their graphitic character and coated with lithium alloying elements, such as Sn and Sb, to increase their electrochemical capacity.

Approach

This project exploits autogenic reactions to prepare spherical carbon quickly, cost-effectively and reliably. The initial basic science research on the as-prepared carbon spheres was funded by the EFRC, the Center for Electrical Energy Storage – *Tailored Interfaces*. Industrial collaborations and studies with Superior Graphite and ConocoPhillips were initiated and funded by ABR. These collaborations were initiated to access high-temperature furnaces to increase the graphitic order in the carbon spheres (CS). For example, the particles were heated to 2,400 °C (CS-24) by Superior Graphite and to 2,800 °C by ConocoPhillips (CS-28) in an inert atmosphere.

To increase their intrinsic capacity, carbon spheres (CS and CS-24) were sonochemically combined with lithium alloying elements such as Sn, and Sb and metal oxides such as SnO_2 to form carbon-composite anode materials. Industrial carbon products were also coated with these materials, for comparison. Processing conditions were tailored; chemical, electrochemical and physical properties of these materials were evaluated in collaboration with industry.

Results

The electrochemical properties of carbon sphere electrodes, heated at 2,800 °C for 1h in an inert atmosphere by ConocoPhillips, were evaluated in lithium-ion full cells against an Argonne high-capacity counter electrode of nominal composition $0.5Li_2MnO_3 \bullet 0.5LiNi_{0.44}Co_{0.25}Mn_{0.31}O_2$. The initial two discharge/charge curves of a cathode-limited lithium-ion cell with a carbon sphere anode and a $0.5Li_2MnO_3 \bullet 0.5LiNi_{0.44}Co_{0.25}Mn_{0.31}O_2$ cathode, cycled between 4.6 and 2.0 V at a constant current density of 100 mA/g (~C/3 rate) and a corresponding cathode capacity vs. cycle number plot are provided in Figure IV - 101a and Figure IV - 101b, respectively. When charged above 4.6 V, a process that activates the Li_2MnO_3 component by Li_2O extraction to leave an electrochemically-active MnO_2 component within the cathode structure, very high cathode capacities (>200 mAh/g) can be delivered. The electrochemical profile in Figure IV - 101a demonstrates that the lithium ions extracted from the $LiNi_{0.44}Co_{0.25}Mn_{0.31}O_2$ and Li_2MnO_3 components of the cathode above ~2.9 V and ~4.2 V, respectively, are intercalated into the carbon sphere anode during the initial charge; the large irreversible capacity loss on the first cycle is attributed predominantly to the electrochemical activation of the Li_2MnO_3 component of the cathode. Figure IV - 101b indicates that approximately 160 mAh/g

is delivered reversibly by the cathode for more than 100 cycles, reflecting the excellent cycling stability of the carbon spheres in a full lithium-ion cell configuration.
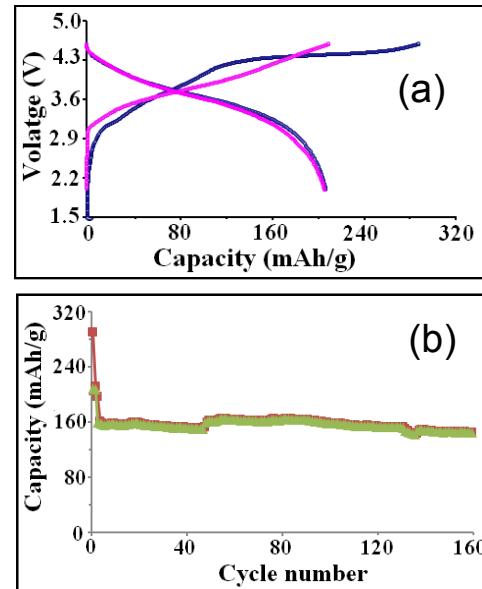
Figure IV - 101: a) First and second charge-discharge profiles, and b) cathode capacity vs. cycle number plot of a lithium-ion cell with a heat-treated (2800 ºC) carbon sphere anode and a lithium manganese rich cathode between 4.6 and 2.0 V at a C/3 rate. (Note: the capacity refers to the cathode only).

To further enhance the capacity of the carbon microspheres, they were first heated at 2400 ºC for one hour before being decorated with Sn nanoparticles using sonochemistry, as described in previous quarterly reports. Scanning and transmission electron micrographs of the Sn-coated carbon spheres (Figure IV - 102a) and energy dispersive X-ray analysis indicated that the surface of the carbon particles were uniformly covered by <10nm Sn nanoparticles (~10 wt.%) that were identified by X-ray powder diffraction as metallic Sn. Although it was apparent that no crystalline SnO_2 was formed during the sonication or heating processes under inert conditions, the Sn nanoparticles oxidized readily if exposed to air.

Electrochemical evaluations were carried out in coin cells using a lithium metal foil electrode, a Sn-decorated carbon sphere counter electrode, and an electrolyte consisting of 1.2M $LiPF_6$ in a 3:7 mixture of ethylene carbonate (EC) and ethylmethyl carbonate (EMC). Figure IV - 102b (inset) shows the discharge/charge behavior of a typical cell during the first two cycles between 1.5 to 0.01 V at a current density of 136 mA/g (about C/2.7 rate). The first-cycle charge and discharge capacities of the Sn-carbon composite electrode were 454 mAh/g and 293mAh/g, respectively, reflecting a first-cycle irreversible capacity loss of 35%. Thereafter, the cell demonstrated stable cycling; it delivered a steady reversible capacity of approximately 340 mAh/g at a C/2.7 rate for 100 cycles (Figure IV - 102b), which is

considerably higher than that delivered by the carbon spheres alone (250 mAh/g).
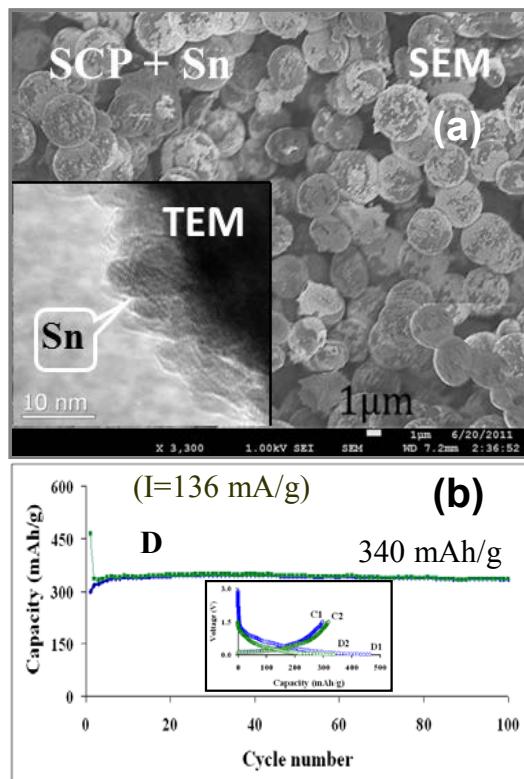
Figure IV - 102: a) SEM and TEM (inset) of Sn-coated carbon spheres and b) First and second discharge-charge- profiles (inset) and capacity vs. cycle number plot of a lithium half-cell with Sn-carbon sphere electrodes between 1.5 V and 0.01 V at a C/2.7 rate.

Sonochemistry was also used to coat the surface of carbon spheres, prepared at 700 °C, with a Sn/Sb nanoparticle mixture. The powder X-ray diffraction patterns of the coated spheres showed that the coating was essentially amorphous to X-rays, whereas, after drying and heating the product to about 500 °C for about 3 hours in air, it was apparent that body centered tetragonal SnO_2 and hexagonal Sb phases crystallized on the surface of the spheres during thermal treatment. Scanning and transmission electron micrographs of the SnO_2/Sb-coated carbon spheres (Figure IV - 103a) and energy dispersive X-ray analysis indicated that the surface of the carbon particles was uniformly covered by <10 nm SnO_2/Sb nanoparticles and that they were strongly attached/bonded to the surface. EDX analysis showed that the SnO_2 and Sb accounted for approximately 11% by weight of the carbon sphere-SnO_2/Sb composite product. It appears that, under similar experimental conditions, Sn is more sensitive to oxidation than Sb. Note that in these SnO_2/Sb-coated carbon sphere electrodes, all three components (SnO_2, Sb and the carbon spheres) are electrochemically active.
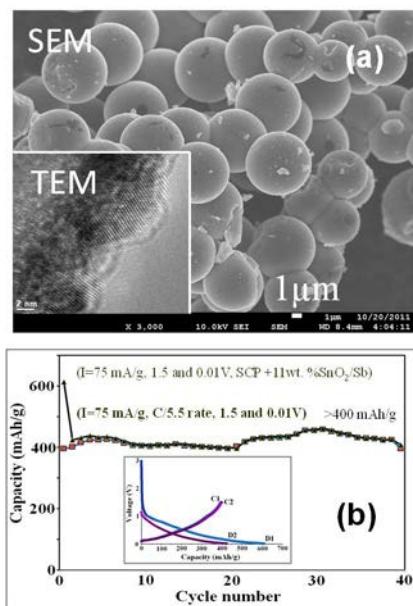
**Figure IV - 103:** (a) SEM and TEM (inset) images of SnO_2/Sb-coated carbon spheres, (b) First and second discharge-charge-profiles (inset) and capacity vs. cycle number plot of a lithium half-cell with a SnO_2/Sb-carbon sphere electrode cycled between 1.5 and 0.01 V at a C/5.5 rate.

Electrochemical evaluations were carried out in coin cells using a lithium metal foil electrode, a SnO_2/Sb-decorated carbon sphere counter electrode, and 1.2M $LiPF_6$ in EC:EMC (3:7 ratio) electrolyte. Figure IV - 103b shows the discharge/charge behavior of a Li/carbon sphere-SnO_2/Sb cell during the first two cycles at a current density of 75 mA/g (~C/5.5 rate) when cycled between 1.5 and 0.01 V). The first-cycle discharge and charge capacities of a SnO_2/Sb-carbon sphere composite electrode are 612 mAh/g and 394mAh/g, respectively. The first cycle irreversible capacity loss is about 35%, which is significantly lower than that delivered by a pure carbon sphere electrode (60%). A steady reversible capacity of 425 mAh/g, obtained at a C/5.5 rate for 40 cycles, is significantly higher than the capacity delivered by the carbon spheres alone (Figure IV - 103b). The coating of ~11 wt% nanosized tin oxide/antimony therefore significantly improves the discharge and charge capacity of the SnO_2/Sb-carbon sphere composite electrode relative to the capacity of a bare carbon sphere electrode (~250 mAh/g).

In a further study, 25 wt.% of SnO_2 nanoparticles were sonochemically deposited on the surface of industrial graphite (G8), supplied by ConocoPhillips. Figure IV - 104a shows the discharge/charge behavior of a Li/G8 graphite-SnO_2 cell during the first two cycles at a C/4 rate, when cycled between 1.5 and 0.005 V. The discharge and charge capacities of a composite G8 graphite-SnO_2 electrode are 665 mAh/g and 427mAh/g, respectively. The capacity delivered at 0.9-0.8 V during the initial discharge was attributed to the reduction of the Sb and SnO_2 components, the latter reaction (to Li_2O and Sn) being largely

irreversible. The first-cycle irreversible capacity loss is about 36%. Nevertheless, a steady reversible capacity of 390 mAh/g was delivered by the electrode for 50 cycles (C/4 rate), which is significantly higher than the capacity delivered by the G8 graphite electrode alone (306 mAh/g, Figure IV - 104b).
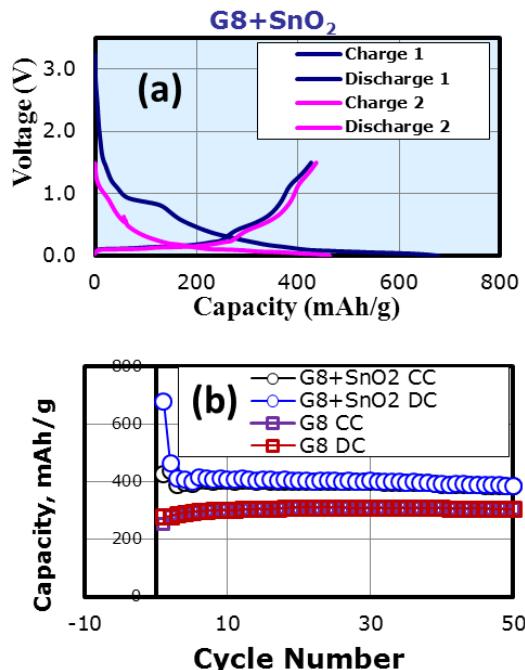
Figure IV - 104: (a) First and second discharge-charge-profiles of a lithium cell with a G8 graphite/25wt.% SnO_2 electrode, and (b) capacity vs. cycle number plot of a lithium half-cell with a SnO_2-graphite electrode, cycled between 1.5 and 0.01 V at a C/4 rate (top), relative to a cell with a standard G8 graphite electrode (bottom).

Conclusions

Autogenic reactions offer a relatively simple and facile method to fabricate carbon spheres from hydrocarbons. They behave like a hard carbon, delivering 250 mAh/g when cycled between 1.5 and 0.01 V. Higher capacities (400mAh/g) can be achieved by sonochemically depositing Sn and/or Sb nanoparticles on the surface of the spheres. These results are encouraging and bode well for further improvement. The project is being terminated but will be continued with funding from other sources.

FY 2012 Publications/Presentations/Patents

1. V.G. Pol and M. M. Thackeray, *Thermal Treatment, Structural Evolution and Electrochemical Performance of Carbon Spheres Prepared by Autogenic Reactions*, MRS Spring Meeting, San Francisco, 9-13 April (2012).

2. V. G. Pol and M. M. Thackeray, *Spherical Carbon Particles: Synthesis, Characterization and Electrochemical Performance*, ConocoPhillips, Houston, 18 January (2012).

3. V. G. Pol, *High Capacity Composite Carbon Anodes Fabricated by Autogenic Reactions,* Annual Merit Review, Arlington, Virginia, Washington, D.C. May 14-18 (2012).

4. M. M. Thackeray and V. G. Pol, *Electrochemical Performance of Spherical Carbon Particles, 16th International meeting on Lithium Batteries*, (IMLB) Jeju, Korea. June 17-22 (2012).

5. V. G. Pol, K.C. Lau, L. A. Curtiss and M. M. Thackeray, *Autogenically-Prepared Spherical Carbon Particles (SCPs) and SCP-Sn Composites as Anodes for Li-ion Batteries*, 222nd ECS meeting, Honolulu, Hawaii October 7-12 (2012)

IV.B.3.3 Functionalized Surface Modification Agents to Suppress Gassing Issue of Li$_4$Ti$_5$O$_{12}$-Based Lithium-Ion Chemistry (ANL)

Yan Qin, Zonghai Chen, Khalil Amine

Argonne National Laboratory
9700 S. Cass Ave.
Lemont, IL 60439
Phone: (630) 252-3838; Fax: (630) 252-4176
E-mail: amine@anl.gov

Collaborators:
EnerDel
University of Colorado

Start Date: October 2010
Projected End Date: March 2012

Objectives

- To understand the mechanism of gassing issue of lithiated Li$_4$Ti$_5$O$_{12}$ during high temperature aging or operation.
- To develop functionalized surface modification agents to address the gassing issue. This can be the enabling technology for Li$_4$Ti$_5$O$_{12}$ for long life, high power PHEV batteries with unmatched safety.

Technical Barriers

- Lithium titanate (LTO) is a promising anode material for lithium ion batteries. Despite its long cycling life, safe operation and good power capability, there is still one technical barrier that hinders the deployment of LTO as the lithium ion anode material: it produces a large amount of gas when aging at temperatures above 50°C. This issue was hardly noticed in small size batteries, such as coin cells and pouch cells with capacity less than 50 mAh, due to the small amount of gas generated. It came out as a big hurdle for the large scale batteries where large amount of gassing has posed problem for power and safety performance.

Technical Targets

The objective of this work is to investigate the gassing mechanism of Li$_4$Ti$_5$O$_{12}$ and to develop advanced technologies to solve this problem.

- Identify gassing mechanism.
- Identify and develop advanced technologies to mitigate the gassing issue.

Accomplishments

- Lithiated LTO, lithium salt and carbonate solvents have been identified as the three key components in LTO gassing issue.
- *In situ* XANES technique has revealed that the self-discharge of lithiated LTO during high temperature aging is responsible for the gassing.
- The additive proposed before and ALD coating technique has been tested and shown promising outcome.

✧　　✧　　✧　　✧　　✧

Introduction

The Li$_4$Ti$_5$O$_{12}$ (LTO) is a promising alternative anode material which demonstrates extremely long life, high power, low cost and unmatched safety characteristics for HEV applications. The long cycle life is coming from the good structure stability of LTO which is able to accommodate up to three lithium ions in the spinel structure without volume expansion unlike the conventional carbon anode which will expands up to 16 vol% during charging. Coupling Li$_4$Ti$_5$O$_{12}$ (LTO) with cathode materials like LiMn$_2$O$_4$ (LMO) deliver long cycle life with reasonable capacity retention and energy density, as well as superior tolerance to various abuse conditions.[1-4]

Despite these advantages, there is still one technical barrier that hinders the deployment of LTO as the lithium ion anode material: it produces a large amount of gas when aging at temperatures above 50°C, which deteriorates the power capability of the cells. Belharouk *et al.*[5] have reported this gassing problem previously, and H$_2$ was revealed as the major component of the gas generated. However, the mechanism of H$_2$ generation was not well understood.

Approach

In situ gas chromatograph (GC) has been employed to identify the key component of the gas. *In situ* x-ray adsorption spectroscopy technique (XAS), specifically XANES, has been applied to observe the Ti valence change during aging at various temperatures. Correlated with gas chromatograph data, we can link the valence change of Ti to the H$_2$ evolution. Surface modification through additive and Atomic Layer Deposition shows positive effect in reducing the gassing.

Results

Key factors and Major gassing component determined by *In situ* GC measurement. *In situ* GC analysis was employed to measure the concentration change of H_2 and CO_2 in the gas emitted from the cells. About 0.8 gram of Lithiated LTO was added in the reactor beaker together with electrolyte with or without lithium salt, $LiPF_6$. The concentration of H_2 measured at each sampling interval with or without $LiPF_6$ in the electrolyte is shown in Figure IV - 105. In the electrolyte with $LiPF_6$, the H_2 production peaked between 20 and 40 min after reaction started, and then decreased dramatically afterwards. The total amount of H_2 is 2 mmol. Without $LiPF_6$ in the system, the reaction rate was much lower. Although presumably, a small amount of $LiPF_6$ residue was present on the lithiated LTO, the amount of H_2 produced was greatly reduced to about 0.6 mmol. Assuming 1 mole $Li_7Ti_5O_4$ will produce 1.5 moles H_2 if all the electrons participate in the hydrogen evolution, then 0.8 g of $Li_7Ti_5O_4$ produced about 2.45 mmol H_2. This value is close to the 2 mmol H_2 measured with GC. This finding indicates that the lithium salt is another important component besides lithiated LTO in the gassing process. Further studies on the different lithium salts indicated that some salts will result in more gas than others. For example, the cell with $LiBF_4$ seems to produce less gas than the one with $LiPF_6$.

Source of H_2. The above results confirm that the LTO anode material and lithium salt play important roles in the gassing process. However, they are unlikely to be the sources of protons for the formation of H_2. The moisture inside the cell could only account for part of the H2, the alternative H2 source could be carbonates solvent.

***In situ* XANES of the Ti K-edge during aging at various temperatures.** To better understand the role $Li_7Ti_5O_{12}$ played in this process, we utilized the *in situ* XANES measurements to monitor the change of LTO during aging.
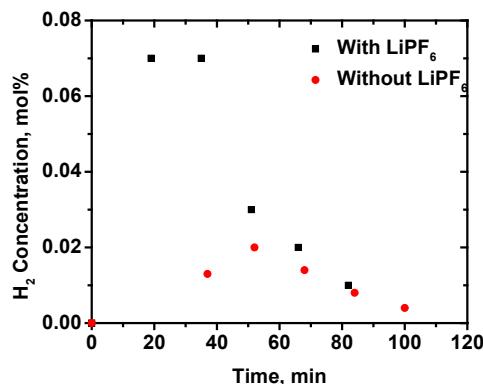

Figure IV - 105: Hydrogen concentration change with reaction time measured by *in situ* GC. The supporting Ar flow rate is 14 mL/min. Black squares represent condition with $LiPF_6$ in the electrolyte; red circles, no $LiPF_6$ in the electrolyte.

Figure IV - 106 shows the XANES plots of the Ti K-edge during aging at 60°C. The whole XANES plots shifted to a higher energy with aging time. Aging at another two temperatures, 50°C and 70°C shows the similar trend, but with different time scale. In general, the lower the temperature, the longer the transition time from Ti^{3+} to Ti^{4+}. Overall, the peaks A, B, and C in the spectra for the different aging temperatures behaved similarly to each other. The only difference was the time to initiate and finish the transition of the valence state of Ti at different aging temperatures. The higher the temperature, the shorter is the transition time. This finding can be well explained by the increased reaction rate constant at higher temperature.
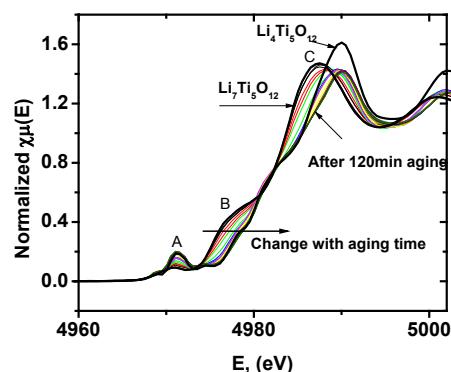
Figure IV - 106: Evolution of XANES spectra of Ti K-edge during aging at 60°C. The spectra were taken every 5 minutes.

The transition stages can be clearly demonstrated in energy contour plots obtained from the derivatives of the normalized plots. Figure IV - 107 displays the contour plots during aging for the three temperatures. The whole transition process can be divided into four stages regardless of the time scales for the different temperatures, denoted as T1, T2, T3, and T4. T1 is the incubation period; no significant change in valence state occurs at this stage, and the majority of the phase is $Li_7Ti_5O_{12}$. For the different temperatures, the incubation period is different. The difference between 50°C and 60°C is much greater than that between 60°C and 70°C. It took about 390 min at 50°C to initiate the phase transition while it only took about 20 and 10 min at 60°C and 70°C, respectively. T2 represents a major phase transformation period, where the peak shifted largely from Ti^{3+} to Ti^{4+}. Similar to the incubation stage T1, the higher the temperature, the shorter is the transition time. The major phase transition took about 60 min at 50°C, 30 min at 60°C, and 15 min at 70°C. T3 represents the minor phase transition stage where the Ti^{4+} state dominates with a small percentage of Ti^{3+} state. The length of this stage at the different temperatures was smaller as the temperature increased. The minor phase change lasted about 40 min at 50°C, 20 min at 60°C, and 10 min at 70°C. T4 is the final stage where the phase transitions had quenched.
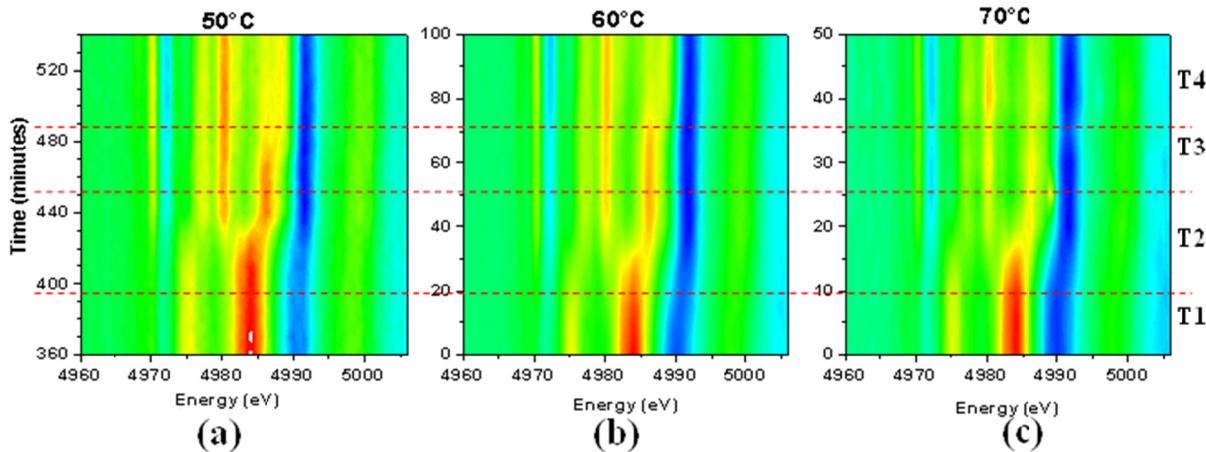
Figure IV - 107: Contour plots of the derivatives of the normalized energy for three temperature settings, (a) 50°C, (b) 60°C and (c) 70°C.

The interface between the electrolyte and electrode is key to the electrochemical properties of the lithium ion batteries.[6] The gassing issue is ultimately the consequence of an interfacial reaction between electrode and electrolyte. Self-discharge of $Li_7Ti_5O_{12}$ is only the first step toward gassing. Although there is no direct evidence proving the mechanism of how electrolyte interacts with LTO to generate gas, we speculate that the electrolyte underwent electron transfer reaction on the electrode surface to produce gas. TiO_2 is a well-known photocatalyst to generate H_2 from solar radiation.[7-9] Its building-up unit is a TiO_6 octahedron which is also the main building unit inside LTO. The structure similarity between TiO_2 and LTO might suggest that LTO might also attain the ability to produce H_2. The difference is that the driving force is from electrochemically induced electron transfer instead of solar radiation. Nevertheless, the interface plays a very important role in the gassing process by aiding both lithium ion and electron transfer.

Surface modification to mitigate gassing issue. The absence of SEI on the LTO surface used to be an advantage of LTO over graphitic carbon as an anode material because there is no initial irreversible capacity loss caused by forming SEI, and no capacity fade caused by the need to dynamically maintain the SEI during cycling. However, the progressively side reactions at high temperature aging on LTO electrode suggests the need for the SEI to prevent undesired side reaction at elevated temperature. A potential solution to the gassing issue is to create SEI-like layer artificially through surface modification techniques. We expect this SEI-like layer to prevent or slow down the electron transfer, and thereby mitigate the gas production. This surface protection can be provided by the use of electrolyte additives. As a rule of the thumb, we sought chemical species that can effectively consume acidic functional groups like –OH on the surface of LTO and convert such acidic groups to inert ones. Based on

this idea, we chose SL2, whose structure is shown below, to demonstrate the effectiveness of surface modification.

Figure IV - 108 shows the effect of SL2 in reducing the gas volume for the LTO/LMO pouch cell at 63°C. With the addition of 1% SL2, the gas volume was reduced by half after 40 days of aging. Although the additive doses not completely eliminate the gassing problem, it does suggest a sound approach to solving it.
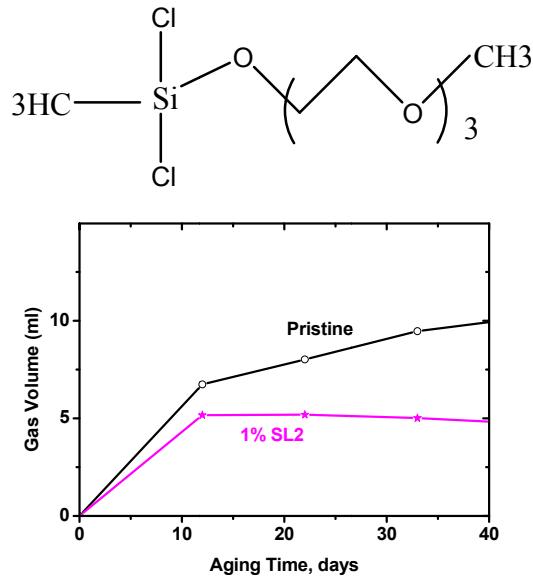

Figure IV - 108: Gas evolution in pouch cells LTO/LMO with /without 1% SL2 as the additive in the electrolyte of 1.2M $LiPF_6$ in EC/EMC in 3:7 in weight.

Another way to form the surface protection layer is to implement direct surface coating technique, such as atomic layer deposition (ALD). The coating material has to be inert to electron transfer, but thin enough not to interrupt

lithium ion moving in and out of the particles. Although the Figure IV - 109 shows a positive example of the ALD coating of Al_2O_3 in reducing the gas, more work needs to be done to search for the best coating material and tune the coating thickness.
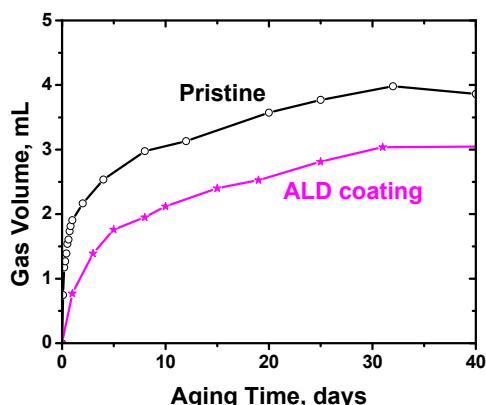
Figure IV - 109: Gas volume change for the LTO/LMO pouch cells with and without ALD coating on the LTO particle surface. The pouch cells have capacity of 100 mAh which is different from the ones used in the previous figure.

Conclusions and Future Directions

We have investigated the gassing mechanism in lithium titanate/ lithium manganese oxide spinel cells when aged at elevated temperature. The major components of the gas were identified as H_2 and CO_2, and the key cell components responsible for gassing were found to be lithiated lithium titanate, lithium salt, and solvent. The *in situ* XANES measurements at elevated temperature showed that the Ti K-edge energy continuously shifted to higher values during aging which indicates that the valence state increase from Ti^{3+} to Ti^{4+}, accompanying by a phase transition from $Li_7Ti_5O_{12}$ to $Li_4Ti_5O_{12}$. These changes are attributed to the electron loss due to the self-discharge of $Li_7Ti_5O_{12}$ at elevated temperature. The lost electrons participate in a reaction between the electrolyte and electrode surface to generate gas. The interface between the electrode and electrolyte was believed to play an important role in the gassing reaction. We have demonstrated that the addition of an appropriate additive to the electrolyte or coating LTP particle surface through ALD technique could positively alter the interface and reduce the gas generation.

FY 2012 Publications/Presentations

1. 2012 ECS Spring meeting presentation.

References

1. Belharouak, I.; Koenig, G. M.; Amine, K., J. Power Sources 2011, 196, (23), 10344-10350.
2. Amine, K.; Belharouak, I.; Chen, Z. H.; Tran, T.; Yumoto, H.; Ota, N.; Myung, S. T.; Sun, Y. K., Adv. Mater. 2010, 22, (28), 3052-3057.
3. Belharouak, I.; Sun, Y. K.; Lu, W.; Amine, K., J. Electrochem. Soc. 2007, 154, (12), A1083-A1087.
4. Chen, Z.; Belharouak, I.; Sun, Y. K.; Amine, K., Adv. Funct. Mater. 2012, n/a-n/a.
5. Belharouak, I.; Koenig, G. M.; Tan, T.; Yumoto, H.; Ota, N.; Amine, K., J. Electrochem. Soc. 2012, 159, (8), A1165-A1170.
6. Xu, K.; von Cresce, A., J. Mater. Chem. 2011, 21, (27), 9849-9864.
7. Linsebigler, A. L.; Lu, G. Q.; Yates, J. T., Chem. Rev. 1995, 95, (3), 735-758.
8. Hashimoto, K.; Irie, H.; Fujishima, A., Jpn. J. Appl. Phys. 2005, 44, (12), 16.
9. Liao, J.-Y.; Lei, B.-X.; Chen, H.-Y.; Kuang, D.-B.; Su, C.-Y., Energy Environ. Sci. 2012, 5, (2), 5750-5757.

IV.B.4 Applied Battery Research on Cathodes

IV.B.4.1 Engineering of High Energy Cathode Material (ANL)

Khalil Amine

Argonne National Laboratory
9700 South Cass Avenue
Argonne, IL 60439-4837
Phone: (630) 252-3838; Fax: (630) 972-4520
E-mail: amine@anl.gov

Collaborators:
Huiming Wu, Argonne National Laboratory
Ilias Belharouak, Argonne National Laboratory
Ali Abouimrane, Argonne National Laboratory
Xiao Qing Yang, Brookhaven National Laboratory
Y.K. Sun, Hanyang University
Alan W. Weimer group, University of Colorado Boulder

Start Date: October 1, 2008
Projected End Date: September 30, 2014

Objectives

- Enable the use of the Argonne high-energy composite layered cathode, $xLi_2MnO_3 \cdot (1-x)LiNiO_2$, in a plug-in hybrid vehicle (PHEV) with electric drive range of 40 miles.
- Optimize cathode composition and engineer this material to improve its packing density and rate capability for PHEV applications.
- Explore surface protection to enable high capacity and long cycle life at high voltage (4.6 V).

Technical Barriers

- Poor continuous charge and discharge rate capability.
- High electrode impedance.
- Low pulse power.
- Low packing density, which translates to low volumetric energy density.
- Reactivity with the electrolyte at high voltage.

Technical Targets

- Improve the rate capability.
- Increase the rate capability from C/10 to 1C ~ 2C.
- Improve the packing density to 2~2.4 g/cc.
- Stabilize the surface of the particles to improve significantly the calendar and cycle life.

Accomplishments

- Optimized and identified a suitable composition based on the Argonne high-energy composite layered cathode that provide high energy, high density and cycle life Developed AlF_3 coating process based on a co-precipitation process and confirmed effect on performance and rate.
- Identified particle cracking issues with materials prepared by carbonate process
- Developed a hydroxide process to mitigate particle cracking during electrode calendaring.

✧   ✧   ✧   ✧   ✧

Introduction

The 40-mile electric-drive PHEV requires development of a very high-energy cathode and/or anode that offers 5,000 charge-depleting cycles, a 15 year calendar life, and excellent abuse tolerance. These challenging requirements make it difficult for conventional cathode materials to be adopted in PHEVs. Here, we report on a very high-energy material based on a layered lithium-rich nickel manganese oxide composite electrode as a potential cathode for PHEV and all-electric vehicle applications. This material exhibits over 200 mAh/g of capacity, relatively good stability, and improved safety characteristics.

Approach

- Develop a process that leads to very dense material to increase the electrode loading density and, therefore, the electrode capacity per unit volume. Focus on hydroxide process to mitigate particle cracking during the electrode calendaring process.
- Optimize suitable composition and engineer the material to improve the electrochemical performance for PHEV applications.
- Investigate nano-coating of the material with AlF_3 by co-precipitation) to reduce the initial interfacial impedance and stabilize the cathode interface in order to improve the cycle life at elevated temperature.

Results

In the past years, our main focus was on developing an advanced process that can allow for obtaining high-energy cathodes based on the layered lithium-rich nickel manganese oxide with high packing density, spherical morphology, high

rate performance and good cycle life. Our initial step was to optimize the composition that provides the best physical and electrochemical performance. This work has led to the identification of a Co-free composition of $Li_{1.2}Ni_{0.3}Mn_{0.6}O_{2.1}$ (Ni/Mn ratio=1:2) with a spherical morphology and a Tab density of 2.1g/cc. This material shows also a high capacity of 200mAh/g at 1C rate with good cycle performance. Furthermore, this composition was easy to reproduce and to scale up. We have already produced the material at the kilogram scale in our bench Laboratory. The process was shared with the Scale up facility at Argonne for further scale up and distribution to the ABR team for testing and diagnostics.

The material was prepared from a spherical nickel manganese carbonate precursor. Figure IV - 110 shows scanning electron microscopy (SEM) images of $Li_{1.2}Ni_{0.3}Mn_{0.6}O_{2.1}$ high-energy cathode material with uniform spherical second particles (10 μm) and dense 80 nm primary particles, which would yield higher tap density of 2.1g/cc. The small nano-primary particles will allow for a reduction of the lithium pathway diffusion in lithium ion batteries and thus improve the rate capability. This material was made using a carbonate process based on co-precipitation using $NaCO_3$ as co-precipitating agent.
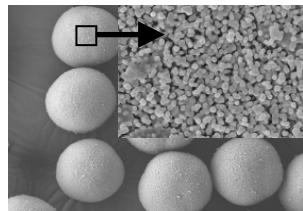

Figure IV - 110: SEM images of $Li_{1.2}Ni_{0.3}Mn_{0.6}O_{2.1}$ showing spherical secondary particle and dense nano-primary particles.

In the past report, we have shown that the $Li_{1.2}Ni_{0.3}Mn_{0.6}O_{2.1}$ cathode exhibits good cycling performance at room temperature. However, at high temperature (55^oC), the capacity faded gradually with cycling. This is caused by the reactivity of charged cathode with the electrolyte at 4.6V. This reaction is accelerated by the increase in the temperature during cycling. In order to mitigate this reactivity at high voltage, we have investigated in the past coating the material with Al_2O_3 using the ALD process. The idea was to protect each particle with a very stable thin coating that can act as a barrier against any interfacial reaction between charged cathode and electrolyte. Also, the coating can either eliminate or reduce significantly the dissolution of the manganese which is known to affect the SEI of carbon in the full cell configuration. The result of the study shown in the last report was very positive. The performance of the material coated with Al_2O_3 nano film shows a significant improvement in the cycling performance at 55^oC with no capacity fade after 50 cycles. As comparison, the non-coated material shows 30% capacity after cycling at 55^oC. Unfortunately, the use of ALD in the coating process is not commercially feasible, especially for scale up. In addition, the use of an oxide such as Al_2O_3 as coating material could be compromised by the possible

reactivity with HF in the electrolyte which can lead to the disintegration of the coating because of the chemical reaction. To overcome these issues, we decided to use AlF_3 as coating material and we selected the co-precipitation as a process for coating the cathode particles. The choice of AlF_3 is dictated by the fact that Al-F bond is very strong and Al is trivalent and will remain in the trivalent state during cycling at high potential. Furthermore, AlF_3 cannot react with HF in the electrolyte. The co-precipitation process for coating the cathode with AlF_3 is highly scalable and uses the same reactor as the one used for making the precursor for the cathode.

Figure IV - 111 shows the TEM figures of coated and uncoated cathode materials. After the coating process, a 10 nm film of AlF_3 can be easily observed. The coating was carried out by dispersing the cathode powder in water inside the reactor. A solution of aluminum nitrate and ammonium fluoride is added gradually to the reactor for the purpose of co-precipitating AlF_3 on the cathode powder.

None **coated** AlF_3 **coated**
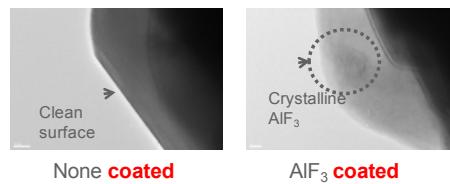
Figure IV - 111: TEM images of high energy cathode coated and uncoated with AlF_3.

Figure IV - 112 shows the cycling performance of coated and uncoated $Li_{1.2}Ni_{0.3}Mn_{0.6}O_{2.1}$ vs. Lithium at 55^oC. The coated material shows excellent cycling performance with far much limited capacity fades than the uncoated cathode. This result is caused by the limited growth in the interfacial impedance of the cell in the coated material vs. the uncoated one (see **Figure IV - 113**). The AlF_3 coating was able to suppress the reactivity between the charged electrode at 4.6V and the electrolyte and thus minimize the growth of the cell impedance. A secondary effect of the AlF_3 coating was to increase significantly the power capability of the material as shown in Figure IV - 114. The increase in the rate capability of the coated material can be attributed to the initial low interfacial impedance of the cell because of the very thin AlF_3 coating of the cathode.
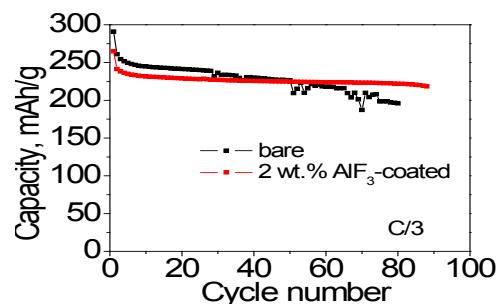
Figure IV - 112: Cycling performance of AlF_3 coated and uncoated (bare) high energy cathode at 55^oC.
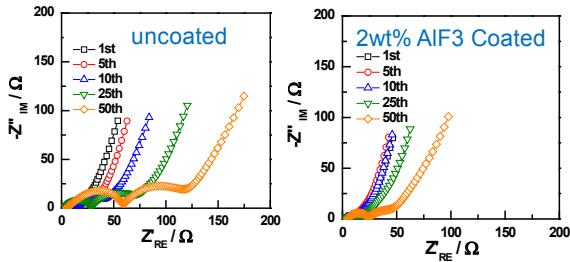
Figure IV - 113: AC Impedance of cells based on coated and uncoated high energy cathode material.
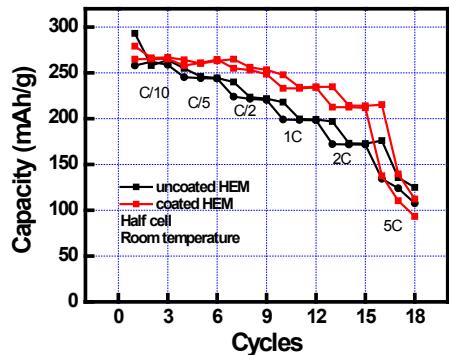
Figure IV - 114: Rate capability of cells based on coated and uncoated high energy cathode material.

Synthesis of High energy cathode using hydroxide process. One of the main reasons behind shifting to the hydroxide process in the making of the high energy material is the cracking of the particle made by the carbonate process, especially during the calendaring of the electrodes as shown in Figure IV - 115. This cracking of the particle is caused by the large porosity inside the particle when the carbonate process is used (Figure IV - 116). The material shows high surface area of 5.5 m^2/g and a porosity of 16.5%. The high internal porosity is caused by the release of CO_2 during the calcinations process of the carbonate based precursor.
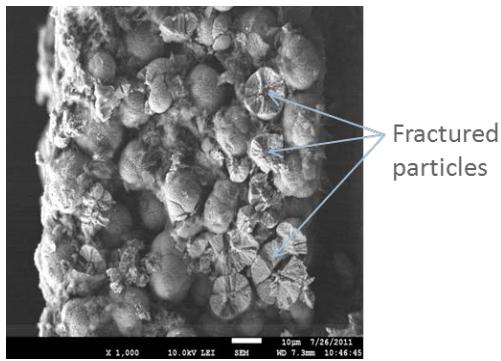
Figure IV - 115: SEM images of high energy electrode made by the carbonate process.
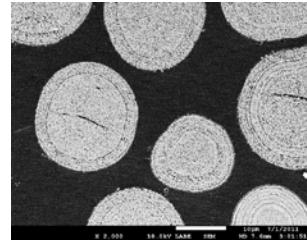
Figure IV - 116: Cross section of high energy cathode particles made by the carbonate process.

Figure IV - 117 shows the SEM image of a high energy electrode made from the hydroxide process. The active particle in the electrode remains intact after repeated calendaring of the electrode. This positive result is caused by the fact that the porosity of the particles is 6.6% which is much less than that of particles made by the carbonate process. As a result, the surface area of the material made by hydroxide process is smaller (3.8m^2/g)
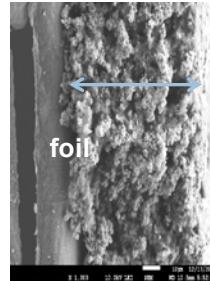
Figure IV - 117: SEM images of high energy electrode made by carbonate process.

Figure IV - 118 shows the initial charge and discharge as well as cycling performance of cells made from high energy cathode made by the carbonate and hydroxide process. Both materials show high capacity of 250~260mAh/g during the initial cycling. The cell-based on material made by the hydroxide process shows higher first cycle efficiency. At C/3 cycling, both material shows over 200mAh/g with good cycle life.
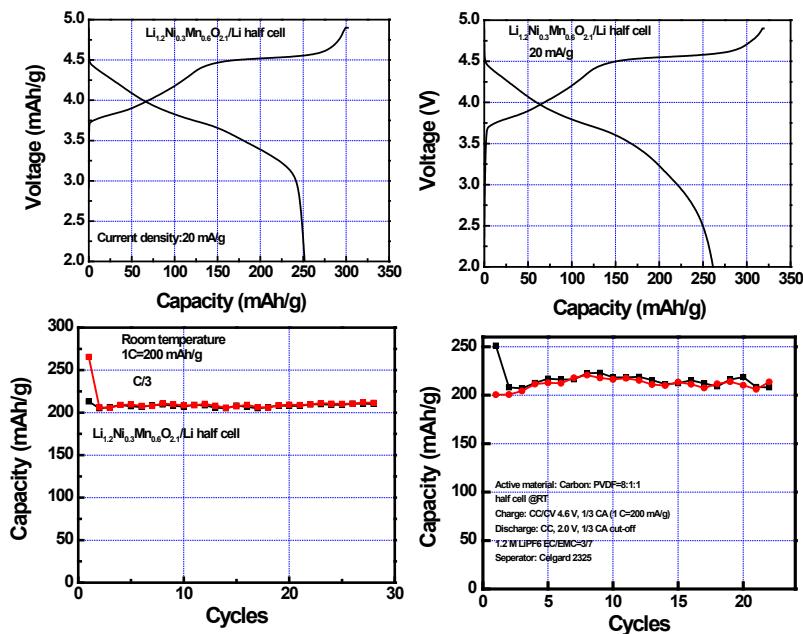
Figure IV - 118: First charge and discharge cycle and capacity vs cycling of cells based on cathodes made by the hydroxide and the carbonate process.

Figure IV - 119 compares the rate performance of cells made by cathodes from hydroxide and carbonate processes. At high rates (1C and 2C rate), the cell based on cathode made by the hydroxide process shows higher capacity than that of cells made by the carbonate process. This is because the primary particles of the cathode made by the hydroxide process are much smaller than the one prepared by the carbonate process. As a result, lithium pathway diffusion in smaller primary particle is faster resulting in higher rate performance.
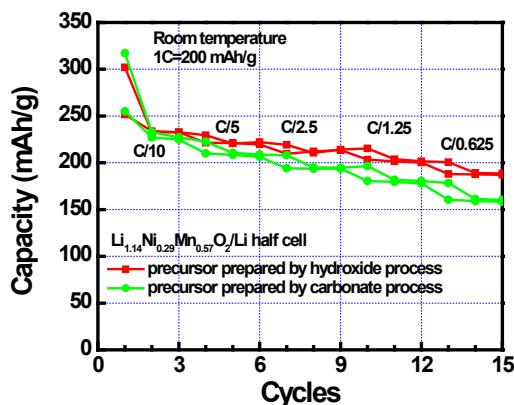
Figure IV - 119: Rate performance of cells based on cathodes made by hydroxide and carbonate process.

Conclusions and Future Directions

- Surface modification of the high energy cathode with AlF_3 using Co-precipitation process shows good cycle life at 55°C and improved rate performance. The coating reduces significantly the interfacial impedance growth in the cell during cycling.

- Particle cracking during the calendaring process of the electrode was observed. The cracking is caused by the high internal porosity of the cathode made by the carbonate process.

- An alternative hydroxide process was developed to mitigate the particle cracking issue.

- This project was terminated because DOE decided to refocus the funding on fixing the voltage fade of the high energy cathode material.

FY 2012 Publications/Presentations

1. Sun, Y.-K., M.-J. Lee, C.S. Yoon, J. Hassoun, K. Amine, and B. Scrosati, *The Role of AlF3 Coatings in Improving Electrochemical Cycling of Li-Enriched Nickel-Manganese Oxide Electrodes for Li-Ion Batteries.* Advanced Materials, **2012**. 24(9): p. 1192-1196.

2. K. Amine and H/ Wu, 2011 DOE Annual Peer Review Meeting Presentation, May 9-13, 2011, Washington DC.

3. H. Wu and K. Amine, 5th International Conference Polymer Batteries and Fuel Cells (PBFC-5), Argonne, IL, August 1-5, 2011.

4. K. Amine, USDrive Electrochemical Energy Storage Tech Team Applied Battery Research for Transportation (ABR) Program Informational Meeting, Argonne National Laboratory, October 5-6, 2011.

5.   K. Amine, H. Wu, 4th International Conference on Advanced Lithium Batteries for Automobile Application, Bejing, China, Sept. 21-23, 2011.

6.   A. Abouimrane, O.C. Compton, H.X.Deng, I. Belharouak, D.A. Dikin, S. T. Nguyen, K. Amine, "Improved Rate Capability in a High-Capacity Layered Cathode Material via Thermal Reduction," Electrochem. Solid. State Lett., **14** (9) A126.

7.   I. Belharouak, G.M. Koenig, J. W. Ma, D. P. Wang, K. Amine, "Identification of $LiNi_{0.5}Mn_{1.5}O_4$ spinel in layered manganese enriched electrode materials," Electrochem.Comm. **13** (3) 232.

8.   D. P. Wang, I. Belharouak, G. M. Koenig, G.W. Zhou, K. Amine, "Growth mechanism of $Ni_{0.3}Mn_{0.7}CO_3$ precursor for high capacity Li-ion battery cathodes," J. Mater. Chem., **21** (25): 9290.

9.   H. Deng, I. Belharouak, C. S. Yoon, Y. K. Sun, K. Amine, "High temperature performance of surface-treated $Li_{1.1}Ni_{0.15}Co_{0.1}Mn_{0.55}O_{1.95}$ layered oxide," J. Electrochem. Soc., **157** (10) A1035.

IV.B.4.2 Developing New High Energy Gradient Concentration Cathode Material (ANL)

Khalil Amine

Argonne National Laboratory
9700 South Cass Avenue
Argonne, IL 60439-4837
Phone: (630) 252-3838; Fax: (630) 972-4451
E-mail: amine@anl.gov

Collaborators:
Zonghai Chen, Argonne National Laboratory
Yang-Kook Sun, Hanyang University

Start Date: October 1, 2008
Projected End Date: September 30, 2014

Objectives

- The objective of this work is to develop a high energy cathode material for PHEV applications. The material is being developed to provide:
- Over 200 mAh/g reversible capacity
- Good rate capability
- Excellent cycle and calendar life
- Good abuse tolerance

Technical Barriers

The technical barrier is to develop a cathode material for PHEV batteries that meets or exceeds DOE technical objectives, including outperforming the NMC baseline material.

Technical Targets

- Develop a model to predetermine the gradient in concentration in particles produced in a coprecipitation process.
- Develop a process for precursors with a gradient in transition metal composition that have enriched manganese compositions.
- Demonstrate in a proof-of-principle experiment that precursors could be synthesized with predetermined compositional profiles.
- Demonstrate high capacity (>200 mAh/g) in final materials produced using the gradient precursors.
- Demonstrate that a tailored relative transition metal composition at the surfaces of gradient particles influences safety and cycle life.

Accomplishments

- Synthesized high energy full gradient concentration precursors and cathode materials.
- Characterized the material and demonstrated that both the precursor and lithiated final material had a full gradient in relative transition metal concentration at the individual particle level.
- Demonstrated that the full gradient concentration cathode materials exhibit high capacity, long life and improved safety.

✧　　　✧　　　✧　　　✧　　　✧

Introduction

In the past decade, major efforts have been devoted to searching for high-capacity cathode materials based on $LiNi_{1-x}M_xO_2$ (M = transition metal), mostly on account of their very high practical capacities (220~230 mA h g^{-1}) at high voltages (4.4~4.6 V). However, at such high operating voltages, these materials react aggressively with the electrolyte due to the instability of tetravalent nickel in the charged state, leading to very poor cycle and calendar life. Therefore, these materials operate reversibly only at a potential range below 4 V, resulting in low capacities of 150 mA h g^{-1}. To improve the stability of these materials, several researchers have investigated the effect of Mn substitution on cycle and calendar life. The introduction of Mn to the transition metal layer can help stabilize the transition metal oxide framework, since part of the Mn does not change valence state during charge and discharge. Recently, we reported several approaches to improve both the life and safety of nickel-rich cathode materials for potential use in plug-in hybrid electric vehicles. For instance, a core-shell approach resulted in a nickel-rich $LiNi_{0.8}Co_{0.1}Mn_{0.1}O_2$ that delivered high capacity at high voltage, and a manganese-rich $LiNi_{0.5}Mn_{0.5}O_2$ shell that stabilized the surface of the material. However, due to the structural mismatch and the difference in volume change between the core and the shell, a large void forms at the core/shell interface after long-term cycling, leading to a sudden drop in capacity. We also demonstrated that this structural mismatch could be mitigated by nano-engineering of the core/shell material, where the shell exhibits a concentration gradient. However, because of the short shell thickness, the manganese concentration at the outer layer of the particle is low; therefore, its effectiveness in stabilizing the surface of the material is weak, especially during high temperature cycling (55 ºC).

In this report, we describe a novel full gradient concentration cathode material that offers very high capacity, long life and excellent safety.

Results

Synthesis, characterization and electrochemical performance of full Gradient cathode materials. The nickel-rich lithium transition metal oxide investigated here has a nominal composition of $LiNi_{0.75}Co_{0.10}Mn_{0.15}O_2$, and the concentration gradient of transition metals shown in Figure IV - 120; the concentration of nickel decreases gradually from the center toward the outer layer of the particle, while the concentration of manganese increases gradually so that the manganese-rich and nickel-poor outer layer can stabilize the material, especially during high voltage cycling. The full concentration gradient (FCG) cathode material was prepared by a newly developed co-precipitation method involving the precipitation of transition metal hydroxides from the precursor solutions, where the concentration ratio of Ni:Mn:Co changes continuously with the reaction time.
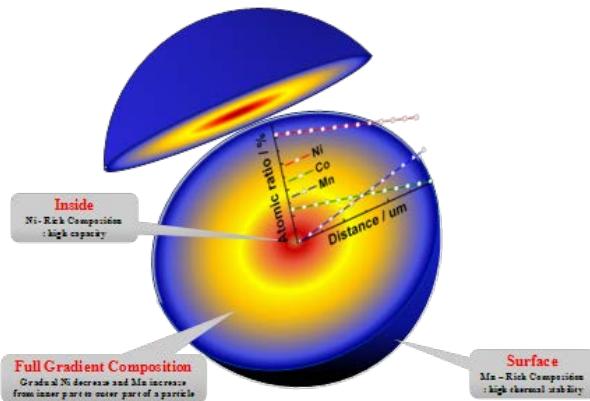

Figure IV - 120: Schematic diagram of the full concentration gradient lithium transition metal oxide particle with the nickel concentration decreasing from the center toward outer layer and the concentration of manganese increasing accordingly.

Figure IV - 121 shows scanning electron microscopy images and elemental distribution of Ni, Co, and Mn within a single particle of both the precursor $((Ni_{0.75}Co_{0.10}Mn_{0.15})(OH)_2)$ and the final lithiated product $(LiNi_{0.75}Co_{0.10}Mn_{0.15}O_2)$ having concentration gradient. The atomic ratio between Ni, Co, and Mn was determined by integrated 2D electron probe micro-analysis (EPMA). Figure IV - 121 clearly demonstrates that the atomic percentage of Co remained constant at about 10% in both the precursor and the lithiated particles as originally designed, while the concentration of Ni decreased and Mn increased continuously from the center toward the outer layer of the particle. Note that the slopes representing the metal (Ni and Mn) concentration change of the precursor are greater than those of the lithiated material because of the directional migration of the metal elements during the high temperature calcination to increase the entropy.
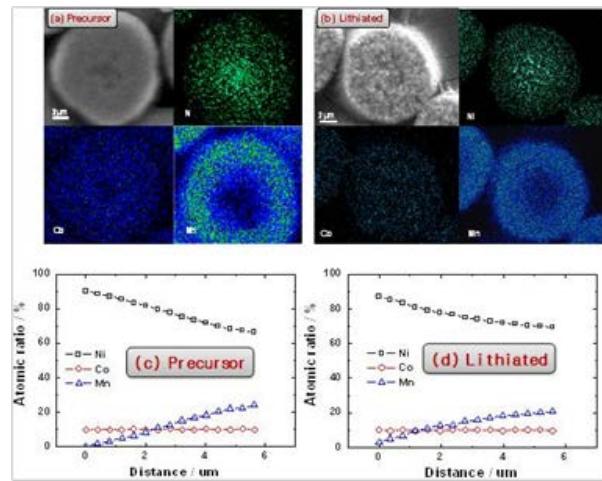
Figure IV - 121: Scanning electron microscopy images and electron-probe X-ray micro-analyzer mapping of (a) a precursor particle and (b) a lithiated particle; and integrated atomic ratio of transition metals as a function of the distance from the center of the particle for (c) the precursor and (d) the lithiated material.

Hard X-ray nano-tomography was used to determine the 3D distribution of Ni in a single lithiated particle. Similar to medical computerized tomography, this technique uses X-rays to obtain a 3D structure at up to 20-nm resolution. Figure IV - 122a shows the 3D volume rendering of a particle acquired with the technique. The data are imaged with the particle's volume partially removed to reveal the central cross section. With this 3D image, we are able to illustrate the concentration profile of Ni at any given plane (see Figure IV - 122b for a view of a plane going through the center of the particle). Figure IV - 122a and Figure IV - 122b show that the structure of the center, with a diameter of about 2 μm, was dramatically different from that of the outer layer. The central core is mainly composed of bright islands with numerous voids represented by the dark background. This structure could result from the different formation kinetics of the transition metal hydroxide seed at the beginning of the co-precipitation process, during which the seed developed along with many stacking voids. After the initial formation process, the growth of the particles reached a relatively steady state, and a denser layer developed above the loosely stacked core. Figure IV - 122b also confirms the results of EPMA (see Figure IV - 121b). A striking feature in Figure IV - 122b is that the bright area with high nickel content tends to form needle-shaped spikes pointing from the center toward the edge; this feature was clearly captured in the transmission electron microscopy image as highly aligned large-aspect-ratio nano rods (see Figure IV - 122c). We believe that this nano-pattern was the result of the directional transition metal migration during the high temperature calcination that led to the reduction in the slope of the concentration gradient (Figure IV - 121c vs. Figure IV - 121d). Due to the pre-conditioned concentration gradient in the particles of the precursor, the crystal growth during the high temperature calcination was energetically

preferred to forming a highly percolated nano-rod network, which minimizes the diffusion length between the center and the edge for transition metal ions. In the particle center, the migration of transition metal had to rely on the limited contact of loosely packed primary particles, and the development of aligned nano-rod network was limited, as shown in Figure IV - 122d.
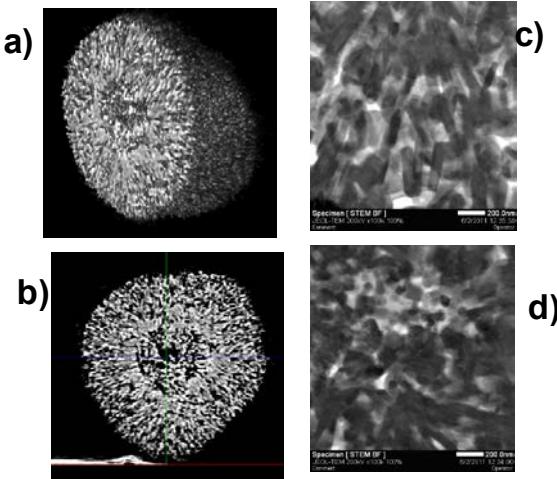

Figure IV - 122: (a) 3D presentation of nickel distribution in a single lithiated full concentration gradient lithium transition metal oxide particle; (b) 2D distribution of nickel on a plane going through the center of the particle; (c) transmission electron microscopy image of local structural feature near the edge of the particle; and (d) transmission electron microscopy image of local structural feature at the center of the particle.

A potential benefit of forming such a percolated aligned nano-rod network is that it also provides a shorter pathway for lithium-ion diffusion during normal charge/discharge cycling at ambient temperatures, leading to a better rate capability. Figure IV - 123a shows the rate capability of the FCG material along with inner composition (IC, $LiNi_{0.86}Co_{0.10}Mn_{0.04}O_2$) and outer composition (OC, $LiNi_{0.70}Co_{0.10}Mn_{0.20}O_2$) materials, both of which were synthesized by the conventional constant concentration approach. When discharged at the C/5 rate, the IC material delivered a reversible capacity of 210.5 mA h g^{-1}; the OC material, 188.7 mA h g^{-1}; and the FCG material, 197.4 mA h g^{-1}; these results are as expected because the IC material has the highest nickel content and the OC material has the lowest nickel content. However, when discharged at the 5C rate, the FCG material delivered the highest reversible capacity. As a cross-validation, the diffusion coefficient of lithium ions in the three materials was measured by the galvanostatic intermittent titration technique (GITT). The results showed that the FCG material has, in general, the highest lithium-ion diffusion coefficient. Meanwhile, the electronic conductivity was measured to be the highest for the IC material, 1.67×10^{-4} S cm^{-1}, followed by the FCG material, 3.10×10^{-5} S cm^{-1}, and the OC material, 7.30×10^{-6} S cm^{-1}. Therefore, we believe that the high rate capability of the FCG material has no strong correlation with the electronic conductivity, but mostly originated from the special

percolated aligned nano-rod network that shortened the diffusion pathway of lithium ions in the particle.

Figure IV - 123b shows the initial charge and discharge curve of coin type half cells based on IC, FCG, and OC materials. Both the IC material (highest nickel content) and FCG materials delivered higher capacity of 220.7 mAh g^{-1} and 215.4 mAh g^{-1}, respectively; while the OC material (lowest nickel content) showed lower capacity of 202 mAh g^{-1}. Note that the columbic efficiency of FCG was higher (94.8%) when compared to both IC and OC electrodes (91%) due to a well-developed aligned nano-rod network in FCG materials which facilitates Li$^+$ diffusion, and thus high lithium utilization.
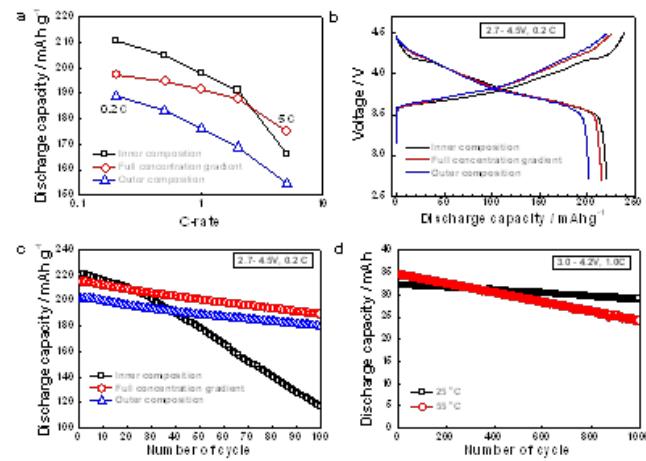
Figure IV - 123: Charge–discharge characteristics of $LiNi_{0.86}Co_{0.10}Mn_{0.04}O_2$, $LiNi_{0.70}Co_{0.10}Mn_{0.20}O_2$, and full concentration gradient $LiNi_{0.75}Co_{0.10}Mn_{0.15}O_2$. a, Rate capabilities of the full concentration gradient material against the inner composition [$LiNi_{0.86}Co_{0.10}Mn_{0.04}O_2$] and outer composition [$LiNi_{0.70}Co_{0.10}Mn_{0.20}O_2$] materials (upper cutoff voltage of 4.3 V vs. Li$^+$/Li); b, initial charge-discharge curves and c, cycling performance of half cells using the full concentration gradient material, inner composition [$LiNi_{0.86}Co_{0.10}Mn_{0.04}O_2$] and the outer composition [$LiNi_{0.70}Co_{0.10}Mn_{0.20}O_2$] materials cycled between 2.7 V and 4.5 V vs. Li$^+$/Li; and d, discharge capacity of MCMB/full concentration gradient cathode full cells at room and high temperature. The electrolyte used was 1.2 LiPF$_6$ in EC/EMC (3:7 by volume) with 1 wt% vinylene carbonate as electrolyte additive.

Another important observation is that the reversible capacity of IC material decreased dramatically with cycling (Figure IV - 123c). This rapid capacity fade was mainly caused by the direct exposure of a high content of Ni(IV)-based compound to non-aqueous electrolyte at high potential; this exposure led to the chemical decomposition of both the surface of the electrode material and the electrolyte. By contrast, the OC material had higher manganese content and lower oxidizing capability toward non-aqueous electrolyte. Therefore, this material had a lower reversible capacity, but much better capacity retention. Figure IV - 123c shows that the FCG material had combined advantages of high capacity from the high nickel content in the bulk and high electrochemical stability from the high manganese content on the surface.

We assembled a pouch cell using the FCG material as the cathode and mesocarbon microbeads (MCMB, graphite) as the anode. This cell was cycled between 3.0 V and 4.2 V with a constant current of 1C (33 A). The full cell showed outstanding capacity retention after 1,000 cycles both at room and high temperature (Figure IV - 123d). The capacity of the cells increased with cut off voltage due to the higher lithium utilization at high voltage.

To investigate the safety of the FCG approach, we developed an *in situ* high energy X-ray diffraction (HEXRD) technique and used it to study the thermal decomposition of delithiated cathode materials in the presence of the electrolyte. The delithiated cathode material was recovered from the charged cell at 4.3 V and mixed with an equivalent amount of non-aqueous electrolyte, and the mixture was placed in a stainless steel high-pressure vessel for differential scanning calorimetry (DSC). The sample was then heated from room temperature to 375 ^{o}C with a heating rate of 10 ^{o}C min^{-1}. During the thermal ramping, a high energy X-ray beam (~0.1 Å), which is able to penetrate through a 4-mm-thick stainless steel block, was deployed to continuously monitor the structural change of the delithiated material. Figure IV - 124a and Figure IV - 124b show zoomed (2.40^{o} – 2.80^{o}) contour plots of the *in situ* HEXRD profiles of delithiated IC and FCG material during thermal ramping In these profiles, red represents a high intensity; blue, a low intensity. Three diffraction peaks can be seen in Figure IV - 124a and Figure IV - 124b; the left one starting at 2.57^{o} is the (101) peak for layered transition metal oxides, and the right weak one starting at 2.68^{o} is the (012) peak for layered oxides. The one in the middle (starting at 2.62^{o}) is the diffraction peak from the DSC vessel and can be used as a semi-reference. Figure IV - 124a shows that the delithiated IC material (Li$_{1-x}$Ni$_{0.86}$Co$_{0.10}$Mn$_{0.04}$O$_2$) starts converting to a new phase at around 100 ^{o}C; the (101) and (012) peaks shift toward a smaller angle. Figure IV - 124b shows that the low temperature phase transformation occurred at about 140 ^{o}C for the FCG material.

Figure IV - 124c shows the DSC profiles of delithiated cathodes in the presence of non-aqueous electrolyte. No heat flow was detected with DSC within the temperature range between 100 ^{o}C and 150 ^{o}C for both samples. Thus, this phase transformation is not related to the safety of the cathode materials, but can cause the degradation of electrochemical performance of high nickel-content cathode materials. Ahn et al. previously reported that Li(Ni$_{0.9}$Co$_{0.1}$)O$_2$ dramatically loses its reversible capacity when aged at 90 ^{o}C[21]. Therefore, we believe that the better capacity retention of the FCG material (as shown in Figure IV - 123b) can be attributed to the suppressed kinetics of detrimental phase transformation at temperatures around 100 ^{o}C. The *in situ* HEXRD data also showed that the newly formed phase

started to disappear at about 200 ^{o}C for the delithiated IC material (Li$_{1-x}$Ni$_{0.86}$Co$_{0.10}$Mn$_{0.04}$O$_2$), and the DSC data indicated significant exothermal reaction at about 210 ^{o}C (Figure IV - 124c). The corresponding phase transformation for the FCG material was much slower: the new phase disappeared at about 250 ^{o}C, and DSC data showed an exothermal reaction starting at about 250 ^{o}C (Figure IV - 124c). Thus, the FCG material appears to have better safety characteristics than the IC material by deferring its exothermal reaction to higher temperature.
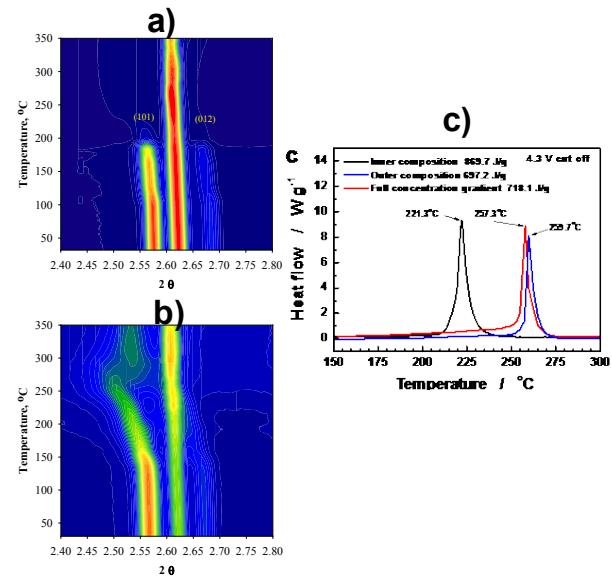
Figure IV - 124: a) Contour plots of *in situ* high energy X-ray diffraction profile. a, delithiated inner composition material [Li$_{1-x}$Ni$_{0.86}$Co$_{0.10}$Mn$_{0.04}$O$_2$] and b), delithiated full concentration gradient material during thermal ramping from room temperature to 375 ^{o}C with a scanning rate of 10 ^{o}C min^{-1}. c), differential scanning calorimetry profiles of the delithiated full concentration gradient material, the delithiated inner composition [Li$_{1-x}$Ni$_{0.86}$Co$_{0.10}$Mn$_{0.04}$O$_2$], and the delithiated outer composition [Li$_{1-x}$Ni$_{0.70}$Co$_{0.10}$Mn$_{0.20}$O$_2$] with a scanning rate of 1 ^{o}C min^{-1}. The cells were constant-voltage charged to 4.3 V vs. Li$^+$/Li before disassembling.

Conclusions and Future Directions

In conclusion, we have developed a high-performance cathode material composed of lithium transition metal oxide with FCG within each particle. The structure takes advantage of the high capacity from nickel-rich materials, high thermal stability of manganese-rich materials, and high rate capability of highly percolated and aligned nano-rod morphology. This newly developed material can deliver a specific capacity of up to 215 mA h g^{-1} with outstanding cycling stability in a full cell configuration, maintaining 90% capacity retention after 1,000 cycles. This novel material can lead to the rational design and development of a wide range of functional cathodes with better rate capability, higher energy density, and better safety characteristics.

This project was terminated because DOE has shifted funding to address voltage fade for the Argonne high energy composite cathode.

FY 2012 Publications/Presentations

1. Sun, Y.-K., Z. Chen, H.-J. Noh, D.-J. Lee, H.-G. Jung, Y. Ren, S. Wang, C.S. Yoon, S.-T. Myung, and **K. Amine**, *Nanostructured high-energy cathode materials for advanced lithium batteries.* Nature Material 11, 942 (2012)

2. Yang-Kook, S., L. Bo-Ram, N. Hyung-Ju, W. Huiming, M. Seung-Taek, and K. Amine, *A novel concentration-gradient Li Ni 0.83Co 0.07Mn 0.10 O 2 cathode material for high-energy lithium-ion batteries.* Journal of Materials Chemistry, 2011. 21(27): p. 10108-12.

3. 2011 DOE Annual Peer Review Meeting Presentation, May 9th-13th 2011, Washington DC.

4. 2010 American Institute of Chemical Engineers Annual Meeting Presentation, November 7th-12th 2010, Salt Lake City, UT.

5. 2010 Electrochemical Society Annual Meeting, October 10-15 2010, Las Vegas, NV.

---

1. G. M. Koenig, I. Belharouak, H. Deng, Y.-K. Sun, and K. Amine, *Chem. Mater,* **23** (7) (2011) 1954.

2. G. M. Koenig, I. Belharouak, H. M. Wu, and K. Amine, *Electrochim. Acta,* **56** (3) (2011) 1426.

IV.B.4.3 Novel Composite Cathode Structures (ANL)

Christopher S. Johnson

Argonne National Laboratory
9700 South Cass Avenue
Argonne, IL 60439-4837
Phone: (630) 252-4787; Fax: (630) 252-4176
E-mail: cjohnson@anl.gov

Collaborators:
Mike Slater, Argonne National Laboratory
Eungje Lee, Argonne National Laboratory
Donghan Kim, Argonne National Laboratory
Prof. Stephen Hackney, Michigan Technological
University

Start Date: October 2010
Projected End Date: September 2012

Objectives

The project objective is to conduct ion-exchange reactions that are used to make new cathode materials with high-energy and high-rate. We will produce an optimized material that shows an improvement over the drawbacks of standard high-energy cathodes. These ion-exchange cathodes should thus demonstrate <10% irreversible capacity in the first cycle, > 200 mAh/g at a C rate, no alteration in voltage profile during cycling, lower cost, and improved safety.

Technical Barriers

- Low energy density.
- High cost.
- Low abuse tolerance.

Technical Targets

- 96 Wh/kg, 316 W/kg (PHEV 40 mile requirement).
- Cycle life: 3000 cycles.
- Calendar life: 15 years.
- Improved abuse tolerance.

Accomplishments

- The synthesis of $Na_xLi_y(Ni_{0.25}Mn_{0.75})O_z$ cathode precursors was continued; x+y = 1.2. Synchrotron X-rays were used to determine the phases present in these materials. Li ion-exchange reactions of the above Na-Li materials (IE-LNMO) were successfully conducted in alcohols as well as water. Compositions measured by AA confirmed Ni and Mn ratio is

maintained. Na is effectively removed (2% left) in these ion-exchange reactions. Materials were heat-treated which resulted in the formation of 5 V spinel domains in the composite. These domains were confirmed by TEM.

- For the heat-treated samples, the capacity measured at a C/15 rate was 240 mAh/g between 4.8 to 2.0 V in Li-half cells. Over 50 cycles were completed with no loss in capacity. The C rate capacity is about 200 mAh/g, but at higher current rates the capacity drops off. There is also a voltage fade which appears overtime with cycling. For non-heat-treated samples, there are no changes in the XRD pattern after 50 cycles indicating excellent stability in the material.

- DIFFAX modeling of the stacking arrangement of IE-LNMO indicates a combination of O2, O4 and O6 layers. The DIFFAX model compares favorably with the XRD pattern. This type of stacking confirms the gliding nature of the layers. This soft-bonding character may allow for rapid diffusion of Li within the layers as is seen in the rate performance results of this material.

✧　　✧　　✧　　✧　　✧

Introduction

To improve the mileage range of plug-in hybrid electric vehicles (PHEV) and electric vehicles (EV) it requires a cathode material that possesses an energy density as high as possible. Layered transition metal (TM) oxides, $LiTMO_2$, are the leading candidate cathodes for implementation. If one Li per TM in $LiTMO_2$ can be reversibly cycled, then it may be possible to reach the maximum capacity of ~ 280-300 $mAhg^{-1}$. In cases where $LiTMO_2$ contains extra Li and Mn with Ni, then the Li forms $LiMn_6$ structural units in the TM layer that store the extra Li in their structure thereby helping to achieve the 280 $mAhg^{-1}$ specific capacity. $LiMn_6$ units in Li-rich $LiTMO_2$ form 'layered-layered' composite cathodes with the formulation $xLi_2MnO_3 \cdot (1-x)LiMO_2$ (M=Ni, Mn, Co), where the notation represents a nano-domain structure composite material. In some cases, particularly where Ni is present in these materials, it is possible to get site – intermixing between Ni^{2+} and Li^+ because the ionic radii are nearly equal: Ni^{2+} (0.69Å) and Li^+ (0.76 Å). In this case the Ni^{2+} can reside in the Li layer and hinder flow of Li cations during cycling. To solve this issue, we have been making use of $NaMO_y$ precursors for subsequent Li ion-exchange (IE). The Na creates a condition where there is no site mixing in the resultant structure because of the mismatch in radii between much larger Na^+ (1.02 Å) versus Ni^{2+} (0.69Å). This material is then IE with Li.

Approach

We will synthesize, characterize, and develop new cathode materials that exploit the difference in sodium versus lithium cation radii and their respective coordination properties. The Na is then ion-exchanged with Li. In our work, we have upped the Li content by making precursors containing extra Li in their structures such as $Na(Li,M)O_2$. Upon ion-exchange with Li, we expect that Li_2MnO_3-type composite will be formed due to the extra Li. Therefore IE makes a material that compositionally looks like $xLi_2MnO_3 \bullet (1-x)LiMO_2$, but intrinsically possesses a $LiMO_2$ component ultimately derived from $Na(M)O_2$. It is hoped that the synthesis route produces a material that is fundamentally different from those made by direct reaction of transition metal hydroxide, carbonate, or oxalate with Li salts. We will focus on electrode materials that contain redox active Ni, and low cost Mn and, if possible, Fe transition metals.

Results

$Na(Li,M)O_2$ precursor. Ideally the $Na(Li,M)O_2$ precursor must be synthesized in single phase in order to integrate the extra Li into the structure. From the synthesis, a P2 layered stacked product is made as shown in Figure IV - 125. The P2 arrangement of the layers is consistent with the presence of prismatic (P) 6-coordinated Na in the alkali metal layers.
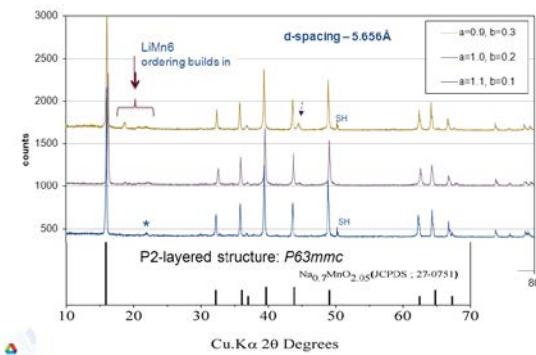
Figure IV - 125: X-ray powder diffraction patterns of $Na_aLi_bNi_{0.25}Mn_{0.75}O_\delta$ precursor. The asterisk indicates a superlattice peak, and the additional peaks in the top pattern indicate the formation of $LiMn_6$ sites within the $Na(Li,M)O_2$ structure.

Figure IV - 126 shows that $LiMn_6$ ordering peaks are present ($Na_{1.1}Li_{0.1}$). For $Na_{1.1}Li_{0.1}$, Li_2MnO_3 as a separate phase is not present but, instead begins to emerge when more Li is added into the system ($Na_{1.0}Li_{0.2}$). The high-resolution XRD (synchrotron source) of $Na_{1.0}Li_{0.2}Ni_{0.25}Mn_{0.75}O_y$ and $Na_{0.7}Ni_{0.25}Mn_{0.75}O_{2+\delta}$ (as control) is indicated in Figure IV - 127. Clearly $Na_{1.0}Li_{0.2}Ni_{0.25}Mn_{0.75}O_y$ contains both a secondary phase of Li_2MnO_3, and a strong $LiMn_6$ ordering peak. This means that some of the added Li used to make $Na(Li,M)O_2$ forms directly Li_2MnO_3 in the sample. The amount of Li_2MnO_3 together with Li incorporated in $Na(Li,M)O_2$ is unknown,

but, in principle could be determined by careful 6-Li solid-state NMR.
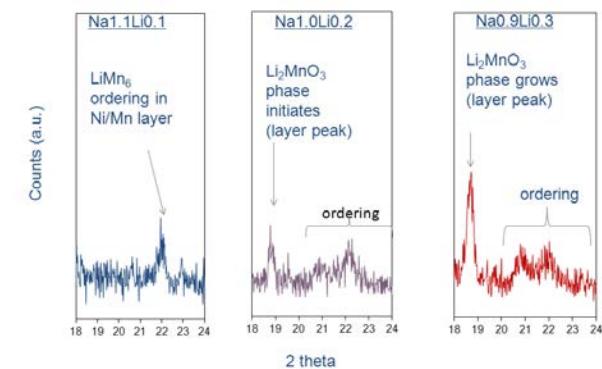
Figure IV - 126: X-ray powder diffraction patterns magnified between 18 and 24 degrees CuKα 2-theta of $Na_aLi_bNi_{0.25}Mn_{0.75}O_\delta$ precursor.
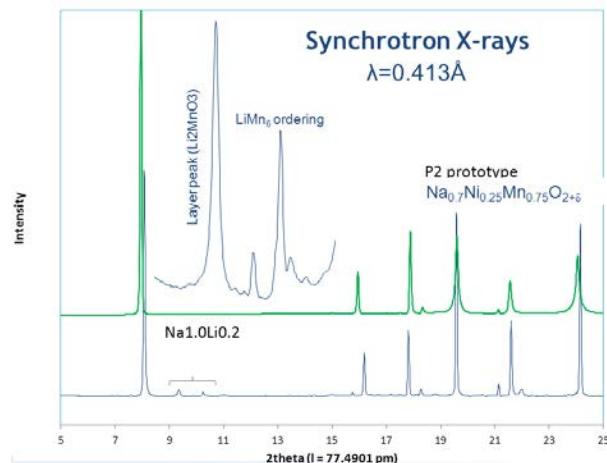
Figure IV - 127: X-ray powder diffraction patterns measured using a synchrotron source. Bottom pattern is $Na_{1.0}Li_{0.2}Ni_{0.25}Mn_{0.75}O_y$ and the top is synthesized $Na_{0.7}Ni_{0.25}Mn_{0.75}O_y$ to show the clean pattern for non-Li P2 precursor.

IE sample from $Na(Li,M)O_2$ precursor. Li ion-exchange of $Na_{1.0}Li_{0.2}Ni_{0.25}Mn_{0.75}O_y$ is typically conducted by stirring the powder in a solvent with an excess of Li salt. A huge number of variables exist in this reaction such as precursor morphology, time, temperature, solvent, and Li-salt used. Figure IV - 128 gives the XRD pattern of a sample made by ion-exchange. The material has a strong layering peak, ordering peaks (Li_2MnO_3-like domain), and the remainder broad peaks. This suggests that the material is quite layered in the c-direction, but the layers themselves possess a large number of stacking faults. DIFFAX analysis was conducted on the XRD patterns, and it is clear that the P2 Na precursor upon Li-exchange sheers to a conglomeration of O2, O4 and O6 as shown in Figure IV - 129. The visualization of O2, O4 and O6 stacking arrangements are schematically shown in Figure IV - 130.
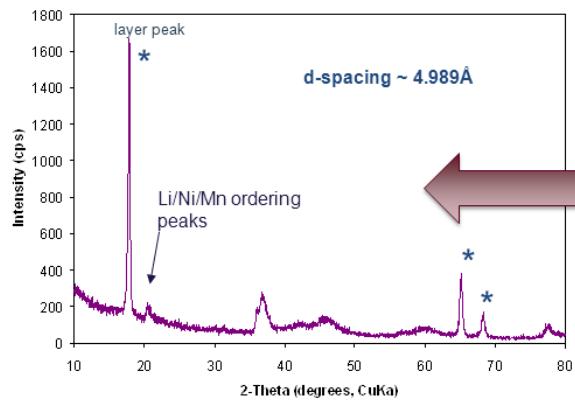
Figure IV - 128: XRD pattern of IE product, made by refluxing $Na_{1.0}Li_{0.2}Ni_{0.25}Mn_{0.75}O_y$ in hexanol with 2 fold LiCl for 4 hours, followed by washing with methanol, and vacuum drying.
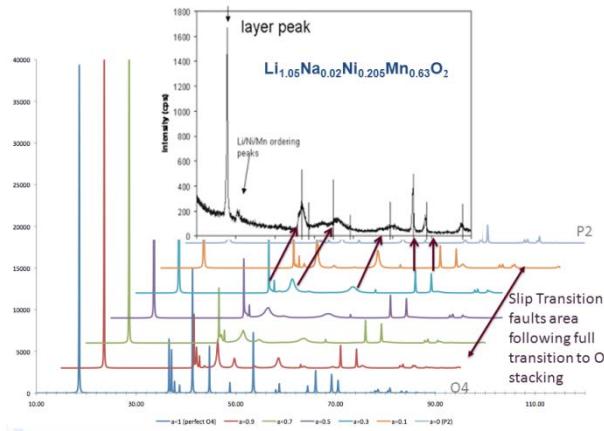
Figure IV - 129: P2 to O4 transition showing the DIFFAX results which models the XRD patterns. Note the middle area is the transition whereby stacking faults are present, and the likelihood of mixed O2, O4 and O6 is possible.
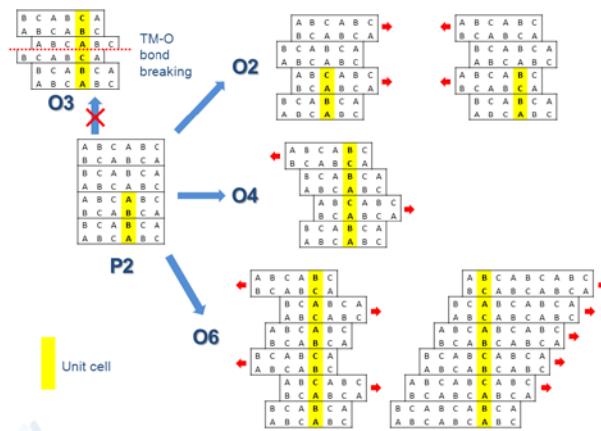
Figure IV - 130: This is a schematic model showing the layer gliding process of P2 to O2, O4 or O6 stacking. O stacking occurs when Li enters the alkali metal layer for Na. Li prefers octahedral coordination instead of prismatic coordination so a shear occurs leaving the stacking faults in the material.

The O3 stacked sample is not made because there is no driving force to do M-O bond breaking. Instead, layers glide relative to each other to accommodate the entry of Li for Na. Na TM oxides are known to have propensity to have layers that can glide. Evidently the gliding and stacking is somewhat random, but the electrochemistry may be affected by the stacking faults.

A graphical summary of the electrochemical performance of a number of ion-exchanged materials synthesized under various conditions is shown in Figure IV - 131. There is a large scatter of data in the results indicating the various effects of ion-exchange. The capacity at various rates resides in a window difference between 80-110 mAhg^{-1}. Evidently the condition of ion-exchange makes a big difference in the material as a cathode. In general, best results were obtained when the TM precursor was formed by the sol-gel process, then, stirred with alcohol under reflux, for a moderate time of 4h.
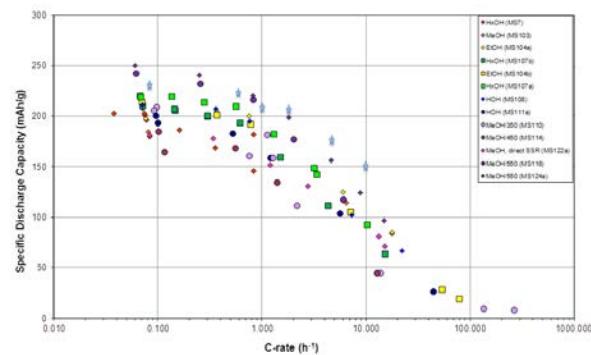
Figure IV - 131: Electrochemical performance of a number of IE samples.

Next, experiments on heat-treatment were performed and the best cycling results occurred with the 550 °C samples. When this procedure is done, then a 5 V spinel ($LiNi_{0.5}Mn_{1.5}O_4$) is formed within the sample composite.

In Figure IV - 132, the charge-discharge voltage profiles (1st, 16th and 31st cycles), are shown for HT-$Li_{1.05}Na_{0.02}Ni_{0.21}Mn_{0.63}O_2$. Note the following characteristics:

- On the first charge, there is a plateau at 4.5 V indicative of a Li_2MnO_3 component (i.e. Li in $LiMn_6$ arrangments in the TM layer).
- On the first charge, the 5 V spinel signature is evident.
- The coulombic efficiency is nearly equivalent for charge and discharge.
- There is a layered region at the mid-voltage area with two processes or Li sites in the layers (i.e. i and ii).
- One of the Li sites in the layer could have been generated from the 'activation' of the Li_2MnO_3 component.
- The other voltage feature for the layered component is likely due to the Ni redox.

- The < 2.8 V spinel plateau is associated with the 5 V spinel and involves the Mn redox.
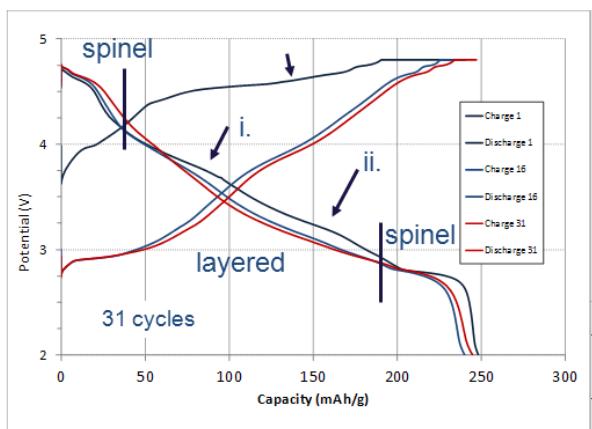
Figure IV - 132: Charge-discharge voltage profiles of 550 °C HT-$Li_{1.05}Na_{0.02}Ni_{0.21}Mn_{0.63}O_2$ IE cathode materials.

The discharge profile of a number of samples made by different routes is given in Figure IV - 133. One can clearly see the 5 V spinel signatures at high-voltage. Based on the capacities observed, the amount is about 20% generally for each sample. Nevertheless, good cycling stability is observed over 50 cycles (Figure IV - 134) with a capacity nearly 250 mAhg^{-1} or about 0.9Li/TM.
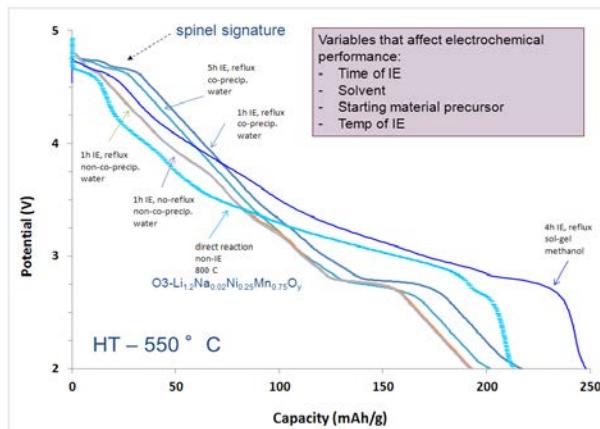
Figure IV - 133: Discharge voltage profiles of various IE cathode materials.
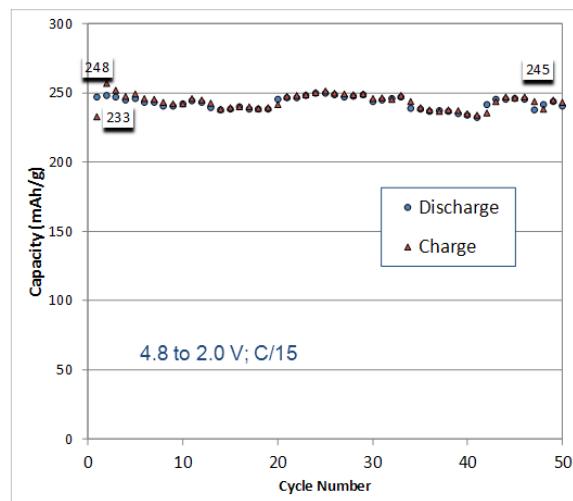
Figure IV - 134: Cycling of IE cathode material over 50 cycles at a C/15 rate.

The IE cathode material electrode was X-rayed before and after 50 cycles and one can see that the material exhibits nearly the same XRD pattern (Figure IV - 135). Thus, the disordered stacking arrangement remains fixed on cycling. It is reasonable to suggest that Li, once ion-exchanged into the material fuses the stacking faults into their place and in a rigid array that does not alter with cycling. The amount of Li in the TM layer as evident from the ordering peaks, however, is decreased which indicates that the Li_2MnO_3 domains in the material have been 'activated', which is consistent with the high-capacities delivered.
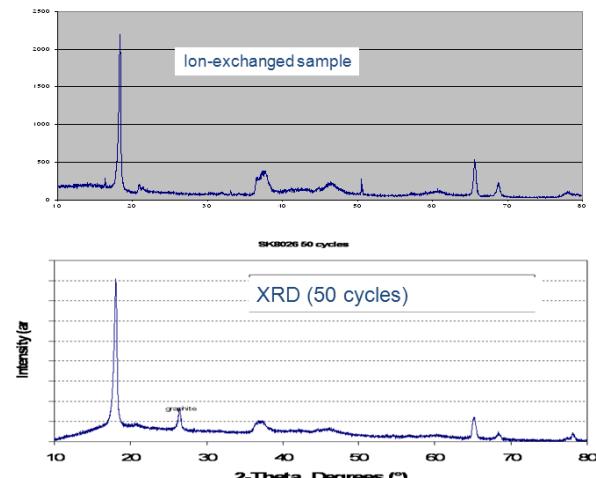
Figure IV - 135: XRD pattern of IE material electrode laminate before (top) and after (bottom) 50 cycles.

Lastly we compare the electrochemical voltage profiles of a material which is $Li_{1.2}Ni_{0.25}Mn_{0.75}O_y$ that is directly synthesized from $(Ni_{0.25}Mn_{0.75})C_2O_4 \cdot zH_2O$ and $0.6Li_2CO_3$ at 800 °C, with an IE sample which has a similar composition, i.e. $Li_{1.26}Na_{0.02}Ni_{0.25}Mn_{0.75}O_2$. The result is shown in Figure IV - 136. The IE material

electrode has a higher mid-point or average voltage versus the direct synthesis sample indicating a higher-energy density material. The presence of 5 V spinel in the IE-LNMO sample is more prevalent. To compare this we conducted TEM studies on the IE-LNMO. The TEM micrograph is in Figure IV - 137. A spinel domain is identified.
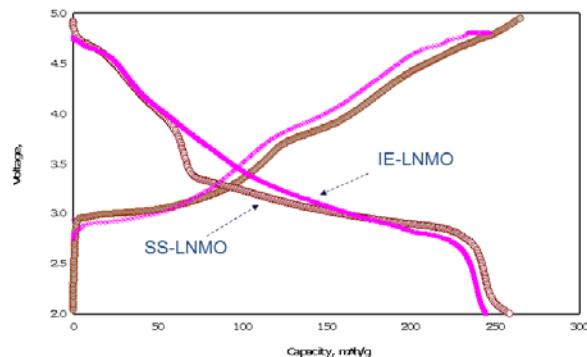
Figure IV - 136: Voltage profiles of direct synthesized $Li_{1.2}Ni_{0.25}Mn_{0.75}O_y$ (SS-LNMO) and ion-exchange sample $Li_{1.26}Na_{0.02}Ni_{0.25}Mn_{0.75}O_2$ (IE-LNMO). Current rate for both is 15 mAg^{-1}
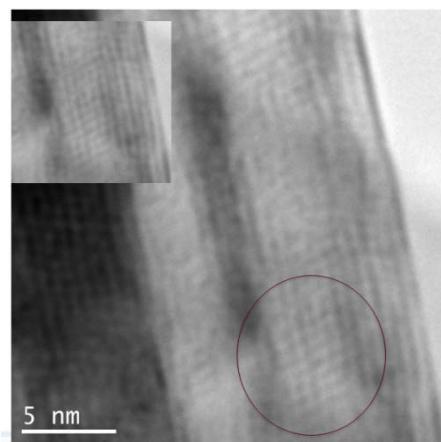
Figure IV - 137: TEM of IE-LNMO showing the spinel regions in the marked circle.

Conclusions and Future Directions

Li-containing $Na(Li,M)O_2$ precursors incorporate Li into the transition metal plane along with the formation of Li_2MnO_3 at higher contents of Li. Upon Li ion-exchange a new material that is layered with $LiMn_6$ ordering is synthesized. This material having a composite structure forms a 5 V spinel domain component upon heat-treatment at 550 °C. The Mn/Ni ratio of 3 supports the 5 V spinel formation (i.e. $LiNi_{0.5}Mn_{1.5}O_4$). Over 20 reactions with various ion-exchange conditions were studied. The best materials are those made from a sol-gel precursor, an alcohol for ion-exchange under reflux conditions, and with a Li salt in excess.

Discharge capacities of these IE samples are around 250 mAhg^{-1} and stable long-term cycling (50 cycles) is

possible. The voltage curves alter during cycling indicating a material that is constantly altering its structure. However, the layer stacking (O type; Li 6-coordination) and the Li-alkali layer appear to remain fixed in the c-direction not changing with cycling (50 cycles) as is evident by the XRD pattern that shows essentially the same peak positions, and intensities. In conclusion, the IE process produces new layered-spinel materials that operate well in Li-ion batteries.

Future studies should be devoted to NMC-type $Na(Li,M)O_2$ precursors as sell as NCA-types which are ion-exchanged with Li. In this way higher performance (a greater average voltage) and greater capacities may be realized.

FY 2012 Publications/Presentations

1. <u>C. S. Johnson</u> et al., 2012 DOE Annual Peer Review Meeting Presentation, May 14th-18th 2012, Washington DC.

2. <u>C. S. Johnson</u> et al., *Ion-exchange Synthesis and Intercalation Process of $Li_xNi_{0.25}Mn_{0.75}O_y$ Cathodes for Li-ion Batteries",* The 222nd Electrochemical Society Meeting, Honolulu, Hawaii, October 2012 (Invited Oral).

IV.B.4.4 Development of High-Capacity Cathodes with Integrated Structures (ANL)

Michael Thackeray

Argonne National Laboratory
9700 South Cass Avenue
Argonne, IL 60439
Phone: (630) 252-9184; Fax: (630) 252-4176
E-mail: thackeray@anl.gov

Collaborators:
ANL: D. Kim, J. Croy, K. Gallagher, G. Sandi
APS (ANL); P. Chupas, K. Chapman, M. Suchomel
MIT: Y. Shao-Horn

Start Date: October 1, 2009
Projected End Date: September 30, 2014

Objectives

The major objective of this project is to develop Li- and Mn-rich cathode materials with integrated structures that promise low cost, good thermal stability and improved cycling stability while maintaining a high capacity at an acceptable rate (e.g., ≥200 mAh/g at a 1C rate). Cathode performance goals are a reversible 230 mAh/g capacity with >85% first-cycle efficiency. Specific objectives of this study are to:

- Design and synthesize Li- and Mn-rich oxides with integrated structures, notably 'layered-spinel' materials, to counter the *voltage fade* phenomenon observed in 'layered-layered' electrode materials.
- Identify and overcome degradation issues.
- Exchange information and collaborate closely with others in ABR's 'voltage fade' team.
- Supply promising high-capacity cathode materials for PHEV cell build.

Technical Barriers

- Low energy density.
- Poor low temperature operation.
- Abuse tolerance limitations.

Technical Targets (USABC - End of life)

- 142 Wh/kg, 317 W/kg (PHEV 40 mile requirement).
- Cycle life: 5,000 cycles.
- Calendar life: 15 years.

Accomplishments

- The electrochemical properties of lithium-nickel-manganese-oxide composite electrode structures in three-component 'layered-layered-spinel' systems, prepared by lowering the lithium content of 'layered-layered' $Li_2MnO_3 \cdot LiMO_2$ materials (M=Mn, Ni), were evaluated.
- The effects of Mg substitution and AlF_3 coatings on 'layered-layered-spinel' electrode materials were studied.
- A baseline system, $xLi_2MnO_3 \cdot (1-x)LiCoO_2$, was used to initiate in-depth studies at the Advanced Photon Source to determine structural features that would shed light on, and provide clues to counter, the voltage decay phenomenon in 'layered-layered' electrodes.

✧   ✧   ✧   ✧   ✧

Introduction

Li- and Mn-rich oxide electrodes with integrated or composite 'layered-layered' structures such as $xLi_2MnO_3 \cdot (1-x)LiMO_2$ (M=Mn, Ni, Co), are known to deliver a high capacity (~250 mAh/g) when charged to high potentials (>4.4 V *vs.* Li^+/Li). Present limitations of these cathode materials are 1) voltage fade on cycling, 2) a relatively poor rate capability, 3) high impedance, particularly at a low state of charge (SOC), and 4) poor cycling stability, notably at high temperatures. These performance limitations are attributed to poor electronic/ionic conductivity in the oxide bulk, surface damage from repeated high-voltage cycling, and Mn dissolution effects. In addition to the above-mentioned limitations, 'layered-layered' electrode materials exhibit significant voltage decay on extended cycling, which creates issues not only in terms of a decrease in cell energy but also in battery management (voltage monitoring). This project addresses the above-mentioned limitations in an attempt to meet the targeted electrode and cell performance goals for PHEVs using structurally-integrated electrode materials.

Approach

To address the limitations associated with 'layered-layered' $xLi_2MnO_3 \cdot (1-x)LiMO_2$ electrodes, several approaches were adopted:

- Use compositional phase diagrams to design integrated 'layered-layered-spinel' structures and to stabilize the electrode to electrochemical cycling,

- Elucidate the causes of voltage decay by investigating both bulk and surface effects, and

- Undertake detailed structural analyses of composite electrodes at the Advanced Photon Source (APS) by X-ray diffraction, X-ray absorption and pair-distribution-function (pdf) analyses to understand the complexity of the parent and cycled structures.

Results

'Layered-Layered-Spinel' Electrodes. Using knowledge gained from previous work and recognizing the potential of using a $LiMn_{1.5}Ni_{0.5}O_4$ spinel component to stabilize high capacity 'layered-layered' $0.5Li_2MnO_3 \cdot 0.5LiMn_{0.5}Ni_{0.5}O_2$ electrodes and to counter voltage decay, and given the tendency for manganese-rich layered electrode structures to convert readily to spinel, studies of 'layered-layered-spinel' materials were continued by exploring electrode compositions with a lower manganese content. Focus was placed specifically on the '$Li_xMn_{0.65}Ni_{0.35}O_y$' system, for which the end members are $0.3Li_2MnO_3 \cdot 0.7LiMn_{0.5}Ni_{0.5}O_2$ (x=1.3; y=2.3), in which the average manganese and nickel oxidation states are 4+ and 2+, respectively, and $LiMn_{1.3}Ni_{0.7}O_4$ (x=0.5; y=2) in which the corresponding average oxidation states are expected to lie between 4+ and 3.77+ for Mn, and 2.57+ and 3+ for Ni. This system is highlighted by the dotted tie-line between $0.3Li_2MnO_3 \cdot 0.7LiMO_2$ and LiM'_2O_4 (M and M' = Mn, Ni) in Figure IV - 138. In particular, compounds with a lithium content of x=1.3, i.e., the parent 'layered-layered' composition, and x=1.25 were selected for detailed evaluation, the latter value corresponding to a targeted spinel content of 6%. The beneficial effects of 1) using Mg^{2+} as a dopant ion and 2) treating the electrode particle surface with an acidic solution of AlF_3 to enhance cycling stability, reduce first-cycle capacity loss, and to slow voltage decay on cycling were also studied.
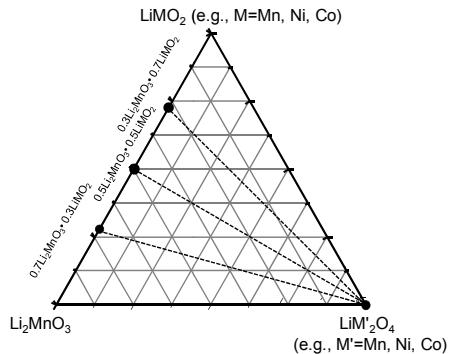
Figure IV - 138: A compositional phase diagram of a 'layered-layered-spinel' system with $Li_2MnO_3 \cdot (1-x)LiMO_2$ ('layered-layered') and LiM'_2O_4 (spinel) components.

Spinel Content. Based on the hypothesis that small amounts of spinel are more likely to be effective in stabilizing high capacity 'layered-layered' composite electrode structures without impacting their rate capability, initial electrochemical experiments were conducted on $Li_xMn_{0.65}Ni_{0.35}O_y$ compounds in which the targeted values of x and y fell within the range $1.10 \leq x \leq 1.30$ and $2.22 \leq y \leq 2.30$, respectively, corresponding to compounds with a spinel content between 0 and 25%. The maximum discharge capacity and first-cycle efficiency, plotted as a function of the lithium content, x, for these five samples are shown in Figure IV - 139. The data clearly show that for higher spinel content (i.e., lower values of x) the first cycle efficiency is high because the spinel component can accommodate the oversupply of lithium released from the electrode during the activation of the Li_2MnO_3 component on the initial charge; for lower spinel content, the first-cycle efficiency decreases, reaching about 78% when no spinel is present (x=1.3). Conversely, when targeting a high spinel content, e.g., 25% (x=1.10) and 19% (x=1.15), the capacity delivered by the composite 'layered-layered-spinel' electrode is relatively low (92 and 140 mAh/g, respectively). Figure IV - 139 therefore demonstrates that optimum capacity and first-cycle efficiency are likely to be obtained when x lies between 1.20 and 1.25, i.e., from electrodes containing between about 6 and 12% spinel.
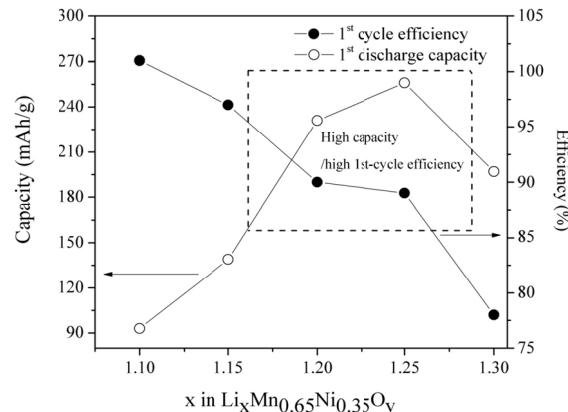
Figure IV - 139: Variation in capacity (mAh/g) and first-cycle efficiency (%) as a function of x in $Li_xMn_{0.65}Ni_{0.35}O_y$ electrodes.

Structural Characterization. The X-ray powder diffractions of various products are provided in Figure IV - 140, which include (a) a baseline 'layered-layered' $Li_{1.3}Mn_{0.65}Ni_{0.35}O_{2.3}$ (equivalent to $0.3Li_2MnO_3 \cdot 0.7LiNi_{0.5}Mn_{0.5}O_2$); (b) a Mg-substituted product of (a), $Li_{1.3}Mn_{0.65}Ni_{0.33}Mg_{0.02}O_{2.3}$; (c) a 'layered-layered-spinel' product with targeted composition $Li_{1.25}Mn_{0.65}Ni_{0.35}O_{2.28}$ equivalent to $0.94\{0.3Li_2MnO_3 \cdot 0.7LiNi_{0.5}Mn_{0.5}O_2\} \cdot 0.06LiMn_{0.65}Ni_{0.35}O_2)$ with 6% spinel; (d) a Mg-substituted equivalent of (c), $Li_{1.25}Mn_{0.65}Ni_{0.33}Mg_{0.02}O_{2.28}$; and (e) an AlF_3-treated equivalent of (d). The X-ray diffraction patterns are consistent with those expected for composite Li_2MnO_3-

based 'layered-layered' or 'layered-layered-spinel' structures.

Given the close similarity that can exist in the XRD patterns of cubic-close-packed layered and spinel lithium metal oxides, it is not surprising that the low spinel content (6%) in the layered-layered-spinel' products, $Li_{1.25}Mn_{0.65}Ni_{0.33}O_{2.28}$ and Mg-substituted $Li_{1.25}Mn_{0.65}Ni_{0.33}Mg_{0.02}O_{2.28}$, made it difficult to distinguish the layered- and spinel components from one another (Figure IV - 140c and Figure IV - 140d). Nevertheless, the asymmetric broadening of the peaks at approximately 37, 44 and 64 °2θ, indicative of spinel formation, was clearly evident in the XRD pattern of the latter sample, as highlighted by the arrows in Figure IV - 140d. These two spinel peaks were unquestionably visible in the AlF$_3$-treated sample (Figure IV - 140e); in this case, the slight increase in peak magnitude and improved peak resolution is attributed to the AlF$_3$ surface treatment that increases the spinel content through Li removal (by acid leaching) and subsequent drying and annealing, consistent with the compositional analysis of this compound. It was therefore concluded that an advantage of AlF$_3$ surface treatment using acidic conditions is that it provides a technique to simultaneously stabilize the surface and tailor the amount of stabilizing spinel in the bulk of composite 'layered-layered-spinel' electrode structures.
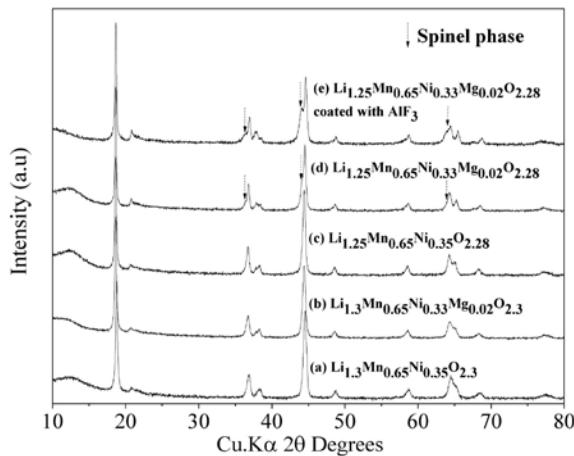
Figure IV - 140: XRD patterns of various materials derived from the 'layered-layered-spinel' $Li_xMn_{0.65}Ni_{0.35}O_y$ system.

Electrochemistry. An experiment was conducted to assess the feasibility of activating a 'layered-layered-spinel' $Li_{1.25}Mn_{0.65}Ni_{0.33}Mg_{0.02}O_{2.28}$ electrode at 4.95 V for 2 cycles to access the high capacity of the electrode, and then to lower the upper cut-off voltage to 4.6 V to a) minimize side reactions with the electrolyte solvent and b) provide greater cycling stability (Figure IV - 141a-c). Figure IV - 141a shows the voltage profiles of the first two cycles of a $Li/Li_{1.25}Mn_{0.65}Ni_{0.33}Mg_{0.02}O_{2.28}$ cell obtained between 4.95 and 2.5 V, and the subsequent 11th and 51st cycles between 4.6 and 2.5 V. This procedure yielded a discharge capacity of almost 200 mAh/g. Of

particular interest are the dQ/dV plots of lithium cells with (i) an untreated $Li_{1.25}Mn_{0.65}Ni_{0.33}Mg_{0.02}O_{2.28}$ 'layered-layered-spinel' cathode for the 1st, 2nd, 11th and 50th cycles between 4.6 and 2.5 V (Figure IV - 141b), and (ii) a corresponding AlF$_3$-treated cathode that was subjected to two activation cycles between 4.95 and 2.5 V, followed by an additional 49 cycles between 4.6 and 2.5 V (Figure IV - 141c). These data indicate that the untreated $Li_{1.25}Mn_{0.65}Ni_{0.33}Mg_{0.02}O_{2.28}$ cathode suffers from continuous voltage fade, which is apparent in two dominant reduction peaks (indicated by arrows in Figure IV - 141b), when cycled over a 4.6 to 2.5 V range, whereas the AlF$_3$-treated electrode, despite being activated twice at 4.95 V and displaying some voltage fade during the early cycles, ultimately reaches a stable state, as indicated by the reduction peaks at both 3.65 and 2.9 V.
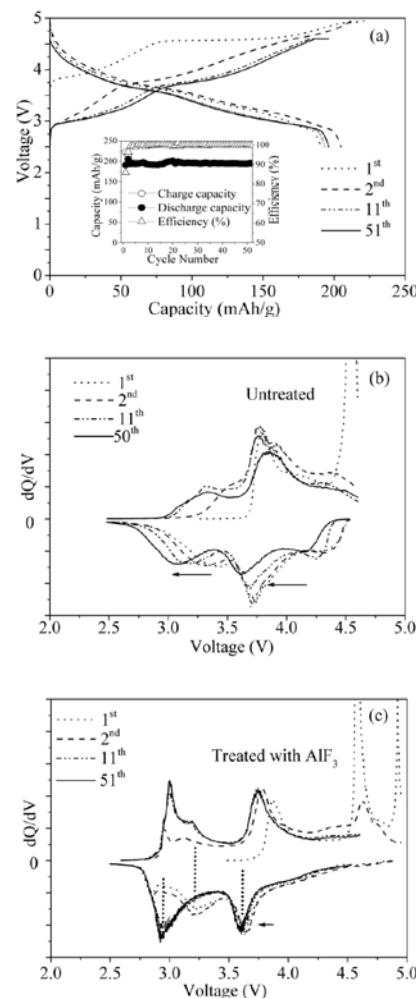
Figure IV - 141: Effect of activation voltage on the performance of 'layered-layered-spinel' $Li_{1.25}Mn_{0.65}Ni_{0.33}Mg_{0.02}O_{2.28}$ and AlF$_3$-treated electrodes: a) typical voltage profile of an uncoated electrode; b) and c) dQ/dV plots of lithium cells with uncoated and AlF$_3$-coated electrodes, respectively. The cells in a) and c) were subjected to two activation cycles between 4.95 and 2.5 V, before being cycled between 4.6 and 2.5 V, whereas the cell in b) was cycled only between 4.6 and 2.0 V.

Structure analysis of composite structures. To obtain a deeper understanding of the voltage decay exhibited by 'layered-layered' lithium-metal-oxide structures, high-resolution X-ray diffraction (XRD) and pair-distribution function measurements (PDF) have been initiated at the Advanced Photon Source. As a baseline, $xLi_2MnO_3 \bullet (1-x)LiCoO_2$ samples with x=0.1, 0.3, 0.7, and 0.9 were prepared and annealed at 850°C. XRD and PDF plots are shown in Figure IV - 142a and Figure IV - 142b. These preliminary data suggest the formation of a complex structure, exhibiting solid-solution behavior within a composite "Li_2MnO_3" and "$LiCoO_2$" matrix.
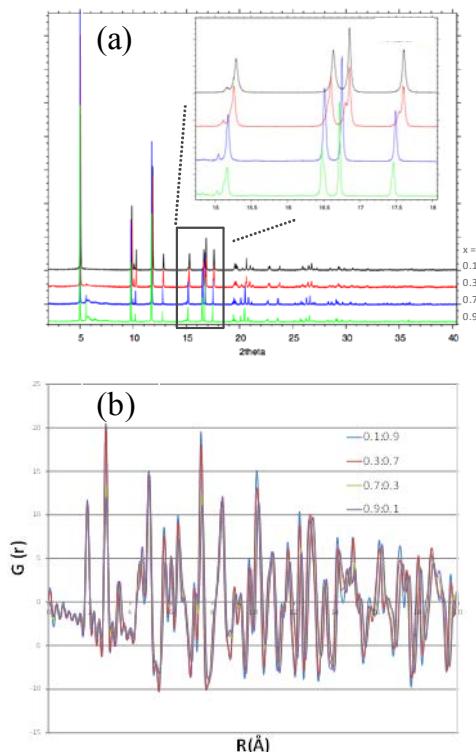
Figure IV - 142: a) XRD patterns and b) PDF spectra of $xLi_2MnO_3 \bullet (1-x)LiCoO_2$, for x=0.1, 0.3, 0.7, and 0.9 annealed at 850°C.

Conclusions and Future Directions

- Too much spinel reduces the overall capacity of the 'layered-layered-spinel' electrodes.

- Optimum capacity, coupled to a high first-cycle coulombic efficiency, is obtained for electrodes that contain between about 6 to 12% spinel.

- Relative to 'layered-layered' electrodes, 'layered-layered-spinel' and Mg-doped electrode compositions provide 1) enhanced electrochemical capacity; 2) higher rate capability; and 3) lower ASI, particularly at low states of charge.

- AlF$_3$-treatment of 'layered-layered-spinel' particles 1) increases the spinel content of the electrode, 2) improves surface stability, 3) enhances cycling

stability, and 4) slows the voltage decay of cells; however, this treatment does not appear to provide any significant rate advantage to the electrode.

- Structural analyses of composite electrodes are being conducted at the Advanced Photon Source to provide detailed insights of their structural complexity before and after cycling.

The results obtained are encouraging; they hold clues that may be used to advance the compositional and structural design of high capacity lithium metal oxide cathodes. This project is a work-in-progress; it will be continued to exploit, optimize and characterize 'layered-layered-spinel' composite electrode structures further. This project will be rolled into ABR Project IV.B.1: *Mitigation of Voltage Fade in Lithium-Manganese-rich Oxide Cathode Materials* in FY2013.

FY 2012 Publications/Patents/Presentations

Publications

1. D. Kim, G. Sandi, J. R. Croy, K. G. Gallagher, S.-H. Kang, E. Lee, M. D. Slater, C. S. Johnson, and M. M. Thackeray, *Composite 'Layered-Layered-Spinel' Cathode Structures for Lithium-ion Batteries*, J. Electrochem. Soc., (2012). In press.

Patent Applications

1. D. Kim, J. R. Croy, and M. M. Thackeray, *Electrode Structures and Surfaces for Li Batteries.* Submitted for filing, September 2012.

Presentations

1. M. M. Thackeray, *Development of High-Capacity, Cathode Materials with Integrated Structures*, Presentation at the Annual Merit Review Meeting, DOE Vehicle Technologies Program, Arlington VA, 14-18 May, 2012.
2. M. M. Thackeray, J. R. Croy, D. Kim, G. Sandi-Tapia, K. G. Gallagher and M. Balasubramanian *High Capacity Li- and Mn-rich Metal Oxide Electrodes: Challenges and Opportunities*, IMLB 16, Jeju Korea, June 2012.

IV.B.5 Applied Battery Research on Electrolytes

IV.B.5.1 Develop Electrolyte Additives (ANL)

Zhengcheng Zhang (PI)

Argonne National Laboratory
9700 South Cass Avenue
Argonne, IL 60439-4837
Phone: (630) 252-7868; Fax: (630) 972-4440
E-mail: zzhang@anl.gov

Collaborators:
Khalil Amine, Argonne
Lu Zhang, Argonne
Libo Hu, Argonne

Start Date: FY09
Projected End Date: September 2012 (last report)

Objectives

- The objective of this work is to develop novel electrolyte additives that can improve the state-of-the-art lithium-ion battery electrolyte, especially with regard to cycle and calendar life, safety, and the electrochemical window, to meet the requirements of electric vehicle (EV) and plug-in hybrid electric vehicle (PHEV) applications.

Technical Barriers

The general technical barrier is the development of novel functional electrolytes for lithium-ion batteries tailored to EV and PHEV applications that meet or exceed all performance goals. Specific barriers of electrolyte development include:

- Insufficient voltage stability,
- High flammability and low safety,
- Poor cycle and calendar life, and
- Surface reactivity with electrodes.

Technical Targets

- Screening and evaluation of novel electrolyte additives to improve the cycle and calendar life of lithium-ion cells,
- Establishment of connections between chemical structures and cell performance, and
- Synthesis of novel solid-electrolyte interface (SEI) additives tailored to improvements of cell performance and safety.

Accomplishments

- A growing candidate list of SEI additives has been established based on empirical guidance, which is solely based on chemical structures.
- As a previous example, 3-Oxabicyclo[3.1.0]hexane-2,4-dione (OBD) was fully characterized using various techniques, including XPS, FTIR, SEM, to help understand the mechanism behind the cell performance.
- Phosphor III was used to build novel SEI additives, not only working on anode but also on cathode.
- Cathode SEI additives are being explored and some preliminary results have shown some promise.

✧   ✧   ✧   ✧   ✧

Introduction

The electrolyte is an indispensable component of lithium-ion batteries. Due to its physical position of being sandwiched between the cathode and anode, the electrolyte is in close interaction with both electrodes and thus significantly affects cell performance. When new electrode materials emerge, the need for compatible electrolytes usually arises. Conventional carbonate-based electrolyte has been used predominantly by the state-of-art lithium-ion battery industry; however, the flammability, and instability at low and high potentials pose specular challenges to wider applications, such as high voltage, energy and power batteries. With numerous advanced electrode materials emerging, the electrolyte must become more safe and stable without diminishing the cell electrochemical performance.

Among the efforts to develop novel electrolytes, utilization of additives is an efficient method to improve the cell performance and safety properties without significantly changing the electrolyte composition. Additives tend to work on the interphases, where most electrochemical reactions take place in the cell system. Whether or not these reactions proceed properly determines the cell performance and safety properties. By strengthening the interfaces, major improvements could be achieved in terms of cycle life, calendar life, and safety. Development of novel additives tailored to prolonged cell cycle life and improved safety is one of the most important goals of lithium-ion battery research.

Approach

The approach for development of a novel electrolyte and additives consists of three phases. The first phase is the screening of commercially available compounds by using density functional theory (DFT) and quick test procedures. DFT calculation can assess whether the candidates bear appropriate potential ranges (i.e. usually > 0.8 V vs. Li$^+$/Li), which is one important criterion of anode SEI additives. Due to a lack of understanding regarding the connections between chemical structures and cell performance, the screening process is based on trial and error. Empirical knowledge combined with such understanding can be used to generate screening candidates for quick evaluation. In this phase, some candidates will stand out with superior features. In the second phase, the promising candidates undergo thorough study and mechanism analysis to gain insights into their superior performance. Various techniques, including electrochemical analysis, spectroscopies, and computation and simulation, are utilized to gather as much information as possible about the connections between the chemical structures and the cell performance. In this phase, better understanding should be obtained in terms of how the chemical compounds work in the cell system. In the third phase, based on the knowledge earned, promising electrolytes and additives are proposed, and organic synthesis is conducted to make these compounds. Evaluations of the novel compounds gives feedback regarding our electrolyte designs, thus leading to modifications and even more new designs.

Results

Candidate list for SEI additives. Screening of promising candidates is regarded as one of the most efficient method for additive development. Rational criteria have to be established for generating the screening list. Degree of unsaturation (DU) is used as one criterion. DU usually means cyclic structure or double bonds, which are both considered as important components for constructing additive molecules due to their relative high reactivity. Some representative examples from previous studies prove this criterion is valid to some extent, including vinylene carbonate (VC), vinyl ethylene carbonate (VEC), 3,9-divinyl-2,4,8,10-tetraoxaspiro[5,5] undecane (TOS), lithium bis(oxalato)borate (LiBOB), and lithium oxalyldifluoroborate (LiODFB). Increased DU usually means that more cyclic and double bond structures are available during the film formation process and more readily to form a more crosslinking or a stronger polymer passivation layer. Other considerations for building novel additives include redox properties, polymer propagation, and coordination behavior.

Based on that simple guidance, we are able to generate a growing screening list and some of them are shown in Figure IV - 143. From additive 1 to additive 47,

the DUs are increased to incorporate more active structure components. In addition, some redox active elements, such as phosphor III in additive 47, are also included to build additives tailored to cathode material.

The screening list keeps growing and more related factors are taken into account.
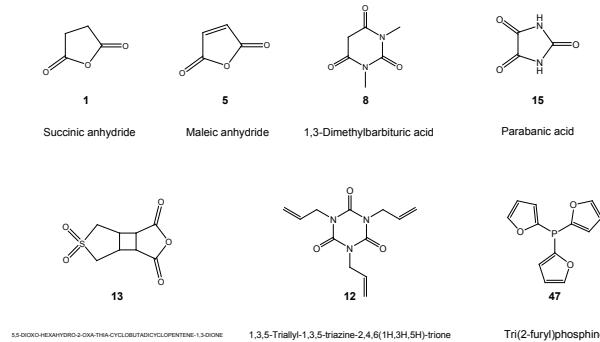
Figure IV - 143: Representative examples of screening list.

Mechanism discussion: 3-Oxabicyclo[3.1.0]hexane-2,4-dione (OHD). OHD was proved as a good anode SEI additive with attractive features, such as improved cycle life and controlled impedance increase when tested in cells. To further understand how OHD worked in the cell system, extensive characterizations have been conducted using FTIR, SEM, and XPS. Figure IV - 144 shows the FTIR spectra of MCMB electrodes harvested from cells containing no or different amount of OHD additive. All the spectra have some common peaks such as 1758cm^{-1}, 1396 cm^{-1}, 1301 cm^{-1}. 1758cm^{-1} peaks can be attributed to the C=O stretch of the carbonate groups, and 1396 cm^{-1} and 1301 cm^{-1} peaks are from C-H bend of alkanes groups. However, peak shifts and changes are also observed when OHD amount changes. For instance, in the gen 2 electrolyte sample with no OHD, 1622 cm-1 peak was observed, which should be attributed to the C=C stretch. As OHD increased to 0.2w% and 1.0 w%, this peak was dramatically depressed, and a new peak at 1557 cm^{-1} showed up and became stronger. The new peak is also in the range of C=C stretch but with lower wavenumber. Similar trend was also observed at the peak of 1301 cm^{-1}, which can be attributed to C-O stretch. This peak decreased significantly as OHD was added, implying the decreased component of ether structure in SEI layer as OHD increased. The peak of 1150 cm-1, which is also in the range of C-O stretch, however, is a new peak observed in OHD samples evolving from the peak of 1186 cm^{-1} in the gen 2 sample. All those changes clearly propose that with the addition of OHD, the structural components of SEI lay are changed, especially for C=O and C-O structures.
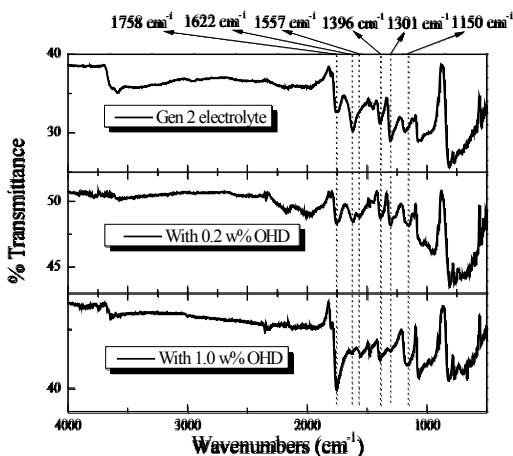
Figure IV - 144: FTIR spectra of MCMB electrodes obtained from MCMB/NCM coin cells containing different amounts of OHD in electrolyte of 1.2M LiPF$_6$ with EC/DEC (3:7 weight ratio) after formation cycles.

Figure IV - 145 shows SEM images of MCMB and NCM electrodes harvested from cells after formation cycles containing different amount of OHD. Image B is of MCMB electrode with 0.2w% OHD, compared with image A, the one with no additive, no noticeable difference can be observed, which is consistent with the impedance results. However, image C with 1.0w% OHD does show different appearance. Compared to image A, the electrode surface of image C is covered with a thick SEI layer and has less porosity, which is consistent with the much increased impedance result. On the other hand, the images of NCM with different amount of OHD have no obvious difference, indicating less impact on the impedance increase on cathode surface.
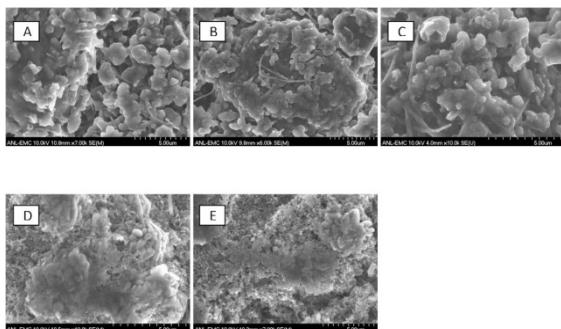
Figure IV - 145: SEM images of electrodes harvested after formation cycles. (a) MCMB electrode from Gen 2 electrolyte; (b) MCMB electrode from Gen2 electrolyte with 0.2 w% OHD; (c) MCMB electrode from Gen2 electrolyte with 1.0w% OHD; (d) NCM electrode from Gen2 electrolyte; (d) NCM electrode from Gem 2 electrolyte with 0.2 w% OHD.

Tri(2-furyl)phosphine: novel additive working on anode and cathode. Tri(2-furyl)phosphine (TPP) was evaluated as a promising electrolyte additive for both anode and cathode application. TPP is built on a phosphor III center, which is regarded as an easy oxidative site to form passivation film on cathode. On the other hand, the

incorporated furyl groups tend to reduce on the anode surface. Therefore, depending on specific SOC status, TPP can function as either anode or cathode additive or even both.

As shown in Figure IV - 146, TPP shows additional peak in the capacity differential profiles, compared to the one of gen 2 electrolyte, indicating that TPP did participate in the SEI formation process.
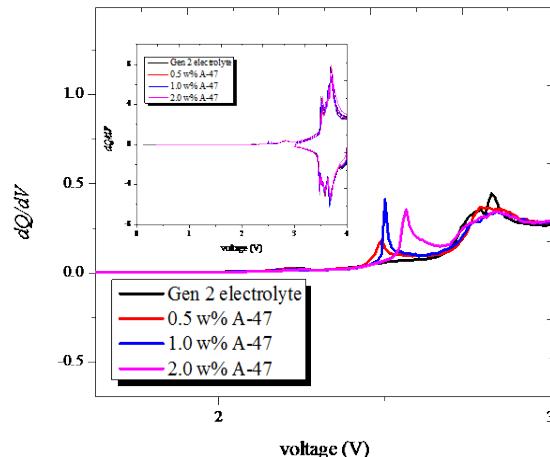
Figure IV - 146: Diff. Capacity vs voltage MCMB/NCM coin cells in 3E7EMC/PF12 with none or various amount of TPP (A-47). The cells were cycled at 55 ◦C. The charge rate was C/10. The cut-off voltages were 3 ~ 4V.

Figure IV - 147 shows capacity retention profiles of cells containing no or various amount of TPP. Clearly, 0.5w% and 1.0w% of TPP gave better performance compared to straight Gen 2 or 2.ow% cells. The ac impedance profiles of the cells containing none or various amount of TPP before and after 200 cycles under 55°C at 1C rate shown in Figure IV - 148. As the amount increased, the impedance increased as well. When the amount reached 2.0 w%, the impedance nearly doubled the value of straight Gen2 electrolyte before 200 cycles and tripled after 200 cycles. The much increased impedance may imply the reason of no improvement observed in the capacity retention test at 2.0 w%
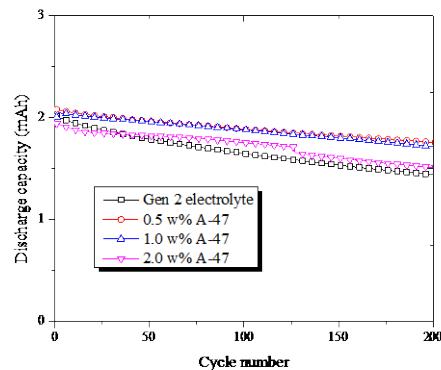
Figure IV - 147: Capacity retention of MCMB/NCM coin cells in 3E7EMC/PF12 with none or various amount of TPP (A-47). The cells were cycled at 55 ◦C. The charge rate was 1C. The cut-off voltages were 3~4 V.
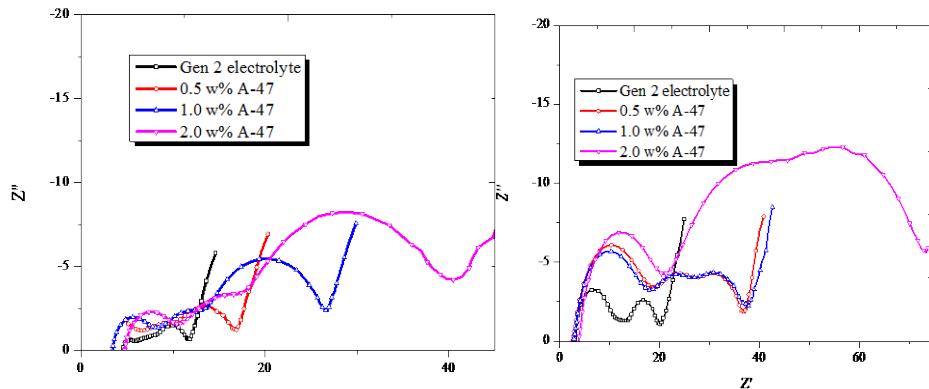
Figure IV - 148: AC impedance profiles of MCMB/NCM coin cells in 3E7EMC/PF12 with none or various amount of TPP (A-47) before (left) and after (right) 200 cycles under 55 °C at 1C rate. The cells were charged to 3.8 V. The charge rate was 1C.

Figure IV - 149 shows the cyclic voltammogram of 10 mM TPP in Gen 2 electrolyte. Fresh samples were scanned under both cathodic and anodic directions. For cathodic scan, a reduction peak was observed at 2.4 V vs Li^+/Li, indicating TPP's readily reduction. For anodic direction, a huge peak was observed at around 4.2 V, which may imply TPP could also react on the cathode side to help form passivation film.
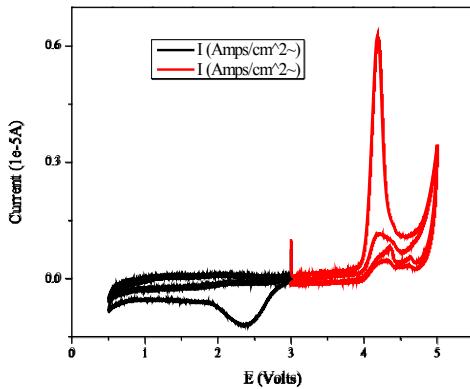
Figure IV - 149: Cyclic voltammetry profile 10mM TPP in Gen 2 electrolyte using Pt/Li/Li three electrode system. Scan rate is 100 mV/s.

Additive working on cathode side. Due to the strong electron negativity of lithium, additives are readily to reduce on the anode surface. However, compared to the reduction process, oxidation reactions on the cathode surface are less favorable for the additives to take place. In addition, unlike the anode SEI study, little extensive research efforts have been put into this field and therefore not much literature study can be referred to for initial study. Two strategies were proposed by us to set off the initial cathode additive study: first, coordination chemistry or supramolecular chemistry will be used to engineer additive molecules to control the solvation behavior in the cell system, in order to control the electrochemical behavior. Second, functional groups that are easy to

oxidize will be used to construct additives for cathode materials. One example is shown here:

PDP (A-45) was built on the reductive center, thus is easy to oxidize. As shown in Figure IV - 150, PDP shows a huge oxidation peak at around 4.0 V vs Li^+/Li, which can function as a formation trigger. Figure IV - 151 indicates the capacity profiles of half cells containing none or 1 wt % PDP. Clearly, the cell with PDP has a better capacity retention profiles and can survive nearly 70 cycles without obvious fading. However, the cell with no PDP only cycled for 40 cycles. The results indicate that PDP could be a promising cathode additive for high voltage cell system.
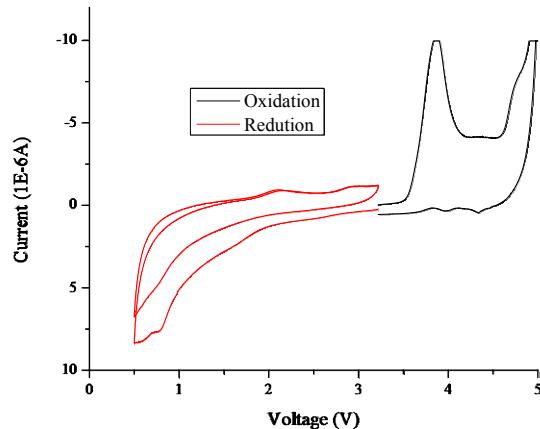
Figure IV - 150: Cyclic voltammetry profile 10mM PDP in Gen 2 electroylte using Pt/Li/Li three electrode system. Scan rate is 100 mV/s.

Figure IV - 151: Capacity retention of Li/LNMO coin cells in 3E7EMC/PF12 with none or 1 wt % additives. The cells were cycled at room temperature. The charge rate was C/5 (1mA). The cut-off voltages were 3.5 ~ 4.95 V.

Conclusions and Future Directions

We have established a growing screening list based on empirical and experimental experience, as well as theoretical computation. Many factors have been taken into account to make the screening list more diverse and promising.

ODB, as an established example, has been fully characterized using various techniques, including spectroscopies, theoretical analysis and microscopies. As identified, ODB forms passivation film very efficiently on the anode surface, and the film resistance is very much related to the amount of additive.

TPP, a novel additive, showed promising results in terms of capacity retention and impedance control. In addition, TPP shows both reduction and oxidation potentials that could be used to trigger the film formation process. This may lead to a new series of bifunctional additives.

PDP, as another example, shows clear oxidation peak in cyclic voltammetry result, which make it a good candidate for cathode additive. Preliminary cell test results showed that PDP does have positive impact on the cathode interface stabilization, which leads to improved cell capacity retention. Further study is ongoing to explore more possibilities using this kind of additive for high voltage cathode system.

FY 2012 Publications/Presentations

1. Lu Zhang, Zhengcheng Zhang, Paul C. Redfern, Larry A. Curtiss, and Khalil Amine, "Molecular engineering towards safer lithium-ion batteries: a highly stable and compatible redox shuttle for overcharge protection", Energy & Environmental Science, DOI: 10.1039/C2EE21977H.

2. Lu Zhang, Zhengcheng Zhang, Huiming Wu, and Khalil Amine, "Novel Redox Shuttle Additive for High Voltage Cathode Materials: Tetraethyl 2,5-di-tert-Butyl-1,4-Phenylene Diphosphate", Energy & Eviromental Science, 2011,4, 2858-2862.

3. Lithium Ion Batteries - New Developments, Chapter 7, Redox Shuttle Additives for Lithium-Ion Battery, Published on: 2012-02-24. Authors: Lu Zhang, Zhengcheng Zhang and Khalil Amine.

4. Zhang, Lu; Zhang, Zhengcheng; Amine, Khalil "Recent Development of Redox Shuttles for Li Ion Batteries at Argonne National Laboratory", invited talk, THE 29TH INTERNATIONAL BATTERY SEMINAR & EXHIBIT, March 12 - 15, 2012, Fort Lauderdale, Florida.

5. Zhang, Lu; Zhang, Zhengcheng; Amine, Khalil, "Redox shuttles for overcharge protection of lithium-ion batteries", Oral presentation, 221st ECS Meeting in Seattle, Washington.

6. Zhang, Zhengcheng; Zhang, Lu; Kyrrilos Youssef; and Amine, Khalil "Advanced Electrolyte Additives for PHEV/EV Lithium-ion Battery", ES025, DOE ABR annual merit meeting, Washington D. C., May 14th~18th, 2012.

7. Zhang, Zhengcheng; Zhang, Lu; Libo Hu, Kyrrilos Youssef; and Amine, Khalil. 6th International Forum on Lithium-ion Battery Technology and Industry development, Invited Talk, September 19th -20th, 2011, Beijing, China.

8. Zhang, Zhengcheng; Libo Hu, Zhang, Lu; Wei Weng and Amine, Khalil. EV Battery Tech USA 2011, September 27th-28th, Invited Talk, Troy, MI, USA.

9. Zhang, Zhengcheng; Libo Hu, Zhang, Lu; Wei Weng and Amine, Khalil. Advanced Electrolyte and Electrolyte Additive for lithium ion batteries, invited talk on 4th International Conference on Advanced Lithium Batteries for Automotive Application (ABAA-4), Sep. 20-23, 2011, Beijing, China.

10. Zhang, Zhengcheng; Huiming Wu, Amine, Khalil. Advanced Battery Materials for EV Applications, invited talk on EV Battery Tech: 5th Global Cost Reduction Initiative, Feb. 28-29, 2012 London, United Kingdom.

11. "Functional Electrolyte for Lithium-Ion Battery", (internal # ANL-IN-12-023).

12. "Non-Aqueous Electrolyte for Lithium-Ion Batteries", (internal # ANL-IN-12-022).

IV.B.5.2 High Voltage Electrolyte for Lithium-ion Battery (ANL)

Zhengcheng Zhang

Argonne National Laboratory
9700 South Cass Avenue
Argonne, IL 60439-4837
Phone: (630) 252-7868; Fax: (630) 972-4440
E-mail: zzhang@anl.gov

Collaborators:
Libo Hu, Argonne National Laboratory
Wei Weng, Argonne National Laboratory
Larry Curtiss, Argonne National Laboratory
Richard Jow, US Army Research Laboratory
Daikin America, Ltd.

Start Date: October 2010 (New Project)
Projected End Date: September 2012 (last report)

Objectives

The objective of this work is to develop an electrolyte with wide electrochemical window that can provide stable cycling performance for cathode materials that can be charged above 4.5 V vs Li^+/Li.

Technical Barriers

A primary technical barrier to the development of a safe and cost-effective PHEV battery with a 40 mile all-electric range that meets or exceeds all performance goals is the availability of a suitable high voltage electrolyte. The energy density of the battery can be increased by using high voltage and high capacity cathode materials. However, the conventional electrolyte does not meet the requirement for normal operation of these batteries especially under harsh conditions. Poor electrochemical stability is one of the drawbacks of the conventional electrolyte which tends to decomposes on the surface of the charged electrode, especially by oxidative decomposition on the cathode surface above 4.5V.

Technical Targets

The technical target of this project is to develop an electrolyte system which can meet the operation requirement for the high energy density lithium-ion battery system for PHEV/HEV applications. The new electrolyte will meet the following requirements:

- Wide electrochemical window (>5 V Li^+/Li).
- High ionic conductivity (>10^{-3} S/cm, high power).
- High thermal stability (abuse tolerance).

- Non-flammability (improved safety).
- Solid electrolyte interphase formation capability (extended life).

Accomplishments

- New material synthesis and purification, December, 2011 (Complete)
- Physical properties of the new high voltage electrolyte candidates, February, 2012 (Complete)
- Electrochemical stability evaluation, April, 2012 (Complete)
- Material evaluation in the LTO cell system, June, 2012 (Complete)
- Material evaluation in graphite cell system, September, 2012 (Complete)

✧ ✧ ✧ ✧ ✧

Introduction

The lithium-ion battery is an ideal power source for electrified vehicles due to its long cycle life and high energy and power density. To further increase the energy density, the general approach is to use cathode materials with high operating voltages (5 V vs. Li^+/Li) and high specific capacity (250 mAh/g). Tremendous attention has been paid to raising the specific capacity and the discharge voltage of the cathode materials. For example, two-Li+-ion material such as silicate Li_2FeSiO_4 and fluorophosphate Li_2FePO_4F have been proposed and investigated as high capacity cathodes. Very few efforts have been dedicated to the development of improved performance electrolytes including the high voltage solvents. The state-of-the-art electrolyte is a non-aqueous solution of a lithium salt ($LiPF_6$) dissolved in a carbonate solvent mixture such as ethylene carbonate and diethyl carbonate. However, these carbonate solvents are organic chemicals, which are very flammable and can be oxidatively cleaved into gaseous products at a potential between $4.5 \sim 5.0$V vs Li^+/Li. A high voltage electrolyte is in urgent need to meet the requirement for the high energy density of lithium ion battery for PHEV application.

Approach

The approach for the high voltage electrolyte activity is to develop an electrolyte system suitable for cathode materials that can be charged to higher potentials (>4.5V vs Li^+/Li) based on the previous experiences of electrolyte development. The first stage of the research is to select a LTO anode coupled with

5V spinel LNMO cathode to demonstrate the anti-oxidation capability of the solvents other than the non-carbonate solvents.

The final stage of the research will be focused on the graphite anode coupled with the high voltage cathode to gain the practical energy density. This stage is a continuation for the solvents discovered in the first stage in LMO/LTO cell and further explores the applicability in LMO/graphite chemistry. Tailored electrolyte additive is proposed to address the electrode especially the graphite anode surface reaction with the electrolyte to form solid electrolyte interphase film.

Results

Calculations of the new fluorinated electrolytes for the highest occupied molecular orbital (HOMO) and lowest unoccupied molecular orbital (LUMO) energy with the B3LYP/6-311+G(3df,2p) basis set are included in Table IV - 9, since it has been shown that B3LYP HOMO and LUMO energies can be successfully correlated with molecular properties such as ionization potential and electron affinity in a semiquantitative manner.

Based on the DFT results shown in Table IV - 9, fluorine substitution in organic carbonate and ether lowers both HOMO and LUMO levels, resulting in simultaneously higher oxidation stability and higher reduction potential. The results also indicate that the fluorinated electrolytes are thermodynamically more stable than their non-fluorinated counterparts under certain high voltage conditions.

It is worth noting that the oxidation potential of the linear carbonate EMC can be greatly increased, from 6.63 V to 7.01 V, through fluorine substitution (Table IV - 9). The calculated oxidation potentials of the fluorinated carbonates and ether are much higher compared with other high voltage electrolytes. Shao and coworkers reported the oxidation potential of ethyl methyl sulfone, calculated with DFT method, to be around 6.0 V.

Table IV - 9: Theoretical Oxidation and Reduction Potential of Some Fluorinated Carbonate Solvents.

Code Name	Chemical Structure	P_{ox} / V	P_{red} / V
EC		6.91	1.43
PC		6.80	1.35
EMC		6.63	1.30
FCC-1		6.97	1.69
FEC		7.16	1.63
FCC-3		6.93	1.50
FLC-1		7.10	1.58
FE-1		7.29	1.82

To investigate the stability of the various electrolytes against oxidation under high voltage conditions, one conventional electrolyte and six new fluorinated electrolytes were formulated as follows: 1.2M LiPF$_6$ EC/EMC 3/7-Gen2, 1.2 M LiPF$_6$ in EC/EMC/FE-1 2/6/2-E1, 1.2 M LiPF$_6$ in EC/EMC/FE-1 2/5/3-E2, 1.2 M LiPF$_6$ in FCC-1/EMC/FE-1 2/6/2-E3, 1.2 M LiPF$_6$ in FCC-1/EC/EMC/FE-1 1/1/6/2-E4, 1.2 M LiPF$_6$ in FCC-1/FLC-1/FE-1 2/6/2-E5, 1.2 M LiPF$_6$ in EC/FLC-1/FE-1 2/6/2-

E6. The ambient conductivities of these fluorinated electrolytes are comparable with the Gen2 electrolyte. Figure IV - 152 is the summary of the leakage current in a floating test using Pt/Li/Li electrochemical cell. At 5.7 V, the fluorinated carbonate electrolyte showed much smaller leakage current than Gen2, the traditional electrolyte, indicating the improved voltage tolerance of the fluorinated one.
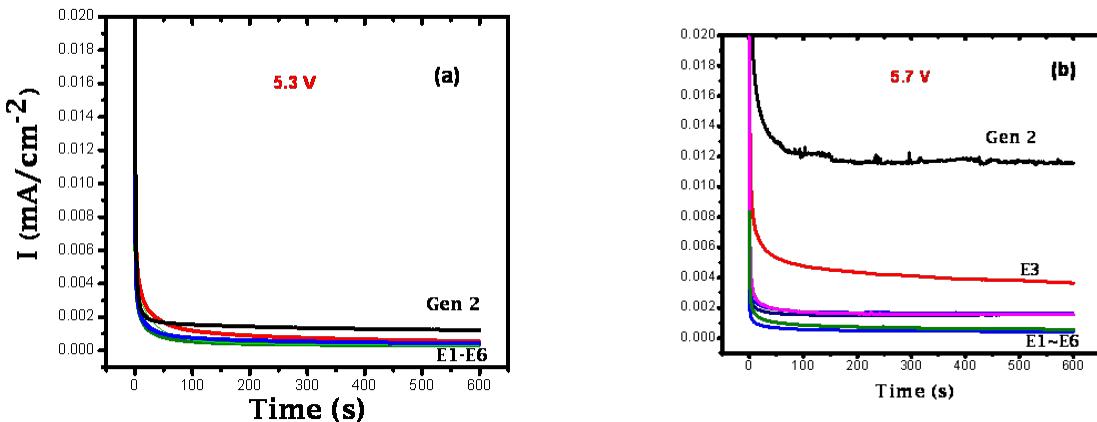
Figure IV - 152: Gen2 electrolyte and fluorinated electrolyte leakage currents at various potentials with Pt/Li/Li cell.

To further confirm the improved voltage stability, a high voltage cell (LNMO/Li) was used to conduct the floating test and the test results are summarized in Figure IV - 153. At 5.3V, the leakage current of

fluorinated electrolyte is only about 25% of that of Gen2 electrolyte. This test is agreed well with LNMO/LTO cell performance reported in our last quarter.

* (1) Working electrode: LiNi$_{0.5}$Mn$_{1.5}$O$_4$ /Carbon Black/Binder: 84%/8%/8% in weight
   (2) Electrode disc area: 1.6cm^2
   (3) Reference electrode: Li metal
   (4) CC-CV charge the LNMO/Li cell with C/10 rate to 5.0V, 5.1V, 5.2V and 5.3V, respectively.
   Maintain at each voltage for 10h to observe the leakage current.
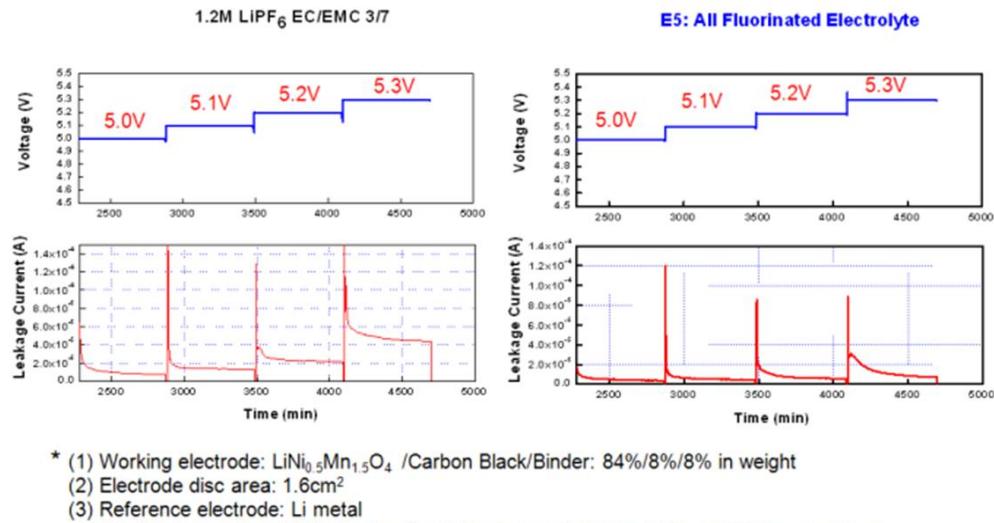
Figure IV - 153: Gen2 electrolyte and fluorinated electrolyte leakage currents at various potentials with LNMO/Li cell.

The first cyclic voltammetry scan of LNMO/graphite cell with new formulated fluorinated electrolytes is shown in Figure IV - 154. Electrolyte E1 and E4 showed more symmetrical redox curves than electrolyte E2 and E5, indicating the different SEI formation process.
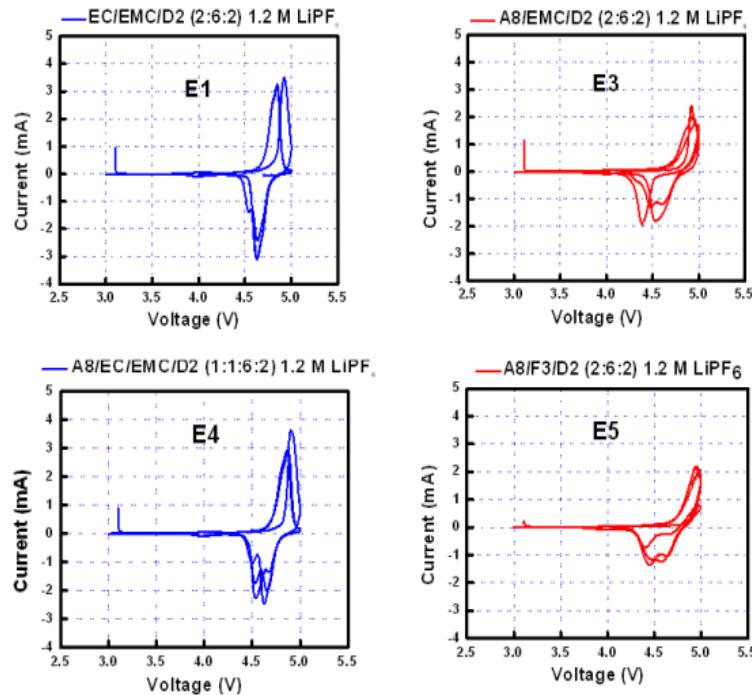
Figure IV - 154: Cyclic voltammetry profiles of LNMO/graphite cells using fluorinated electrolytes.

As evidenced from the cycling data shown in Figure IV - 155(a), electrolyte E5 has a very low initial charge and discharge capacity and a fading cycling performance indicating a poor SEI formation with continuous Li consuming side reaction occurring on the graphite abode. Among the fluorinated electrolytes, E1 showed the best compatibility with 5V LNNO and graphite electrode (Figure IV - 154). It is speculated that EC component in E1 electrolyte formulation accounts for the SEI formation while FE-1 provides voltage stability and surface wetting. This formulation also cycles better than Gen2 electrolyte at room temperature (Figure IV - 155 (b)).
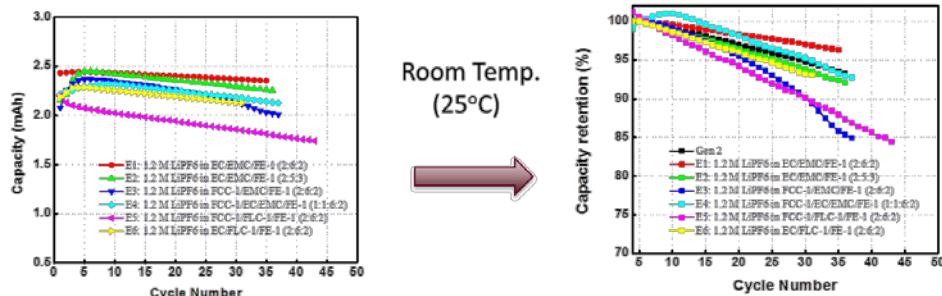
Figure IV - 155: LNMO/Graphite cell cycling profiles at room temperature (a) and the cycling performance using fluorinated electrolytes (b) Normalized capacity retention of fluorinated electrolyte and Gen2. Cycling rate is C/10, cutoff voltage is 3.5-4.9 V.

The ambient cycling performance of the E1, E2, E4 fluorinated electrolytes showed improved cyclability, however at high temperature, their performance getting worse, indicating the instability of the SEI layers (Figure IV - 156). E4's formulation includes EC, which is good for SEI formation, and FCC-1, FLC-1 and FE-1, which are all high voltage solvent and additives. This quarter's research clearly indicates that we need to develop the integrated SEI formation additive for this new electrolyte system.
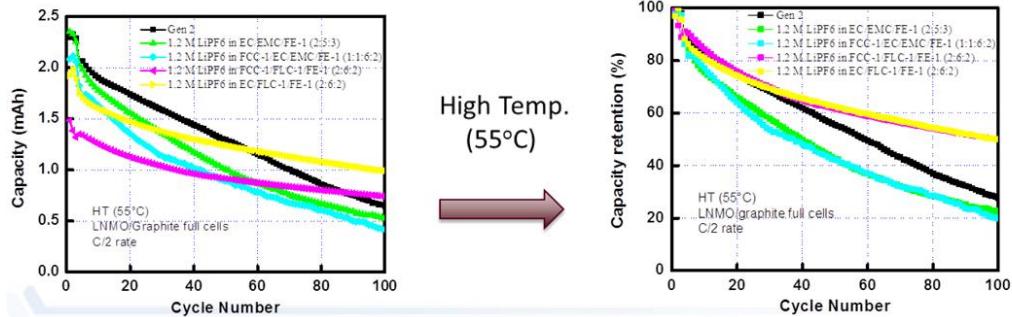
Figure IV - 156: LNMO/Graphite cell cycling profiles at 55°C(a) and the cycling performance using fluorinated electrolytes (b) Normalized capacity retention of fluorinated electrolyte and Gen2. Cycling rate is C/10, cutoff voltage is 3.5-4.9 V.

Previous study using LTO/LNMO system suggested that the electrolyte E5 which used all fluorinated components FCC-1, FLC-1 and FE-1 is the most stable on the LNMO cathode surface. However, when used in a graphite cell, E5 electrolyte showed inferior performance than Gen 2 electrolyte, suggesting the possible inability of FCC-1 to form stable SEI. To test this theory, Li/A12 anode half cells with different electrolytes were made to study the SEI formation of these electrolytes.

The dQ/dV data of the high voltage electrolytes compared with Gen 2 electrolyte were summarized in Figure IV - 157. The electrolytes that employed EC as the cyclic carbonate such as E1 and E6 all show similar SEI formation peaks as Gen 2 does at around 0.6 V. However,

when EC was substituted with FCC-1 as in E5 and E3, the peaks were either gone or shifted to a lower potential. When EC was reintroduced into the system as in E4, the peaks reappeared but to a lesser intensity. All these data point out that FCC-1 is unable to form stable SEI. The inability of FCC-1 to form a stable SEI explains the poor performance of E5 in A12/LNMO full cells in comparison with its excellent performance in LTO/LNMO full cells where no SEI is needed. In a more interesting case, when EC was substituted with FEC, the SEI formation peak shifted to a much higher potential at around 1.0 V, which suggests a more stable SEI was formed.
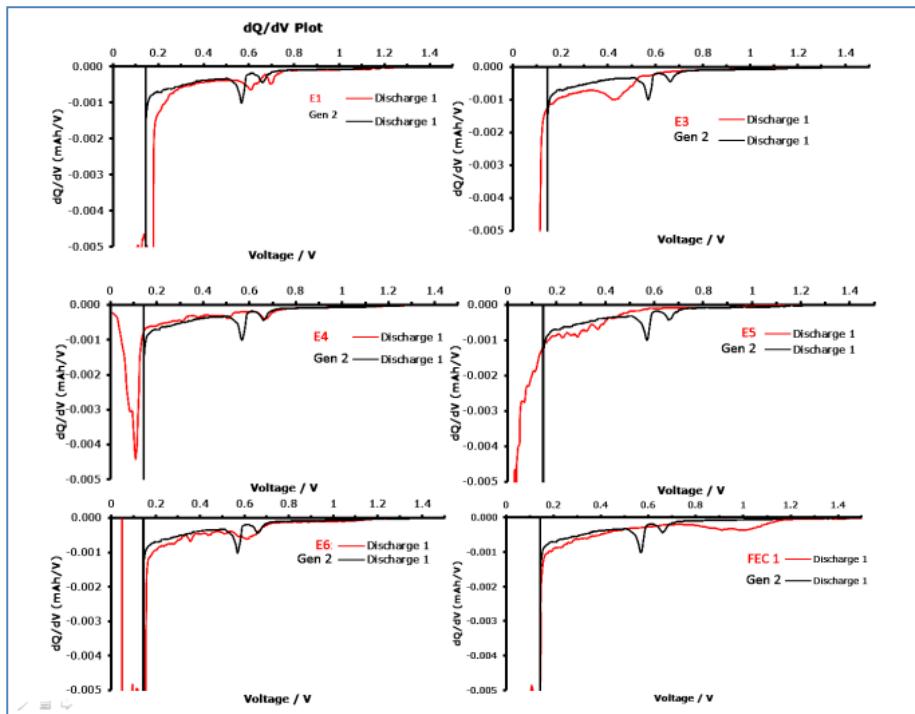
Figure IV - 157: dQ/dV plots of Gen2 electrolyte compared with fluorinated electrolytes.

Conclusions and Future Directions

Fluorinated carbonate and ether compounds were developed as high voltage electrolyte. These new electrolyte showed excellent voltage stability and good cycling performance at elevated temperature.

When cycled between 2.0~3.45 V, the LNMO/LTO showed good cycle stability at room temperature and at 55°C with a capacity loss less than 4% at 200 cycles. These preliminary data indicated that the fluorinated electrolytes have potential use for high voltage cathode materials especially under harsh conditions.

Future direction will be focused on the new additive development for the fluorinated electrolyte to further improve the cell performance both in graphite based high voltage cathode cells.

FY 2012 Publications/Presentations

1. 2012 DOE Annual Peer Review Meeting Presentation, May, 2012, Washington DC, USA.
2. DOE-USABC Electrolyte Workshop, Invited Presentation, August, 18th -19th, 2011, Southfield, MI, USA.
3. 6th International Forum on Lithium-ion Battery Technology and Industry development, Invited Talk, September 19th -20th, 2011, Beijing, China.
4. EV Battery Tech USA 2011, September 27th-28th, Invited Talk, Troy, MI, USA.
5. Argonne-Daikin Joint Workshop on High Voltage Electrolyte, Feb. 25, 2012.
6. Electrolyte for electrochemical cells. US patent application ANL-IN-09-039.
7. Advanced Electrolyte and Electrolyte Additive for lithium ion batteries, invited talk on 4th International Conference on Advanced Lithium Batteries for Automotive Application (ABAA-4), Sep. 20-23, 2011, Beijing, China.
8. Advanced Battery Materials for EV Applications, invited talk on EV Battery Tech: 5th Global Cost Reduction Initiative, Feb. 28-29, 2012 London, United Kingdom.
9. Fluorinated High Voltage Electrolyte for 5V Lithium Ion Battery. Manuscript submitted.
10. Voltage stability of carbonate based electrolytes. Manuscript submitted.
11. High voltage electrolyte, patent application, ANL-IN-12-084.

IV.B.5.3 High Voltage Electrolytes for Li-ion Batteries (ARL)

Kang Xu, Arthur von Cresce, Jan L. Allen, Oleg Borodin, Wishvender Behl, Janet Ho, T. Richard Jow

Point of Contact:
T. Richard Jow / Kang Xu
U.S. Army Research Laboratory
2800 Powder Mill Road
Adelphi, MD 20783
Phone: (301) 394-0340 / (301) 394-0321
Fax: (301) 394-0273
E-mail: t.r.jow.civ@mail.mil
              conrad.k.xu.civ@mail.mil

Objectives

- Develop high voltage electrolytes that enable high voltage cathode chemistries for plug-in hybrid electric vehicles (PHEV).

Technical Barriers

This project addresses the following technical barriers of today's Li-ion batteries:

- SOA electrolytes does not support chemistries beyond 4.5 V;

- New electrolyte solvents, such as sulfones and nitriles, although remain stable at high voltages on cathode, fail to cater anode SEI needs simultaneously.

- Replacing SOA carbonates with highly fluorinated solvents drives up the overall cost.

- Lack of reliable 5 V cathodes as testing vehicles for electrolyte development.

Technical Targets

- Design and synthesize new electrolyte additives that target the interphasial chemistry on high voltage cathode surfaces.

- Understand the mechanism of interphase formation on high voltage cathode surfaces.

- Evaluate the additives containing electrolytes using 4.6 V $LiNi_{0.5}Mn_{1.5}O_4$ and 4.8 V $LiCoPO_4$ as testing vehicles.

Accomplishments

- Continued to confirm performance of tris(hexafluoroisopropyl) phosphate, HFiP, in different electrochemical environment:

  - in cathode half cells using 4.6 V $LiNi_{0.5}Mn_{1.5}O_4$ or 4.8 V $LiCoPO_4$; in full Li ion cells using 4.6 V $LiNi_{0.5}Mn_{1.5}O_4$ and A12 Graphite

- Analyzed the break-down mechanism of HFiP on cathode surface

  - Identified the key-ingredients responsible for cathode/electrolyte interface protection

- Continued to perfect structures of the fluorinated electrolyte additives:

  - Synthesized 5 new additives, 4 of which are perfluorinated;

  - Synthesized Al- and B-based additives;

  - Measured their preliminary electrochemical properties on various electrode surfaces

- Computed intrinsic oxidative stability of additives in implicit solvent using polarized continuum model (PCM).

- Investigated oxidative and reductive stability of additives in $LiPF_6$ in EC-EMC experimentally using linear voltammetry.

- Continued the development of stabilized $LiCoPO_4$ cathode and its compatible electrolytes.

✧   ✧   ✧   ✧   ✧

Introduction

In order for 5 V class cathode chemistries such as $LiNi_{0.5}Mn_{1.5}O_4$ (LMNO) and $LiCoPO_4$ (LCP) to be used for HEV/PHEV/EV applications, electrolytes must maintain kinetic stability beyond 4.5 V. Despite the developments of new electrolyte solvents that were claimed to be able to support the above chemistries, the accompanying intrinsic weaknesses often make the effort impractical, such as the instability of sulfone and nitriles on graphitic anode, or the high cost of highly-fluorinated co-solvents FEC or D2. We believe that by using properly-designed electrolyte additives the above intrinsic weaknesses could be circumvented, as our previous work on tris(hexafluoro-iso-propyl)phosphate (HFiP) demonstrated.

This year's work focused on further confirmation of HFiP on different cathode chemistries, surface analysis of these cathodes for understanding of HFiP breakdown mechanism, as well as design and synthesis of new additives with perfected structures. Computational assistance was also employed to understand the thermodynamic oxidation of these new additives.

Approach

Instead of replacing bulk carbonate solvents, our approach leverages the use of surface-modifying additives, so that most of the intrinsic weaknesses of using new solvents, such as poor SEI on anode and high cost, could be circumvented. The core tasks are the design and synthesis of new additives that can effectively deliver the desired species to the cathode surface.

Results

Further confirmation and understanding of HFiP (Cresce, Xu). HFiP-based electrolytes were formulated using the skeleton formulation of Gen 2 electrolyte, i.e., 1.0 M LiPF$_6$ in EC/EMC 30:70. LMNO from various sources (courtesy of Argonne National Lab, Rutgers University and University of Texas-Austin) and LCFP from ARL (courtesy of Dr. J. Allen) were used as testing platforms. After evaluation of HFiP at different concentration levels, it was determined that the optimum content of HFiP is between 5~10 mM for ANL and UT-Austin LMNO cathodes, while higher concentration (1%) is needed for high surface area cathodes such as Rutgers LMNO or ARL LCFP. Test results of LCFP are reported in a later section. Figure IV - 158 summarized some of the tests.
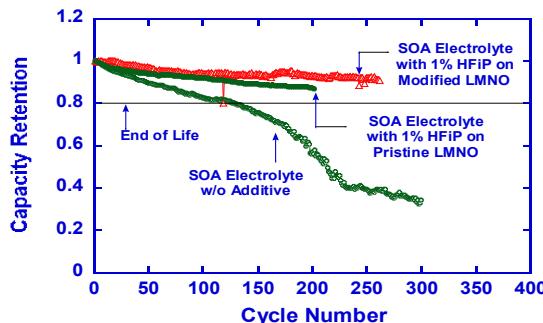
Figure IV - 158: Capacity as a function of cycle number plots at room temperature LMNO half cells in 1 m LiPF$_6$/EC:EMC (30:70) with HFiP. Baseline electrolyte was also used as benchmark.

Full Li-ion cells using ANL LMNO and A12 graphite anode were also constructed, both at ARL and at our industry partner's lab. The benefits of HFiP-based electrolytes were confirmed, in terms of longer cycle-life, lower impedance and better rate-capability of the latter. Figure IV - 159 shows the results from our industry partner on full Li ion cells.

It is of great significance to understand how HFiP work on cathode surface. Especially when we need to design better additives with improved structures, we want to know whether the phosphate or the fluorinated alkyl moieties serve as the active ingredients (Figure IV - 160a).
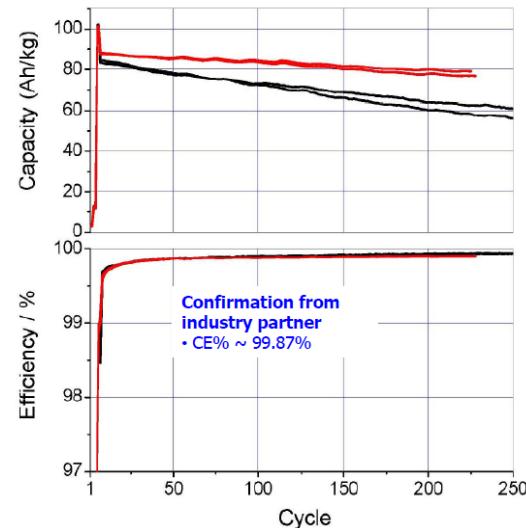
Figure IV - 159: Capacity as a function of cycle number plots at room temperature LMNO/A12 full Li ion cells in 1 m LiPF$_6$/EC:EMC (30:70) with 5 mM HFiP. Baseline electrolyte was also used as benchmark.

However, due to its small presence in electrolyte, HFiP leaves only elusive traces on the electrode surfaces. With the help of high-resolution X-ray photoelectron Spectra (XPS), we were able to determine that fluorinated moieties might be the key-ingredient, while phosphate skeleton only functions as "delivering" system that breakdown at cathode surfaces under charged condition.
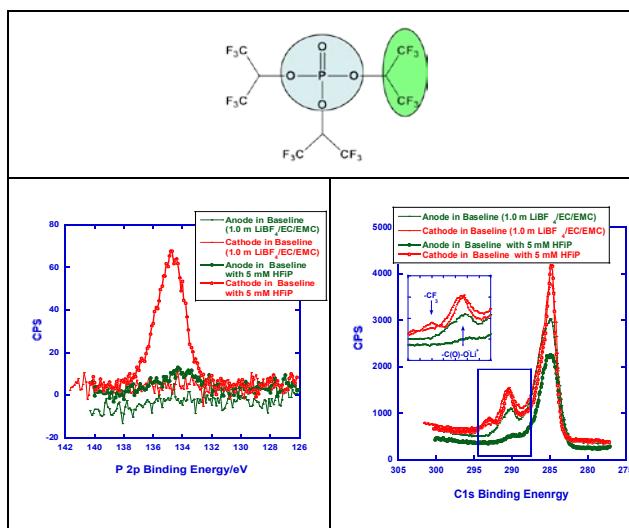
Figure IV - 160: Sub-structures of HFiP (a), and HR-XPS of cycled anode (b) and cathode (c) surfaces in baseline and HFiP-based electrolytes.

New Additives (Cresce, Ho, Xu). As Figure IV - 160 shows, the most conspicuous signature detected on cycled LMNO cathode is that from CF$_3$- functionality, while P-functionality can be found on both anode and cathode surfaces at very low concentrations.
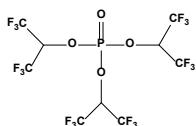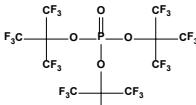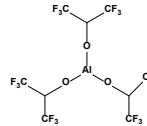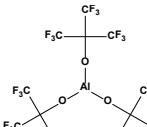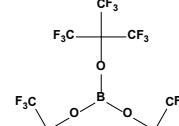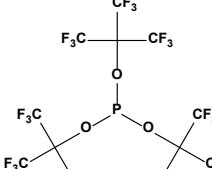
The analysis led us to the design of new additives with higher fluorination degree alkyl moieties and more effective "delivering" skeletons. Table IV - 10 summarized

the newly-synthesized additives, some of which are per-fluorinated to ensure an improved electrochemical performance. Most of these additives were characterized for their physical properties and chemical structures. Table IV - 10 and Figure IV - 161 showed selected results.

Interestingly, we noted that most of these additives have secondary relaxations similar to those of plastic crystals below the major melting transition, as indicated by the DSC traces.

Table IV - 10: Additives and Physical Properties.

Additive Acronyms	Structures	m.p.
HFiP		34
PFBP		144
Al(HFiP)₃		95~100
Al(PFB)₃		
B(PFB)₃		
PFBP-III		140
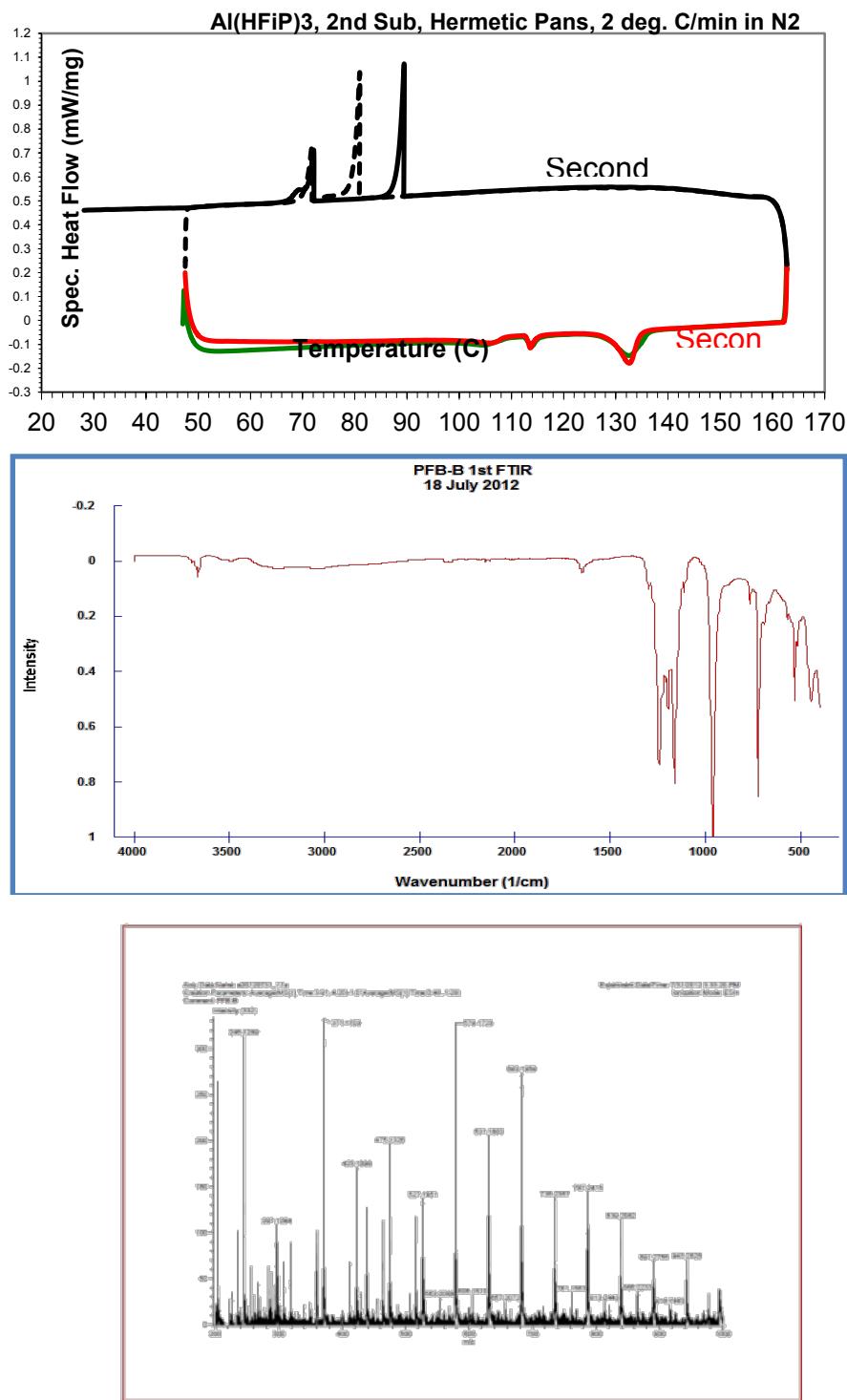
Figure IV - 161: DSC traces of Al(HFiP) (a); FTIR (b) and MS (c) of B(PFB)₃.

Preliminary tests of new additives (Cresce, Xu).
New electrolytes were formulated using these new additives, and currently we are actively testing these additives against high voltage cathode (ANL LMNO) in both half and full cells. Figure IV - 162 showed some selected results, where the perfluorinated additive PFBP demonstrated superior performance to that of HFiP. Newer

members of Table IV - 10 are still to be tested due to limited man-power and battery cycling resources in the lab. Meanwhile, after filing for IP protection, we also send out these additives to different academic and national labs to be tested on other new battery systems, such as Li/air, Li/S and Na ion etc.
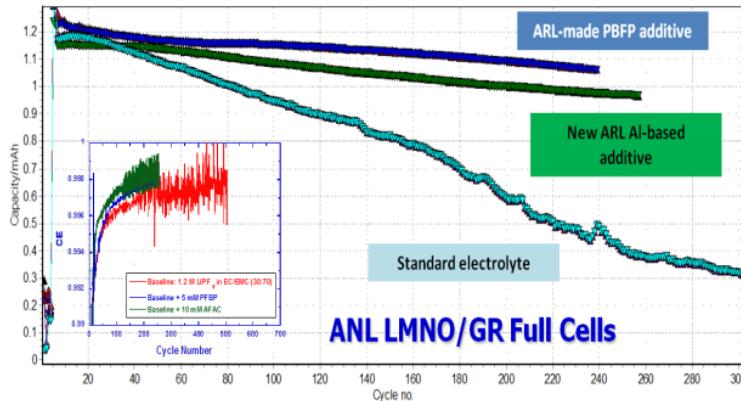
Figure IV - 162: Preliminary cycling results of electrolytes based on new additives in ANL LMNO/A12 full Li ion cells.

Oxidation Stability Limits of Additives (Borodin). Intrinsic oxidation potential was calculated for selected additives listed in Table IV - 11 using polarized continuum model PCM (ε=23). Fluorination of trimethyl phosphate $PO(OCH_3)_3 \rightarrow PO(OCF_3)_3$ increases its intrinsic oxidation potential by 1.4 V. HFiP and HFiAl additives have 0.2 -0.3 V lower intrinsic oxidative stability compared to f-TMP, while HFiB has the highest oxidative stability of 8.5 V among additives. Presence of fluorinated anions such as BF_4^- significantly decreases additive oxidative stability, for example, $HFiB/BF_4^-$ oxidative stability is 1.6 V lower than that of HFiB due to spontaneous fluorine transfer from BF_4^- to HFiB and B-O bond cleavage as shown in Figure IV - 163. Similarly, PF_6^- anion transferred F to HFiP and decreased stability of P-O bond. Thus, fluoro-containing anions and other nucleophilic groups influence oxidation stability of additives and their oxidation induced decomposition reactions [8-9]. Oxidation potentials of $HFiP/PF_6^-$ and $HFiB/BF_4^-$ are higher than oxidation potentials of carbonate/anion and EC_2 complexes [8-9], while reduction potentials of additives (HFiP, HFiAl) are higher than calculated and measured $(EC:PC)/LiPF_6$ [1]. Thus, preliminary DFT data indicates that additives preferentially get reduced during first charge cycle, decompose followed by oxidation of the decomposition fragments at the cathode instead of direct oxidation.

Table IV - 11: Oxidation ΔG^{ox} and reduction ΔG^{red} potential vs. Li$^+$/Li calculated with PCM(ε=23).

	ΔG^{ox} (V)	ΔG^{red} (V)
$PO(OCH_3)_3$ (TMP) [a]	6.9	
$PO(OCF_3)_3$ (f-TMP) [a]	8.3	1.7
$PO(OCH(CF_3)_2)_3$ (HFiP) [a]	8.1	1.5
$B(OCH(CF_3)2)_3$ (HFiB) [a]	8.5	0.2
HFiB/Li$^+$ [a]		0.6
$Al(OCH(CF_3)_2)_3$ (HFiAl) [a]	8.0	1.4
$B(OCH(CF_3)_2)_3/BF_4^-$ (HFiB/BF$_4^-$) [a]	6.9	
$(EC_nPC_m)/Li^+$, n+m=1 [b]		0.4-0.7 [b]

a) M05-2X/6-31+G**, b) LC-ωPBE/6-31+G**
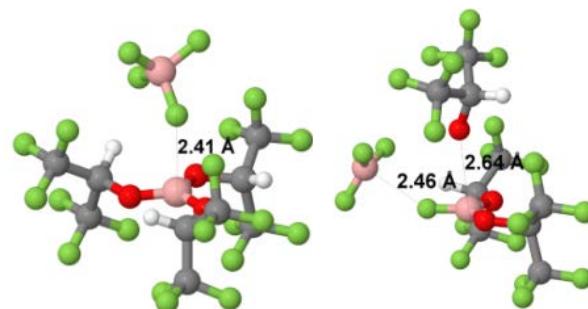
Figure IV - 163: Optimized geometry of HFiB/BF$_4^-$ complex before (a) and after (b) oxidation. From M05-2X/6-31+G** calculations with PCM(ε=23).

Oxidation Limits of EC (Borodin). The study of the oxidation induced decomposition of EC, EC_2 and EC_4 and decomposition products was completed using DFT, MP4 and G4 levels. The polarized continuum model (PCM) was used to implicitly include the rest of the surrounding solvent. The oxidation potentials of EC_2 and EC_4 were found to be significantly lower than the intrinsic oxidation potential of an isolated EC and also lower than the

oxidation potential of EC-BF$_4^-$. The exothermic proton abstraction from the ethylene group of EC by the carbonyl group of another EC was responsible for the decreased oxidative stability of EC$_2$ and EC$_4$ compared to EC. The most exothermic path with the smallest barrier for EC$_2$ oxidation yielded CO$_2$ and ethanol radical cation. The reaction paths with the higher barrier yielded oligo(ethylene carbonate) suggesting a pathway for the experimentally observed poly(ethylene carbonate) formation of EC-based electrolytes at cathodes surfaces. The decomposition products and oxidation potentials obtained from these calculations are summarized in [9].

Impact of HFiP on Oxidation and Reduction Limits of Baseline Electrolytes (Behl). The impact of HFiP on the oxidation and reduction limits of 1.2 M LiPF$_6$-EC:EMC electrolytes was also investigated using cyclic voltammetry technique. We observed almost identical cyclic voltammograms at glassy carbon electrodes at a scan rate of 10 mV/s in 1.2 M LiPF$_6$-EC-EMC (3:7) solutions with HFiP, in an amount of 0.28% for oxidative scans and without HFIP. Same CVs were observed in the baseline electrolyte with HFiP (1.7%) and without for the reductive scans.

Stabilized LiCoPO$_4$ (LCP) as Testing Vehicles for High Voltage Electrolytes (Allen). Substantial improvement in cycling LCP in 1.0 M LiPF$_6$ in EC:EMC (3:7) baseline electrolyte was achieved through doping Fe in LCP, Li$_{0.92}$Co$_{0.8}$Fe$_{0.2}$PO$_4$, or LCFP, alone. The use of HFiP in baseline electrolyte has no significant impact on the cycling of LCP. However, HFiP in baseline electrolyte improved the capacity retention of LCFP/Li half cells with 20% capacity loss in 500 cycles (see also *J. Power Sources*, 2011, 196, 8656–8661). The current efforts involve the scale-up of LCFP, fabrication of LCFP and other high voltage electrodes, assembly and test of full cells with different formulations of electrolytes containing additives.

Conclusions and Future Directions

Based on the achievements made in this year, we planned for FY 2013:

- Continue to test new additives synthesized on various test platforms.
- Support scale-up efforts at ANL.
- Formulate new electrolytes with multiple additives.
- Explore new electrolyte solvents such as sulfones and nitriles with the new additives.
- Characterize additives on cathode surfaces to further understand the mechanism, using advanced imaging techniques such as AFM.
- Leveraging more computational efforts for basic understanding of electrolyte/additive breakdown mechanism.

- Formulate high voltage electrolytes for LCFP, LNMO and other high voltage cathodes and test in full cells.

FY 2012 Publications/Presentations

Publications

1. "Correlating Li+-solvation sheath structure with interphasial chemistry", A. v. Cresce, O. Borodin, and K. Xu, to be published in *J. Phys. Chem. C.*
2. "Genetically Programming the Interfaces between Bio-templated Cathode Nano-particles and Current Collector in Li Ion Batteries", K. Xu, D. Oh, H. Yi, J. Qi, A. Xu, J. Snyder, and A. Belcher, *ECS Trans.*, **2012**, *41*, 55~64.
3. "Tailoring an Ideal Interphases for Faster Li Ion Transport with Ionic Additives", J. Ho, and K. Xu, *ECS Trans.*, **2012**, *41*, 159~166.
4. "Li+-Solvation Structures Directs Interphasial Processes at Graphitic Anodes", K. Xu, and A. v. Cresce, *ECS Trans.*, **2012**, *41*, 187~193.
5. "Phosphate-based compounds as additives for 5-volt lithium ion electrolytes", A. v. Cresce, and K. Xu, *ECS Trans.,* **2012**, *41*, 17~22.
6. "Li+-solvation/desolvation dictates Interphasial Process at Graphitic Anode in Li Ion Cells", K. Xu, and A. v. Cresce, **invited contribution** to *J. Mater. Research,* **2012**, 27, 2327~2341.
7. "Graphene sheets stabilized on genetically engineered M13 viral templates as conducting frameworks for hybrid energy-storage materials", D. Oh, X. Dang, H. Yi, M. Allen, K. Xu, Y. J. Lee, and A. Belcher, *Small*, **2012**, 8, 1006~1011.
8. Xing, L.; Borodin, O.; Smith, G. D.; Li, W., "Density Functional Theory Study of the Role of Anions on the Oxidative Decomposition Reaction of Propylene Carbonate". *J. Phys. Chem. A* **2011**, *115*, 13896-13905.
9. Xing, L.; Borodin, O. "Oxidation induced decomposition of ethylene carbonate from DFT calculations – importance of explicitly treating surrounding solvent" *Phys. Chem. Chem. Phys.* **2012**, 2012, 14 (37), 12838 – 12843.
10. Jow, T. R.; Marx, M. B.; Allen, J. L., Distinguishing Li$^+$ Charge Transfer Kinetics at NCA/Electrolyte and Graphite/Electrolyte Interfaces, and NCA/Electrolyte and LFP/Electrolyte Interfaces in Li-Ion Cells. *J. Electrochem. Soc.* 2012, 159, A604-A612.

Presentations

1. "Studies on Interphases in Li ion Batteries", K. Xu, **invited speech** at the 5th International Conference on Advanced Lithium Batteries for Automobile Applications, Istanbul, Turkey (Sept. 17, 2012).

2. "Studies on Interphases in Li ion Batteries", K. Xu, **invited speech** at the 244th ACS National Meetings, Philadelphia, PA (August 23, 2012).

3. "Interfacing Electrolytes and Electrodes in Li Ion Batteries", K. Xu, **invited speech** at the 16th International Meeting on Lithium Batteries, Jeju Island, Korea (June 18, 2012).

4. "Interphasial Chemistry on Graphitic Anode Directed by Li+-Solvation Sheath", K. Xu, **invited speech** at Gordon Research Conference on Batteries, Ventura, CA (March 5, 2012).

5. "Interphasial Chemistry and Processes in Li ion Devices", K. Xu, **invited speech** at American Ceramic Society Meeting, Orlando, FL (Jan 18, 2012).

6. (invited) O. Borodin, "Insight into Electrolyte Stability and Transport from Simulations" at Gordon Research Conference on Batteries "Advanced Characterization, Theory and Mechanisms of Processes in Rechargeable Batteries Across Length Scales", March 4-9, 2012, Ventura, CA.

7. (invited) O. Borodin, T. R. Jow, L. Xing, "Insight into Electrolyte Stability, Decomposition and Transport Properties from DFT and MD Simulations" PRiME 2012, 222nd Meeting of Electrochem. Soc. Honolulu, Hawaii, October 7-12, 2012.

IV.B.5.4 Development of Novel Electrolytes for Use in High Energy Lithium-Ion Batteries with Wide Operating Temperature Range (JPL)

Marshall C. Smart

Jet Propulsion Laboratory
Electrochemical Technologies Group
Power and Sensor Systems Section
California Institute of Technology
4800 Oak Grove Drive, M/S 277-207
Pasadena, CA 91109-8099
Phone: (818) 354-9374; Fax: (818) 393-6951
E-mail: Marshall.C.Smart@jpl.nasa.gov

Start Date: October 1, 2009
Projected End Date: September 30, 2014

Objectives

- Develop a number of advanced Li-ion battery electrolytes with improved performance over a wide range of temperatures (-30° to +60°C) with projected long-life characteristics (5,000 cycles over 10-yr life span).
- Improve the high voltage stability of these candidate electrolyte systems to enable operation up to 5V with high specific energy cathode materials.
- Define the performance limitations at low and high temperature extremes, as well as, life limiting processes.
- Demonstrate the performance of advanced electrolytes in large capacity prototype cells.

Technical Barriers

This project addresses the following technical barriers associated with the development of PHEVs:

(A) Narrow operating temperature range.
(B) Limited life.
(C) Poor abuse tolerance.

Technical Targets

- The technology development program is focused on enabling a number of technical targets, including:
  1. 750 W/kg (10 mile) and 316 W/kg (40 mile).
  2. Cold cranking capability to -30°C.
  3. Cycle life: 5000 cycles (10 mile) and 3000 cycles (40 mile).
  4. Calendar life: 15 years (at 40°C).

Accomplishments

- *Demonstrated operational capability over a wide temperature range (-60° to +60°C) in prototype cells, with good life characteristics being observed at ambient and high temperatures.*
- Demonstrated improved performance with wide operating temperature electrolytes containing methyl butyrate in A123 $LiFePO_4$-based prototype (26650) cells.
- Demonstrated excellent cycle life characteristics (over 7,000 cycles) and good high temperature resilience of A123 $LiFePO_4$-based cells containing MB-based wide operating temperature electrolytes. These cells were previously demonstrated to support >11C discharge rates at -30°C, with over 90% of the room temperature capacity being delivered
- Demonstrated excellent low temperature performance of prototype 12 Ah cells manufactured by Quallion containing JPL-developed methyl propionate-based electrolytes (i.e., supporting 2C discharge rates down to -50°C).
- Investigated the effect of increasing amount of mono-fluoroethylene carbonate (FEC) as a co-solvent in methyl propionate-based electrolytes in NCA-based prototype cells.
- Investigated the use of methyl butyrate-based electrolyte containing additives in conjunction with $LiNi_{1/3}Co_{1/3}Mn_{1/3}O_2$, $Li(Li_{0.17}Ni_{0.25}Mn_{0.58})O_2$, $LiNi_{0.50}Mn_{1.50}O_2$ (LMNO), $LiNiMnCoO_2$ cathode materials in experimental cells, with good performance being exhibited thus far, outperforming the baseline systems at low temperatures.
- Of the electrolytes evaluated, the MB-based system with LiBOB displayed the best cathode kinetics with the lithium excess NMC-based material, which is attributed to the beneficial filming characteristic of the additive. However, generally poor lithium de-intercalation kinetics are observed with the LLC-NMC electrodes (received from Argonne) compared to NCA electrodes.

✧   ✧   ✧   ✧   ✧

Introduction

JPL is working to develop electrolytes that enable the operation of Li-ion cells over a wide temperature range, while still providing the desired life characteristics and resilience to high temperature (and voltage). To meet the proposed objectives, the electrolyte development includes the following general approaches: (1) optimization of carbonate solvent blends, (2) use of low viscosity, low melting ester-based co-solvents, (3) use of fluorinated esters and fluorinated carbonates as co-solvents, (4) use of "SEI promoting" and thermal stabilizing additives, and the (5) use of novel non-fluorine based salts. Many of these approaches will be used in conjunction in multi-component electrolyte formulations (i.e., such as the use of low viscosity solvents and novel additives and salts), which will be targeted at improved operating temperature ranges while still providing good life characteristics.

Approach

In the process of developing improved electrolyte formulations, they are characterized using a number of approaches, including performing ionic conductivity and cyclic voltammetry measurements, and evaluating their performance in coin cells as well as larger experimental ~400 mAh three-electrode cells equipped with reference electrodes. Initial characterization is typically performed using state-of-art electrode couples, such as (a) MCMB /LiNi$_{0.8}$Co$_{0.2}$O$_2$ or (b) graphite/LiNi$_{1/3}$Co$_{1/3}$Mn$_{1/3}$O$_2$. More recent work has been extended to the high capacity, lithium excess mixed NMC-based cathode materials. In addition to performing charge/discharge characterization over a wide range of temperatures and rates on these cells, a number of electrochemical characterization techniques are employed, including: (1) Electrochemical Impedance Spectroscopy (EIS), (2) DC linear (micro) polarization, and (3) Tafel polarization measurements. The electrochemical evaluation in proven three-electrode test cells enables the electrochemical characterization of each electrode (and interface) and the identification of performance-limiting mechanisms. Electrodes are easily harvested from these test cells and samples are delivered to collaborators (i.e., URI and Hunter College). In addition to evaluating candidate electrolytes in spirally wound experimental cells, initial screening studies are also performed in coin cells, most notably in conjunction with high voltage cathode materials.

Performance testing of large capacity prototype cells containing candidate advanced electrolytes has been performed under a number of conditions (i.e., assessment of wide operating temperature capability and life characteristics). JPL has on-going collaborations with a number of battery vendors and also has the capability to perform extensive testing. Under this program, a number of prototype cells containing JPL developed electrolytes have been under evaluation, including (i) A123 2.2 Ah cylindrical cells, (ii) Quallion BTE prismatic cells (0.25 Ah size), and (iii) Quallion large capacity prismatic cells (12 Ah size). In the future, additional cells will be procured and obtained through on-going collaborations

Results

We continued to evaluate the life characteristics of a number of A123 Systems cells that possess methyl butyrate-based electrolytes developed under this program (i.e., specifically 1.20M LiPF$_6$ in EC+EMC+MB (20:20:60 vol %) + 4% FEC and 1.20M LiPF$_6$ in EC+EMC+MB (20:20:60 vol %) + 2% VC). As reported in the previous year, these cells have exhibited excellent rate capability over a wide temperature range (-60 to +20°C) being able to support up to 10C rates at temperatures as low as -50°C and C rates at -60°C. As illustrated in Figure IV - 164, excellent full depth of discharge cycle life performance has been obtained with cells containing these MB-based electrolytes, exhibiting over 7,000 cycles to-date and displaying comparable performance to the baseline electrolyte (i.e., delivering over 83% of the initial capacity). We have also evaluated the high temperature resilience of these systems by implementing a number of cycle life tests (i.e., at 40° and 50°C), demonstrating over 2,500 cycles, with the cells containing the 1.20M LiPF$_6$ in EC+EMC+MB (20:20:60 vol %) + 2% VC electrolyte outperforming the baseline system, and the FEC containing variant displaying somewhat increased capacity fade. We have also performed cycling at 60°C and a cell containing the MB+VC electrolyte variant was observed to deliver ~ 50% of the initial capacity after completing 2,000 cycles, being comparable to the baseline electrolyte. These results are notable given the demonstrated low temperature performance capability of these systems.
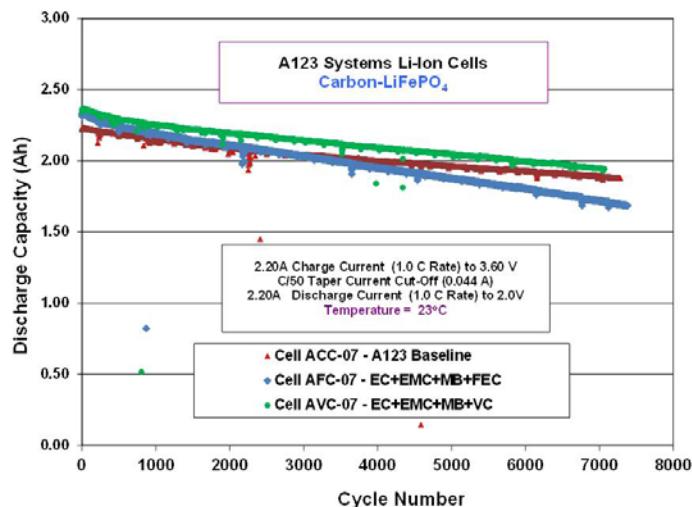
Figure IV - 164: Cycle life performance of LiFePO4-based A123 cells containing various electrolytes at +23ºC.

We also continued to evaluate the high temperature resilience of these systems and whether the low temperature capability can be preserved throughout its life by implementing variable temperature cycling tests, in which the cells are continuously cycled between temperature extremes (i.e., at - 20° and +50°C) with twenty discharge/charge cycles at the respective temperatures alternatively, as shown in Figure IV - 165. Although the electrolyte variant with FEC was observed previously to be less resilient to high temperature exposure compared to the VC-containing electrolyte, good performance was observed over the temperature with only modest loss in capacity.
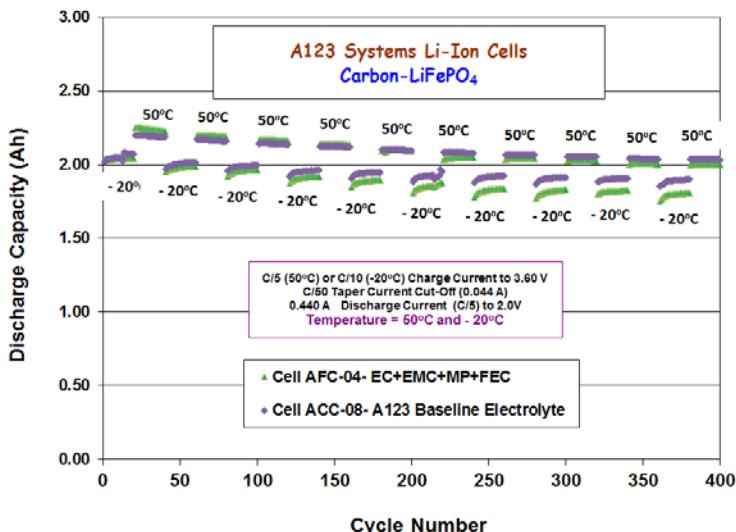
Figure IV - 165: Cycle life performance of LiFePO4-based A123 cells containing various electrolytes subjected to variable temperature cycling between +50ºC and -20ºC.

We are also evaluating a number of larger capacity 12 Ah cells (MCMB Carbon/LiNiCoAlO$_2$) obtained from our collaborator, Quallion, LCC, that contain electrolytes previously developed under this program and identified to have excellent wide operating temperature range. One of the electrolyte formulations investigated, namely 1.20M LiPF$_6$ in EC+EMC+MP (20:20:60 vol %) (where MP=methyl propionate), was previously demonstrated to have excellent rate capability at low temperatures in smaller prototype Quallion 0.250Ah cells, which has been reported previously. In an attempt to improve the life characteristics, especially at high temperature, formulations incorporating mono-fluoroethylene carbonate (FEC) were further investigated, based on favorable characteristics ascertained in experimental cells. In particular, the electrolyte 1.20M LiPF$_6$ in EC+EMC+MP

(20:20:60 vol %) + 4% FEC was evaluated in the larger 12 Ah cell. As illustrated in Figure IV - 166, excellent performance was observed down to temperatures as low as -50°C, with over 75% of the room temperature capacity being delivered up to 2C rates with both MP-based formulations. The cell containing the1.20M LiPF$_6$ in

EC+EMC+MP (20:20:60 vol %) electrolyte displayed the best rate capacity at -30°C and the least amount of polarization, as shown in Figure IV - 167. These cells have been evaluated over a wide temperature range (-60 to +20°C) and are currently being subjected to cycle life testing.
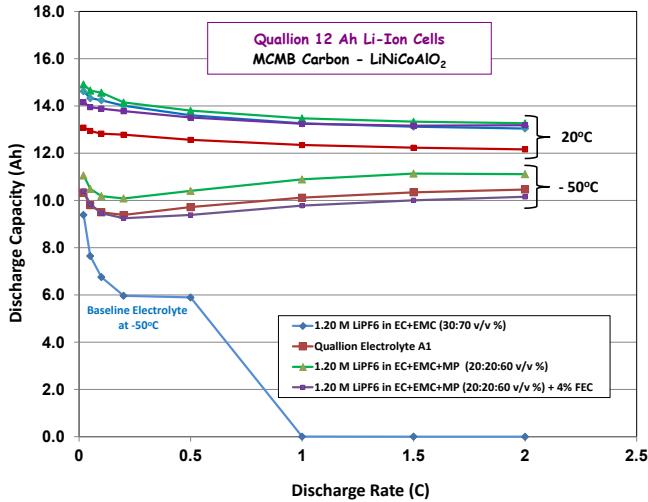
Figure IV - 166: Discharge rate capability of 12 Ah MCMB-LiNiCoAlO$_2$ cells (Quallion, LCC) containing various electrolytes at +20°C and -50°C (See first figure, A).
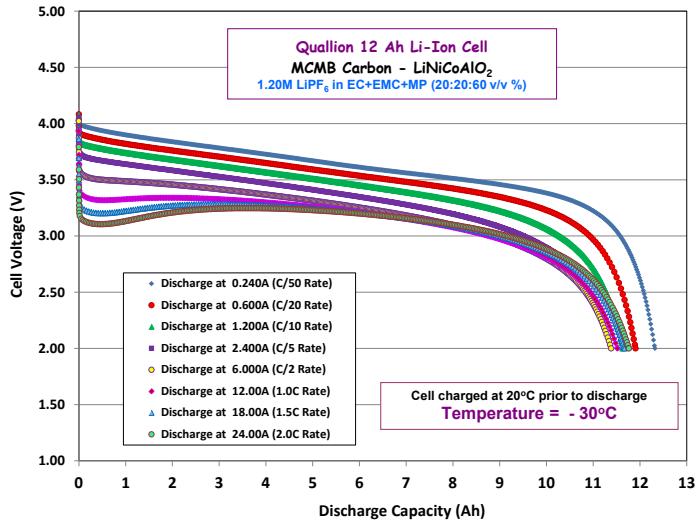
Figure IV - 167: Discharge rate capability of 12 Ah MCMB-LiNiCoAlO$_2$ cells (Quallion, LCC) containing various electrolytes at +20°C and -50°C (See first figure, A).

After completing extensive low temperature discharge rate testing, the cells were placed on partial depth of discharge cycling (approximately 50% DOD) consisting of one cycle performed each day using a variable load profile with low to moderate rates. After completing 100 days of operation under this cycling regime (100 cycles), the cells were re-characterized to determine the capacity, impedance, and low temperature discharge rate capability. Good capacity retention was observed with all of the cells after completing initial characterization, low temperature

testing (~100 cycles), and the life testing described, representing approximately one year of testing.

The best capacity retention observed was with the cell containing the methyl propionate-based electrolyte that contains FEC as an additive (4%), slightly outperforming the baseline electrolyte, suggesting that the additive has produced a desirable, protective SEI layer. In addition to performing 100% DOD capacity and impedance determination after cycling, the cells were subjected to discharge rate testing at low temperature (-20° to -50°C)

over a range of rates (C/10 to 2C) to determine the extent to which the low temperature capability has degraded. Good retention of low temperature capability was observed at -20° and -40°C when evaluated at C/5 and 2C rates, with generally 2-4% loss in capacity and energy under these conditions, with the cells containing the methyl propionate-based cells delivering the highest capacity and energy. It is interesting to note that under certain conditions (i.e., 2C rate at -40°C) high capacity was observed after life testing, which is attributed to the increased impedance leading to enhanced internal cell heating during discharge.

We are also investigating a number of electrolytes that are permutations of this approach and consist of methyl propionate with varying amounts of mono-fluoroethylene carbonate (4, 10, and 20%). In one case, we have entirely replaced the cyclic carbonate ethylene carbonate with FEC. These electrolytes have been investigated in experimental three-electrode cells, and are also being evaluated in hermetically sealed prototype 0.25Ah

MCMB/LiNiCoAlO$_2$ cells (manufactured by Quallion, LCC). Cells possessing 1.20M LiPF$_6$ in EC+EMC+MP (20:20:60 vol %) + 0.10M LiBOB were also fabricated, since the use of LiBOB as an additive has been previously identified to result in improved low temperature performance and improved cathode kinetics. These electrolytes were envisioned to have improved high temperature resilience compared to the baseline MP-containing electrolyte. A number of performance tests are currently being implemented on these cells, including discharge rate characterization as a function of temperature, charge rate characterization, and cycle life performance under various conditions (including cycling at high temperatures). As illustrated in Figure IV - 168, good discharge rate capacity has been observed at low temperature with the cells, with all formulations displaying enhanced performance at -50°C compared with the baseline using a C rate discharge, with the permutation possessing LiBOB delivering the highest capacity.
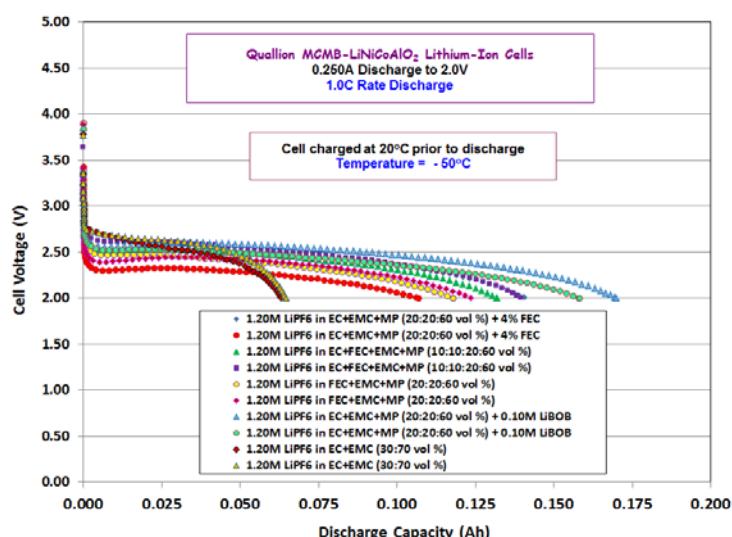
Figure IV - 168: Discharge performance of 0.25Ah MCMB-LiNiCoAlO$_2$ cells (Quallion, LCC) containing various electrolytes -50°C using a C-rate discharge.

Of this series of electrolytes investigated in the NCA-based system, the formulation containing LiBOB has been observed to have the best low temperature performance and cycle life performance at high temperature. As illustrated in Figure IV - 169, excellent discharge rate capability has been observed at -40°C (delivering 49 Wh/kg at a 5C discharge rates) and at -50°C

(delivering over 40 Wh/kg at a 4C discharge rate). We have also performed discharge rate characterization using very aggressive discharge rates at low temperature and have demonstrated that cells containing 1.20M LiPF$_6$ in EC+EMC+MP (20:20:60 vol %) + 0.10M LiBOB were capable of supporting 20C discharge rates while still providing over 60 Wh/Kg, as shown in Figure IV - 170.
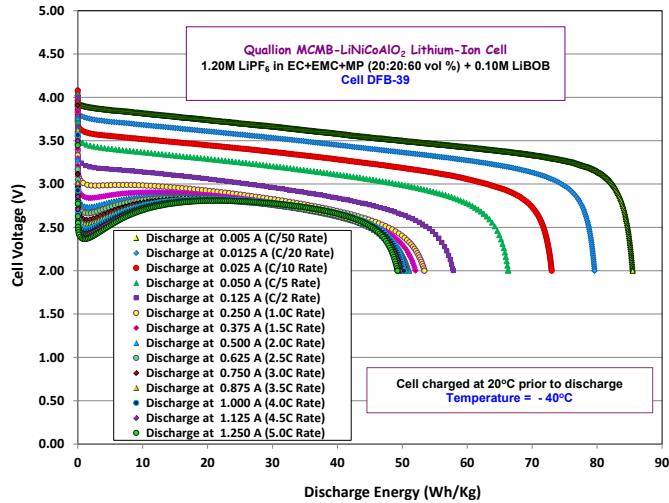
Figure IV - 169: Discharge performance of a 0.25Ah MCMB-LiNiCoAlO$_2$ cell containing a methyl propionate-based electrolyte with LiBOB at -40°C
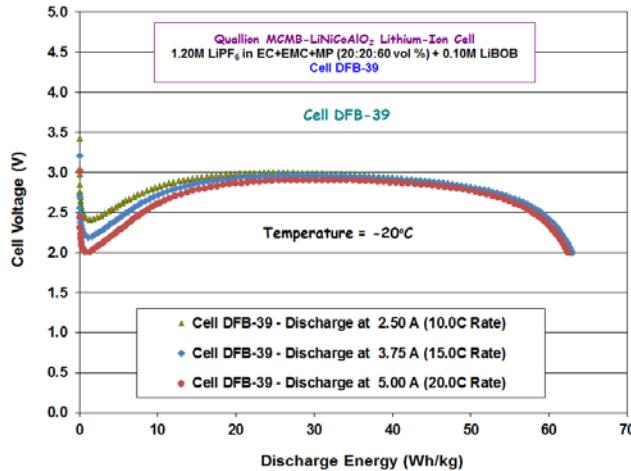
Figure IV - 170: Discharge performance of a 0.25Ah MCMB-LiNiCoAlO$_2$ cell containing a methyl propionate-based electrolyte with LiBOB at -20°C.

We also are currently subjecting these cells to full depth of discharge cycle life characterization, including at 20°, 40°, and 50°C, as well under variable temperature conditions in a manner similar to that described previously. Good cycle life performance of all of the cells has been observed at 20°C, thus far, as illustrated in Figure IV - 171. An interesting aspect of the ambient temperature cycling results is that the cells that contain FEC as a co-solvent have continued to increase in capacity even after completing over 600 cycles, to date. This is contrasted by the fact that these cells generally have lower initial capacity compared with cells containing the baseline electrolyte solution (i.e., 1.20M LiPF6 in EC+EMC (30:70 v/v %).
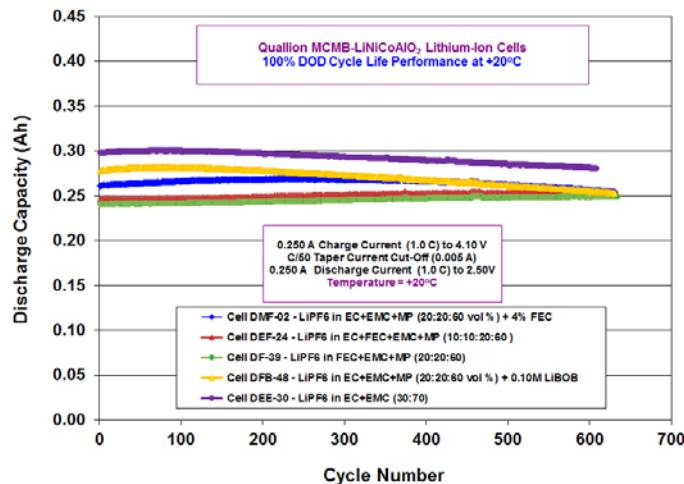
Figure IV - 171: Cycle life performance of 0.25Ah MCMB-LiNiCoAlO$_2$ cells (Quallion, LCC) containing various electrolytes at 20°C, using C rate charge and discharge over a voltage range of 2.50V to 4.10V.

Recent work has also been devoted to studying these electrolytes in high voltage systems. We have investigated ester-based solutions in conjunction with LiNi$_{1/3}$Co$_{1/3}$Mn$_{1/3}$O$_2$, LiNi$_{0.5}$Mn$_{1.5}$O$_2$ (LMNO), and the excess lithium layered-layered composite Li(NiCoMn)O$_2$ (NMC) materials (from two sources). In our most recent efforts, we have investigated the effect of electrolyte type upon the performance Conoco graphite anodes and NMC cathodes supplied by Argonne National Labs. We have generally observed good compatibility of the methyl butyrate-based electrolytes with this high voltage system. The rate capability of cells at room temperature containing 1.20M LiPF$_6$ in EC+EMC+MB (20:20:60 vol %) is very comparable to cells containing the baseline all carbonate blends. Based on previously published work under a NASA-funded project, we have demonstrated that the addition of LiBOB to flame retardant additive-containing electrolytes increases its compatibility with high voltage systems. Utilizing this approach, we have investigated wide operating temperature range electrolytes (i.e., methyl butyrate and methyl propionate-based) that contain LiBOB, with the intent of improving the cathode interface. We have also investigated the use of comparable type of compounds as additives, such as the lithium malonate borate-based salt (LiDMMDFB) developed by LBNL and the URI (Li Yang, John Kerr, and Brett Lucht). As illustrated in Figure IV - 172, a modest improvement in the cycle life performance is obtained with MB-based electrolytes containing LiBOB, whereas the use of LiDMMDBB appears to have a detrimental effect on life (in contrast the LiDMMDBB was observed to have a positive effect in the NMO-based systems). We are currently evaluating other additives and co-solvents, including mono-fluoroethylene carbonate as well as other fluorinated carbonates, with the intent of improving the life characteristics. As a comparison, we have also evaluated the life characteristics of the low flammability electrolyte developed under a NASA funded program, namely 1.0M LiPF$_6$ + 0.15M LiBOB in EC+EMC+TPP (20:70:10 vol %) (where TPP = triphenyl phosphate), with the Argonne developed electrode materials. As shown, good cycle life performance is obtained with this electrolyte formulation, outperforming the baseline all carbonate-based electrolytes (i.e., 1.0M LiPF$_6$ in EC+DEC+DMC (1:1:1). As a result of interest that DOE has expressed, some of the low flammability electrolytes developed at JPL are currently being subjected to safety testing by collaborators at Sandia National Laboratory. In support of this activity we have been actively assessing the compatibility of TPP-containing electrolytes in conjunction with NMC (1:1:1)-based cell chemistry, using electrodes supplied by Sandia National Laboratory, with good compatibility being displayed.
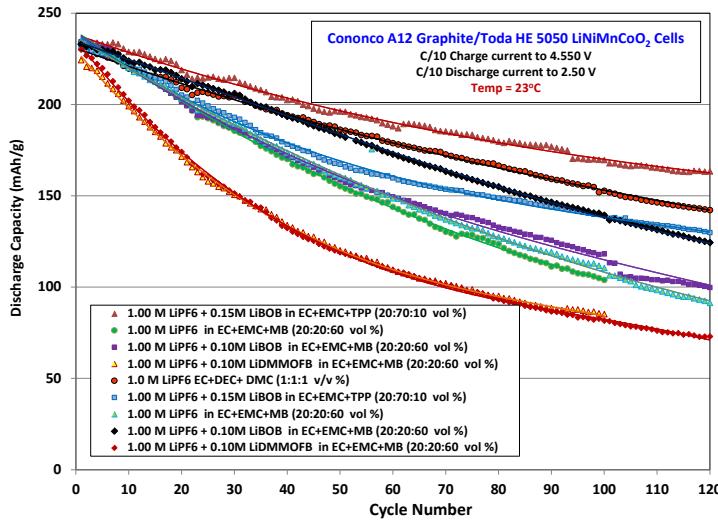
Figure IV - 172: Cycle life performance of Cononco A12 graphite/Toda HE 5050 LiNiCoMnO$_2$ cells containing containing various electrolytes (Fig. 2B).

We continued to study a number of methyl butyrate-based electrolytes (with various additives, including vinylene carbonate, lithium oxalate, FEC and LiBOB) in larger three-electrode cells consisting of Conoco graphite anodes and NMC cathodes supplied by Argonne National Labs. Being equipped with lithium reference electrodes; these cells enabled us to study the lithium kinetics of the respective electrodes by electrochemical techniques. In particular, both anodes and cathodes were subjected to a number of electrochemical measurements, including Electrochemical Impedance Spectroscopy (EIS), Tafel polarization, and linear micro-polarization measurements. Upon performing Tafel polarization measurements on each electrode (which possess relatively heavy loadings), it was observed that both NCA and NMC displayed poor lithium kinetics (limiting electrode) compared to the anode. Of the two cathodes investigated in this study, the LLC-NMC electrodes (received from Argonne) displayed much lower lithium de-intercalation kinetics compared to the NCA electrodes (attributed to poor charge transfer resistance of the electrodes), which is exacerbated at lower temperatures, as shown in Figure IV - 173. Of the electrolytes evaluated, the MB-based system with LiBOB displayed the best cathode kinetics. EIS measurements support these findings and suggest that the charge-transfer kinetics of the cathode is particularly slow and contributes significantly to the overall cell impedance and poor rate capability.
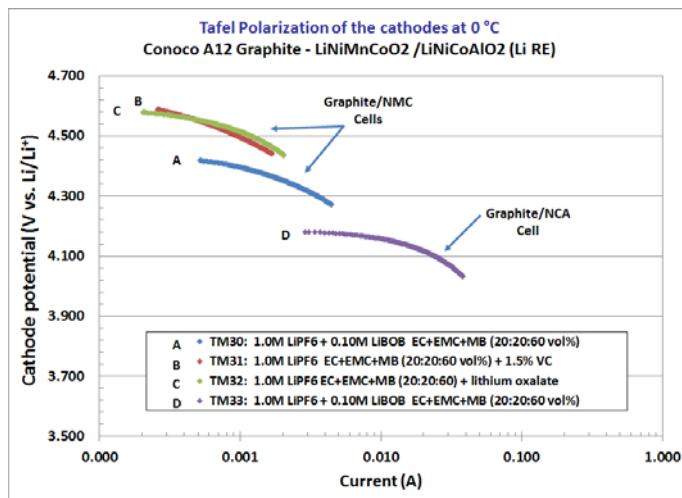
Figure IV - 173: Tafel polarization measurements at 0°C of three electrode cells consisting of Cononco A12 graphite/Toda HE 5050 LiNiCoMnO$_2$ or LiNiCoAlO$_2$ and containing various MB-based electrolytes.

We have also recently characterized the discharge rate capability of these cells as a function of temperature (down to 0^oC, as shown in Table IV - 12) and all of the methyl butyrate-based electrolytes (with various additives) displayed improved low temperature capability compared with the baseline, with 1.20M $LiPF_6$ in EC+EMC+MB (20:20:60 vol %) + 0.10M LiBOB delivering the best performance which is attributed to improved cathode kinetics, as substantiated by the Tafel polarization measurements, and improved ionic conductivity. Although improved low temperature performance has been demonstrated, it should be noted that the rate capability of the system (which is dominated by the NMC) is much poorer than comparable NCA-based systems, which is magnified at low temperatures.

Table IV - 12: Discharge capacity (Ah) as a function of temperature and discharge rate.

Electrolyte Type →		1.0M $LiPF_6$ + 0.10M LiBOB EC+EMC+MB (20:20:60 vol%)			1.0M $LiPF_6$ EC+EMC+MB (20:20:60 vol%) + 1.5% VC			1.0M $LiPF_6$ EC+EMC+MB (20:20:60) + lithium oxalate			1.2M $LiPF_6$ EC+EMC (30:70 vol%)		
Temperature	Current (mA)	Capacity (Ahr)	Capacity (mAh/g)	Percent (%)	Capacity (Ahr)	Capacity (mAh/g)	Percent (%)	Capacity (Ahr)	Capacity (mAh/g)	Percent (%)	Capacity (Ahr)	Capacity (mAh/g)	Percent (%)
23^oC	C/20	0.1100	243.87	100.00	0.1018	224.33	100.00	0.1168	257.10	100.00	0.1211	266.57	100.00
	C/10	0.1059	234.95	96.34	0.1001	220.53	98.31	0.1130	248.60	96.69	0.1108	243.84	91.47
	C/5	0.0973	215.91	88.54	0.0947	208.66	93.01	0.1039	228.57	88.90	0.1029	226.42	84.94
	C/2	0.0843	186.92	76.65	0.0840	185.03	82.48	0.0900	197.97	77.00	0.0896	197.16	73.96
10^oC	C/20	0.0972	215.59	88.40	0.0829	182.73	81.45	0.0974	214.33	83.37	0.1037	228.15	85.58
	C/10	0.0911	201.99	82.82	0.0798	175.82	78.37	0.0894	196.81	76.55	0.0858	188.84	70.84
	C/5	0.0798	177.06	72.60	0.0717	158.05	70.46	0.0798	175.55	68.28	0.0599	131.77	49.43
	C/2	0.0636	141.14	57.88	0.0526	116.01	51.71	0.0585	128.72	50.07	0.0335	73.81	27.69
	C/2	0.0642	142.39	58.39	0.0500	110.25	49.15	0.0567	124.85	48.56	0.0360	79.11	29.68
0^oC	C/20	0.0848	187.98	77.08	0.0668	147.14	65.59	0.0808	177.86	69.18	0.0748	164.70	61.78
	C/10	0.0745	165.15	67.72	0.0559	123.14	54.89	0.0670	147.33	57.30	0.0349	76.85	28.83
	C/5	0.0646	143.21	58.72	0.0467	102.91	45.88	0.0559	123.02	47.85	0.0250	55.12	20.68
	C/2	0.0491	108.92	44.66	0.0235	51.71	23.05	0.0334	73.53	28.60	0.0130	28.57	10.72

Collaborations

During the course of this program, we have collaborated with a number of institutions, including: (a) Univ. Rhode Island (Brett Lucht: perform analysis of harvested electrodes, on-going collaborator), (b) Argonne National Laboratory (Khalil Amine: source of electrodes, on-going collaborator), (c) LBNL (John Kerr) (evaluation of novel salt), (d) A123 Systems, Inc. (electrolyte development, on-going collaborator), (e) Quallion, LCC. (electrolyte development, on-going collaborator), (f) Yardney Technical Products (electrolyte development, on-going collaborator), (g) Saft America, Inc. (collaborator, industrial partner under NASA program), (h) NREL (Smith/Pesaran) (supporting NREL in model development by supplying data), and (i) the Univ. of Southern California (Prof. Prakash, electrolyte salt development).

Publications

1. M. C. Smart, A. S. Gozdz, L. D. Whitcanack, and B. V. Ratnakumar, "Improved Wide Operating Temperature Range of High Rate Nano-Lithium Iron Phosphate Li-Ion Cells with Methyl Butyrate-Based Electrolytes", 220th Meeting of the Electrochemical Society, Boston, MA, October 11, 2011.
2. S. Dalavi, M. C. Smart, B. L. Lucht, F. C. Krause, and B. V. Ratnakumar, 220th Meeting of the Electrochemical Society, Boston, MA, October 10, 2011.
3. M. C. Smart, B. L. Lucht, S. Dalavi, F. C. Krause, and B. V. Ratnakumar, "The Effect of Additives upon the Performance of $MCMB/LiNi_xCo_{1-x}O_2$ Li-ion Cells Containing Methyl Butyrate-Based Wide Operating Temperature Range Electrolytes", *J. Electrochem. Soc.*, **159 (6)**, A739-A751 (2012).
4. S. DeSilvan, V. Udinwe, P. Sideris, S. G. Greenbaum, M. C. Smart, F. C. Krause, K. A. Smith and C. Hwang, "Multinuclear NMR Studies of Electrolyte Breakdown Products in the SEI of Lithium-Ion Batteries", *ECS Trans. 41 (41), 207 (2012).*
5. M. C. Smart, M. R. Tomcsi, C. Hwang, L. D. Whitcanack, B. V. Ratnakumar, M. Nagata, V. Visco, and H. Tsukamoto, "Improved Wide Operating Temperature Range of $LiNiCoAlO_2$-Based Li-ion Cells with Methyl Propionate-Based Electrolytes", 221st Meeting of the Electrochemical Society, Seattle, WA, May 6-10, 2012.

IV.B.5.5 Novel Phosphazene-based Compounds to Enhance Safety and Stability of Cell Chemistries for High Voltage Applications (INL)

Kevin L. Gering, PhD

Idaho National Laboratory
2525 N. Fremont Avenue
Idaho Falls, ID 83415-2209
Phone: (208) 526-4173; Fax: (208) 526-0690
E-mail: kevin.gering@inl.gov

Collaborators (INL): Mason K. Harrup, Harry W. Rollins, Sergiy V. Sazhin, Fred F. Stewart
(non-INL): John Burba, Princess Energy Systems

Contract No. DE-AC07-05ID14517

Start Date: January 2009
Projected End Date: Ongoing

Objectives

Our focus is producing electrolyte and electrode compounds resilient in both temperature and voltage regimes, while meeting a competitive baseline performance in transport properties and SEI characteristics. In meeting these goals we aim to reduce the presence of carbon in Li-ion cells to produce a more inorganic-based cell chemistry. We seek compounds that will:

- enable prolonged usage of advanced higher-voltage electrode couples,
- promote better safety performance under abuse conditions, and
- enhance cell life.

Another objective is to gain fundamental understanding of molecular-scale interactions between phosphazenes and other electrolyte species and cell components.

Technical Barriers

Safety and longevity of Li-ion batteries continues to be an issue for future vehicular applications. This is complicated by the drive toward higher voltage cells (5V+) and some usage patterns and conditions that would cause batteries to operate at higher temperatures. A viable alternative electrolyte for Li-ion batteries must simultaneously meet multiple criteria regarding transport properties, SEI film formation, voltage stability, flammability, aging mechanisms, chemical compatibility, performance at high and low temperatures, etc. A

fundamental challenge remains to produce electrolyte components that will provide noteworthy levels of flame retardance while reducing viscosity to competitive levels to maintain attractive transport properties, and some success has been had at the INL toward that goal in 2012.

Technical Targets

With regard to higher voltage systems, our targets are split between three primary classifications:

- *Phosphazenes as primary solvents* (>40%) to greatly reduce electrolyte flammability. Our requirements for the pure phosphazene (with lithium salt) to be viable as a primary solvent: room temperature viscosity less than 5 cP, conductivity greater than 4 mS/cm, and lithium salt ($LiPF_6$) solubility at least 0.6 M.

- *Phosphazenes as cosolvents* (10-40%) to provide mixed benefits of reduced electrolyte flammability and prolonged cell life. Properties for the pure salted phosphazene to be defined as a cosolvent: room temperature viscosity within 5-40 cP, conductivity 0.2-4 mS/cm, and lithium salt solubility within 0.2-0.6 M.

- *Phosphazenes as additive solvents* (≤10%) to enhance chemical/thermal stability of the bulk electrolyte and improve SEI properties in terms of thermal runaway and stability over life. Viable additive candidates are defined as follows: room temperature viscosity exceeds 40 cP, conductivity ≤ 0.2 mS/cm, and lithium salt solubility < 0.2 M.

- Abuse testing at SNL of INL electrolytes looks squarely at how these compounds provide benefit to cell operation and safety at extreme conditions of temperature and voltage. Improvement over a baseline is sought.

- We have initiated dialog with DOE and ANL regarding scale-up of best phosphazene candidates.

- Replace the typical carbon anode with a highly nonflammable polymer-based host that also adds benefit toward chemical compatibility across the cell.

Accomplishments

- Various generations of heterocyclic phosphazene solvent compounds have been synthesized, characterized, and tested in coin cells. More efficient and economical synthesis routes have been found for some classes of compounds to decrease manufacturing costs.

- Further studies confirmed that low amounts of phosphazenes (as low as 1%) enhance cell stability and performance in comparison to the baseline electrolyte.

- Abuse Testing at SNL was completed with three INL additives (SM6, FM2, PhIL-2). Test results indicate that 3% levels of our additives in the baseline electrolyte provide noteworthy reduction in the peak heating rate under thermal runaway as well as a significant reduction in gas evolution. Also observed in flammability testing was a drastic reduction in the burn time when one of our ionic liquid solvents was present. Best candidates from abuse testing are candidates for the ANL Materials Scale-up facilities.

- Continued coin cell testing has been performed using the INL electrolyte blends against ABR-relevant electrode couples, including HE5050/graphite and NCA/graphite. Overall results show good compatibility of phosphazenes with the various cell environments, promoting stability at elevated temperatures.

- We refined and expanded our methods for voltammetric electrolyte and interface characterization, which has the potential of being an important new tool for materials selection.

- DFT Modeling has established trends between molecular configuration and solvent-to-lithium binding energy.

- Alternative anode materials were synthesized based on phosphazene polymer chemistry. Reversible cycling and stability to 5V was confirmed.

✧   ✧   ✧   ✧   ✧

Introduction

Electrolytes play a central role in performance and aging in most electrochemical systems. As automotive and grid applications place a higher reliance on electrochemical stored energy, it becomes more urgent to have electrolyte components that enable optimal battery performance while promoting battery safety and longevity. Safety remains a foremost concern for widespread utilization of Li-ion technology in electric-drive vehicles, especially as the focus turns to higher voltage systems (5V). This work capitalizes on the long established INL expertise regarding phosphazene chemistry, aimed at battery-viable compounds that are highly tolerant to abuse. Various references document or relate to this work for 2012 [1-3].

Approach

The general heterocyclic phosphazene structure is given as shown in Figure IV - 174.
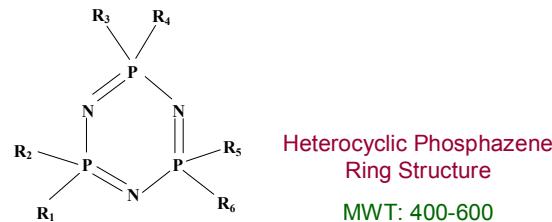
Figure IV - 174: General heterocyclic phosphazene structure.

A change of chemical structure in the ring pendant arms has a strong influence on electrolyte properties, performance, and longevity in a higher-voltage system (5V+) and at higher temperatures. By customizing the pendant structures we seek to improve transport properties while increasing flash point and having acceptable SEI characteristics and cell aging. Benefits include inherent stability and non-flammability, very low vapor pressure, good lithium salt dissolution, and choice of R groups (pendant arms) can be customized to precisely engineer properties. Challenges would include high viscosity and the need to attenuate N$:$Li$^+$ attraction that occurs due to electron doublet transfer. To date, our numerous compounds derive from the following four groups:

SM: ether groups attached to the phosphorus centers

AL: unsaturated analogues of the SM series

FM: fluorinated analogues of the SM series

PhIL: based on an ionic liquid structure.

The ionic liquid series helps to mitigate some of the limitations seen with traditional cyclic phosphazenic solvents, such as N$:$Li$^+$ association that can adversely affect conductivity. Non-cyclic phosphazene compounds are also being targeted, and salts other than LiPF$_6$ are being considered.

We employ a number of diverse testing and characterization methods to determine viability of candidate compounds, including advanced voltammetry techniques, coupled viscosity and conductivity analysis, flash point, EIS, cell testing, as well as DFT modeling. Coin cells (type 2032) are used to test candidate electrolytes in an actual cell environment, covering crucial issues of formation, interfacial impedance, polarization testing, and aging.

Results

Summarized below are salient results from FY 2012. For brevity, only representative summaries are given. The baseline (BL) electrolyte in all cases is 1.2M LiPF$_6$ in EC-EMC (2:8, wt.)

Figure IV - 175 shows coin cell capacity data for our first generation of alternative anode formulations based on phosphazene polymer hosts. While the better capacities are for formulations having small amounts of single-micron silicon, the phosphazene materials alone do

possess a native capacity for lithium. Cycling protocol in Figure IV - 175 advanced the upper voltage by 0.1V per cycle, showing a progressive increase in capacity up to 5V.

C/10 Discharge Capacity with no taper charges (coin cells).
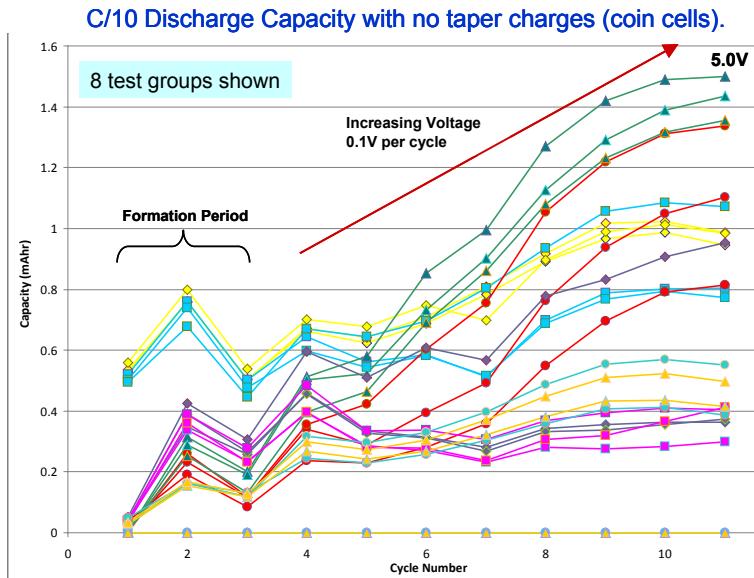
Figure IV - 175: Coin cell capacity data for the first generation INL alternative anode formulations based on phosphazene polymer host.

Figure IV - 176 attests that INL FM-series phosphazene additives extend the electrochemical window (EW) past what is achievable with the BL electrolyte. Presence of the phosphazene more than doubles the EW past the BL value. These additives act to moderate the oxidative processes at the positive electrode, and hence enhance stability at higher voltages. Ni metal was the working electrode at potentials negative to OCV, while Al was used positive to OCV. Li metal served as both the counter and reference electrodes. Regarding thermal resilience, previous work has confirmed that INL phosphazene additives promote chemical stability of the baseline electrolyte, making it more tolerant to higher temperatures over prolonged time.
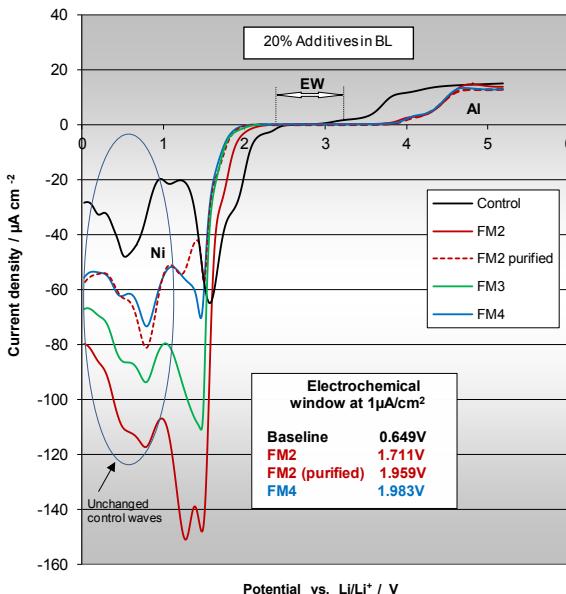
Figure IV - 176: The effect of INL FM-series phosphazene additives on the electrochemical window of the baseline electrolyte.

Cell testing was performed using 2032-type coin cells to judge performance of the electrolytes using a number of metrics. The electrode couples included HE5050/graphite and NCA/graphite. Figure IV - 177 and Figure IV - 178 summarize the early life capacity performance of coin cells using the two couples above, having SM4, SM6, FM2, and

PhIL-1 at 1 and/or 3 wt% in the baseline. In Figure IV - 177, improvement over baseline performance is seen in SM-6 and FM-2 in some cases, with a performance ranking of SM-6 > FM-2 > PhIL-2 > SM-4. Mild polarization is seen at the highest cycling rate over

numerous cycles. Similar behavior is seen in Figure IV - 178, with improvement over the baseline electrolyte observed for some cases of FM-2, SM-4 and PhIL-2.
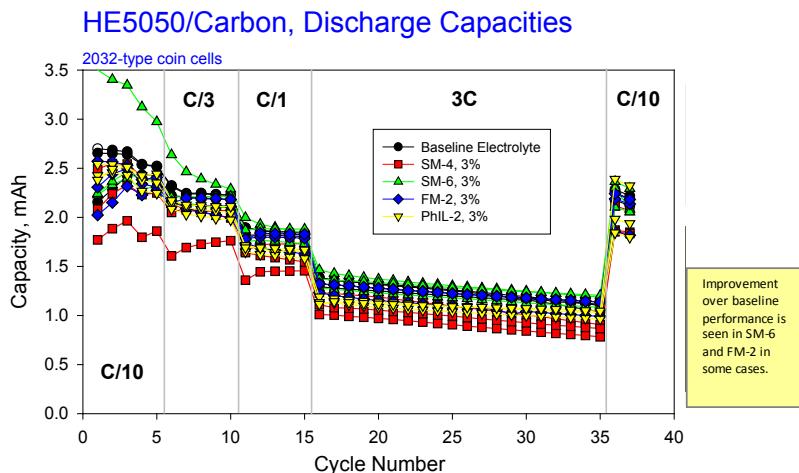
Figure IV - 177: Early life capacity performance of coin cells having SM4, SM6, FM2, and PhIL-1 at 1 and/or 3 wt% in the baseline.
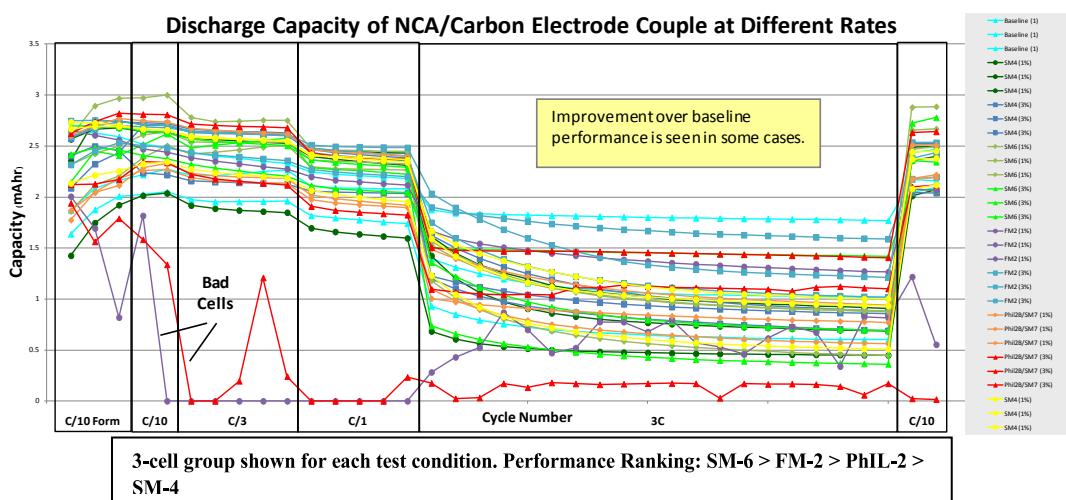
Figure IV - 178: Early life capacity performance of coin cells having SM4, SM6, FM2, and PhIL-1 at 1 and/or 3 wt% in the baseline (cont'd).

Figure IV - 179 and Figure IV - 180 show early results from SNL abuse testing of our electrolyte systems. Results indicate overall benefit of INL phosphazene additives in terms of thermal stability (Figure IV - 179), in the order of {SM-6 > PhIL-2 > FM-2}. For example, at 3% levels SM-6 decreases the peak heating rate by over 100 degrees C per minute, while PhIL-2 cuts the gas evolution to one-third that of the baseline system. Flammability

testing at SNL established that the PhIL-2 additive provides significant benefit. The baseline, SM-6, and FM-2 cells all exhibited similar burn times (100-300s) and relatively short ignition times. However, the PhIL-2 electrolyte showed a significantly shorter burn time (<20 s) and longer ignition times. This suggests reduced flammability for the PhIL-2 electrolyte relative to the baseline and other electrolytes.
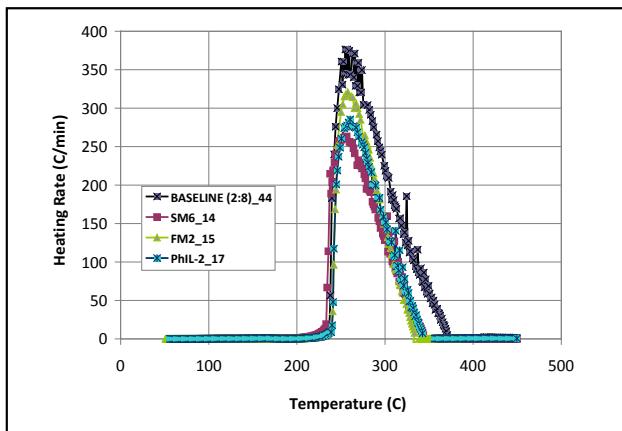
Figure IV - 179: Early results from SNL abuse testing of the INL electrolyte systems.
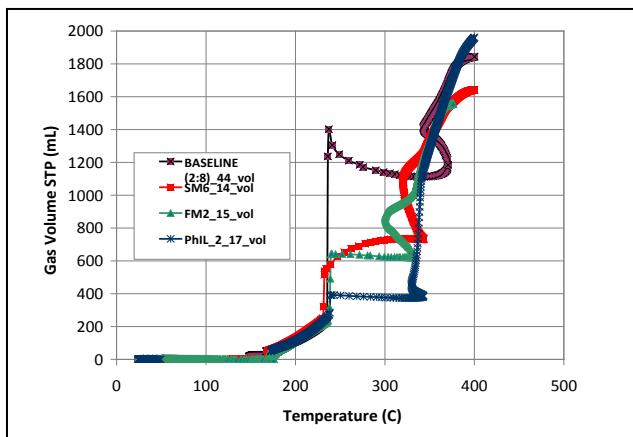
Figure IV - 180: Early results from SNL abuse testing of the INL electrolyte systems (cont'd).

Conclusions and Future Directions

INL phosphazene materials improve electrolyte stability at higher voltage and elevated temperatures. The choice of the pendant R groups allows customization of the molecules to fine tune electrolyte properties tied to fate and performance in Li-ion cells. Ionic liquid phosphazenes drastically reduce the inherent association between nitrogen and Li^+, and have shown superior performance in abuse testing at SNL. In FY 13 we will explore electrolytes having higher amounts of phosphazene solvents to exploit their low flammability, wherein non-cyclic phosphazene compounds will be targeted to reduce viscosity. Newer compounds within the FM and PhIL series will support optimization of these compound classes. NMR studies will continue to be performed to investigate molecular fate and why/how our additives provide resilience to the baseline system. Half-cell studies will be used to look more closely at additive-enhanced SEI behavior on both electrodes. Additional SNL abuse-tolerance testing will be completed with higher amounts of additives (10%), and we will

collaborate with ANL regarding scale-up of INL phosphazene compounds.

FY 2012 Publications/Presentations (selected)

1. M. T. Benson, M. K. Harrup, K. Gering, "Lithium binding in fluorinated cyclic triphosphazenes", submitted to Comp. and Theo. Chemistry.

2. M. K. Harrup, K. L. Gering, H. W. Rollins, S. V. Sazhin, M. T. Benson, D. K. Jamison, C. J. Michelbacher, T. A. Luther, "Phosphazene Based Additives for Improvement of Safety and Battery Lifetimes in Lithium-Ion Batteries", ECS Transactions from the 220th Meeting of the Electrochemical Society (Oct. 2011, Boston, MA).

3. ELECTRODES INCLUDING A POLYPHOSPHAZENE CYCLOMATRIX, METHODS OF FORMING THE ELECTRODES, AND RELATED ELECTROCHEMICAL CELLS, Inventors Kevin L. Gering, Frederick F. Stewart, Aaron D. Wilson, Mark L. Stone.

IV.C Modeling, Diagnostics, and Performance Studies

IV.C.1 Electrochemistry Cell Model (ANL)

Kevin Gallagher and Dennis Dees

Argonne National Laboratory
9700 South Cass Avenue
Argonne, IL 60439-4837
Phone: (630) 252-7349; Fax: (630) 972-4520
E-mail: kevin.gallagher@anl.gov

Collaborators:
Daniel Abraham, Argonne National Laboratory
Sun-Ho Kang, Argonne National Laboratory
Andrew Jansen, Argonne National Laboratory
Wenquan Lu, Argonne National Laboratory
Kevin Gering, Idaho National Laboratory

Start Date: October 2008
Projected End Date: September 2014

Objectives

The objective of this work is to correlate analytical diagnostic results with the electrochemical performance of advanced lithium-ion battery technologies for PHEV applications.

- Link experimental efforts through electrochemical modeling studies.
- Identify performance limitations and aging mechanisms.

Technical Barriers

The primary technical barrier is the development of a safe cost-effective PHEV battery with a 40 mile all electric range that meets or exceeds all performance goals.

- Interpreting complex cell electrochemical phenomena.
- Identification of cell degradation mechanisms.

Technical Targets

- Advance development of PHEV focused electrochemical models in support of programmatic goals.
- Identify new differential algebraic equation solver package with enhanced capabilities and complete conversion of existing models to newly adopted package.
- Initiate parameter estimation of high-energy LMR-NMC/graphite system.

Accomplishments

- Adopted new differential equation solver software (PSE gPROMS) to address several long term issues limiting model advancement: integrating complex dynamic interfaces and streamlining parameter estimation in a statistical fashion.
- Completed first numerical model analysis of the electrochemical impedance spectroscopy of a LMR-NMC cathode material. Identified largest sources of impedance growth.
- Completed initial analysis of hysteresis in LMR-NMC cathode open-circuit voltage curves. Identified unique hysteretic behavior allowing initiation of numerical modeling.

✧　　✧　　✧　　✧　　✧

Introduction

The electrochemical modeling effort is aimed at associating electrochemical performance measurements with post-test diagnostic studies conducted on lithium-ion cells. The methodology for the electrochemical model is described in detail in the literature [1, 2, 3]. Two versions of the model are utilized in this effort. One version of the electrochemical cell model is used to simulate the cell response from Electrochemical Impedance Spectroscopy (EIS) studies, and the other model version is utilized for examining DC studies, such as controlled current or power cycling and diagnostic HPPC tests. The underlying basis for both models is the same, as well as their parameter set.

The general methodology for the electrochemical model follows the work of Professor Newman at Berkeley. Continuum based transport equations using concentrated solution theory describe the movement of salt in the electrolyte. Volume-averaging of the transport equations accounts for the composite electrode geometry. Electrode kinetics, thermodynamics, and diffusion of lithium in the active material particles are also included. The detailed theoretical description of the active material/electrolyte interface, commonly referred to as the solid electrolyte interphase or SEI, is based on post-test analytical diagnostic studies. The SEI region is assumed to be a film on the active material and layer at the surface of the active material. The film is taken to be an ill-defined mixture of organic and inorganic material through which Li-ions from the electrolyte must diffuse and/or migrate across to react electrochemically at the surface of the active material. The

lithium is then assumed to diffuse through the surface layer and into the bulk active material in the particle. Capacitive effects are incorporated into the model at the electrochemical interfaces and a localized electronic resistance between the current carrying carbon and the oxide interface can also be included. The model can also accept multiple particle fractions with unique characteristics.

Approach

The approach for electrochemical modeling activities is to build on earlier successful characterization and modeling studies in extending efforts to new PHEV technologies. The earlier studies involved developing a model based on the analytical diagnostic studies, establishing the model parameters, and conducting parametric studies with the model. The parametric studies were conducted to gain confidence with the model, examine degradation mechanisms, and analyze cell limitations. Efforts this year have focused on expanding and improving the model's capabilities in addition to analyzing the lithium and manganese rich transition metal oxide (LMR-NMC) cathode materials.

Results

Electrochemical Impedance Spectroscopy of LMR-NMC Cathode Materials for Advanced Li-ion Cells. The Electrochemical Impedance Spectroscopy (EIS) cell model was used to examine the impedance characteristics of the LMR-NMC positive electrode. The fit of the model to positive electrode EIS data is given in Figure IV - 181. The experimental results were obtained from diagnostic EIS studies conducted on LMR-NMC positive/graphite negative micro-reference electrode cells. As can be seen in Figure IV - 181, the impedance is dominated by a high frequency interfacial arc associated in the model with the electronic contact resistance between the oxide active material and the conducting carbon additive. Similar to previous positive electrode EIS modeling studies, multiple particle fractions of oxide active material were utilized in the electrochemical model to improve the fit of the low frequency Warburg diffusional impedance.

The interfacial impedance for an electrode typically consists of two circular arcs (i.e. a high-frequency arc and a mid-frequency arc). Ideally, the interfacial parameters can best be determined by fixing the active material and examining a wide variety of impedance studies including variations in state-of-charge, temperature, electrolyte composition, and electrode formulation. Lacking an extensive data set, we must rely on past studies to help guide the present effort. The relative time constant (i.e. fastest to slowest) of the individual interfacial phenomena are listed below.

- Electronic resistance between carbon additive and active material if carbon additive has a significant capacitance.
- Ion migration through surface film on active material (i.e. SEI resistance).
- Lithium ion diffusion through surface film on active material.
- Electrochemical reaction (i.e. Butler Volmer kinetics).
- Lithium diffusion through active material surface layer.

It was assumed that the transport through the SEI was similar to earlier studies, except that the SEI was thicker. This assumption concerning the transport through the SEI, combined with the size of the high frequency circular arc required the electronic contact resistance between the active material and the carbon to be a major part of the interfacial impedance. Probably the best argument that this assumption is correct comes out of limited electrode formulation optimization studies that significantly reduced the size of the high frequency arc by increasing the electrode carbon content. The relative size of the kinetics and the diffusion through the active material surface layer are determined by the impedance curve and their assumed relative time constant. All the interfacial phenomena are significant, but only the electronic contact resistance dominates the interfacial impedance.

The fitted lithium diffusion coefficient in the LMR-NMC active material is an order-of-magnitude lower than that of the conventional NMC333 material. Also, the LMR-NMC positive electrode has a high electronic contact resistance (σ_P). However, the difference is accentuated because the model uses the electrochemically active area to establish the contact area. As seen below, it would be better to use a mass specific resistance (MSR) rather than an area specific resistance (ASR) for this parameter. Ideally, some measure of the electronic contact area would be optimal. In general, the LMR-NMC positive electrode's interfacial characteristics are somewhat worse than the other oxides, but are offset by the higher surface area.
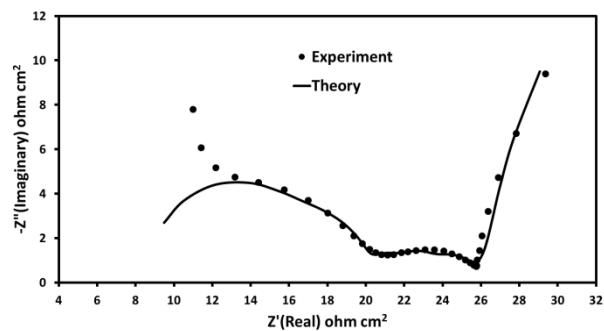
Figure IV - 181: EIS model simulation of LMR-NMC positive electrode impedance data (100 kHz-10 mHz) taken at a cell voltage of 3.75 volts and 30°C.

As shown in Figure IV - 182, the electrochemical modeling studies indicate a correlation between the measured powder electronic conductivity of active materials (i.e. conductivity of the dry powder in a pressed bed of only active material) and their particle contact resistance (i.e. σ_P ASR number from model converted to MSR) in the cell. The NMC electrode active material's lower electronic conductivity make them more challenging to obtain stable high-performance electrodes. On the positive side, limited electrode formulation optimization studies suggest that it is possible to significantly reduce the contact resistance associated with the NMC materials.
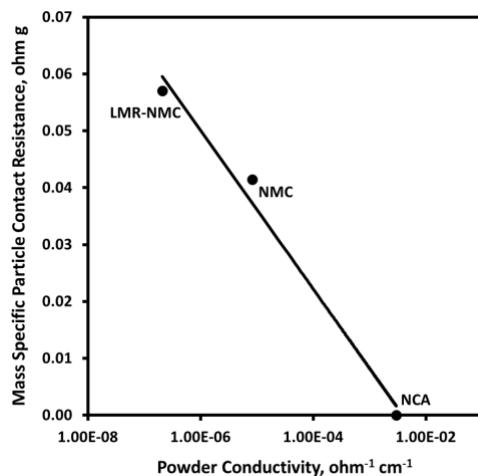
Figure IV - 182: Mass specific particle contact resistance determined by electrochemical model for NCA, NMC333 and LMR-NMC electrodes compared to the dry powder's particle conductivity.

The LMR-NMC positive electrode impedance growth with aging is given in Figure IV - 183. The change in impedance is dominated by the high frequency interfacial arc, but the mid frequency interfacial arc and the low frequency Warburg impedance also increases. The interfacial impedance shifts to lower frequencies as the cell ages. This is generally the case for parallel RC circuits or Warburg diffusive phenomena where there is a significant increase in impedance. Based on the initial assumption that the majority of the high frequency arc impedance is associated with the electronic contact resistance between the oxide and the conductive carbon, it is also the likely source of the increasing high frequency interfacial arc impedance, Figure IV - 183 (middle). It should be noted that because of the high characteristic frequency (~10 kHz) of the arc it is possible that an electronic contact resistance at the electrode/current collector interface is responsible, at least partially, for the increase in impedance.

The three physical processes that can directly affect the mid frequency interfacial arc are lithium diffusion through the SEI (D+), electrochemical kinetics (io), and lithium diffusion through the oxide surface layer (Dsi). The impact on the cathode impedance from reducing the respective parameters by a factor of 5 is given in Figure IV - 183 (bottom). Some combination of a decrease

in any or all these parameters could account for the increase in interfacial impedance, but not the increase in the Warburg impedance. Changes in Warburg impedance could derive from possible changes in the bulk oxide material or a loss in electrochemical active surface area.
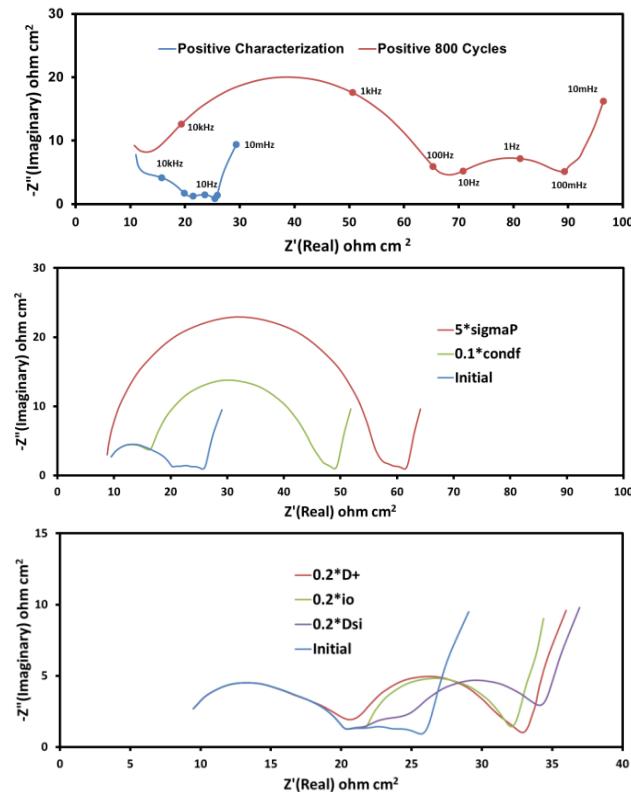
Figure IV - 183: (top) Experimental EIS measurements on Toda HE5050 LMR-NMC material before and after aging taken at an electrode voltage of 3.75 V and 30 °C (100 kHz-10 mHz). (middle) model parameter sensitivity analysis showing sensitivity to contact resistance and SEI film conductivity (bottom) model parameter sensitivity analysis for mid-frequency arc.

Hysteresis in LMR-NMC Cathode Materials. LMR-NMC cathode materials display a hysteresis between the charge and discharge open-circuit voltage (OCV) curves. The hysteresis only appears in the LMR-NMC electrochemistry after the material has been activated. The first step to modeling this material during discharge and charge is to understand the OCV. Figure IV - 184 shows OCV curves generated from the galvanostatic intermittent titration technique (GITT). The LMR-NMC material shows a unique behavior in that lithium removed near 4.3 V does not appear to re-enter the structure until 3.3 V. This 1-V hysteresis in site energy is not seen in typical lithium intercalation materials. Other experiments (not shown here), show the hysteresis to be stable and not a kinetic process. Initial modeling attempts have been able to capture to phenomenon observed in experiment, Figure IV - 185. Work continues to implement this model into the full program.
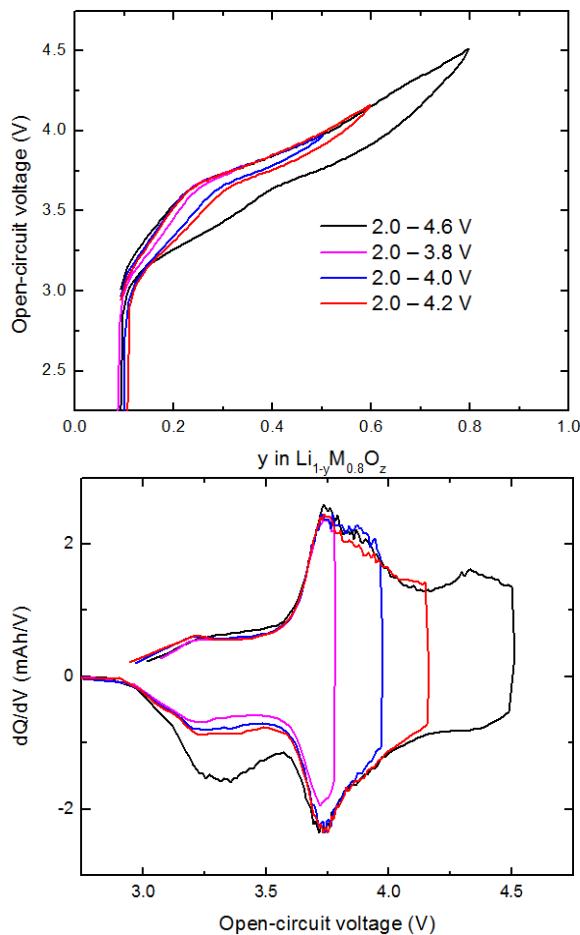
Figure IV - 184: OCV curves from GITT measurements to examine hysteresis in LMR-NMC cathode materials. An approximately 1 V hysteresis in site energy is observed between lithium removed at 4.3 V and that re-entered at 3.3 V.
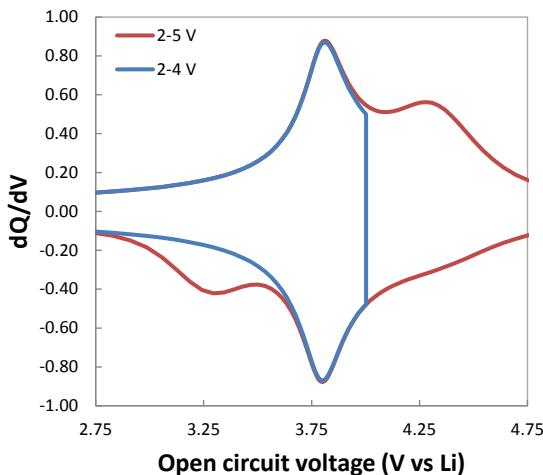
Figure IV - 185: Initial simulation of hysteresis in LMR-NMC OCV curves.

Conclusions and Future Directions

The LMR-NMC cathode materials hold great promise, but also many challenges before commercialization is possible. This work has highlighted the susceptibility of LMR-NMC cathodes to increases in high frequency impedance owing to the lower overall bulk conductivity of the materials. This manifests in a high contact resistance between the particles and the conductive carbon additives that worsens with continued exposure to high potentials (oxidizing electrolyte). Secondly, this work also has demonstrated a hysteresis in the LMR-NMC material that is important to capture within the numerical modeling effort to understand the physicochemical behavior during charge and discharge.

The electrochemistry cell modeling activity is now divided to support the Voltage Fade and the Cell Fabrication Facility projects at Argonne within the ABR program. Future model development efforts will be made to directly support the objective of these projects with a particular focus on developing a complete model of the LMR-NMC cathode materials.

FY 2012 Publications/Presentations

1. Kevin Gallagher and Dennis Dees, "Electrochemistry Cell Model" 2012 DOE Annual Peer Review Meeting Presentation, Washington DC, May 14th-18th (2012).
2. K. G. Gallagher, J. Croy, M. Balasubramanian, D. Dees, D. Kim, S.-H. Kang and M.M. Thackeray, "Promise and Challenges of LMR-NMC Cathodes (xLi$_2$MnO$_3$•(1-x)LiMO$_2$ M = Ni, Co, Mn, etc) "221th Meeting of Electrochemical Society, Seattle, WA USA, May 7-11, 2012.
3. K. G. Gallagher, D. W. Dees, A. N. Jansen, D. P Abraham, S.-H Kang "A volume averaged approach to the numerical modeling of phase-transition intercalation electrodes presented for Li$_x$C$_6$," Journal of the Electrochemical Society **159**, (12) A2029-A2037 (2012).
4. D. W. Dees, K. G. Gallagher, D. P Abraham, A. N. Jansen, "Electrochemical Modeling of a Lithium-Ion Positive Electrode Single Particle" Journal of the Electrochemical Society submitted (2012).

References

1. D. Dees, E. Gunen, D. Abraham, A. Jansen, and J. Prakash, J. Electrochem. Soc., 152 (7) (2005) A1409.
2. D. Abraham, S. Kawauchi, and D. Dees, Electrochim. Acta, 53 (2008) 2121.
3. D. Dees, E. Gunen, D. Abraham, A. Jansen, and J. Prakash, J. Electrochem. Soc., 155 (8) (2008) A603.

IV.C.2 Battery Design Modeling (ANL)

Kevin G. Gallagher, Paul A. Nelson & Dennis W. Dees

Argonne National Laboratory
9700 South Cass Avenue
Argonne, IL 60439-4837
Phone: (630) 252-4473; Fax: (630) 972-4520
E-mail: kevin.gallagher@anl.gov

Collaborators:
Ira Bloom, Argonne National Laboratory
Wenquan Lu, Argonne National Laboratory
Dan Santini, Argonne National Laboratory
Fritz Kalhammer, Electric Power Research Institute
Satish Rajagopalan, Electric Power Research Institute

Start Date: August 2010
Projected End Date: September 2014

Objectives

- The objective of this task is to develop and utilize efficient simulation and design tools for advanced lithium-ion batteries capable of predicting precise overall and component weight and dimensions, as well as cost and performance characteristics.

Technical Barriers

The primary technical barrier is the development of a safe cost-effective PHEV battery with a 40 mile all electric range that meets or exceeds all performance goals. The major challenge specific to this project is accurately predicting the impact of promising new battery materials on the performance and cost of advanced full-size lithium-ion batteries for transportation applications.

Technical Targets

- Develop model for calculating total battery mass, volume, & cost from individual components.
- Predict methods & materials that enable manufacturers to reach goals.
- Evaluate the interplay between performance and cost for advanced materials, such as anodes and cathodes, on end battery pack cost.
- Support policy making process of U.S. Government.
- Document and publically distribute model.

Accomplishments

- Distribution of BatPaC v1.0 and supporting 100+ page report began on November 1, 2011 from the website www.cse.anl.gov/batpac. Over 465 independent downloads have occurred in FY2012 including top companies, universities, and laboratories.
- Added air thermal management, automatic uncertainty calculations, and other improvements for BatPaC v2.
- Successfully supported the EPA and DOT in refining BatPaC to enable use in the 2017-2025 rule making process for CAFE and GHG regulations.
- Continually interacted with ABR program participants to quantify the effect of materials development on cost. Particular focus was made to support the newly formed Voltage Fade program.
- Distribution of BatPaC v2.0 is targeted for November 15, 2012 from the website www.cse.anl.gov/batpac. Updated version includes automatic uncertainty calculation, air thermal management options, and various other additions.

✧　　✧　　✧　　✧　　✧

Introduction

The recent penetration of lithium-ion (Li-ion) batteries into the vehicle market has prompted interest in projecting and understanding the costs of this family of chemistries being used to electrify the automotive powertrain. Additionally, research laboratories throughout the DOE complex and various academic institutions are developing new materials for Li-ion batteries every day. The performance of the materials within the battery directly affects the end energy density and cost of the integrated battery pack. The development of a publically available model that can project bench-scale results to real world battery pack values would be of great use. The battery performance and cost (BatPaC) model, represents the only public domain model that captures the interplay between design and cost of Li-ion batteries for transportation applications.

Approach

BatPaC is the product of long-term research and development at Argonne through sponsorship by the U.S. Department of Energy. Over a decade, Argonne has developed methods to design Li-ion batteries for electric-drive vehicles based on modeling with Microsoft® Office Excel spreadsheets. These design models provided all the data needed to estimate the annual materials requirements

for manufacturing the batteries being designed. This facilitated the next step, which was to extend the effort to include modeling of the manufacturing costs of the batteries. The battery pack design and cost calculated in BatPaC represent projections of a 2020 production year and a specified level of annual battery production, 10,000-500,000. As the goal is to predict the future cost of manufacturing batteries, a mature manufacturing process is assumed. The model designs a manufacturing plant with the sole purpose of producing the battery being modeled. The assumed battery design and manufacturing facility are based on common practice today but also assume some problems have been solved to result in a more efficient production process and a more energy dense battery. Our proposed solutions do not have to be the same methods used in the future by industry. We assume the leading battery manufacturers, those having successful operations in the year 2020, will reach these ends by some means.

Establishing the validity of the model calculation is important in justifying the conclusions drawn from exercising the model. The design assumptions and methodologies have been documented and reported in a number of formats. The most notable of which is the 100+ page public report that accompanies the model at the BatPaC webpage. The report and model have been subjected to a public peer-review by battery experts assembled by the U.S. Environmental Protection Agency as well as many private reviews by vehicle original equipment manufacturers (OEMs) and cell suppliers. Changes have been made in response to the comments received during the peer-reviews. The public peer-review comments are available to all. The battery pack price to the OEM calculated by the model inherently assumes the existence of mature, high-volume manufacturing of Li-ion batteries for transportation applications. Therefore, the increased costs that current manufacturers face due to low scale of production, higher than expected cell failures in the field, and product launch issues are not accounted for in the calculation. BatPaC is the only model that has all of the following attributes: freely available, transparent in methodology and assumptions, links performance and cost, and uses a bottom-up approach.

Results

Distribution of BatPaC v1.0. The first version of BatPaC with supporting documentation was distributed on November 1st, 2011. Since this release date, more than 465 independent downloads have occurred worldwide. The breakdown of these downloads is shown in Figure IV - 186. The majority of downloads originated within the United States. Industrial users, from high profile start-ups to world leading large cap companies, make up the largest percentage of downloads. We note that no lock is placed on the model meaning that once it is downloaded, it may be shared freely. The likely number of owners of the model is much higher than the number of downloads.

Over the last year, improvements have been made to BatPaC and a new version is planned to be released in mid-November of 2012. The improvements to the model include air thermal management options, automatic uncertainty calculation, updated heat generation calculation, new parallel connection options, and other various changes.
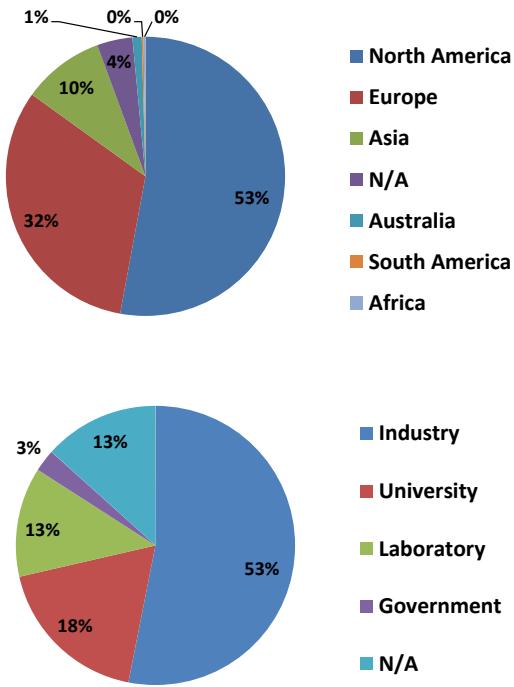
Figure IV - 186: Breakdown of the more than 450 independent downloads of BatPaC during FY2012.

Air thermal management. Air thermal management was added as an option within BatPaC to reflect the range of practices by OEMs today as well as to support the EPA/DOT in their 2017-2025 proposed rule making process. The air thermal management option includes a version that uses only cabin air and an alternative version which use both cooling and heating to regulate the air temperature that manages the battery's temperature.

A new module and pack design was necessary to enable air thermal management, shown in Figure IV - 187. Air is a less efficient heat transfer medium than the ethylene glycol – water (EG/W) mixture commonly used with liquid thermal management approaches. To overcome this challenge, air channels were created between the cells significantly increasing the surface area for heat transfer at the expense of battery pack volume. With this design, cells may be maintained at the temperature needed with only minimal internal gradients.
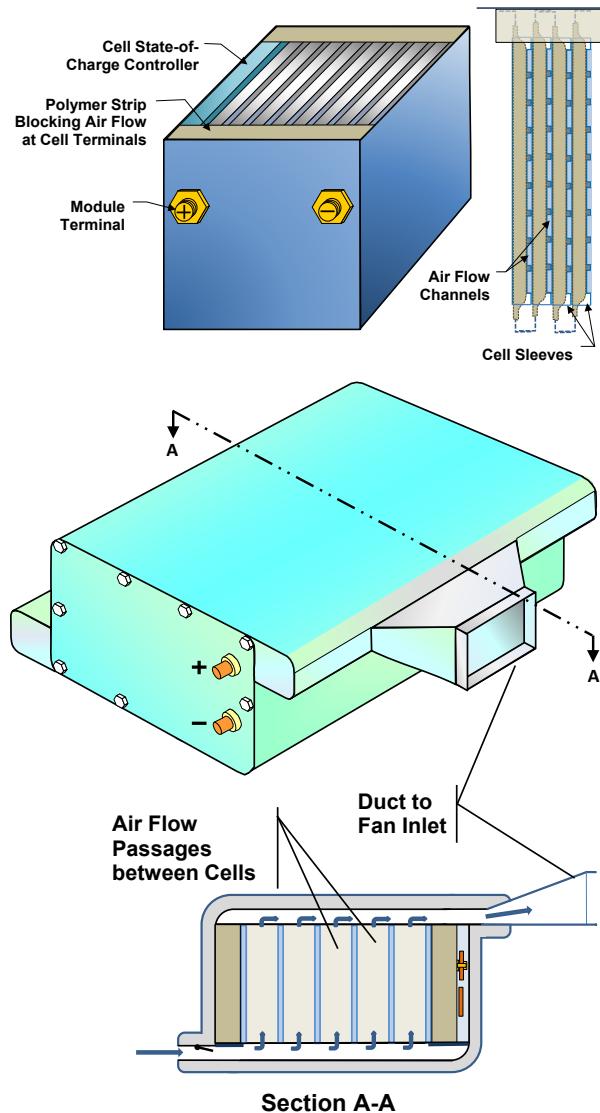
Figure IV - 187: New module (top) and pack (bottom) design for batteries utilizing air thermal management in BatPaC.

The main benefit from using air thermal management appears to be the removal of a conducting fluid (the EG/W mixture) from battery casing resulting in a perceived improvement in safety. The relative price savings is small due to the more complex module and pack design. Additionally, the air thermal management based battery packs have larger volumes, which become untenable as higher energy packs are designed.

Automatic Price Uncertainty Calculation. The potential uncertainty in estimating the price of future Li-ion batteries depends upon many factors. In BatPaC v2.0, the 95% confidence intervals for the price charged to OEM for the battery pack are automatically calculated for each designed HEV, PHEV, and EV. The uncertainty ranges are specific for the performance requirements of the battery. The three major categories of uncertainty in the default calculation of battery price are: 1) input costs of materials and capital equipment, 2) the maximum allowable

thicknesses of the electrode coatings, and 3) the maximum capacity of single cells. Figure IV - 188 below highlights how the user-specified performance requirements tie to the level uncertainty in the price calculated by BatPaC v2.0. In general, error bars increase as the required pack energy increases due to uncertainty in electrode thickness and cell capacity limitations.
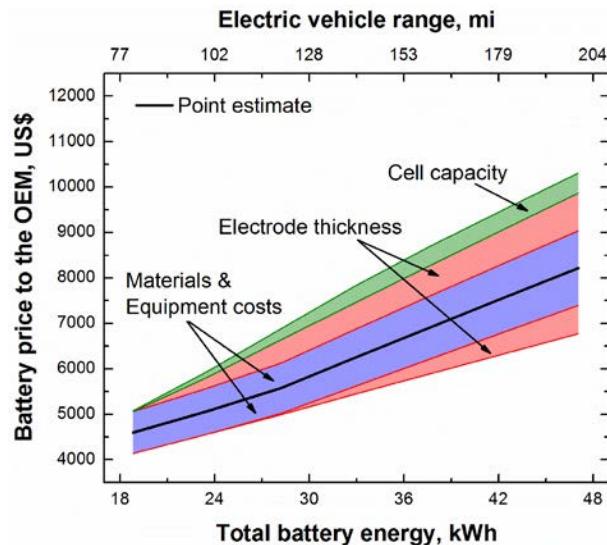
Figure IV - 188: Effects of electric-vehicle range on price and error bars for battery pack with NMC441–Gr cell chemistry, 120-kW 360 V.

Additional Improvements to BatPaC. Recent additions to the model include a separate worksheet that allocates the overhead directly onto the manufacturing processes and materials costs to directly evaluate the impact of each step in the battery process to the overall total cost to the original equipment manufacturer (OEM). The cost for a specific contribution is amplified by the overhead tied to that material or process. For instance, the total cost of capital equipment is 3.9x the equipment cost while materials are only 1.07x purchase price. Figure IV - 189 below shows a comparison between a traditional cost breakdown and the alternative approach with overhead distributed to the various manufacturing steps. The capital equipment is lumped under depreciation (9%) in Figure IV - 189 (top) while in Figure IV - 189 (middle) it is clear that electrode processing, cell fabrication and formation cycling are the most significant manufacturing steps and account for 21% of the total price to the OEM. Thus, the elimination or dramatic simplification of one of these manufacturing steps may be analyzed in a more direct fashion than in previous versions of the model. Figure IV - 189 (bottom) shows the same breakdown but in terms of capital, labor, purchased items, and materials.

Additional revisions to BatPaC include multiple parallel configurations and improved heat generation calculation.

Overall Cost Breakdown

- Materials — 53%
- Purchased Items — 15%
- Direct Labor — 4%
- Variable Overhead — 3%
- General, Sales, Administration — 4%
- Research and Development — 3%
- Depreciation — 9%
- Profit — 4%
- Warranty (includes battery pack(s) only) — 5%

Cost Breakdown with Overhead Distributed to Processes

- Materials, $ — 56%
- Purchased items, $ — 16%
- Manufacturing, $
- Electrode processing — 7%
- Cell assembly — 7%
- Formation cycling, testing and sealing — 7%
- Module and battery assembly — 3%
- Cell and materials rejection and recycling — 1%
- Receiving and shipping — 2%
- Control laboratory — 1%

Breakdown of Costs to Basic Cost Factors

- Materials — 36%
- Purchased items — 23%
- Labor — 12%
- Capital Equipment and Building — 29%

Figure IV - 189: a) Cost breakdown for a PHEV40, b) overhead distributed to processes, and c) summarized in basic cost factors.

Conclusions and Future Directions

The first public distribution of BatPaC began in November 2011 and has since resulted in over 465 independent downloads from leading companies, universities and research laboratories around the world. We have successfully supported the 2017-2025 EPA/DOT GHG and CAFE rule making process. An updated version of BatPaC will be publically released in mid-November 2012 and includes many value added features.

The battery design modeling activity is now divided to support the Voltage Fade and the Cell Fabrication Facility projects at Argonne within the ABR program. Future model development efforts will be made to directly support the objective of these projects.

Analysis of PHEV cost using BatPaC is also detailed as a part of the PHEV Battery Cost Assessment in section III.C.1.4 and III.C.2.1.

FY 2012 Publications/Presentations

1. P. A. Nelson and K. G. Gallagher, "Updates to Support US EPA/DOT Proposed Rules" Chemical Sciences and Engineering Division, Argonne National Laboratory, Argonne, IL USA March 1, 2012.

2. K. G. Gallagher, D. W. Dees, and P. A. Nelson, "PHEV Battery Cost Assessment" DOE Merit Review, Washington D.C. USA, May 14 – May 18, 2012.

3. K. G. Gallagher, J. Croy, M. Balasubramanian, D. Dees, D. Kim, S.-H. Kang and M.M. Thackeray, "Promise and Challenges of LMR-NMC Cathodes ($xLi_2MnO_3 \cdot (1-x)LiMO_2$ M = Ni, Co, Mn, etc) "221th Meeting of Electrochemical Society," Seattle, WA USA, May 7-11, 2012.

IV.C.3 Electrochemical and Physicochemical Diagnostics of High-Energy Lithium-ion Cell Couples (ANL)

Daniel P. Abraham

Argonne National Laboratory
9700 South Cass Avenue
Argonne, IL 60439-4837
Phone: (630) 252-4332; Fax: (630) 972-4406
E-mail: abraham@anl.gov

Colleagues and Collaborators:
Y. Li, Y. Zhu, M. Bettge, M. Balasubramanian,
J. Bareno, D. Dees, A. Jansen, B. Polzin, S. Trask,
W. Lu, K. Gallagher, I. Bloom, all from Argonne
National Laboratory.
R. Haasch, T. Spila, I. Petrov, E. Sammann,
B. Sankaran, all from University of Illinois at Urbana-Champaign
B. Lucht, University of Rhode Island
P. Guduru, Brown University

Start Date: October 2008
End Date: September 2012

Objectives

- To identify constituents and mechanisms responsible for performance and performance degradation of $Li_{1+x}Ni_aMn_bCo_cO_2$//graphite cells through the use of advanced characterization tools
- To recommend solutions which improve performance and minimize performance degradation of materials, and electrodes used in these cells.

Technical Barriers

- To obtain the higher energy densities possible with $Li_{1+x}Ni_aMn_bCo_cO_2$//graphite couples, the cells have to be cycled over a wider voltage window, beyond 4.5V vs. Li. However, this relatively high voltage cycling creates challenges that are detrimental to cell performance and life, which include the following: (i) electrolyte oxidation; (ii) impedance rise, (iii) capacity fade; (iv) hysteresis in electrochemical cycling curves, and (v) voltage fade. These challenges need to be overcome to enable a safe, high-energy density, PHEV battery that will deliver the required performance over a 10 year period.

Technical Targets

- Obtain a positive-electrode material that can operate in the high-voltage range (>4.5V *vs.* Li/Li$^+$) while achieving capacities >240 mAh/g during and after long-term cycling.
- Identify electrode coatings and electrolyte additives which enable the 10 year calendar life goal established for lithium-ion cells being developed for PHEV batteries.

Accomplishments

- Demonstration of 1,500, 30°C, 2.5-4.4V cycles in cells containing $Li_{1.2}Ni_{0.15}Mn_{0.55}Co_{0.1}O_2$– and graphite–based electrodes.
- Demonstrated hysteresis in electrochemical curves of $Li_{1+x}Ni_aMn_bCo_cO_2$–based electrodes
- Determined that cells with $Li_{1+x}Ni_aMn_bCo_cO_2$–based electrodes display severe performance degradation when tested at voltages >4.6 V vs. Li/Li$^+$.
- Established that positive electrode impedance rise is a common feature of all $Li_{1+x}Ni_aMn_bCo_cO_2$–graphite couples tested to date. Impedance changes at the negative electrode are relatively small.
- Concluded that (i) electrolyte oxidation at the positive electrode is a significant contributor to impedance rise; and (ii) lithium trapped in the negative electrode SEI is the main contributor to capacity fade in $Li_{1+x}Ni_aMn_bCo_cO_2$//graphite cells.
- Identified targeted solutions to minimize performance degradation of $Li_{1+x}Ni_aMn_bCo_cO_2$–graphite cells
- Demonstrated that positive electrode reconstitution can significantly reduce cell impedance.
- Established positive electrode additives and coatings that can reduce both cell impedance rise and capacity fade.
- Showed that appropriate electrolyte additives can significantly improve cell capacity retention and reduce cell impedance rise.
- Established that full cells containing reformulated positive electrodes and electrolyte additives show significant performance improvements.
- Transferred knowledge gained from electrode– and cell– diagnostics to cell fabrication facility team.

✧　　✧　　✧　　✧　　✧

Introduction

For lithium-ion batteries to widely power plug-in hybrid electric and all-electric vehicles, they must meet a range of stringent criteria which include the following: high energy densities to allow for more than 100 miles of travel autonomy, good safety, 10y calendar-life, cycle-life of up to a few thousand charge and discharge cycles, and

Table IV - 13: Electrode composition and cell chemistry.

Positive Electrode:	Negative Electrode:
86 wt% $Li_{1.2}Ni_{0.15}Mn_{0.55}Co_{0.1}O_2$ (Toda HE5050)	89.8 %wt A12 graphite (ConocoPhillips)
8%wt PVDF binder (Solvay 5130)	6%wt PVDF binder (KF-9300 Kureha)
4%wt SFG-6 graphite (Timcal)	4 %wt Super P (Timcal)
2 %wt Super P (Timcal)	0.17 %wt Oxalic Acid
6.6 mg/cm^2 active-material loading density	5.6 mg/cm^2 active-material loading density
37.1% electrode porosity	26% electrode porosity
35-μm-thick coating	40-μm-thick coating
15-μm-thick Al current collector	10-μm-thick Cu current collector
Electrolyte:	**Separator:**
1.2 M LiPF6 in EC/EMC (3:7 by wt.)	25 μm thick, Celgard 2325 (PP/PE/PP)

good power densities. The main positive electrode candidate materials to address these stringent criteria are lithium- and manganese- rich transition metal oxides (LMR-NMC). The relatively high Mn content lowers material costs, while the excess lithium boosts theoretical charge and energy densities to above 250 Ah/kg and 900 Wh/kg when cells are charged to ≥ 4.5 V vs. Li^+/Li. However, in practical cells, when these LMR-NMC oxides are cycled against graphite, deliverable energy and power decrease relatively rapidly with cycle number. The goal of this effort is to examine performance degradation of these electrodes and determine the underlying mechanisms responsible for the observed energy and power fade of cells containing these materials.

Approach

We typically employ electrochemical and physicochemical techniques for our diagnostic studies. Our electrochemical measurements are conducted in cells that include coin cells, pouch cells, and reference electrode cells to determine cell performance, performance degradation characteristics, and degradation sources. Our physicochemical examinations employ a combination of spectroscopy, microscopy, diffraction and chemical analysis techniques that include scanning and transmission electron microscopy, energy dispersive spectroscopy, electron energy loss spectroscopy, X-ray diffraction, X-ray absorption spectroscopy, X-ray photoelectron spectroscopy, Secondary Ion Mass Spectroscopy, Fourier Transform InfraRed spectroscopy (FT-IR) with Attenuated Total Reflectance (ATR), and Nuclear Magnetic Resonance (NMR) Spectroscopy.

Results

Materials. The behavior of several LMR-NMC oxides was examined during the year. The aging trends from cells with these various oxides are very similar. Hence only representative data are reported here. Table IV - 13 shows electrode constituents, electrolyte composition, and separator used in our baseline cells. The LMR-NMC material $Li_{1.2}Ni_{0.15}Mn_{0.55}Co_{0.1}O_2$, also expressed as $0.5Li_2MnO_3 \cdot 0.5LiMn_{0.375}Ni_{0.0375}Co_{0.25}O_2$, has a theoretical capacity of 377 mAh/g upon full Li removal.

Electrochemistry. The discharge capacity of $Li_{1.2}Ni_{0.15}Mn_{0.55}Co_{0.1}O_2$//Li cells, in the 2-4.1V range, is ~70 mAh/g, much smaller than the 150 mAh/g and 140 mAh/g obtained in the same voltage window for $LiNi_{0.8}Co_{0.15}Al_{0.05}O_2$ and $LiNi_{0.33}Mn_{0.33}Co_{0.33}O_2$ half cells, respectively. Cycling beyond 4.5 vs. Li/Li^+, is needed to obtain higher capacities. However, after oxide "activation", the charge and discharge profiles are no longer symmetric and display significant hysteresis, as seen in Figure IV - 190.
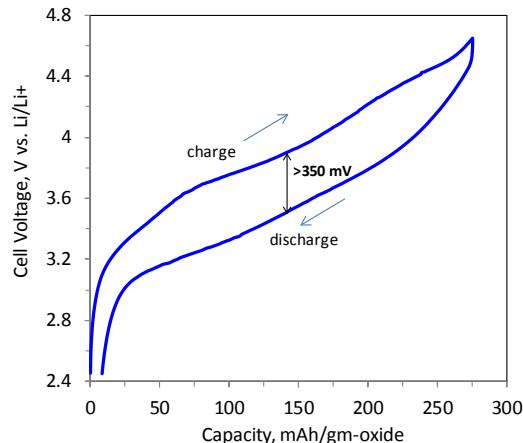
Figure IV - 190: Capacity-voltage plot, at a ~C/35 rate and 30°C, from a $Li_{1.2}Ni_{0.15}Mn_{0.55}Co_{0.1}O_2$//Li cell.

Impedance data are important because they are a measure of the cell's ability to deliver and accept charge at relatively high-rates; for example, capacity data obtained at ≥ C/1 rates are strongly affected by cell impedance. AC impedance data helps identify ohmic, charge-transfer, and diffusion-related contributions to cell impedance. Figure IV - 191 shows full cell, positive electrode, and negative electrode data from a cell with a Li-Sn reference electrode cell. It's evident that the full cell impedance increases on cycling; furthermore, the impedance rise is mainly at the positive electrode – changes at the negative electrode are relatively small. The positive electrode impedance rise is seen in the (i) high-frequency arc (with a maximum in the ~10kHz-1kHz range), which can be attributed to the electronic network that links the oxide particles to the current collector and (ii) mid-frequency arc (with a maximum in the 100 Hz to ~1 Hz range), which is associated with charge transport across the particle-particle and particle-electrolyte interfaces. The data suggest that impedance rise can be minimized by improving the electronic network (through better electrode fabrication) and by improving charge transfer at the electrode surface (through coatings and conducting films).

SFG-6 graphite and SuperP form the electronic network that links the oxide particles to the current collector. To examine their contribution to cell impedance rise on high-voltage cycling an SFG-based electrode and a SuperP-based electrode were prepared using an Al-foil current collector; dQ/dV plots from the first cycle are displayed in Figure IV - 192.
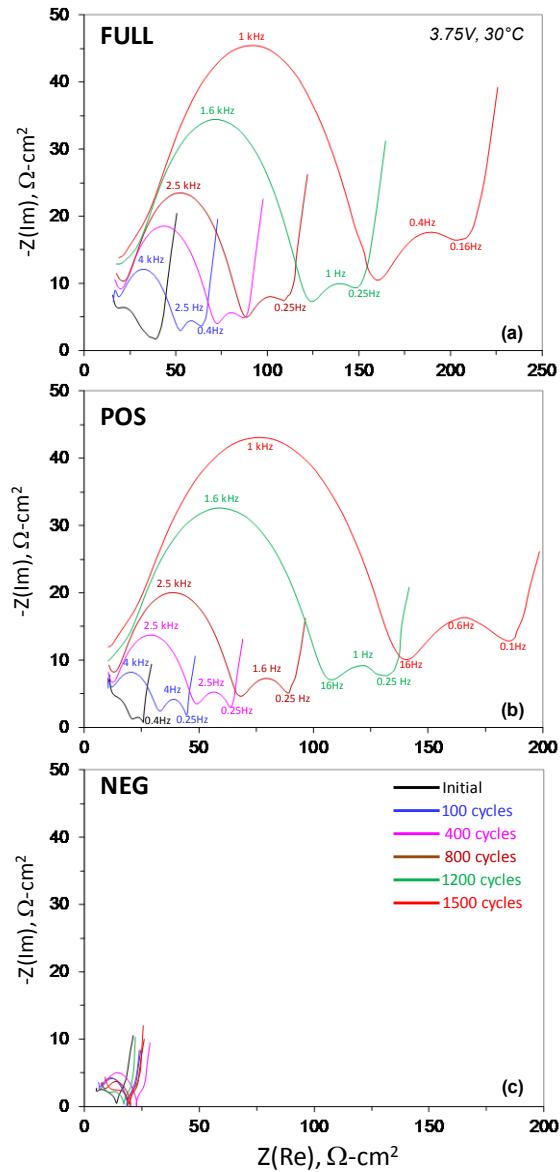
Figure IV - 191: AC impedance data from (a) the full cell, and from the (b), (c) positive and negative electrodes showing changes that result from cell cycling. The data were obtained at 30 ⬜C, at a full cell voltage of 3.75V, in the 100kHz to 0.01 Hz frequency range.
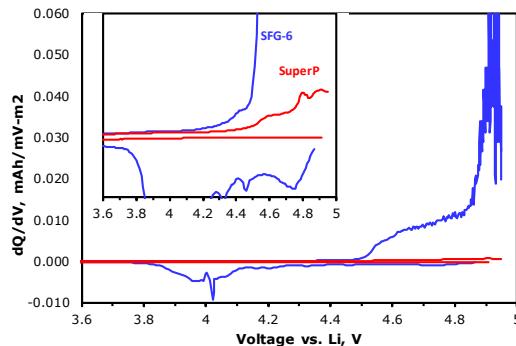
Figure IV - 192: dQ/dV plots from SFG-6 graphite- and SuperP- based electrodes. Inset is an expanded view along the Y-axis.

The SFG-6 graphite electrode data shows features that are associated with the following: (i) PF_6^- intercalation into graphite, which is significant beyond 4.45V vs. Li/Li$^+$; and (ii) electrolyte oxidation, which is significant beyond 4.8V vs. Li/Li$^+$. Note that the charge and discharge curves are asymmetric; the discharge peak at 4V vs. Li/Li$^+$ is probably due to PF_6^- deintercalation from graphite. The SuperP electrode features are indistinct and barely visible when plotted along with the SFG-6 graphite data (after normalizing for electrode surface area); the inset suggests that some PF_6^- intercalation and/or electrolyte oxidation could occur. Based on these data we recommend that SFG-6 (or other graphites) not be used for preparation of high-energy cathodes, wherein the electrode voltage is expected to exceed 4.4V vs. Li/Li$^+$. Graphites may be used as electron conducting agents in cathodes cycled at voltages <4.4V vs. Li/Li$^+$.

Diffraction, Spectroscopy and Microscopy Studies.
X-ray diffraction patterns (Figure IV - 193) were obtained on fresh positive electrode samples and from electrodes harvested from cycled cells; the cells were discharged and held at 2V before electrode extraction. The data were collected at Argonne's Advanced Photon Source. Most diffraction peaks in the fresh electrode can be indexed based on the α–NaFeO$_2$ (R-3m) structure; the data indicates a well-layered structure. A set of small, relatively broad peaks are visible in the 2θ = 22° to 25º range. These peaks are characteristic of cation ordering in the transition metal (TM) layers, as occurs between the lithium and manganese ions in Li$_2$MnO$_3$. For the cycled electrodes, these Li$_2$MnO$_3$–like peaks are not evident. In addition, the (003) oxide peak moves to smaller 2-Theta as the cell ages; this behavior is consistent with the expansion of the c-axis parameter that results from extraction of Li-ions from the oxide. In addition to peaks from the oxide, a relatively sharp graphite (002) peak at 2θ = 26.5° is evident in the fresh sample data; this peak arises from the SFG-6 graphite in the electrode coating. The peak becomes weak and broadens significantly after only a few cycles, which is consistent with the exfoliation that results from PF_6^- intercalation into graphite.
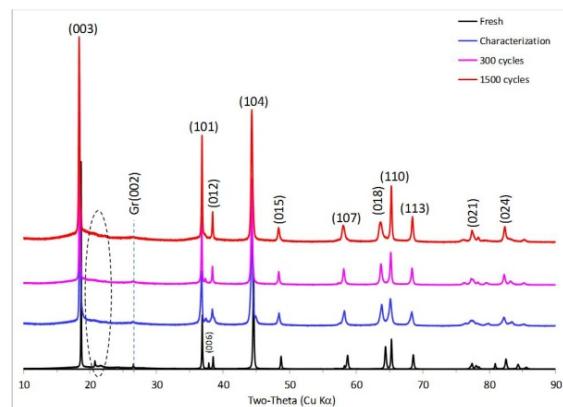
Figure IV - 193: X-ray diffraction patterns from fresh (as-prepared) and positive electrodes harvested from full cells after characterization cycles, 300 cycles, and 1500 cycles.

X-ray absorption spectroscopy (XAS) studies were conducted on the fresh positive electrode and on electrodes harvested from cycled cells, which were discharged and held at 2V before electrode extraction. The experiments were performed at the 20-BM beamline at Argonne's Advanced Photon Source. Data at the Mn- and Ni- edges, shown in Figure IV - 194, provide information on transition metal (TM) oxidation states in the samples.
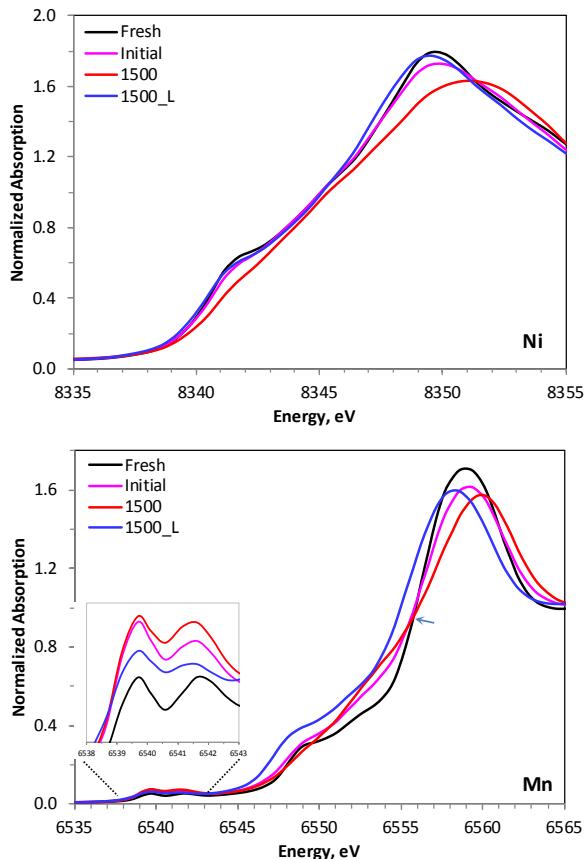
Figure IV - 194: XAS data at the Ni K-edge and Mn K-edge for a fresh positive electrode and for electrodes harvested from cells after initial cycles and after 1500 cycles. The 1500_L data is from a "relithiated" 1500_cycle electrode.

The energy position and edge shapes of the fresh sample data resemble those from $LiNi_{0.5}Mn_{0.5}O_2$, $LiCoO_2$, and Li_2MnO_3 samples, in which Ni and Mn are in the +2 and +4 oxidation states, respectively. The Ni spectrum from the initial–cycle electrode is very similar that of the fresh electrode. The spectrum for the 1500–cycle electrode shows a small shift to a higher energy, which indicates the presence of some oxidized Ni, consistent with the Li-deficiency in the oxide. The spectrum for the relithiated 1500–cycle electrode (1500_L) is similar that of the fresh electrode. That is, Ni can be reduced to +2 by relithiating the highly-cycled electrode.

The shape of the Mn K-edge spectra for the initial– and 1500– cycle electrodes is different from that of the fresh electrode. The harvested electrodes apparently contain Mn+4 because there is no direct evidence of a change in oxidation state. The 1500_L spectrum, however, shows a significant shift to a lower energy, which indicates the presence of reduced Mn in the sample. Note that the harvested positive electrodes only experienced potentials above 2.9V vs. Li/Li^+ during the entire cycling history of the full cell. In contrast, the relithiated electrode was held at 2.0V vs. Li/Li^+ before disassembly. These data indicate that Mn+3 forms only when the positive electrode voltage is lowered to 2.0 V vs. Li/Li^+ during cycling in cells with Li-metal counter electrodes.

SEM images of the fresh and aged negative electrodes are shown in Figure IV - 195. Images of the fresh electrodes show plate-like graphite particles with well-defined edges; In contrast, micrographs of highly cycled electrodes show a thick layer that covers both the graphite surface and edges. The Solid Electrolyte Interphase (SEI) forms on the negative electrode at voltages <0.8V vs. Li. SEI dissolution and reformation processes that occur during cell cycling and aging trap lithium causing an irreversible loss of Li in the cell and increasing thickness of the SEI layer. The SEM images are clear evidence of the SEI layer thickness. Transition metals (Mn, Ni, Co) from the oxide electrode that dissolve in the electrolyte and migrate to and accumulate at the graphite electrode accelerate capacity fade. Evidence of transition metal and lithium accumulation at the graphite negative electrode is seen in the SIMS data shown in Figure IV - 196.
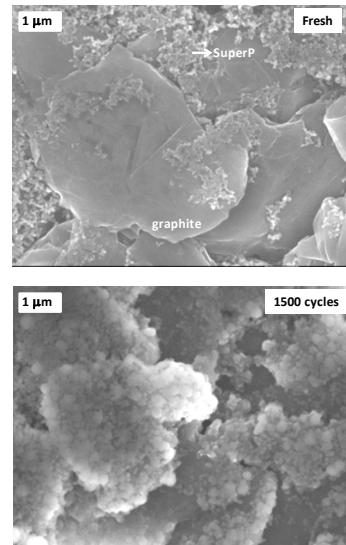
Figure IV - 195: SEM images of the fresh and aged (1500 cycles) negative electrodes.
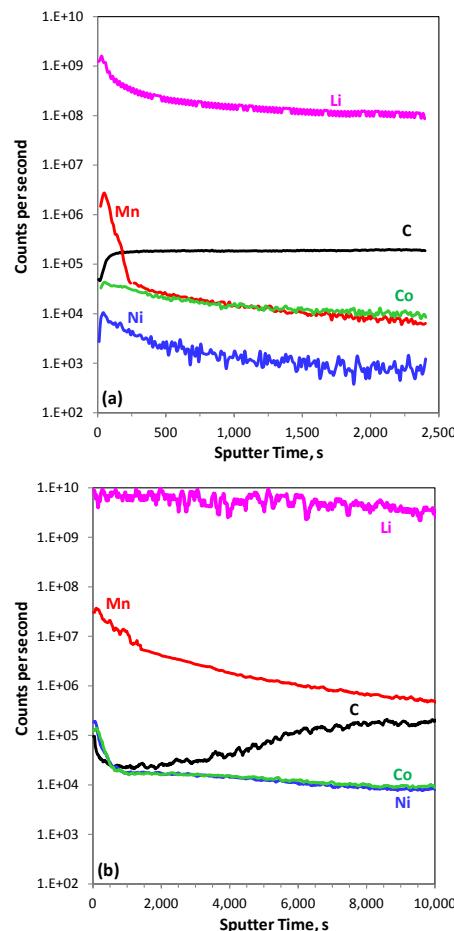
Figure IV - 196: SIMS sputter depth profiles from negative electrodes after (a) characterization cycles, and (b) 1500 cycles. Data for carbon, manganese, nickel, cobalt and lithium are shown. The Y-axis scales are the same for (a) and (b), but the X-axis scales are different.

Solutions to the Performance Degradation Problem. Identifying sources of performance degradation is the first step to designing long-life cells. Diagnostic data from our cells show that cell impedance rise during cycling/aging arises mainly from the positive electrode. We have reduced cell impedance and impedance rise by reconstituting the positive electrode, modifying the electrode through oxide and electrode coatings (pretreatment), and using additives in the electrolyte (*in situ*). Positive electrode reconstitution includes altering (a) the carbon and binder contents, (b) slurry mixing procedures, and (c) calendaring conditions during electrode preparation. The oxide and electrode coatings that show the most promise are based on alumina. These coatings are applied using sonochemical methods (on oxide particles) and by atomic layer deposition (ALD) techniques (on fresh electrodes). Several additives to the baseline electrolyte are being evaluated. Adding 2 wt% lithium difluoro(oxalato)borate (LiDFOB) to the baseline electrolyte significantly reduces cell impedance rise. Sacrificial oxidation of LiDFOB at the positive electrode produces passivation films that protects the electrode from the electrolyte and reduces transition metal dissolution from the oxide that ultimately helps to improve anode SEI stability.

Figure IV - 197 shows EIS data from a full cell containing a reformulated positive electrode, the same negative electrode in Table IV - 13, and 2 wt% LiDFOB in the baseline electrolyte. The initial impedance of these cells is half that of the baseline cells. In addition, the impedance rise after 1000, 30°C, 2.5-4.4V cycles is relatively small and an order of magnitude smaller than for the baseline cell.
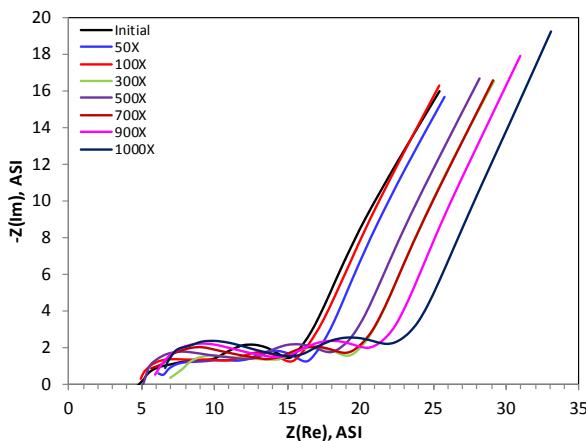

Figure IV - 197: EIS data from a $Li_{1.2}Ni_{0.15}Mn_{0.55}Co_{0.1}O_2$//Graphite cells containing the LiDFOB electrolyte additive.

Our diagnostic data show that capacity fade during cell cycling and aging originates at the positive electrode but manifests itself at the negative electrode through lithium trapping in the negative electrode SEI. We have reduced cell capacity fade (a) thoroughly drying the electrodes thereby reducing HF contents that form by

moisture reactions with the electrolyte, (b) by using alumina in and on the positive electrode that scavenges moisture and HF, and (c) by using electrolyte additives such as lithium difluoro(oxalato)borate (LiBOB) that forms partially passivating films on the negative electrode. Very thin alumina coatings on the negative electrode applied by ALD also improve full cell capacity retention to a relatively small extent.

Conclusions and Future Directions

Performance and performance degradation behavior of electrodes and cells with LMR-NMC based cathodes and graphite based anodes is being studied. Our data show that cell impedance rise on aging arises at the positive electrode, and can be attributed to processes that include electrolyte oxidation especially at cell voltages that exceed 4.5V vs. Li/Li$^+$. Cell capacity loss can be attributed to a variety of factors that include (i) lithium trapping in the negative electrode SEI; (ii) active material isolation in the electrodes; (iii) transition metal dissolution into the electrolyte; and (iv) positive electrode impedance rise, which hinders lithium-ion transport at practical rates of operation. In general, our data show that cell impedance rise and capacity fade can be minimized by "fixing problems at the positive electrode", which includes minimizing transition metal dissolution from the oxide. Our various data are being documented in reports and presentations. Furthermore, our "degradation mitigation solutions" are being incorporated in cells being produced at Argonne's Cell Fabrication Facility. We'll continue to (a) examine other $Li_{1+x}Ni_aMn_bCo_cO_2$–based electrochemical couples, (b) determine mechanisms of performance degradation, and (c) develop solutions to improve performance and minimize degradation. In addition to graphite-based electrodes, the negative electrodes in future cells may also include silicon and silicon-based alloys.

FY 2012 Publications/Presentations

1. 2012 DOE Annual Peer Review Meeting Presentation.
2. Y. Zhu, Y. Li, M. Bettge, D.P. Abraham, "Positive Electrode Passivation by LiDFOB Electrolyte Additive in High-capacity Lithium-ion Cells", J. Electrochemical Society 159 (2012) A2109-2117.
3. K.G. Gallagher, D.W. Dees, A.N. Jansen, D.P. Abraham, S.-H. Kang, "A Volume Averaged Approach to the Numerical Modeling of Phase-Transition Intercalation Electrodes presented for Li_xC_6" J. Electrochemical Society 159 (2012) A2029 – 2037.
4. V.A. Sethuraman, N. Van Winkle, D.P. Abraham, A.F. Bower, P.R. Guduru, "Real-Time Stress Measurements in Lithium-ion Battery Negative-electrodes", J. Power Sources 206 (2012) 334-342.
5. J.-G. Wen, J. Bareño, C. Lei, S.-H. Kang, M. Balasubramanian, I. Petrov, D.P Abraham,

"Analytical Electron Microscopy of $Li_{1.2}Co_{0.4}Mn_{0.4}O_2$ for Lithium-ion Batteries", Solid State Ionics 182 (2011) 98-107.

6. J. Bareño, M. Balasubramanian, S.-H. Kang, J.-G. Wen, C. Lei, S.V. Pol, I. Petrov, D.P Abraham, "Long-Range and Local Structure in the Layered Oxide $Li_{1.2}Co_{0.4}Mn_{0.4}O_2$", Chem. Mater. 23 (2011) 2039-2050.

IV.C.4 Electrochemistry Diagnostics of Baseline and New Materials (LBNL)

Robert Kostecki, Thomas Richardson

Environmental Energy Technologies Division
Lawrence Berkeley National Laboratory
1 Cyclotron Road, MS 90-3026D
Berkeley, CA 94720
Phone: (510) 486-4636; Fax: (510) 486-4260
E-mail: r_kostecki@lbl.gov

Collaborators:
Daniel Abraham, Argonne National Laboratory
Vincent Battaglia, Lawrence Berkeley National
Laboratory

Start Date: October 1, 2011
Projected End Date: September 30, 2012

Objectives

- Enable increased cell specific energy by addressing the impact of high potentials on carbons in the cathode.
- Identify physico-chemical changes of carbon additives when subjected to high potentials, and suggest approaches to improved carbon stability.
- Investigate surface treatment regimens to reduce side reactions.
- Develop strategies to minimize irreversible cell capacity losses.
- Carry out preliminary tests of new carbon additives in model cells.
- Determine the key factors that contribute to the degradation mechanism in the PHEV test cells and individual cell components.
- Carry out post-test characterization of components from ABR test cells.
- Characterize SEI formation on model electrode surfaces to improve understanding of key interfacial phenomena in PHEV cells.

Technical Barriers

- PHEV battery durability and safety, as well as the need for efficient cell-formation processes, are the major barriers addressed by LBNL diagnostic work.
- The primary LBNL role in the ABR Program is to carry out specific diagnostic evaluations to determine the changes in cell components that accompany Li-ion cell power fade, capacity fade, and/or failure.

- LBNL also seeks to identify electrode and electrolyte processes that are significantly influenced by various cell-formation protocols.

Technical Targets

- Cycle life: 5000 (deep) and 300,000 (shallow) cycles (40 mile).
- Available energy: 96 Wh/kg (40 mile).
- Calendar life: 15 years.

Accomplishments

- An effective surface high-temperature treatment in CO_2 atmosphere was successfully developed to lower the electrochemical activity of carbon black additives toward organic electrolytes at high potentials.
- The surface treatment procedure was optimized (temperature, treatment time, gas flow) and applied to commercial carbon black powders.
- Composite cathodes with modified carbon black additives were manufactured and tested in half- and full-cell model systems. The model cells displayed a significantly improved electrochemical performance and extended lifetime vs. control electrodes with standard carbon black additives utilizing the pristine sample
- The chemical "cross-talk" between electrodes in Li-ion cells was investigated and evaluated as the main cause for the impedance rise in high-energy Li-ion cells.

✧   ✧   ✧   ✧   ✧

Introduction

A primary aim of this project is to develop and use advanced diagnostic techniques to characterize basic physico-chemical properties of electrode active and passive components in ABR Program cells that are being developed for use in PHEV and EV applications. The focus of this task is to correlate fundamental processes that occur in Li-ion batteries with the electrochemical performance. The diagnostic results are used to determine cell failure mechanisms, anticipate the system lifetime as well as to suggest new approaches to design more-stable materials, composites and electrodes.

Approach

- Strategies to minimize irreversible capacity losses
  - Determine the mechanisms for carbon additives degradation at high potentials.

- o Investigate mitigating treatments, additives, and procedures.
- · Diagnostic evaluation of ABR Program lithium-ion cell chemistries
  - o Carry out post-test spectroscopic, microscopic and diffraction diagnostic evaluation of components from ABR test cells and model cells (no test cells have been sent to LBNL in FY11).
- · Understand factors that can enhance the stability of SEI layers
  - o Use results to suggest approaches to stabilize interfaces.
- · Establish and investigate degradation mechanisms of PHEV cells.

Results

Impedance growth on both negative and positive electrodes was investigated using three-electrode impedance spectroscopy of cycled model cells. The goal was to determine the origin of the cell impedance rise i.e., whether it is intrinsic to each electrode, or if it results from an exchange of soluble decomposition products, causing deterioration of electrodes interface (a phenomenon known as cell "cross-talk"). Two vacuum-dried baseline graphite electrodes of significantly different areas (20 mm vs. 3 mm diameter) were subjected to three formation cycles in 1.2 M $LiPF_6$ in 3:7 EC:EMC, and then cycled in a coin cell between -0.01 V and +1.22 V at a C/3 rate, referred to the capacity of the small electrode (The potential of the larger (overcapacity) electrode was virtually constant. Every ten cycles, an impedance spectrum was recorded in the discharged state (Figure IV - 198). No significant changes in the spectra were observed after 450 cycles. All spectra exhibit exactly the same shape, and only a small offset along the Re(Z) axis was observed.
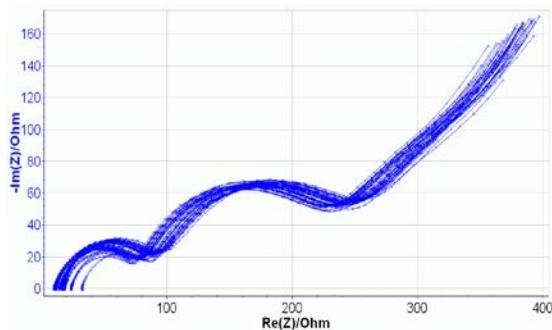
Figure IV - 198: Impedance spectra of a symmetric graphite-graphite cell obtained every ten cycles between 1 and 450 cycles.

Similar experiments with ABR baseline NMC composite cathodes revealed similar behavior i.e., a negligible impedance rise. These preliminary results suggest that the observed impedance rise in the baseline Li-ion cells is not constrained to individual electrodes and their interfaces but it is caused by the chemical interaction between the two electrodes via the electrolyte. The mechanism of these phenomena and their implication on the long-term performance of Li-ion cells are currently under investigation.

The second main area of research in the project was a rigorous examination of composite electrode carbon black (CB) additives at elevated potentials in lithium-ion cells. The work (carried out in FY2011) led to the development of a high-temperature treatment of CBs to lower the electrocatalytic properties and increase the surface stability of this class of materials at voltages exceeding 4.5 V vs. Li/Li^+. This modification of the sample is based on a HT surface treatment with various oxidative agents. It was found that CO_2 at 900°C acts as an effective oxidative agent to modify the surface of CB but preserve the original bulk structure and morphology. This approach was originally investigated utilizing model samples e.g., carbon black obtained from pyrolysis of polyimide thin-films. The structural effect of the modification was determined using Raman spectroscopy and BET measurements.

Figure IV - 199 depicts the TGA analysis of a model CB sample and the Raman spectra obtained at different stages of the HT process. The shape of the thermogravimetric analysis curve indicates that the reaction with CO_2 may initially be surface limited, but later becomes transport limited. The ratio of the D- to the G-band areas of pyrolyzed carbon changed from 0.71 for a sample treated under N_2 at 900°C to 0.65 for a sample processed under CO_2 for two hours at 900°C. The position of the D-band also shifted to lower wavenumbers, indicating a change in the surface structure. However, no significant difference between Raman spectra of samples treated for 1 and 2 hours was observed. The surface structural change appears to be complete after 60 minutes, and further treatment mainly increases the porosity of the carbon film.
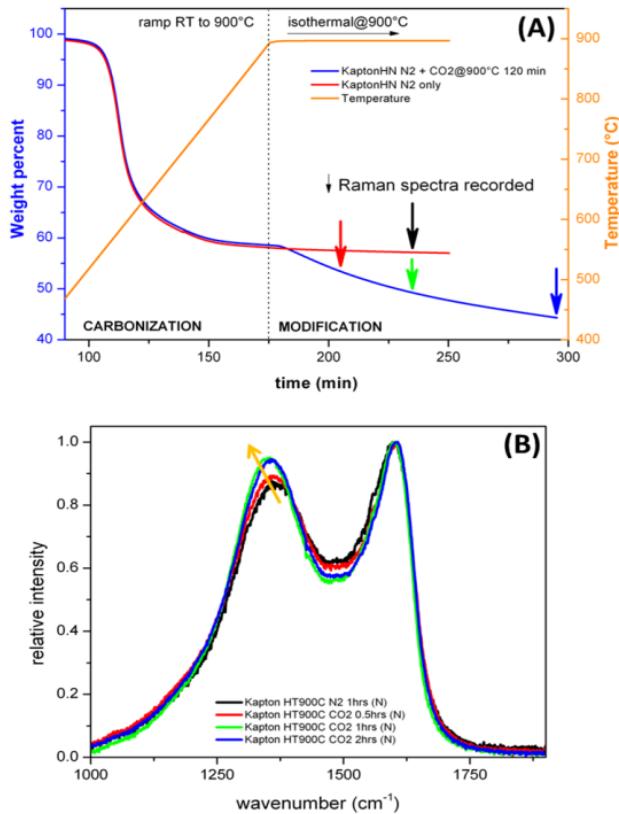
Figure IV - 199: TGA analysis (a) and Raman spectra (b) of pyrolized polyimide sample with and without heat treatments. (Arrows in the TGA curve mark with corresponding colors the points where Raman spectra were obtained).

To investigate the electrochemical behavior of the CB samples a new potentionstatic experimental method was developed. CB electrodes were polarized at the open-circuit potential, and then potential steps were applied at 125 mV increments for 60 min each, and the current response was recorded. The current spike at the beginning of each potential step pulse can be attributed to a capacitive behavior of the carbon black, whereas the charge consumed later in the 60 minutes is mainly correlated to oxidative processes occurring at the CB electrode surface.

To evaluate the overall rate of electrochemical electrolyte oxidation reactions, two different parameters were used: (i) the charge consumed during the entire potentiostatic step, and (ii) the current value at the end of the step. Figure IV - 200 depicts the charge per mg of carbon in electrodes composed solely of carbon clack (pristine or heat-treated) and PVdF.
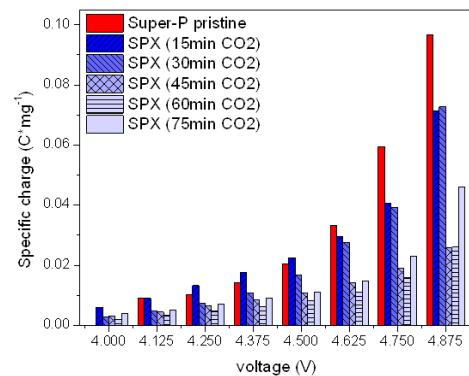
Figure IV - 200: Specific charge of potentiostatic step investigation of pristine and heat-treated Super-P samples.

The charge consumed during the entire step clearly indicates the decreased reactivity of CB vs. the electrolyte of the CO_2 heat-treated samples. Consistent with the Raman spectroscopy results, this positive effect appears to reach its maximum extent after 45 to 60 minutes of heat treatment. This is in concert with the cyclic voltammetry results where the treated CB electrodes display currents lower by almost an order of magnitude than untreated CB samples.

These promising results stimulated a new effort in collaboration with the group of Vincent Battaglia, LBNL. Composite $0.5 Li_2MnO_3 – 0.5 LiNi_{0.375}Co_{0.25}Mn_{0.375}O_2$. (Toda HE 5050) cathodes were manufactured with pristine and modified CB additives. The active material loading was 8.5 mg/cm^2 for both types of electrode. Model coin cells containing the electrodes were charged/discharged following the experimental protocols provided by Dr. Bryant Polzin (ANL). Figure IV - 201 depicts the charge/discharge behavior of the cells with cathodes containing pristine and modified CB additives. The capacity and columbic efficiency during the initial cycles are comparable for both systems. However after changing the C-Rate from C/12 to C/3 (after cycle 4) a difference in performance becomes obvious.
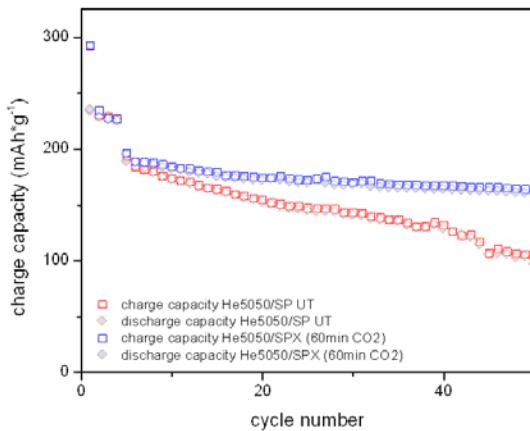
Figure IV - 201: Charge/Discharge capacity vs. cycle number of coin cells utilizing Toda He5050 and pristine (red) or heat treated (blue) carbon black.

The charge capacity of the "unmodified" cathode decreases gradually whereas the capacity of the modified electrode remains quite stable over 50 cycles. This indicates that the electrolyte decomposition is hindered and the negative impact of the chemical cross talk in the cell is diminished.

Conclusions

· The oxidative CO_2 surface treatment decreases the surface reactivity of the carbon black at potentials above 4.35 V vs. Li/Li$^+$

· Surface impurities and sp-coordinated carbon atoms at the surface of carbon black particles are responsible for the reactivity of CB vs. the electrolyte.

· The surface reactivity of CB additives affects the lifetime of high-energy Li-ion cells.

· Li-ion cells utilizing the modified carbon black additives display an improved lifetime and capacity retention over prolonged charge-discharging cycles.

· Impedance rise in the baseline Li-ion cells is not constrained to individual electrodes and their interfaces but it is caused by the chemical interaction between the two electrodes via the electrolyte.

Future Directions

· Investigate the impedance rise of asymmetric cells and expand the study in symmetric cells to different electrolytes and conditions

· Monitor the "cross-talk" utilizing spectroscopic and imaging methods, e.g. Raman and or fluorescence spectroscopy and determine the mechanism of the cross-talk in the cell.

· Expand testing of the effect of modified CB additives to other cathodes e.g., $LiNi_{0.5}Mn_{1.5}O_4$, $LiCoO_2$, etc.

Diagnostics of ABR Program cell components.

· Carry out post-test characterization of components from ABR cells

· Examine electrode composition, structure, and surface films

· Understand factors that can enhance the stability of SEI layers

· Establish and investigate degradation mechanisms of PHEV cells

· Compare degradation mechanisms in ATD *vs*. ABR cells

· Continue studies of ABR cell components and electrode/electrolyte interface stabilization in collaboration with ABR Program partners

· Carry out post-test characterization of components from ABR cells

· Examine electrode composition, structure, and surface films

· Understand factors that can enhance the stability of SEI layers

· Establish and investigate degradation mechanisms of PHEV cells

FY 2012 Selected Publications/Presentations

1. Xiaobo Chen, Can Li, Michaël Grätzel, Robert Kostecki, Samuel S. Mao, "Nanomaterials for Renewable Energy Production and Storage", Chemical Reviews, accepted.
2. Vassilia Zorba, Jaroslaw Syzdek, Xianglei Mao, Richard E. Russo and Robert Kostecki, "Ultrafast laser induced breakdown spectroscopy (LIBS) of electrode/electrolyte interfaces", Applied Physics Letters, 100, 234101 (2012).
3. S.F. Lux, I.T. Lucas, E. Pollak, S. Passerini, M. Winter and R. Kostecki, "The mechanism of HF formation in LiPF$_6$ based organic carbonate electrolytes", Electrochemistry Communications, 14, 47–50, 2012.
4. Robert Kostecki, Thomas Richardson, Ulrike Boesenberg, Elad Pollak, Simon Lux, "Modified carbon black materials for lithium-ion batteries", LBNL Invention Disclosure IB-3193 (Dec. 01, 2011).

IV.C.5 Mechanistic, Molecular, and Thermodynamic Modeling/Diagnostics in Support of ABR Cell Performance and Aging Studies (INL)

Kevin L. Gering, PhD

Idaho National Laboratory
2525 N. Fremont Avenue
Idaho Falls, ID 83415-2209
Phone: (208) 526-4173; Fax: (208) 526-0690
E-mail: kevin.gering@inl.gov

Collaborators (INL): David K. Jamison, Christopher J. Michelbacher, Sergiy V. Sazhin

Contract No. DE-AC07-05ID14517

Start Date: April 2008
Projected End Date: Ongoing

Objectives

- Develop advanced modeling tools that will complement Developmental and Applied Diagnostic Testing (DADT), based on fundamental principles of molecular interactions, chemical physics, reaction kinetics, and thermodynamics.

- Deploy these modeling tools to examine mechanistic contributions to cell performance, cell aging and path dependence (PD) thereof, and ***true prognostic analysis of battery life over arbitrary and diverse use conditions.***

- Use INL modeling tools to support technological advances of materials, and to improve battery management. We can develop/optimize operational protocol to manage and minimize the aging processes for lithium-ion cells within a given application and geographic location (chemistry-specific, but with generalized approach).

Technical Barriers

Batteries employed in electric drive applications (HEV, PHEV, or EV) will undergo diverse usage patterns during their service life, where the extent of aging over time depends on several factors tied to the severity of the duty cycle, environmental conditions, and the onboard thermal management scheme. Path dependence of aging is then a premier consideration for understanding and prolonging the life of batteries in their primary, secondary, and later applications. *If indeed a strong path-dependent correlation exists for battery aging rates, this will have sobering consequences toward meeting battery warranties for HEV, PHEV, and EV systems, since in many such cases battery life is elucidated by the industry from a series of isothermal or other equally oversimplified studies.*

Thus, there has been a need for modeling tools that describe physics-level phenomena within electrochemical systems over multiple domains, since such tools have generally not kept pace with lithium-ion materials technology worldwide. Of keen interest is to develop a purely scientific and mechanistic-based approach to describing aging processes in such systems, where the foundational theories and mathematics lend themselves to true predictive analysis over arbitrary aging conditions. Seeing this need, this work has produced a generalized physics-based modeling platform that can be used for truly predictive analysis of aging mechanisms, wherein this capability looks squarely at the issue of aging path dependence. Added to this is a unique INL molecular-based software tool known as the Advanced Electrolyte Model (AEM) that saw further expansion during 2012 to cover more chemical systems, additional molecular phenomena, and application toward more Private Sector customers.

Technical Targets

- Develop and validate computer modeling and simulation tools that yield accurate interpretation of aging and performance data in terms of meaningful physical and chemical quantities. Demonstrate INL diagnostic/predictive modeling capabilities through software that integrates key modules regarding cell performance over life (INL CellSage).

- Deploy modeling tools toward optimizing battery usage and life given operational and environmental conditions, including geographic location.

- Develop and demonstrate DADT tools that enable materials-level investigations of cell performance.

- Integrate modeling protocols into a chipset to provide real-time dynamic monitoring, diagnosis and evaluation, and prediction of key metrics such as useful life remaining.

- Continue deployment of AEM to support the DOE ABR program and the Private Sector.

Accomplishments

- Key computational methods have been developed and benchmarked on Li-ion cell performance and aging data. Our modeling framework readily adapts these tools to PD scenarios. These methods cover losses of

capacity and cell conductance over aging, kinetic performance over multiple domains, and other diagnostic data.

- Mechanistic analysis is supported, allowing quantification of multiple predominant contributions to aging metrics, e.g., capacity loss.

- Prediction of aging trends under arbitrary conditions is a standard capability, using a generalized physics and thermodynamics-based scheme. This capability allows direct consideration of aging path dependence.

- Ten-year simulations were performed for lithium-ion cells (Gen2 NCA/graphite) operating at fifteen cities within the United States, where the annual temperature cycle, daily thermal cycle (DTC), and HEV duty cycle were considered within the modeling framework. Results support optimizing battery usage conditions and thermal management design to prolong battery life.

<div align="center">✧   ✧   ✧   ✧   ✧</div>

Introduction

Domestic and worldwide vehicle designs are going more toward electric-drive platforms based on advanced batteries (Li-ion), causing a commensurate need for a rational foundation for understanding how battery usage conditions affect the aging rates and the effective service life of batteries. Batteries in vehicle service will encounter diverse usage conditions, and may be placed in secondary or tertiary applications once their performance in vehicles has reached predefined limits. Non-vehicle utilization of advanced batteries will involve several million cells under an inexhaustible assortment of applications and conditions. This collective landscape exposes an obvious need for physical models that can facilitate intelligent, science-based diagnostic analysis and prediction of performance and aging trends for electrochemical cells and cell materials operated at arbitrary conditions.

In 2012 INL continued to successfully demonstrate capability toward meeting this fundamental need by utilizing our capabilities to answer fundamental questions on aging processes, path dependence thereof, and how to mitigate performance limitations over life. We seek to understand how batteries will age in their intended applications, looking at fundamental degradation pathways. Recent references document or relate to this work [1-4].

Approach

This work aims to leverage laboratory test data toward elucidating aging under actual yet arbitrary EDV field conditions through physical (physics-based) models by isolating the predominant aging stress factors of Li-ion cells in EDV service, which would include, for example,

the nature and frequency of duty cycles, annual thermal cycles, as well as the frequency and severity of daily thermal cycles. At INL, such factors are studied in controlled and repeatable laboratory conditions to enable mechanistic evaluation of aging processes and path dependence thereof.

Modeling tools developed are those that promote diagnostic analysis of aging mechanisms over multiple domains. Model parameters strictly represent physical, chemical, electrochemical, or molecular quantities, and the mathematical framework incorporates key governing equations covering thermodynamics and chemical kinetics. These tools are supported by a suite of Diagnostic Testing (for sake of model validation), naturally lend themselves to PD scenarios, and have intellectual property status. Testing provides a means to validate our models in terms of path dependence behavior as functions of temperature and SOC.

Path Dependence (PD) of Cell Aging. The extent and rate of cell aging over time depends on specific operational conditions (stress factors) encountered over the timeline. Path dependence asserts that the *sequence* of aging conditions as well as the nature of conditions has a direct influence on the rate of aging and net aging along the timeline (akin to performance of a "batch reactor"). A change in aging conditions can accelerate or decelerate degradation mechanisms, and can initiate new ones. *The occurrence of path dependence implies the opportunity of path optimization.* Principles of reaction kinetics and thermodynamics are key to understanding the aging process along the path. INL aging models are easily adaptable to PD scenarios.

Modeling Aging Cells as Batch Reactors. Contributions from chemical kinetics and thermodynamics to cell degradation processes determine the effective rate and extent that cells age, affecting losses in capacity, power, general performance, and ancillary quantities over service life of electrochemical cells (**Figure IV - 202**).

Figure IV - 202: Modeling Aging Cells as batch reactors.

Sigmoidal rate expressions are well suited to describe these processes within a batch reactor scenario, e.g., for capacity loss at aging condition i (Ψ_i) we have:

$$\Psi_i = \sum_j 2 M_j \left[\frac{1}{2} - \frac{1}{1+\exp\left(a_j\, t^{b_j}\right)} \right]_i$$

a_j : rate constant attributable to mechanism j,

b_j : related to the order of reaction for mechanism j,

M_j : theoretical maximum limit of capacity loss under mechanism j considering the thermodynamic limit of degradation under j for a batch system.

These mathematical expressions are self-consistent, properly bounded, adaptive, relevant to cell environments, and easily lend themselves to a comprehensive mechanistic rate analysis of performance data.

Results

FY 2012 was a strategic year in applying INL computational tools for evaluating aging mechanisms and related path dependence in long-term simulations. Our key outcomes are summarized below:

- One area of focus in 2012 was to determine the effect of daily thermal cycling (DTC) on aging rates, and how to model this from a physical basis. Figure IV - 203 shows capacity loss results from our testing of Sanyo Y cells (NMC+spinel/carbon), wherein the cells undergo simultaneous PHEV duty cycling and DTC. A strong correlation exists between severity of the thermal conditions and the progression of aging. More aggressive thermal conditions and DTC tend to age the cells at least twice as fast as the isothermal baseline at 20 °C. This accelerated aging is attributed to increased mechanical stress at more severe thermal conditions and DTC, causing particle fracturing and separation. A physical model was developed to interpret this behavior (Figure IV - 204), capturing a key metric, the Particle Stability Parameter (PSP), which is related to particle sizes and bulk shape factors, in terms of accessible area per unit volume, given a particle shape, as well as to mechanical stress-strain response of the materials.
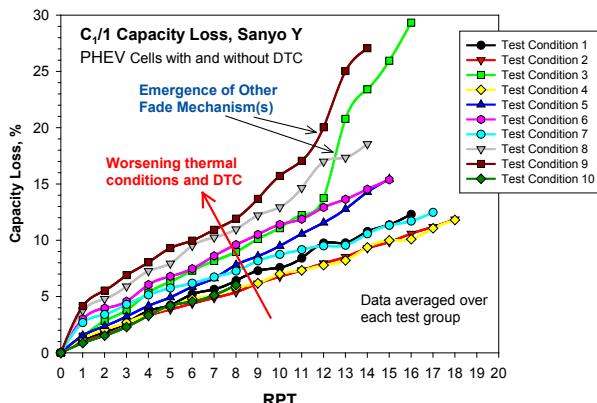
Figure IV - 203: C1/1 Capacity Loss, Sanyo Y.

Test Condition	Thermal cycling regime	Duty cycle frequency
1	Isothermal, 0 °C	Continuous
2	Isothermal, 20 °C	Continuous
3	Isothermal, 40 °C	Continuous
4	Mild, 10 to 40 °C in 30 min.	1 Round trip/day
5	Mild, 10 to 40 °C in 30 min.	Continuous
6	Mild, 10 to 40 °C in 15 min.	Continuous
7	Severe, -20 to 40 °C in 30 min.	1 Round trip/day
8	Severe, -20 to 40 °C in 30 min.	Continuous
9	Severe, -20 to 40 °C in 15 min.	Continuous
10	Severe, -20 to 40 °C in 30 min.	None (cal-L)
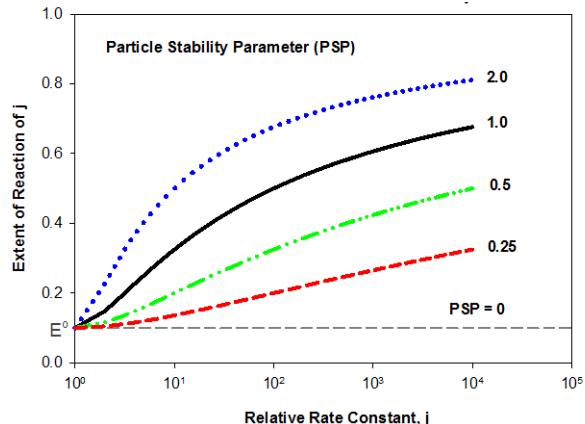
Figure IV - 204: Extent of Reaction versus Relative Rate Constant for various Particle Stability Parameters.

- Using the resultant capability from Figure IV - 204 and other modeling components, we performed simulations wherein we predict capacity loss for C/25 and C/1 rates over a ten year period for Gen2 cells operating at various cities in the US. Figure IV - 205 gives Annual temperature profiles for the chosen cities. Figure IV - 206 and Figure IV - 207 reveal results for CellSage simulations that include DTC and have a presumed maximum permissible temperature of 40 °C under thermal management, while the minimum temperature is determined by the representative monthly temperature at each city. The predicted curves are composite capacity losses for a two-mechanism degradation process involving loss of lithium inventory and loss of active host material. Stair-stepping of capacity loss is seen as the higher summer temperatures cause losses to increase while the colder fall and winter months cause a commensurate decrease in aging rates. If more aggressive thermal management is applied (T_{max} = 30 °C, T_{min} = 15 °C) then the ***reduction*** in capacity loss can be estimated via CellSage relative to Figure IV - 205 and Figure IV - 206. Figure IV - 208 and Figure IV - 209 show these reductions, wherein there is substantial benefit in cell life for the C/25 case, but less so for C/1 due to polarization effects which persist over temperature. Such results can be used to support design of thermal management systems for battery packs destined for various geographic locations.
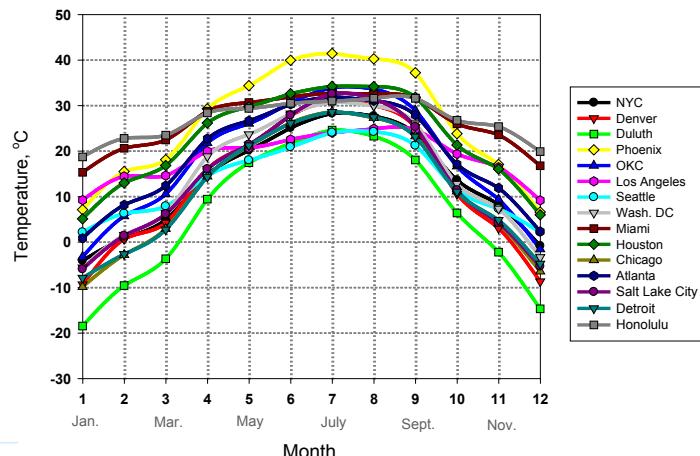
Figure IV - 205: Annual Temperature Profiles for Chosen Cities.
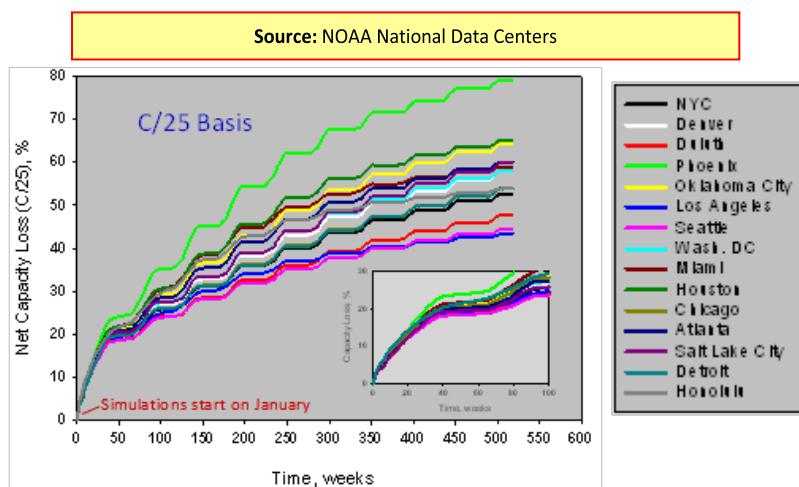
Figure IV - 206: Results for Cellstage Simulations.
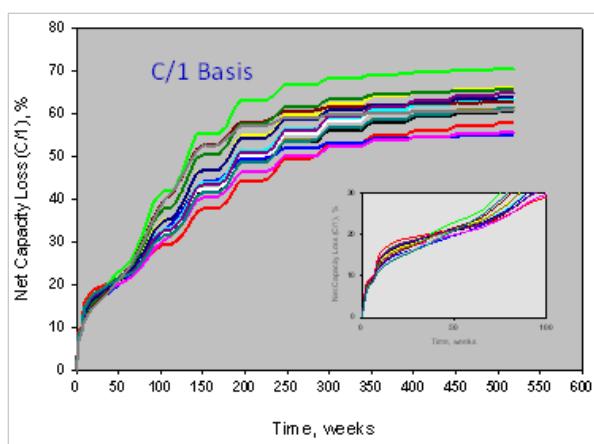
Figure IV - 207: Results for Cellstage Simulations (cont'd).
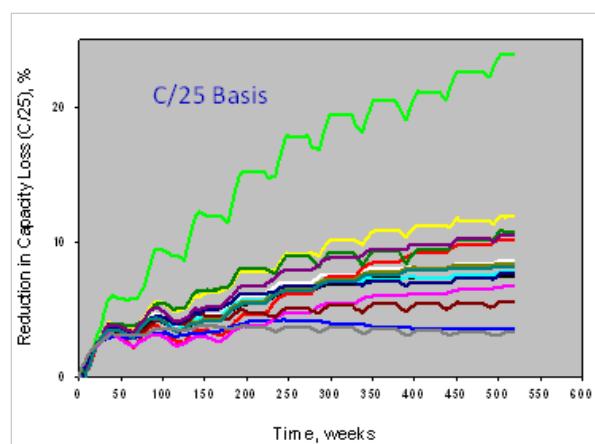
Figure IV - 208: Reductions in Capacity Loss with more aggressive thermal management.
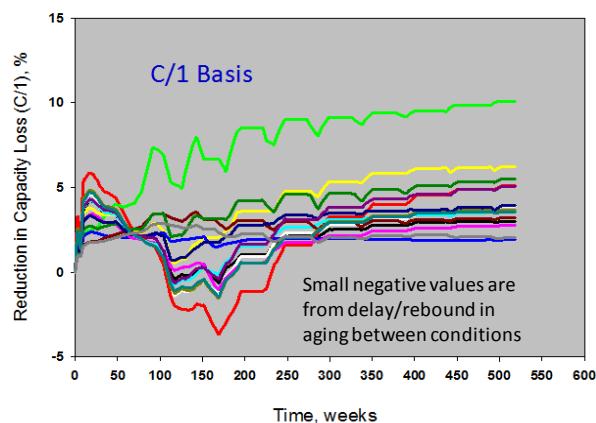
Figure IV - 209: Reductions in Capacity Loss with more aggressive thermal management (cont'd).

Conclusions and Future Directions

INL has developed strategic computational tools used to diagnose, model and predict performance and aging of electrochemical cells and cell components. These tools have been used to guide research by targeting more relevant conditions to the intended applications (e.g., PHEV). These tools are revealing mechanisms of cell degradation, related path dependence, and chief causes and conditions of performance loss. The immediate benefits of this work are (1) to provide more realistic and accurate life predictions by accounting for the influence of thermal cycling effects and related path dependence on aging mechanisms, and (2) enable accelerated battery development, design, and management.

Future simulation work can involve other duty-cycles (e.g., FUDS, DST), other temperature parameters defined for a particular city or region, the effect of DTC, and other Li-ion cell chemistries. Optimizing battery life is an abiding goal of this work, a goal that is reachable through INL intelligent physical models.

FY 2012 Publications/Presentations

1. K. L. Gering, "Consequences of Thermodynamic Processes and Principles in Electrochemical Cell Performance and Aging", Joint meeting of the International Battery Association and Pacific Power Sources Symposium, January 11, 2012 (Waikoloa, HI).

2. K. L. Gering, "Thermodynamic Processes in Electrochemical Cell Performance and Aging", 221st Meeting of the Electrochemical Society, May 9, 2012 (Seattle, WA).

3. K. L. Gering, "Using Thermodynamic Foundations for Simulation and Prediction of Battery Aging Across Diverse and Arbitrary Usage Conditions", Battery Power 2012, September 18, 2012 (Denver, CO).

4. US Patent Application (Full): "METHOD, SYSTEM, AND COMPUTER-READABLE MEDIUM FOR ESTIMATING A PREDICTED ARBITRARY AGING CONDITION OF AN OBJECT," Kevin L. Gering.

IV.D Abuse Diagnostics & Mitigation

IV.D.1 Diagnostic Studies Supporting Improved Abuse Tolerance (BNL)

PI: Kyung-Wan Nam
Brookhaven National Laboratory
Chemistry Department
Upton, NY 11973-5000
Phone: (631) 344-3202; Fax: (631) 344-5815
E-mail: knam@bnl.gov

PI: Xiao-Qing Yang
Brookhaven National Laboratory
Chemistry Department
Upton, NY 11973-5000
Phone: (631) 344-3663; Fax: (631) 344-5815
E-mail: xyang@bnl.gov

Start Date: October 2008
End Date: September 2012

Objectives

- Develop new diagnostic techniques with ability to distinguish bulk and surface processes, to monitor the degradation processes, to determine the effects of structural changes of electrode materials, the interfacial phenomena, and electrolyte decomposition on the cell capacity and power fading, as well as on the abuse tolerance for safety characteristic related issues.
- Using diagnostic techniques to evaluate and screen the new materials, material processing and modification procedures which are aimed to improve the performance, calendar and cycling life, and the abuse tolerance of lithium batteries for HEV, PHEV, and EV.
- Using synchrotron based diagnostic tools to study the new high energy density Li_2MnO_3-$LiMO_2$ (M=Ni, Co, Mn) cathode materials, especially the voltage fading problem during cycling.

Technical Barriers

- Li-ion and Li-metal batteries with long calendar and cycle life.
- Li-ion and Li-metal batteries with superior abuse tolerance.
- To reduce the production cost of a PHEV batteries.

Technical Targets

- To develop new *in situ* diagnostic techniques with surface and bulk sensitivity for studying the thermal stability of various cathode materials.
- To establish and investigate the thermal decomposition mechanisms of various cathode materials.
- To understand the voltage fading mechanism of high energy density Li_2MnO_3-$LiMO_2$ (M=Ni, Co, Mn) cathode materials during cycling
- To provide valuable information about how to design thermally stable cathode materials for HEV and PHEV applications.

Accomplishments

- Developed the new diagnostic tool by combining the synchrotron based time resolve XRD (TRXRD) with Mass spectroscopy (MS) to study cathode materials for Li-ion battery during heating aimed at the improvement of the thermal stability.
- Using the newly developed diagnostic tool of combined TRXRD and MS to study overcharged cathode materials such as $Li_xNi_{0.8}Co_{0.15}Al_{0.05}O_2$ (Gen2) and $Li_xNi_{1/3}Co_{1/3}Mn_{1/3}O_2$ (Gen3). The relationship between the structural changes and the gas release of oxygen (and CO_2) at different temperatures during heating has been studied. The effects of these structural changes and the gas releases on the thermal stability of the cathode materials have been obtained.
- Through collaboration with Argonne National Lab. (ANL) and General Motors (GM), and other collaborators, carried out diagnostic studies of new high energy density cathode materials Li_2MnO_3-$LiMO_2$ (M=Ni, Co, Mn) for Li-ion batteries, especially the voltage fading problem during cycling.
- Initiated the studies of new electrolytes and the formation of SEI layers on anode and cathode surface through collaboration with Army Research Lab. (ARL).

✧   ✧   ✧   ✧   ✧

Introduction

Achieving DOE goals of power batteries for HEV, PHEV, and EV require in depth understanding of how to improve rate, capacity and long-term cycling performance. These understandings will provide the guidance on discovery of new materials and new mechanisms. This project has been working on these issues by developing new diagnostic tools to investigate battery materials both *in situ* and *ex situ*, and then applies these to understand relationships between structure and function for new material development.
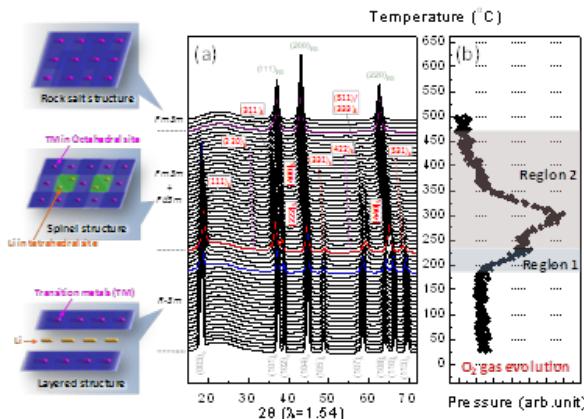
BNL team works closely with other ABRT teams, such as ANL and ARL, as well as with industrial partners, such as GM and Johnson Controls through extensive collaborations.

Approach

- A combination of time resolved X-ray diffraction (TRXRD) and mass spectroscopy (MS), *in situ* and hard X-ray absorption (XAS), *ex situ* soft XAS, *in situ* transmission electron microscopy (TEM) techniques during heating to study the thermal stability of the electrode materials.

- Apply the atomic layer deposition (ALD) technique for the surface modification of new cathode materials, using time resolved X-ray diffraction (XRD) to study the effects of surface modification on the thermal stability.

- *In situ* XRD, soft and hard XAS studies of new electrode materials during charge-discharge cycling to understand the power and energy density fading mechanism for longer cycling life of Li-ion batteries.

- Extended collaborations with other US and international academic institutions and US industrial partners and improving the capabilities of the new diagnostic tools.

Results

In order to understand the thermal degradation of the electrodes in Li-ion cells, we have developed techniques using the combination of the *in situ* time resolved X-ray diffraction (TR-XRD) and mass spectroscopy to study the structural changes and gas evolution during the thermal decomposition of charged cathode materials. Here we report our new studies on the structural changes of layered nickel based cathode materials (e.g., $Li_{1-x}NiO_2$, $Li_{1-x}Ni_{0.8}Co_{0.15}Al_{0.05}O_2$ and $Li_{1-x}Ni_{0.33}Co_{0.33}Mn_{0.33}O_2$) during thermal decomposition. The combined results from TR-XRD coupled with mass spectroscopy technique provide valuable information for the development of new cathode materials as well as for the improvement of thermal stability of the materials being used currently. The middle panel in Figure IV - 210 shows the TR-XRD patterns of $Li_{0.5}Ni_{0.8}Co_{0.15}Al_{0.05}O_2$ in the absence of electrolyte as a function of heating temperature together with the mass spectra (MA) in the right panel. A rapid structural change appeared at about 207°C with oxygen evolution as demonstrated by the MS results shown in the right panel of Figure IV - 210. In the temperature range from 207 to 238°C, the coalescence of the original (108) and (110) forms a new peak (marked as (440)), giving clear indication for the formation of the disordered $LiMn_2O_4$ type spinel phase (space group of *Fd3m*). Heating above 238°C, further decomposition of spinel phase to MO-type with rock-salt structure was formed slowly up to the temperature as high as 500°C. By introducing mass spectroscopy during TR-XRD experiment, we are able to verify and identify the noticeable oxygen gas evolution with these structural changes. Left panel shows the ideal crystal-structure models for rhombohedral-, spinel-, and rock-salt-structures.

Figure IV - 210: (a) Time-resolved (TR) XRD patterns, and, (b) results from simultaneously measured mass spectroscopy (MS) that trace oxygen gas released from the overcharged $Li_{0.33}Ni_{0.8}Co_{0.15}Al_{0.05}O_2$ during heating up to 500 ºC. The cathode sample in a glass tube was heated from 25- to 500-ºC for 4 h during the TR-XRD and MS measurements (heating rate = 2.0 ºC min-1). Left panel shows the ideal crystal-structure models for rhombohedral-, spinel-, and rock-salt-structures.

$$Li_{0.1}Ni_{1/3}Co_{1/3}Mn_{1/3}O_2$$

**Figure IV - 211:** TR-XRD of $Li_{0.1}Ni_{1/3}Co_{1/3}Mn_{1/3}O_2$ (G3) with released oxygen MS during heating.

We also completed the comparison studies on the structural changes of layered nickel based cathode materials between $Li_{1-x}Ni_{0.8}Co_{0.15}Al_{0.05}O_2$ and $Li_{1-x}Ni_{0.33}Co_{0.33}Mn_{0.33}O_2$) during thermal decomposition. Figure IV - 211 and Figure IV - 212 show the comparison of combined TR-XRD patterns with oxygen release from MS for $Li_{0.1}Ni_{0.33}Co_{0.33}Mn_{0.33}O_2$ (Figure IV - 211) and $Li_{0.1}Ni_{0.8}Co_{0.15}Al_{0.05}O_2$ (Figure IV - 212) in the absence of electrolyte as a function of heating temperature. The $Li_{0.1}Ni_{0.33}Co_{0.33}Mn_{0.33}O_2$ sample shows a clear phase transition from O1 structure to the Co_3O_4 type structure starting at about 170 °C and remained in this structure until 550 °C. During this phase transition, the oxygen release from MS shows a quite broad peak. In contrast, for the $Li_{0.1}Ni_{0.8}Co_{0.15}Al_{0.05}O_2$ sample, the phase transition from a hexagonal layered structure with *R3-m* space group at room temperature to the $LiMn_2O_4$-type spinel phase (space group of *Fd3m*) only covers a narrow temperature between 160 to 200 °C, and then quickly changed to the MO-type rock-salt structure. As can be seen in the right panel of Figure IV - 211, the phase transitions of $Li_{0.1}Ni_{0.8}Co_{0.15}Al_{0.05}O_2$, especially the transition to the rock-salt structure are accompanied with a very sharp oxygen release, indicating a poor thermal stability.

We also completed the Time resolved x-ray diffraction (TRXRD) studies of atomic layer deposition (ALD) coated Al_2O_3 on the surface of $Li_{1.2}Ni_{0.17}Co_{0.07}Mn_{0.56}O_2$ new cathode material during heating in FY2012. As shown in Figure IV - 213, at the fully charged state, when heated from room temperature to 600 °C, the uncoated $Li_{1.2}Ni_{0.17}Co_{0.07}Mn_{0.56}O_2$ sample went through a phase transition from layered phase (R-3m) to the spinel phase (Fm3m) starting at around 350 °C. In contrast, the starting temperature for this phase transition from layered to spinel for the fully charged sample with Al_2O_3 ALD coating moved up to 450 °C range, a more than 100 °C increase. These results clearly demonstrated the significant improvement in thermal stability obtained by the ALD coating of Al_2O_3 on the surface of $Li_{1.2}Ni_{0.17}Co_{0.07}Mn_{0.56}O_2$ materials.

We also studied the structural changes of high energy density lithium rich $Li_{1.2}Ni_{0.15}Co_{0.1}Mn_{0.55}O_2$ (Toda HE5050) cathode material during prolonged cycling using *in situ* and *ex situ* synchrotron based X-ray diffraction (XRD) and the relationship between these changes as well as the voltage fading during cycling. As shown in Figure IV - 214, the crystal structural changes during the first cycle are quite similar as the conventional layer structured cathode materials, signature by the expansion of "c" axis and contraction of "a" and "b" axes during charge (and reversing the changing directions during discharge) However, as shown in Figure IV - 215, after 45 cycles. The structural changes exhibit more and more features of spinel-like structured materials, with less and less changes of the "c" axis during charge and discharge.

$$Li_{0.1}Ni_{0.8}Co_{0.15}Al_{0.05}O_2$$
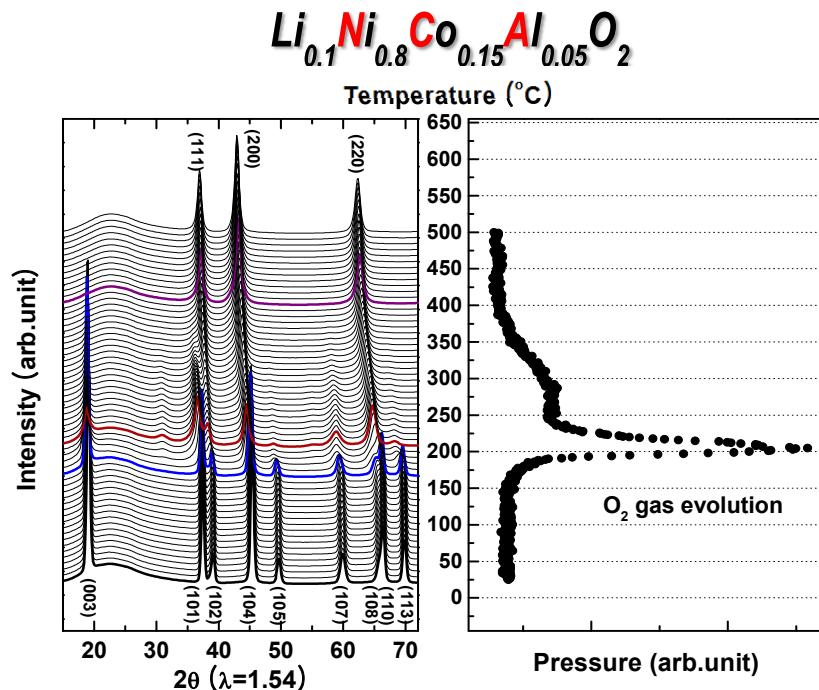
**Figure IV - 212:** TR-XRD of $Li_{0.1}Ni_{0.8}Co_{0.15}Al_{0.05}O_2$ (G2) with released oxygen MS during heating.
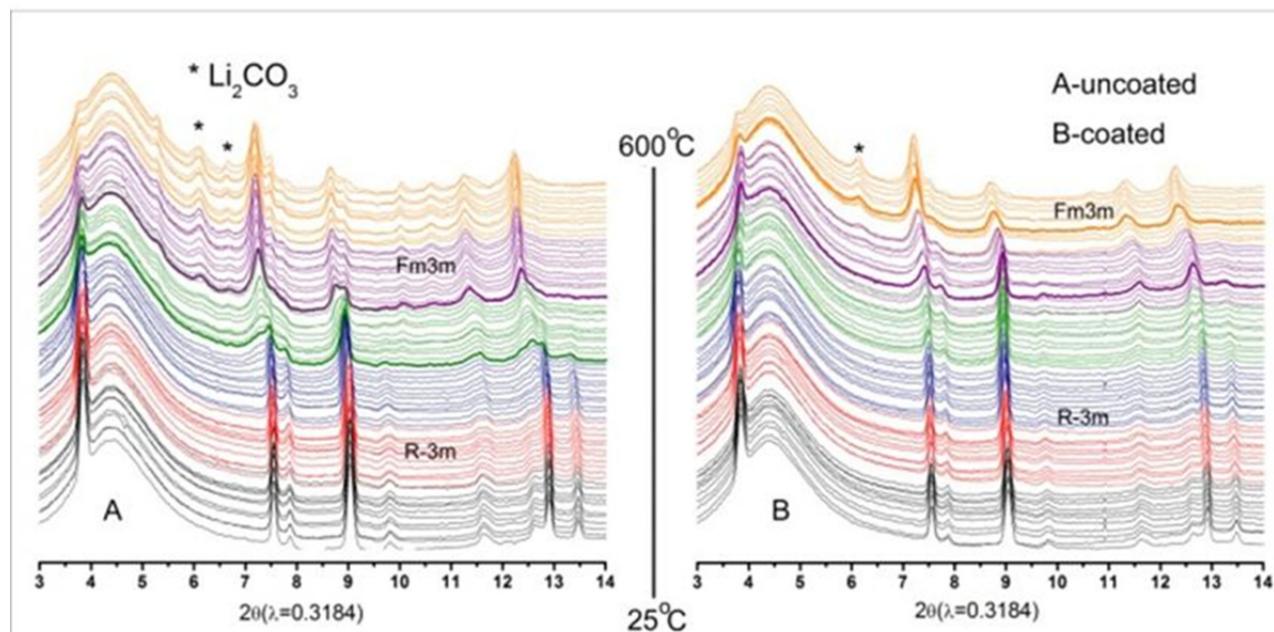
Figure IV - 213: Crystal structure changes of fully charged cathode material $Li_{1.2}Ni_{0.17}Co_{0.07}Mn_{0.56}O_2$ with (B) and without (A) Al_2O_3 ALD coating studied by TR-XRD during heating from 25 °C to 600 °C.
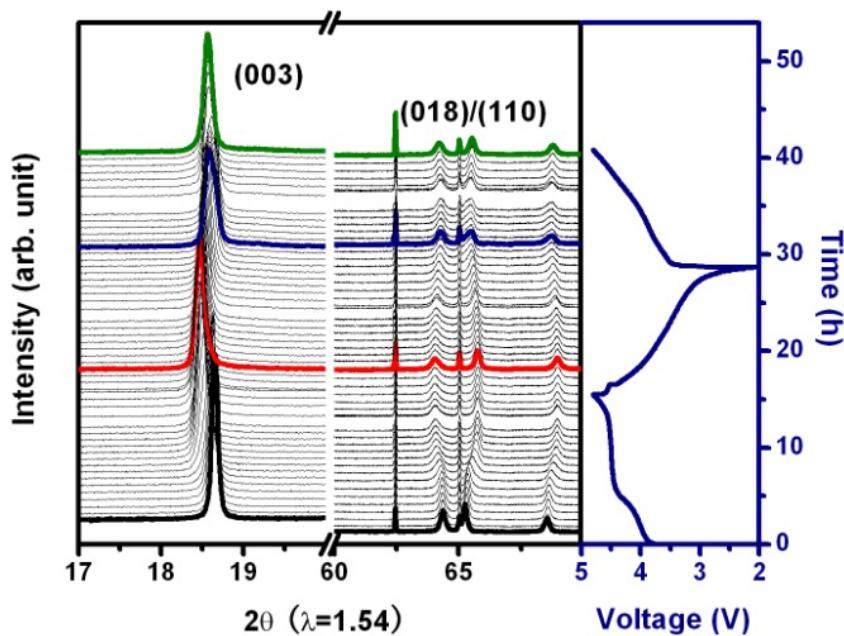
**Figure IV - 214:** Crystal structure changes of Li-rich cathode material $Li_{1.2}Ni_{0.15}Co_{0.1}Mn_{0.55}O_2$ during first one and half charge-discharge cycle.
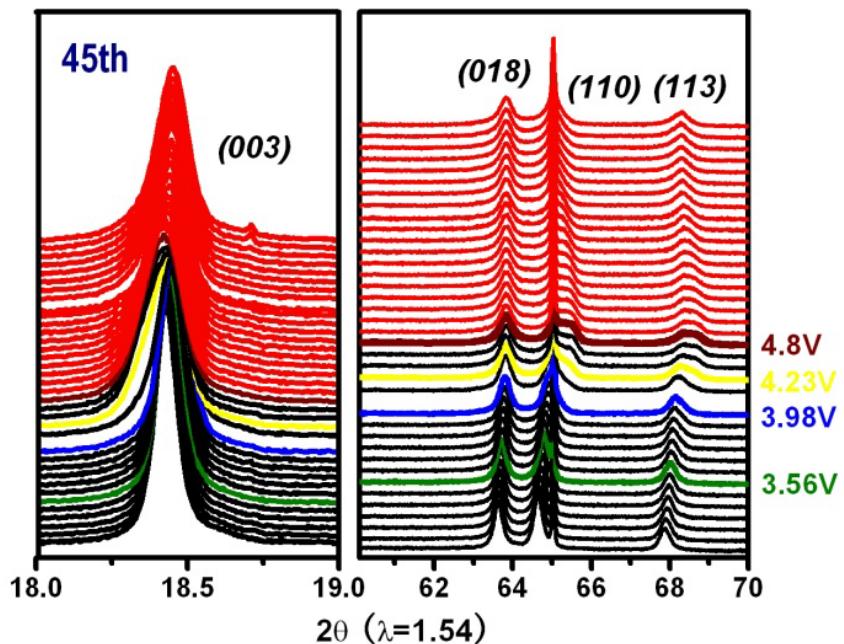
Figure IV - 215: Crystal structure changes of Li-rich cathode material $Li_{1.2}Ni_{0.15}Co_{0.1}Mn_{0.55}O_2$ during 46th charge-discharge cycle.

Conclusions and Future Directions

- In the Multi Year Program Plan (MYPP) of VTP, the goals for battery were described as: "Specifically, lower-cost, abuse-tolerant batteries with higher energy density, higher power, better low-temperature operation, and longer lifetimes are needed for the development of the next-generation of HEVs, PHEVs, and EVs." In this project, progress has been made to achieve these goals through diagnostic studies and collaborations with US industries and international research institutions.

- The BNL team has developed the new diagnostic tool by combining the synchrotron based time resolve XRD (TRXRD) with Mass spectroscopy (MS) to study cathode materials for Li-ion battery during heating. This technique has been used to study the

correlation of crystal structural changes and with oxygen release for $Li_{0.1}Ni_{0.33}Co_{0.33}Mn_{0.33}O_2$ and $Li_{0.1}Ni_{0.8}Co_{0.15}Al_{0.05}O_2$ as a function of heating temperature.

- The Crystal structure changes of fully charged cathode material $Li_{1.2}Ni_{0.17}Co_{0.07}Mn_{0.56}O_2$ with and without Al_2O_3 ALD coating have been studied by TR-XRD during heating from 25 °C to 600 °C.

- Through collaboration with Dr. Amine and Dr. Abraham at ANL and Prof. Hong Li at IOP, CAS in China, BNL team has carried out studies on crystal structural changes during the first cycle and the 46th cycle after extended 45 charge-discharge cycles. The structural changes exhibit more and more features of spinel-like structured materials, with less and less changes of the "c" axis during charge and discharge, with increasing number of cycling.

BNL team will continue the collaboration with ANL, ARL and other ABRT teams, as well as US industrial partners, such as GM and Johnson Control to perform *in situ* diagnostic studies for cathode, anode and electrolyte materials for lithium-ion batteries

FY 2012 Publications/Presentations

1. Won-Sub Yoon, Kyung-Wan Nam, Donghyuk Jang, Kyung Yoon Chung, Seungdon Choi Xiao-Qing Yang, "The Kinetic Effect of Structural Behavior of Mixed $LiMn_2O_4$-$LiNi_{1/3}Co_{1/3}Mn_{1/3}O_2$ Cathode materials studied by Time-Resolved X-ray diffraction technique" *Electrochemistry Communications* Vol. 15, pp 74-77 (2012). doi:10.1016/j.elecom.2011.11.027

2. Kyung-Wan Nam, Songmin Bak, Enyuan Hu, Xiqian Yu, Yongning Zhou, Xiaojian Wang, Lijun Wu, Yimei Zhou, and Xiao-Qing Yang, "Combining *in situ* Synchrotron X-ray Diffraction and Absorption Techniques with Transmission Electron Microscopy to Study the Origin of Thermal Instability in Overcharged Cathode Materials for Lithium-ion Batteries", *Adv. Funct. Mater.*, (2012), 10.1002/adfm.201200693

3. Won-Sub Yoon, Kyung-Wan Nam, Donghyuk Jang, Kyung Yoon Chung, Jonathan Hanson, Jin-Ming Chen, Xiao-Qing Yang, "Structural study of the coating effect on the thermal stability of charged MgO-coated $LiNi_{0.8}Co_{0.2}O_2$ cathodes investigated by *in situ* XRD", *Journal of Power Sources*, **217**, 128-134 (2012).

4. Seong-Min Bak, Kyung-Wan Nam, Won-Young Chang, Xiqian Yu, Enyuan Hu, Soo-Yeon Hwang, Eric A. Stach, Kwang Bum Kim, Kyung Yoon Chung and Xiao Qing Yang, "Thermal Decomposition Mechanism of Charged Cathode Materials for Li-Ion Batteries: New *in situ* Synchrotron XRD coupled with

Mass Spectroscopy study during heating", submitted to *Chemistry of Materials* (2012).

Presentations

1. 2012 DOE Annual Peer Review Meeting Presentation, May 14th-18th 2012, Washington DC.

2. Xiqian Yu, Kaifu Zhong, Xiangbo Meng, Kyung-Wan Nam, Hong Li, Xueliang Sun, and Xiao-Qing Yang, "Studies of Surface Modified $Li_{1.2}Ni_{0.17}Co_{0.07}Mn_{0.56}O_2$ as Cathode Material for Lithium Ion Batteries ", presented at the 220th Meeting of the Electrochemical Society, October 9-14, 2011, Boston, USA.

3. Seongmin Bak. Kyung-Wan Nam, Xiqian Yu, Kyung-Yoon Chung, Kwang Bum. Kim and Xiao-Qing Yang, "Using Combined Time-Resolved XRD and Mass Spectroscopy to Study the Thermal Decomposition Mechanism of Charged Cathode Materials Studied by X-ray Diffraction Coupled with Mass Spectroscopy during Heating", presented at the 220th Meeting of the Electrochemical Society, October 9-14, 2011, Boston, USA.

4. Kyung-Wan Nam, Lijun Wu, Yimei Zhu, Seongmin Bak, Kyung-Yoon Chung, Xiao-Qing Yang, "Structural Changes of Layered Cathode Materials during Thermal Decomposition Studied by Synchrotron Based X-rays and TEM Techniques", presented at International Conference on Advanced Electromaterials (ICAE2011), November 7-10, 2011, Jeju, South Korea**, Invited**.

5. Kyung-Wan Nam, Xiqian Yu, Seongmin Bak, Xiao-Jian Wang, Enyuan Hu, Lijun Wu, Yimei Zhu, Xiao-Qing Yang, Nathalie Pereira, Glenn G. Amatucci, "Application of synchrotron based X-ray techniques to the study of lithium ion battery materials", presented at Samsung Advanced Institute and Technology (SAIT), November 14, 2011, Yongin, South Korea, **Invited**.

6. Kyung-Wan Nam, Xiao-Qing Yang, Xiqian Yu, Xiao-Jian Wang, Enyuan Hu, Seong Min Bak, Kyung-Yoon Chung, Lijun Wu, Yimei Zhu, Nathalie Pereira, Glenn G. Amatucci, "Structural Changes of Cathode Materials for Lithium-ion Batteries during Charge-Discharge Cycling and Heating Studied by Synchrotron-based XRD, X-ray Absorption and TEM", presented at the 2012 Meeting of the International Battery Materials Association (IBA), Kona, Hawaii, January 9-13, 2012**, Invited Keynote Speaker.**

7. Xiqian Yu, Xiao- Qing Yang, Kyung-Wan Nam, Xiaojian Wang, Seong-Min Bak, Xiangbo Meng and Hung-Sui Lee, Hong Li, Xuejie Huang, Clare P. Grey, and Yunxu Zhu, "The Structural changes of Layer and Olivine Structured Cathode Materials for Li-ion Batteries during Charge-discharge Cycling and Heating Studied by Synchrotron Based XRD and XAS", presented at the 2012 MRS Spring Meeting, April 9-13, San Francisco, USA**. Invited.**

8. <u>Xiao-Qing Yang</u>, Kyung-Wan Nam, Xiqian Yu, and Yongning Zhou, "Diagnostic studies of lithium battery materials at Brookhaven National Lab", presented at the" 5th U.S. – China Electric Vehicle and Battery Technology Workshop", Hangzhou, China, April 15-17, **Invited.**

9. <u>Kyung-Wan Nam</u>, Sung-Jin Cho, Frederic Bonhomme, Enyuan Hu, Xiqian Yu, Seongmin Bak, Xiao-Qing Yang, "Structural Investigation of Layered LiNixMnyCozO2 (x+y+z=1) Cathode Materials during charge/discharge using Synchrotron X-ray techniques", (poster) presented at the 16th International Meeting of Lithium Batteries (IMLB-16), June 18 to 22, 2012, Jeju, Korea.

10. <u>Kyung-Wan Nam</u>, Xiqian Yu, Enyuan Hu, Xiao-Qing Yang, Kaifu Zhong, Hong Li, Daniel Abraham, "Structure Evolution and Charge Compensation Mechanism of Li-rich Layered Li1.2Ni0.15Co0.1Mn0.55O2 Cathode Material during Cycling", (poster) presented at the 16th International Meeting of Lithium Batteries (IMLB-16), June 18 to 22, 2012, Jeju, Korea.

IV.D.2 Develop & Evaluate Materials & Additives that Enhance Thermal & Overcharge Abuse (ANL)

Zonghai Chen & Khalil Amine

Argonne National Laboratory
9700 South Cass Avenue
Argonne, IL 60439-4837
Phone: (630) 252-6551
E-mail: Zonghai.chen@anl.gov

Collaborators:
Yang ren, Argonne
Yan Qin, Argonne
Chi-kai Lin, Argonne
Lu Zhang, Argonne
John Zhang, Argonne
Christopher J. Orendorff, Sandia
EnerDel

Start Date: October 2008
Projected End Date: September 2012

Objectives

- Determine the role of cell materials/components in the abuse tolerance of lithium-ion cells.
- Identify and develop more stable materials that will lead to more inherently abuse-tolerant cell chemistries.
- Secure sufficient quantities of these advanced materials (and electrodes) to supply them to Sandia National Laboratories (SNL) for validation and quantification of the safety benefits in 18650-type cells.

Technical Barriers

- Determine role of the solid-electrolyte interface (SEI) layer on carbon anodes in cell safety.
- Determine role of cathode in cell safety.
- Provide overcharge protection of lithium-ion batteries.

Technical Targets

- Understand the response of the SEI layer to thermal abuses.
- Develop functional additives that enhance the stability of the SEI layer.
- Understand the response of cathode materials to thermal abuses.

- Develop functional protection strategies to enhance the thermal stability of batteries.
- Benchmark and develop advanced redox shuttles to improve the overcharge tolerance of lithium-ion batteries.

Accomplishments

- An *in situ* high energy X-ray diffraction (HEXRD) technique was successfully established to study the thermal decomposition pathway of electrolyte materials.
- The *in situ* HEXRD study revealed that the continuous heat generation of lithiated graphite, with the presence of a non-aqueous electrolyte, was caused by the delithiation of the anode to form new SEI layer.
- Investigation on delithiated $Li_{1-x}[Ni_{1/3}Mn_{1/3}Co_{1/3}]_{0.9}O_2$ revealed that $LiPF_6$ plays a negative role on the thermal stability of the delithiated NMC cathode.
- The investigation on delithiated composite materials (HE5050) clearly indicated that the thermal stability of the materials decreases with the upper working potential.
- *In situ* HEXRD study also revealed local heat deposition at the anode side when a redox shuttle was activated to provide overcharge protection.

✧　　✧　　✧　　✧　　✧

Introduction

The safety of lithium-ion batteries is currently the major technical barrier for their application in hybrid electric vehicles and plug-in hybrid electric vehicles. Understanding the mechanism of thermal runaway reactions is a key to develop advanced technologies that improve the abuse tolerance and mitigate the safety hazard of lithium-ion batteries.

Approach

The following approaches are being taken to tackle the safety issue of lithium-ion batteries:

- Understanding the impact of graphite surface functional groups on the safety of lithium-ion cell.
- Develop synthesis route to alternate the surface functional groups on resulted natural graphite.

- Exploring new redox-shuttle materials to (a) improve the overcharge protection of lithium batteries and (b) achieve automatic capacity balancing of battery packs.

- Quantifying the role of the additives and surface area of carbon on 18650-type cells in collaboration with SNL.

Results

Establishment of *in situ* High Energy X-ray Diffraction (HEXRD). Figure IV - 216 shows the setup for *in situ* high energy X-ray diffraction during thermal ramping of a DSC sample. The material required for the experiment can be down to 1 mg, and one XRD pattern will be collected every 20 seconds. Figure IV - 217 shows a picture of a special design of sample holder to maintain the electrode material in the detection zone of high energy X-ray during thermal abuse, as well as an exemplary HEXRD pattern of delithiated $Li_{1-x}[Ni_{1/3}Mn_{1/3}Co_{1/3}]_{0.9}O_2$ (charged to 4.1 V vs. Li^+/Li). The diffraction peaks of layered materials can be clearly indexed as shown with red labels in Figure IV - 217.
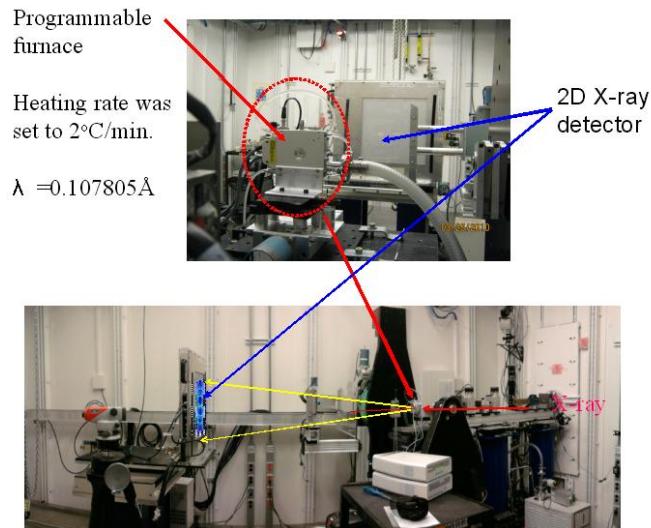
Figure IV - 216: Picture of *in situ* XRD set up at APS.
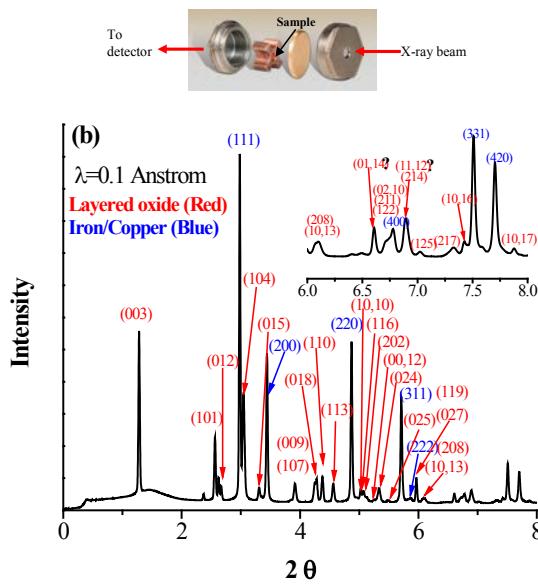
Figure IV - 217: Image of the sample holder used for *in situ* high energy X-ray diffraction, and an exemplary high energy X-ray diffraction pattern that was fully indexed with sample holder and layer lithium transition metal oxide.

In situ HEXRD study continuous formation/decomposition of SEI layer. The *in situ* XRD technique was also applied to study the thermal decomposition of solid electrolyte interface (SEI) as shown in Figure IV - 218. The (002) peaks for graphite, LiC_{12}, and LiC_6 are labeled on Figure IV - 218. After full intercalation, only LiC_6 and LiC_{12} were presented in the anode electrode. When the temperature was below 110^oC, only lattice expansion was observed for LiC_6 and LiC_{12}, but no change on concentration. When the temperature was above 110^oC, when SEI decomposition was triggered, the intensity of LiC_6 and LiC_{12} decreased, and the diffraction peak of graphite appeared at about 250^oC, when the SEI decomposition finished. It is clear that lithium was continuously consumed during SEI decomposition.
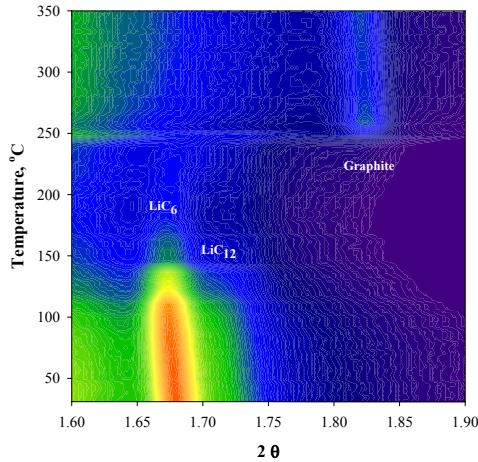

Figure IV - 218: Contour plot of *in situ* HEXRD data during thermal decomposition of lithiated graphite.

In situ HEXRD study the impact of LiPF₆. With the help of *in situ* HEXRD, we have investigated the thermal decomposition of delithiated $Li_{1-x}(Ni_{1/3}Mn_{1/3}Ni_{1/3})O_2$ (@ 4.1 V) at different environments. Figure IV - 219 shows the 2D contour plot of *in situ* XRD data collected during the thermal decomposition of delithiated NMC (charged to 4.1 V). The characteristic peaks (101) and (012) for layer materials are labeled on Figure IV - 219a. It clearly shows that the material decomposed at about 180^oC. Figure IV - 219b shows the *in situ* HEXRD data for delithiated NMC mixed with solvent only, no $LiPF_6$; it shows that the thermal decomposition of delithiated NMC started at about 280^oC, about 100^oC than that of the sample with $LiPF_6$. In order to confirm the finding, $LiPF_6$ was replaced with LiTFSI, $LiBF_4$ and $Li_2B_{12}F_{12}$, respectively. Figure IV - 219c shows a typical result of that containing LiTFSI instead of $LiPF_6$. It can be seen that the thermal decomposition started at about 240^oC. It is clear that lithium salt plays an important role on the thermal stability of delithiated cathodes, and $LiPF_6$ is responsible for a relatively low thermal stability of delithiated cathodes.
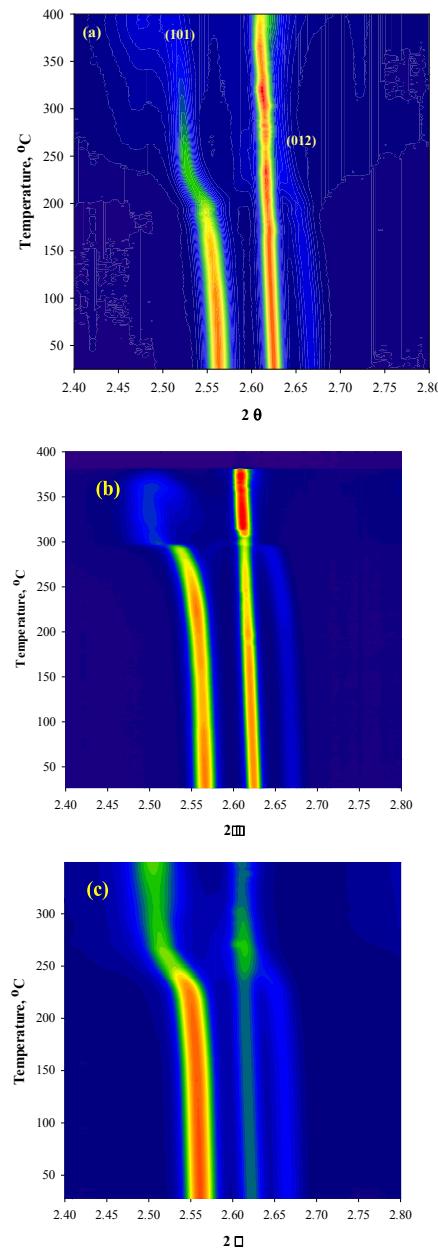

Figure IV - 219: Contour plot of *in situ* HEXRD data during thermal decomposition of delithiated NMC with the presence of (a) 1.2 M $LiPF_6$ in EC/EMC (3:7, by weight), (b) EC/EMC (3:7, by weight), and (c) 1.0 M LiTFSI in EC/EMC (3:7, by weight).

In situ HEXRD study the thermal decomposition of composite material HE5050 $(0.5Li_2MnO_3 \bullet 0.5LiNi_{0.375}Mn_{0.375}Co_{0.25}O_2)$. Figure IV - 220a shows a comparison of HEXRD patterns for delithiated HE5050 $(0.5Li_2MnO_3 \bullet 0.5LiNi_{0.375}Mn_{0.375}Co_{0.25}O_2$, charged to 4.6 V vs. Li^+/Li) after being thermally abused at different chemical environments. The composition is further summarized in Table IV - 14. When no solvent or electrolyte was added to the delithiated HE5050 sample, the material converted to M_3O_4 spinel structure after the thermal abuse, and M_3O_4

type structure was maintained up to 400°C. However, rock-salt type $M_xNi_yCo_{1-x-y}O$ (M=Mn and Co) and $MnCO_3$ was detected when an equivalent amount of solvent (EC/EMC 3:7 by weight) was added to the sample. With the presence of electrolyte (1.2 M $LiPF_6$ in EC/EMC, 3:7 by weight), the final product is $M_xNi_{1-x}O$, $MnCO_3$ and MnF_2. Figure IV - 220b shows the *in situ* HEXRD profile of the sample with the presence of non-aqueous electrolyte and during the thermal abuse. It was found that the layered structure converted to regular spinel structure (LiM_2O_4) at about 206°C and that the regular spinel structure converted to M_3O_4 type spinel at about 234°C. At 310°C, the material finally decomposed into $MnCO_3$, $M_xNi_{1-x}O$ and MnF_2. This mechanism is further summarized in Figure IV - 220c.
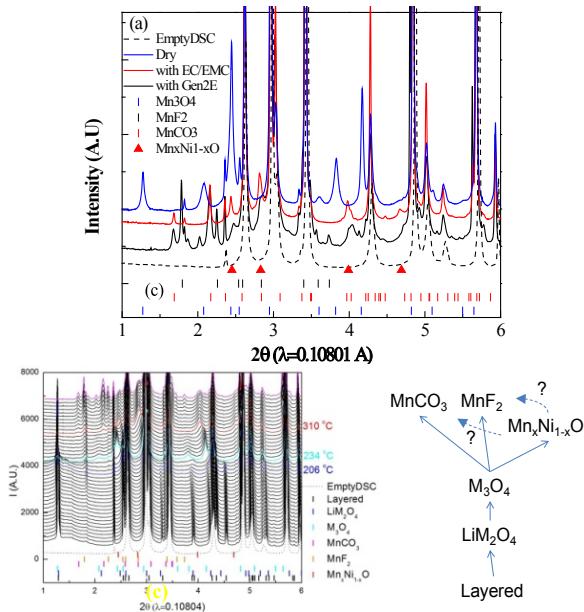

Figure IV - 220: (a) Comparison of HEXDRD patterns of abused delithiated HE5050 (charged to 4.6 V vs. Li+/Li) showing that the decomposition pathway strongly depended on the chemical environmental it was exposed to, (b) *in situ* HEXRD pattern of delithiated HE5050 with the presence of electrolyte, and (c) proposed decomposition pathway for delithiated HE5050 with the presence of electrolyte.

Table IV - 14: Decomposition products of delithiated HE5050 (charged to 4.6 V vs. Li+/Li) after thermal abuse.

	$M_xNi_{1-x}O$	$MnCO_3$	MnF_2	M_3O_4-type
With Gen2E	Yes	Yes	Yes	No
With EC/EMC	Yes	Yes	No	No
Dry	No	No	No	Yes

Figure IV - 221 shows a comparison of thermal decomposition of delithiated HE5050 as a function of upper cutoff voltage and with the presence of 1.2 M $LiPF_6$

in EC/EMC (3:7 by weight). It was clear that the thermal stability of the delithiated HE5050 decreased steadily with the increase of the cutoff voltage. When the cutoff voltage was limited to 4.4 V vs. Li+/Li, the material started to decompose at about 280°C, and this onset temperature decreased to 250°C, 230°C, and 210°C respectively when the cutoff voltage was increased to 4.5 V, 4.6 V and 4.8 V.
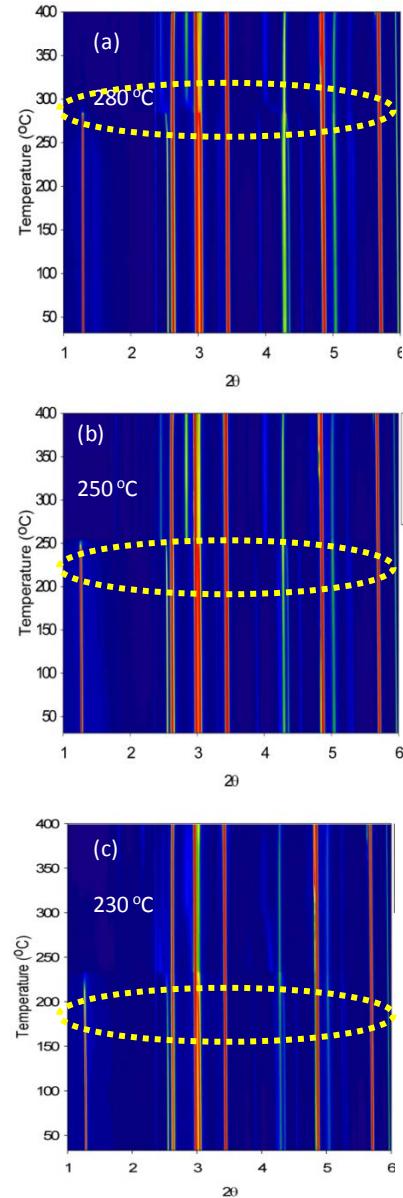

Figure IV - 221: Contour plot of *in situ* HEXRD data during thermal decomposition of delithiated HE5050 charged to (a) 4.4 V, (b) 4.5 V, (c) 4.6 V, and (d) 4.8 V with the presence of 1.2 M $LiPF_6$ in EC/EMC (3:7, by weight).

***In situ* HEXRD study the local heta deposition of redox shuttles.** Figure IV - 222a shows a schematic energy diagram illustrating the potential impact of this heat generation. In general, under normal conditions, the energy level of the electrons in the anode is higher than that in the cathode, and the energy level of the highest occupied

molecular orbital (HOMO) of the redox shuttle is lower than that of the electrons in the cathode. During normal charge, the external charger keeps pumping electrons from the cathode to the anode (Figure IV - 222a, top). The redox shuttle remains inactive since the energy level of its HOMO is still lower than that in the cathode. When the cell is overcharged, the electron level in the cathode is drained to a level below the HOMO of the redox shuttle, which then donates an electron to the cathode to prevent over draining of electrons from the cathode. The redox shuttle with singly occupied HOMO then diffuses to the anode and obtains an electron from the anode. Transferring electrons over the huge energy gap between the anode and the redox shuttle (~4.5 eV) leads to the generation of heat or breaking of chemical bonds at the anode side (Figure IV - 222a, bottom). To validate this mechanism, we prepared a 180 mAh pouch cell using $LiMn_2O_4$ as the cathode and $Li_4Ti_5O_{12}$ as the anode. The electrolyte was 0.4 M $Li_2B_{12}F_9H_3$ in EC/EMC (3:7, by weight). After being charged/discharged for 2 cycles between 1.5 V and 2.8 V using a constant current of 0.2 A, the cell was continuously charged at a constant current of 0.2 A for 90 minutes, leading to about 50% overcharge. Figure IV - 222b shows a contour plot of spectra around the (111) peak of aluminum between 2.64° and 2.66°. It can be seen that the lattice parameter of aluminum did not change throughout the experiment. However, the (111) peak of copper shifted towards smaller angles when the cell was overcharged at about 0.8 hours; this peak shift was caused by the thermal expansion of copper when the cell was overcharged (see Figure IV - 222c). This finding confirms that the activation of the redox shuttle deposits a large amount of heat at the anode side and can lead to thermal decomposition of the conventional SEI layer.

Conclusions and Future directions

Using *in situ* HEXRD, we were able to demonstrate that the thermal stability of charged battery materials was kinetically governed by the charge/mass transfer through the interfacial layer between the electrode materials and the electrolyte. As we will push the boundary to develop high energy density chemistries, we will not be able to have the luxury to use intrinsically safe materials like $Li_4Ti_4O_{12}$ or $LiFePO_4$. Therefore, we suggest that proper surface modifications be the future direction to further improve the safety of future high energy chemistries, for both cathodes and anodes.
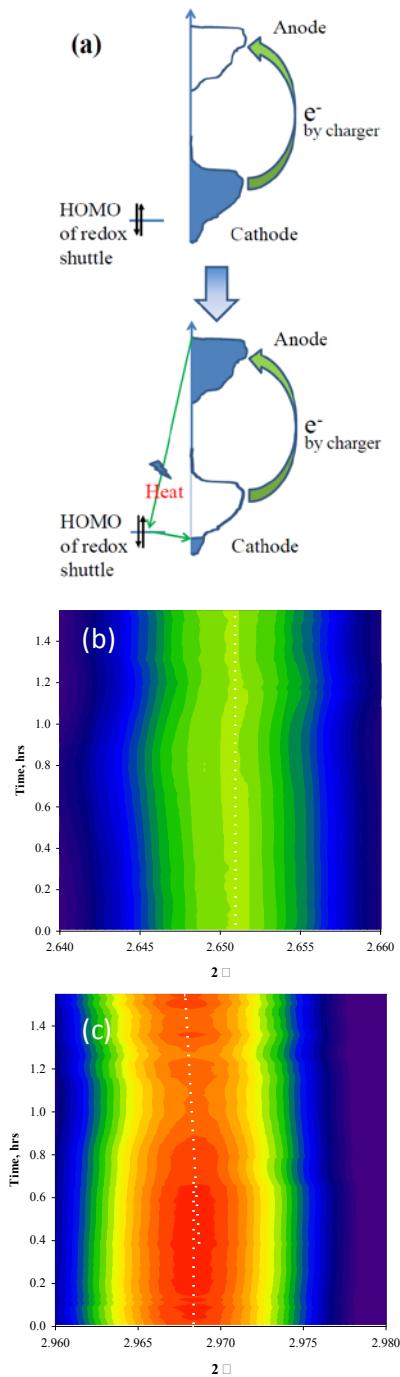

Figure IV - 222: (a) Schematic energy diagram illustrating the potential heat generation at the anode side. *In situ* HEXRD profiles of a $Li_4Ti_5O_4/LiMn_2O_4$ cell during overcharge test showing the lattice variation of (b) Al and (c) Cu. The electrolyte was 0.4 M $Li_2B_{12}F_9H_3$ in EC/EMC (3:7, by weight). The current was 0.2 A (~1C).

FY 2012 Publications/Presentations

1. 2012 DOE Annual Peer Review Meeting presentation.
2. Z. H. Chen, Y. Ren, E. J. Lee, C. Johnson, Y. Qin, and K. Amine, Study of Thermal Decomposition of $Li_{1-x}(Ni_{1/3}Mn_{1/3}Co_{1/3})_{0.9}O_2$ Using *In situ* High-Energy

X-ray Diffraction, to be submitted to *Adv. Ener. Mater.*, (**2012**).

3. Z. H. Chen, Y. Ren, A. N. Jansen, C. K. Lin, W. Weng, and K. Amine, New class of nonaqueous electrolytes for long life and safe lithium-ion batteries, submitted to *Nat. Comm.*, (**2012**).

4. Y.-K. Sun, Z. H. Chen, H.-J. Noh, D.-J. Lee, H.-G. Jung, Y. Ren, S. Wang, C. S. Yoon, S.-T. Myung, and K. Amine, Nano-Structured High-Energy Cathode Materials for Advanced Lithium Batteries, *Nat. Mater.*, (in press) (**2012**).

5. N.-S. Choi, Z. H. Chen, S. A. Freunberger, X. L. Ji, Y.-K. Sun, K. Amine, G. Yushin, L. F. Nazar, J. Cho, and P. G. Bruce, Challenges Facing Lithium Batteries and Electrical Double-Layer Capacitors, *Angew. Chem. Int. Ed.*, 51:9994–10024 (**2012**).

6. Z. H. Chen, I. Belharouak, Y.-K. Sun, and K. Amine, Titanium-Based Anode Materials for Safe Lithium-Ion Batteries, *Adv. Func. Mater.*, in press, (**2012**).

7. Z. H. Chen, A. N. Jansen and K. Amine, Novel functionalized electrolyte for MCMB/Li$_{1.156}$Mn$_{1.844}$O$_4$ lithium-ion cells, *Energy Environ. Sci.*, 4:4567-4571 (**2011**).

8. K. Amine, Z. H. Chen, Z. Zhang, J. Liu, W. Q. Lu, Y. Qin, J. Lu, L. Curtis, and Y.-K. Sun, *J. Mater. Chem.*, 21:17754-17759 (**2011**).

IV.D.3 Impact of Materials on Abuse Response (SNL)

Christopher J. Orendorff, Kyle R. Fenton, Josh Lamb, Ganesan Nagasubramanian, Travis Anderson

Sandia National Laboratories
P. O. Box 5800, Mail Stop 0614
Albuquerque, NM 87185-0614
Phone: (505) 844-5879; Fax: (505) 844-6972
E-mail: corendo@sandia.gov

Collaborators:
Argonne National Laboratory
Idaho National Laboratory
National Renewable Energy Laboratory
Binrad Industries

Start Date: October 2011
Projected End Date: September 2012

Objectives

- Elucidate degradation mechanisms in lithium-ion cells that lead to poor abuse tolerance (runaway thermodynamics, gas evolution, electrolyte combustion).
- Develop and evaluate advanced materials (or materials combinations) that will lead to more abuse tolerant lithium-ion cell and battery systems.
- Build 18650 cells in the SNL fabrication facility for cell level evaluation of new materials in support of all ABR thrust areas.

Technical Barriers

There are several technical barriers to achieving the goals stated above including:

- Develop lithium-ion cells that are intrinsically abuse tolerant and do not lead to high order catastrophic failures.
- Mitigate the gas evolution and decomposition of the electrolyte.
- Passivation of cathode runaway reactions and interfacial reactions with electrolyte.
- Limited quantities of advanced materials (and numbers of cells with new materials) to evaluate abuse response.

Technical Targets

- Quantify the thermal runaway response of materials at the cell level (18650).

- Determine the effect of electrolyte salts, solvents and additives on the abuse response of lithium-ion cells.
- Evaluate the thermal response of candidate active materials.
- Identify materials that could be used to reduce gas evolution and the heat and kinetics of runaway reactions.

Accomplishments

- Continued evaluation of candidate electrolytes and salts that minimize the energetics of thermal runaway.
- Evaluation of additives, electrode coatings, and new materials to improve abuse response and safety of lithium-ion systems.
- Enhanced synthesis capability, and understanding of mechanism for anion binding agents (ABA) used with LiF in carbonate electrolytes for improved cell runaway response.
- Fabricated electrodes to aid in standardization of ABR materials across national laboratories (round robin).

✧　　✧　　✧　　✧　　✧

Introduction

As lithium-ion battery technologies mature, the size and energy of these systems continues to increase (> 50 kWh for EVs); making safety and reliability of these high energy systems increasingly important. While most materials advances for lithium-ion chemistries are directed toward improving cell performance (capacity, energy, cycle life, etc.), there are a variety of materials advancements that can be made to improve lithium-ion battery safety. Issues including energetic thermal runaway, electrolyte decomposition and flammability, anode SEI stability, and cell-level abuse tolerance continue to be critical safety concerns. This report highlights work with our collaborators to develop advanced materials to improve lithium-ion battery safety and abuse tolerance and to perform cell-level characterization of new materials.

Approach

The effect of materials (electrolytes, additives, anodes, and cathodes) on the thermal response of full cells is determined using several techniques. One of the most useful and quantitative techniques is accelerating rate calorimetry (ARC). The ARCs at SNL are fitted with uniquely designed high pressure fixtures to not only measure quantitative heat flow but also gas generation under ideal adiabatic conditions during full cell runaway. Cells were fabricated using a variety of active materials,

electrolytes, and additives in the SNL cell prototyping facility. The in-house prototyping capability gives us the versatility to target candidate materials, perform full cell evaluation, and correlate cell response to fundamental materials properties.

Abuse tolerance tests are performed which evaluate the response to expected abuse conditions and document and evaluate numerous outcomes including 1) failure point of energy storage device 2) conditions that cause failure 3) failure modes and abuse conditions using destructive physical analysis (DPA) 4) quantitative cell or module response to the abuse condition 5) provide feedback to develop new abuse test procedures that more accurately determines cell performance under the most likely abuse conditions.

Possible tests that can be performed cover three main categories of abuse conditions. Mechanical abuse tests include controlled crush, penetration, blunt rod, drop, water immersion, mechanical shock and vibration. Thermal abuse tests include thermal stability, simulated fuel fire, elevated temperature storage, rapid charge/discharge, and thermal shock cycling. Electrical Abuse tests include overcharge/overvoltage, short circuit, overdischarge/voltage reversal, and partial short circuit.

Potential for cells to be exposed to overcharge conditions is becoming a greater concern as electric vehicle designs call for larger and larger battery packs. While control hardware is in place to limit the exposure of cells to overcharge, issues such as overcharge due to cell imbalance exist. This has driven an effort to develop inherently safe cell chemistries. In this work a redox shuttle additive developed at Argonne National Laboratory is tested under overcharge abuse conditions. This is evaluated in particular for potential heat generation from the redox shuttle, with the primary concern being that the additional heat generated may send 18650 sized (and larger) cells into runaway.

Results

Electrode fabrication and testing for full cell evaluations. The SNL cell prototyping facility is fully equipped with three 18650 cell winders (in two separate dry rooms), two prototype-scale electrode coaters, electrode slitter, semi-automatic tabber, and an electrolyte filling station to support the ABR program cell thermal characterization and abuse tolerance of new materials in cells. These fabrication efforts have been instrumental for testing many materials developments that focus on the reducing cell and pack level abuse response. Fabrication efforts for the ABR program vary annually, but are approximately 75 cells (18650) per year.

The ABR program is working toward a common electrode formulation and performance to standardize results across multiple laboratories. Electrodes were fabricated at SNL using the agreed upon formulation and

processing by ABR participants. Figure IV - 223 shows specific capacity per cycle for the $LiNi_{0.5}Co_{0.2}Mn_{0.3}O_2$ cathodes fabricated during the round robin testing in 2032 coin cells vs. lithium. Validation and performance comparison is being conducted at ANL to ensure that all electrode fabrication efforts and collected data across the entire ABR program will be standardized and comparable.
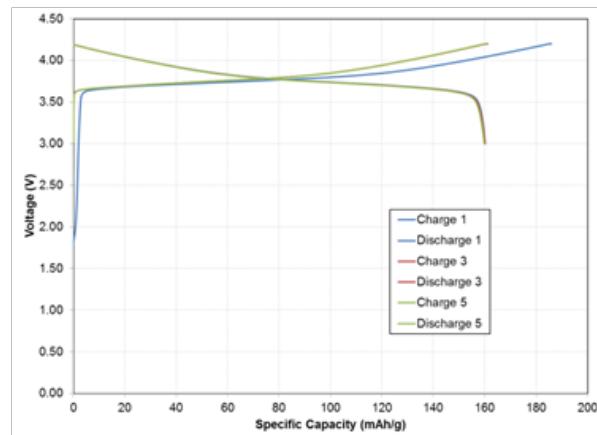

Figure IV - 223: Round robin NMC 523 cathode performance during formation cycling.

ABR abuse testing for round robin effort. Abuse analysis was performed on 300 mAh prismatic cells manufactured at Argonne National Laboratory. Tests performed included overcharge abuse, mechanical nail penetration, thermal ramp and external short circuit.

Figure IV - 224 shows the results of the mechanical nail penetration test applied to the prismatic pouch cell. The nail puncture created a vigorous internal short immediately with accompanying thermal runaway. A peak temperature of 225 $^\circ$C was observed during the initial stages of runaway. No voltage recovery was observed upon removing of the nail.
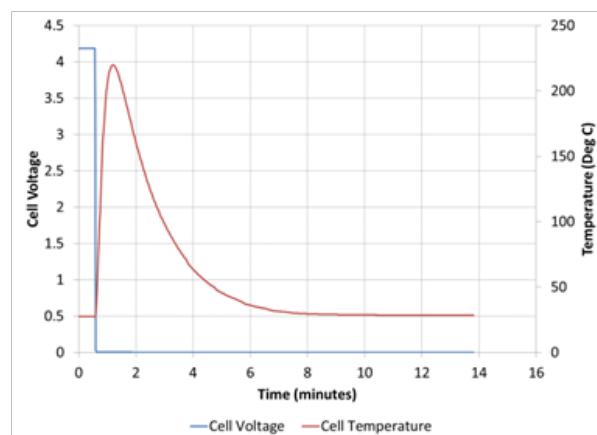

Figure IV - 224: Cell response to sharp nail penetration of 300 mAh prismatic pouch cell.

Flammability testing and ARC measurements of INL developed phosphazene electrolytes. Phosphazene electrolytes have been developed at INL and were tested at the Battery Abuse Testing Laboratory at SNL. 18650 size cells were fabricated using NMC 111 cathodes and Conoco Phillips anodes for ARC testing. Figure IV - 225 shows the ARC performance for the 3 phosphazene based electrolytes compared with baseline carbonate electrolyte. The phosphazene additive resulted in a reduction of the peak heating rate and total enthalpy during runaway. The tradeoff for enhanced abuse tolerance is a slight reduction in cell capacity, as seen in Figure IV - 226.

Flammability tests were also performed on the INL developed phosphazene electrolytes. These tests consisted of 18650 cans with 5 mL of electrolyte set into a heater block with an ignition sources approximately 3 inches from the header of the 18650 can. This setup is used so that when the cell vents, the spray of electrolyte from the cell will immediately come in contact with the ignition source. The PhIL-2 additive showed a significant reduction in the burn time compared to the baseline and other additives, which suggests some reduction in flammability of that electrolyte formulation.
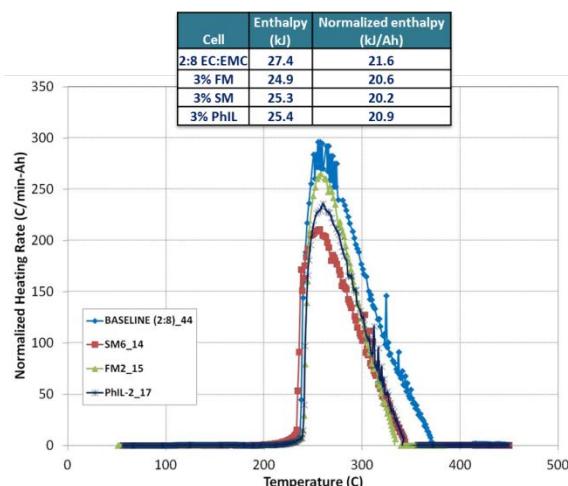

**Figure IV - 225:** ARC performance of INL synthesized phosphazene electrolytes.
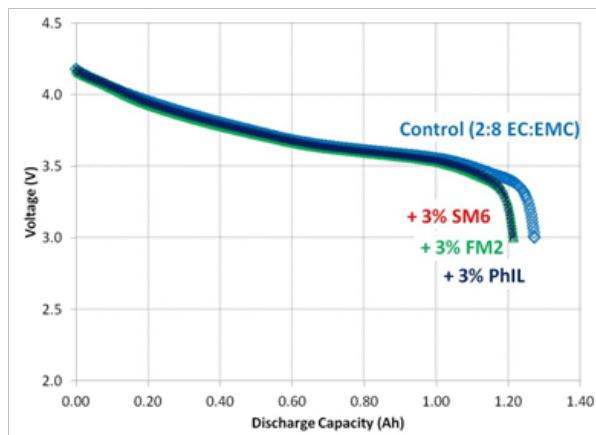
Figure IV - 226: Full cell performance comparison for 18650 cells using phosphazene electrolytes.

18650 Abuse evaluation of cells containing a redox shuttle for overcharge protection. A redox shuttle developed at ANL, RS2, was evaluated for overcharge protection in 18650 cells. Cells containing 0.2 M of the additive in the electrolyte and cells without (control) were constructed both at Sandia as well as at A123. These cells were evaluated under overcharge abuse conditions, under isothermal battery calorimetry and under imbalanced conditions in a two-cell series pack.

Figure IV - 227 shows the behavior for 18650 cells with 0.2M RS2 redox shuttle additive under overcharge abuse as well as control cells without the additive. The cells were charged to 100% SOC followed by a 1 amp overcharge rate (nominally 1C). The control cell failed after 130% SOC with temperature peaking at 105 $^{\circ}$C before cell failure. The cell containing the RS2 shuttle quickly reached a steady state voltage of 3.9V and remained reasonably constant until the test was terminated at 260% SOC. The cell temperature rose gradually until reaching a steady state of 82 $^{\circ}$C. Battery cycling performed after this overcharge test gave a capacity of 980 mAh, showing little degradation in capacity from the test.
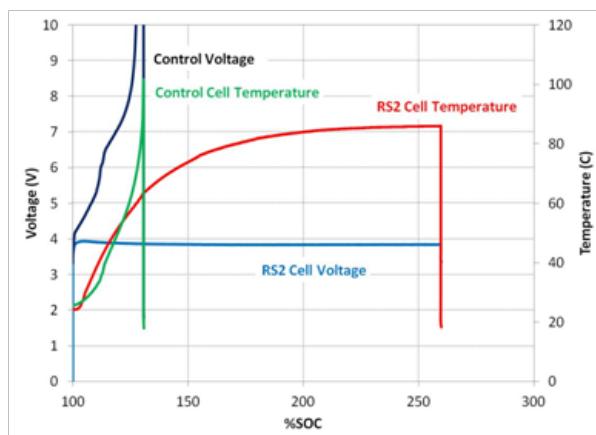

Figure IV - 227: Overcharge abuse behavior of control cells (18650, nom. 1 Ah) as well as cells containing 0.2 M RS2 overcharge shuttle additive.

Two cells in series were charged at a 10% cell imbalance as seen in Figure IV - 228. Cell 1 was initially charged to 100% SOC, while Cell 2 was charge to 100% followed by discharge to bring it to 90% SOC. The two cell series string was then charged at 200 mA (nominally C/5). Cell 1 reached a steady state voltage of 3.8 V after 15 minutes of charge. The cells were brought into balance after 40 minutes of charging as Cell 2 reached 3.8 V as well. The cell temperatures did not climb significantly above room temperature, with the highest peaking at 35 °C.
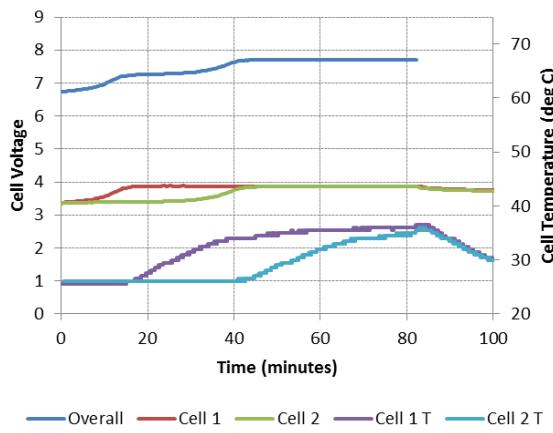

Figure IV - 228: Imbalance charging of a 2-cell series string at 200 mA. Cell 1 was initially at 100% SOC while Cell 2 was initially at 90% SOC.

Materials for enhanced abuse tolerance performance. The use of lithium fluoride (LiF) electrolyte salt has been considered as an alternative to $LiPF_6$ because of its chemical and thermal stability, but early generation anion binding agents (ABAs, used to improve LiF solubility) were large molecules that were inapplicable to lithium-ion cell systems (large molecular weights, low rate capability, low conductivity, voltage instability, etc.). In collaboration with Binrad Industries we have developed LiF/ABA salts for lithium-ion cells to show improved thermal stability and to eliminate some of the shortcomings of using $LiPF_6$ salts.

Figure IV - 229 shows heat flow as a function of temperature as measured by differential scanning calorimetry (DSC) for a variety of cathode materials using the 1M LiF – 1M ABA salt in EC:EMC (3:7 wt%). For comparison, the DSC for $LiNi_{1/3}Co_{1/3}Mn_{1/3}O_2$ using traditional 1.2M $LiPF_6$ in EC:EMC (3:7 wt%) is shown in dark blue. While the onset temperature for runaway using the ABA material is slightly depressed, there is a significant reduction in the overall heat output when using the ABA electrolyte.
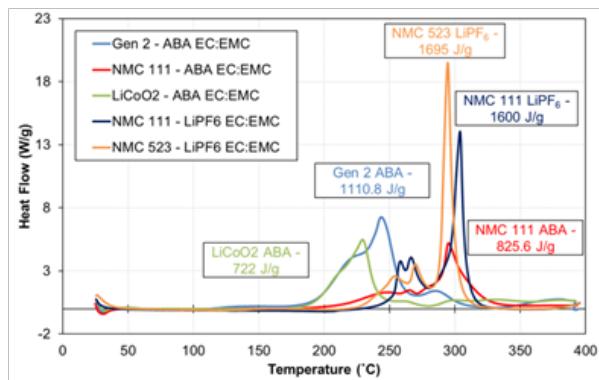

Figure IV - 229: Differential scanning calorimetry results for a variety of cathode materials with 1M ABA: 1M LiF electrolyte in EC:EMC solvent. For comparison, the DSC result for the same electrode material using 1.2 M $LiPF_6$ is also shown (dark blue).

In an effort to understand the mechanism for the overall heat reduction, XPS was performed on cathodes fabricated using both ABA and $LiPF_6$ based electrolytes that have been exposed to runaway scale temperatures (250 °C). The development of new peaks in the Co 2P spectra for both $LiNi_{1/3}Co_{1/3}Mn_{1/3}O_2$ (111) and $LiNi_{0.5}Co_{0.2}Mn_{0.3}O_2$ (523) in ABA electrolyte at approximately 786 eV and 803 eV indicate elevated amounts of oxidized cobalt at the surface of the electrode. This effect was not seen in samples that did not see runaway like temperatures. Samples containing the $LiPF_6$ electrolyte for both NCM 111 and 523 showed no difference in the XPS spectra before and after exposure to elevated temperatures. Efforts for next year will include elucidating the preferential oxidation for the cobalt and how that is facilitated by the ABA molecule.

Additional efforts to develop intrinsically non-flammable electrolytes with enhanced abuse tolerance performance have focused on ionic liquids as an alternative to the carbonate systems. Electrochemical stability studies identified a candidate material, exhibiting 200 µA cm^{-2} peak currents at potentials up to 5V vs Li/Li$^+$. To increase cell performance, the TFSI based ionic liquid was blended with an aliquot of $LiPF_6$ salt to create a blended salt ionic liquid electrolyte with only slightly diminished electrochemical performance as compared to the standard EC:EMC electrolyte, see Figure IV - 230. This can be partially attributed to the viscosity, which is slightly under 100 cP at room temperature, but remains lower than many of the other candidate ionic liquids.
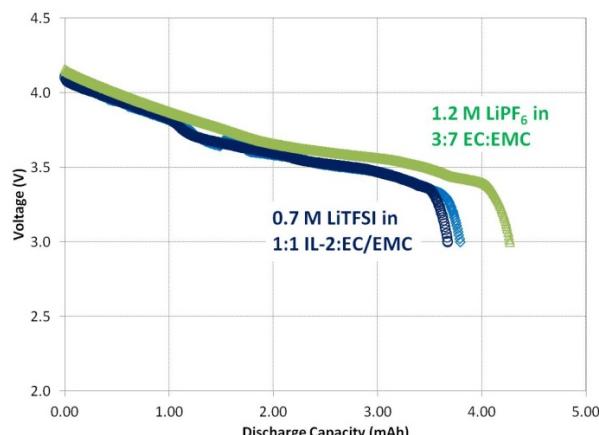
Figure IV - 230: Discharge curve comparison of full cells tested using standard LiPF$_6$ electrolyte and a blended ionic liquid / carbonate electrolyte.

Conclusions and Future Directions

Electrode and cell fabrication efforts have been conducted to enable testing of numerous materials with a focus on enhanced abuse tolerance characteristics. In order to compare program wide, an effort for fabrication and performance standardization was made. The resulting cells were tested for performance and abuse tolerance. This is an example of the potential path forward for emerging materials to benefit the ABR program. Future work will involve larger capacity cells using the new ABR standard formulation to better characterize electrochemical performance, abuse tolerance, and lifetime degradation.

Fabrication and testing efforts were to support a wide variety of project throughout the ABR program. Evaluation of program developed electrolytes was demonstrated with the INL developed phosphazene electrolytes. Cell fabrication, ARC evaluation, and flammability testing were performed, resulting into improved understanding of phosphazene electrolyte behavior.

Abuse and balancing performance of ANL developed redox shuttle RS2 were tested. Overcharge testing on cells containing the redox shuttle RS2 were found to be fairly resilient to overcharge abuse. In particular, because the voltage remains relatively low, the total power input into a cell is somewhat limited under constant current overcharge. The temperatures were not observed to reach high enough levels to initiate a thermal runaway. While little to no capacity degradation was observed in the cell exposed to a 1C overcharge, the temperature reached was high enough it may cause capacity degradation if exposed for a long period of time. Cells in series were found to fully rebalance with sufficient charge time, with little additional heat generation.

The development of anion binding agents has resulted in materials which exhibit lower overall heat output during a thermal runaway event. Confirmation of this has been demonstrated in DSC and ARC evaluations. While the

exact mechanism remains unclear, the full cell evaluations have clearly shown the benefits to using an alternative electrolyte to the carbonates and LiPF$_6$. Future efforts will be made to expand the synthesis of ABA and ionic liquids for electrolyte evaluations. Scale up efforts for these alternative electrolyte materials has potential for future inter-laboratory collaborations within the ABR program.

FY 2012 Publications/Presentations

1. J. Orendorff "A Materials Approach to Abuse Tolerant Lithium-ion Cells" International Battery Association, Waikoloa, HI, January 10, 2012.
2. J. Orendorff "Safety Performance Advancements for Large Scale Lithium-ion Batteries Through Materials Development" SAE 2012 Government Industry Meeting, Washington, DC, January 26, 2012.
3. J. Orendorff "Abuse Tolerance Improvements" DOE Annual Merit Review, Washington, DC, May 17, 2012.

IV.D.4 Overcharge Protection for PHEV Cells (LBNL)

Guoying Chen
Thomas Richardson

Lawrence Berkeley National Laboratory
Environmental Energy Technologies Division
Berkeley, CA 94720
Phone: (510) 486-5843; Fax: (510) 486-5467
E-mail: GChen@lbl.gov
        TJRichardson@lbl.gov

Start Date: October 1, 2009
Projected End Date: March 31, 2013

Objectives

- Develop and implement an inexpensive, long-lasting mechanism that provides self-actuated, reversible and high-rate overcharge protection for high-energy lithium-ion batteries intended for PHEV applications.

Technical Barriers

- Abuse tolerance
- Safety
- Poor cycle life

Technical Targets

- Improved rate capability and cycle life of overcharged Li-ion cells.

Accomplishments

- Achieved 40-fold increase in sustainable current density by using electroactive-polymer composites with fibrous membrane substrates.
- Demonstrated stable long-term overcharge protection for several cell chemistries for the first time, with more than one hundred overcharged cycles completed so far.
- Developed a low-cost electrospinning technique to prepare dense polymer-fiber-composite mats capable of high-rate overcharge protection.
- Demonstrated the effectiveness of using the electrospun-composite separator for overcharge protection in Li-ion cells.

✧   ✧   ✧   ✧   ✧

Introduction

The term "overcharge" is used to describe a variety of conditions, including simple charging at normal rates beyond rated capacity, overvoltage excursions for short or long periods, charging at a rate too high for one electrode (commonly the anode) without exceeding the maximum voltage, and other more complex scenarios. While overcharging is still a major safety issue for lithium batteries, it also has a major impact on battery life. Even slight overcharging reduces the discharge capacity of a cell, potentially causing overdischarging, increased impedance, and local heating. Battery packs for consumer electronics are protected by electronic controls and by internal shutdown mechanisms like melting separators and pressure or temperature-activated disconnects. In a multicell stack capable of delivering several hundred volts, permanently shutting down a cell reduces the usable capacity of the stack and adds to the burden of the remaining cells in parallel circuit. Complex re-routing of current around overcharged cells is impractical in these stacks. Internal protection mechanisms that maintain a cell's potential and discharge capacity can provide protection without adding substantially to the size, weight, or volume of the stack.

The electroactive-polymer approach, developed at LBNL, protects cells by forming a reversible resistive shunt between the current collectors during overcharging. The process is self-activated by voltage, and it does not pose interference during normal cell charge and discharge. Unlike the commonly used redox shuttle method, it conducts overcharge current through an electronic rather than a diffusional path, and therefore is capable of high-rate and low-temperature protection. The polymer can be added to cells in a variety of configurations, opening the possibility for cell designs that best accommodate heat transfer during overcharging. Conversely, overheating in internal redox shuttle protected cells can only be avoided by restricting the cell to low cycling rates.

Approach

Electroactive-polymers are used as self-actuating and reversible overcharge-protection agents. The redox window and electronic conductivity of the polymer are fine-tuned to avoid interference with a given battery chemistry's normal operation. The polymer composite morphology and cell configuration are optimized to maximize the battery's rate capability and cycle life.

Results

Glass-fiber supported electroactive-polymer composites. To investigate the effect of morphology on

the sustainable overcharge current density of electroactive-polymer impregnated composites, non-woven membrane substrates were investigated. Three types of commercial glass-fiber membranes, Whatman GF/D, GF/A, and GF/C, with compressed thicknesses of 160, 85 and 85um, respectively, were evaluated. Compared to the previously used Celgard 2500 membrane, the glass membranes had more open pore structures and higher porosities, as shown in the SEM images in Figure IV - 231. The fiber diameters in GF/C were noticeably smaller.
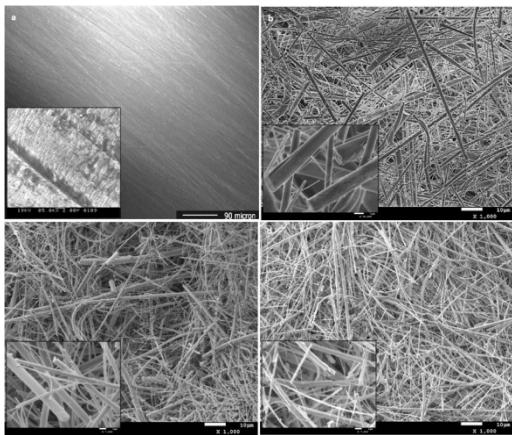

Figure IV - 231: SEM images of the membrane substrates: (a) Celgard 2500, b) GF/D-type, (c) GF/A-type, and (d) GF/C-type glass-fiber membranes.

Composite separators were prepared by solution impregnating poly(3-butylthiophene) (P3BT) into the Celgard and glass-fiber membranes at a weight loading of 5%. Figure IV - 232a shows the performance of the P3BT-GF/C composite at different current densities, evaluated in a "Swagelok-type" cell with the composite membrane as cathode and Li foil as the anode and reference electrode. The cell maintained steady-state potentials by shorting through the conductive polymer at constant current densities up to 20 mA/cm^2. Figure IV - 232b compares the sustainable current densities of the P3BT composites on various substrates. All glass-fiber composites performed better than the Celgard separator, which was limited to a maximum current density of 0.5 mA/cm^2. GF/D and GF/A supported composites sustained current densities of 10 mA/cm^2. The cell potentials were noticeable lower for GF/A because it is nearly half as thick as GF/D. With GF/C composite sustaining a current density of 20 mA/cm^2, it is 40 times higher than for the Celgard composite (Figure IV - 232b). The superior performance of the GF/C composite was attributed to more uniformly-distributed smaller fibers that created a better pore structure for the distribution and utilization of the electroactive-polymer. These results demonstrate the importance of controlling the morphology of the electroactive composites.
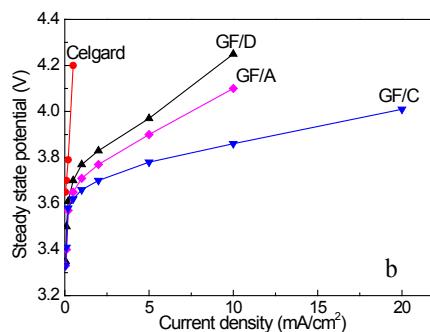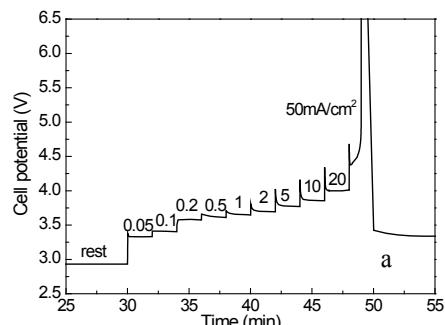

Figure IV - 232: (a) Voltage profile of the P3BT-GF/C composite at the indicated current densities and (b) comparison of the sustainable current densities achieved by the P3BT composites on various substrates.

The cycleability of lithium-ion cells that were protected by the glass-fiber supported electroactive-polymer composites was investigated. Composite separators were prepared by solution impregnating either poly[(9,9-dioctylfluorenyl-2,7-diyl)] (PFO) or P3BT into Whatman GF/D-type glass-fiber membranes. The typical polymer loadings were 1.3 and 0.67 mg/cm^2 for PFO and P3BT composites, respectively. A bilayer configuration with the PFO composite adjacent to the cathode and the P3BT composite adjacent to the anode was used. Figure IV - 233, Figure IV - 234, and Figure IV - 235 show the room-temperature cycling performance of the protected LiFePO$_4$, spinel Li$_{1.05}$Mn$_{1.95}$O$_4$ and LiNi$_{0.33}$Co$_{0.33}$Mn$_{0.33}$O$_2$ (Gen3) half cells with lithium metal counter and reference electrodes, respectively. The LiFePO$_4$ cell was cycled at a 0.5C rate and 80% overcharge. A steady state potential at 4.4 V was reached and maintained, indicating that a soft short was established and that overcharge current passed through the conducting polymers (Figure IV - 233a). Reversible protection was achieved, and the cell has maintained its discharge capacity for 160 cycles with nearly no sign of performance deterioration (Figure IV - 233b). The spinel Li$_{1.05}$Mn$_{1.95}$O$_4$ cell was cycled at a 0.2C rate and 60% overcharge (Figure IV - 233a). The upper potential limit increased to 4.5 V due to the increased current density, and the cell has maintained its discharge capacity for more than 120 cycles (Figure IV - 233b). Figure IV - 235 shows the testing

results of the Gen3 cell at 0.5C and 50% overcharge. A steady state potential at 4.35 V was maintained for nearly 200 overcharged cycles so far. The ability of the electroactive-polymers to provide prolonged overcharge protection for lithium-ion batteries was clearly demonstrated in these studies.
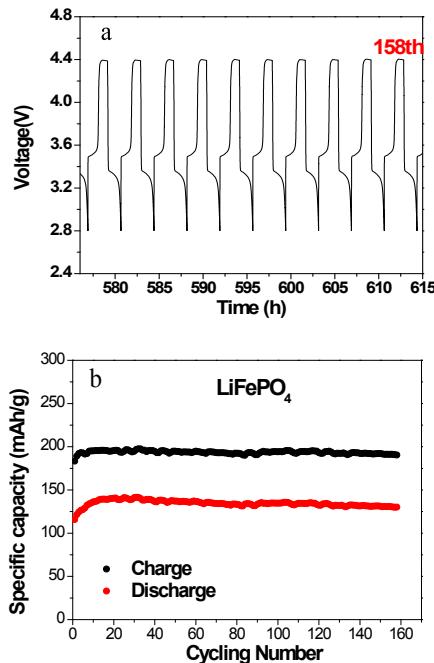

Figure IV - 233: (a) Voltage profile and b) cycling capacities of the polymer-protected cell with a LiFePO₄ cathode.
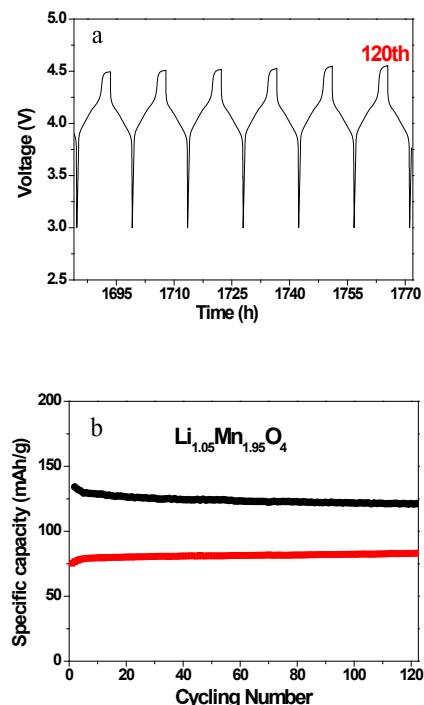

Figure IV - 234: (a) Voltage profile and b) cycling capacities of the polymer-protected cell with a spinel Li$_{1.05}$Mn$_{1.95}$O$_4$ cathode.
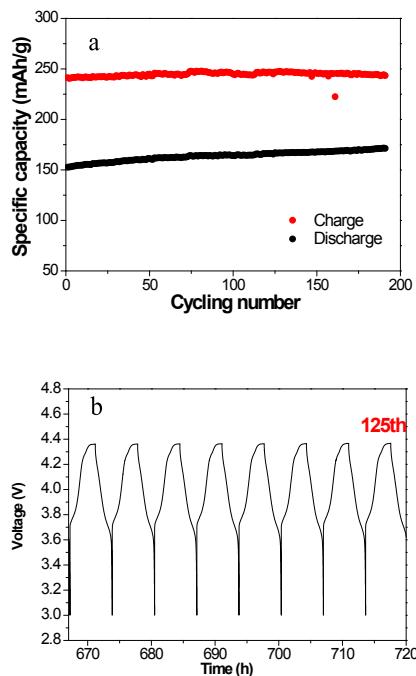

Figure IV - 235: (a) Voltage profile and b) cycling capacities of the polymer-protected cell with a LiNi$_{0.33}$Co$_{0.33}$Mn$_{0.33}$O$_2$ (Gen3) cathode.

Electrospun-polymer-composites. The team previously demonstrated that non-woven electroactive-fiber-composite mats with high porosities and an open pore structures can be produced by electrospinning. Despite the dilution of electroactive-polymer within an inert polymer matrix, *in situ* optical experiments confirmed that charge carriers propagate rapidly within the fibers and across the interconnected fibers. Synthesis conditions were explored to prepare uniform fiber composites with varying degrees of fiber-level mixing between the electroactive and supporting polymers. Figure IV - 236a shows the SEM image of a composite consisting of electroactive P3BT and poly(ethylene-oxide) (PEO) in a weight ratio of 3:1. The fibers have an average diameter of 1 μm, with solvent evaporation during the electrospinning process leaving behind 100 nm pores on the fiber surfaces. Energy dispersive X-ray spectroscopy (EDS) elemental mapping of O and S, which were used to locate PEO and P3BT, respectively, indicated that the two polymers in this composite are intimately mixed at the individual fiber level (Figure IV - 236b and Figure IV - 236c). The even distribution of the electroactive polymer can be expected to improve its utilization and reduce the overall cost of overcharge protection in rechargeable lithium-ion batteries.
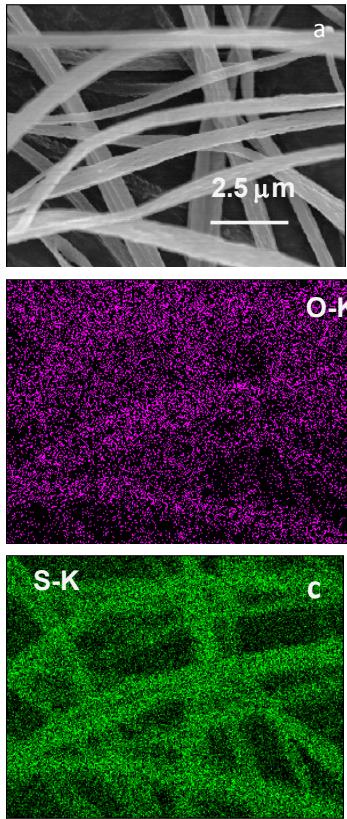
Figure IV - 236: SEM image a) and EDS maps of oxygen b) and sulfur c) of a P3BT and PEO composite prepared by electrospinning.

Dense electroactive-fiber membranes, suitable for use as lithium battery separators, were prepared by electrospinning. Figure IV - 237a shows a 25 μm-thick composite membrane composed of PFO and PEO in a weight ratio of 1:3. Initial results for a $Li_{1.05}Mn_{1.95}O_4$ half-cell protected by a bilayer separator consisting of the PFO/PEO fiber membrane and a P3BT/glass-fiber composite are shown in Figure IV - 237b. When cycled at a C/3 rate and 50% overcharge, a steady state was reached at 4.6 V, and the cell maintained its discharge capacity for more than 50 cycles. Compared to previous composites prepared with a microporous Celgard membrane, these nonwoven membranes provided electronic and dendritic barriers with lower ionic resistance, enabling faster charge and discharge for increased power density. The study suggests that electrospinning can be a cost-effective way to produce lithium-ion battery separators capable of voltage-regulated shunting. In May 2012, this technology was filed in U.S. Patent Application 61/647,389, titled "High-Rate Overcharge-Protection Separators for Rechargeable Lithium-ion Batteries and the Methods of Making the Same".

Conclusions and Future Directions

A 40-fold increase in sustainable current density was achieved when electroactive-polymer composites were prepared on a glass-fiber instead of a microporous

membrane substrate. Excellent long-term overcharge protection was realized in several cell chemistries, including LiFePO₄, spinel $Li_{1.05}Mn_{1.95}O_4$ and Gen3. Dense yet highly porous electroactive-polymer-fiber-composite mats were prepared by an electrospinning process and used as battery separators capable of overcharge protection. A method to achieve overcharge protection in a cost-effective and configuration-flexible way was developed.
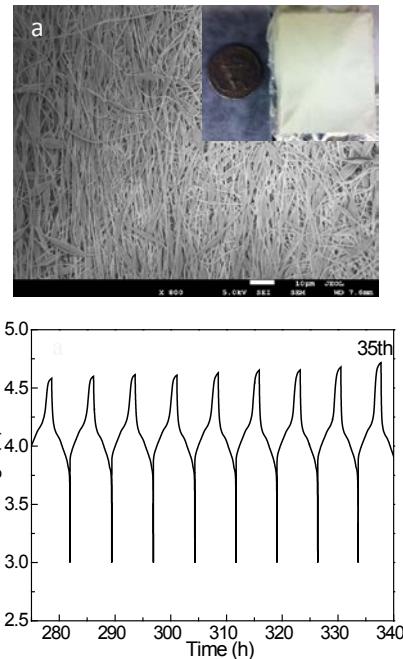

Figure IV - 237: a) SEM and digital (inset) images of the PFO and PEO composite separator and b) cycling voltage profiles of a protected $Li_{1.05}Mn_{1.95}O_4$ half-cell.

Future work will evaluate the rate capability and cycle life of the cells protected by the electrospun electroactive-fiber-separators. Alternative polymer placement in the cells that may lead to improved protection and lowered cost will be accessed. Other high-voltage electroactive-polymers that are suitable for overcharge protection for PHEV batteries will be explored, and their composite morphologies will be optimized for maximum protection. Overcharge protection for the cells with other high-voltage cathodes, particularly the Li and Mn rich $Li_{1+x}M_{1-x}O_2$-type cathodes, will be investigated. Collaboration with industry and other labs will be pursued to evaluate the scalability of overcharge protection based on the "fiber-composite-membrane-separator" approach.

FY 2012 Publications/Presentations

Presentations
1. 2011 DOE Annual Peer Review Meeting Presentation.

Patents

1. G. Chen and T. Richardson, "High-Rate Overcharge-Protection Separators for Rechargeable Lithium-Ion Batteries and The Methods of Making The Same," U.S. Patent Application 61/647,389, May 2012.

IV.E Applied Research Facilities

IV.E.1 Battery Materials Pilot Production Facility

IV.E.1.1 Process Development and Scale up of Advanced Cathode Materials (ANL)

Gregory K. Krumdick

Argonne National Laboratory
9700 South Cass Avenue
Argonne, IL 60439-4837
Phone: (630) 252-3952; Fax: (630) 252-1342
E-mail: gkrumdick@anl.gov

Collaborators:
Young Ho Shin, Argonne National Laboratory
Kaname Takeya, Argonne National Laboratory
Gerald Jeka, Argonne National Laboratory
Mike Kras, Argonne National Laboratory
Wenquan Lu, Argonne National Laboratory

Start Date: June 2010
Projected End Date: September 2013

Objectives

The objective of this task is to conduct process engineering research for scale-up of Argonne's next generation high energy cathode materials. These materials will be based on NMC chemistries and may include lithium rich technology, layered–layered and possibly layered–spinel classes of cathode materials.

Most of these advanced cathode materials have only been synthesized in small batches. Scaling up the process involves modification of the bench-scale process chemistry to allow for the semi–continuous production of materials, development of a process engineering flow diagram, design of a mini-scale system layout, construction of the experimental system and experimental validation of the optimized process. The mini system will be assembled utilizing an existing synthesis reactor system. Cathode materials produced will be analyzed to confirm material properties and for quality assurance. The electrochemical properties of the material will be validated to confirm a performance match to the original materials.

Technical Barriers

Processes for the production of next-generation high-energy cathode materials have been developed only at the bench scale. Sufficient quantity of material cannot be generated for prototype testing, which is required prior to scaling the process to the next level. Therefore, pilot-scale facilities are required for battery materials scale-up research and development.

Technical Targets

- Using the carbonate process, scale-up the synthesis $Li_{1.14}Mn_{0.57}N_{i0.29}O_2$ cathode material. Generate multiple kilogram samples with the ability to control particle size and tap density while maximizing electrochemical performance and cycle life.

- Establish the capability to fabricate and test coin cells to expedite the scale-up process.

- Relocate interim labs to the Materials Engineering Research Facility (MERF).

Accomplishments

- Work on scaling $Li_{1.14}Mn_{0.57}N_{i0.29}O_2$ by the carbonate process has been completed. Multiple kilogram batches have been generated.

- A technique was identified and validated to overcome the particle growth issue, providing accurate particle size distribution control.

- A technique was identified and validated to increase tap density.

- Coin cell fabrication and testing capabilities were established.

- The cathode analytical lab was relocated to the MERF.

✧   ✧   ✧   ✧   ✧

Introduction

Researchers in the battery materials programs across the DOE complex refer to scale up as synthesis of battery materials in gram quantities, and with time consuming, multiple small-scale runs. There is a need to develop scale-up processes for battery materials (primarily lithium-ion based batteries) to the kilogram and tens-of-kilograms quantities at DOE labs to support the transition of these technologies to industry. Currently, there is no systematic engineering research capability or program across the DOE complex or in industry to identify and resolve constraints to the development of cost-effective process technology for the high-volume manufacture of these advanced materials.

Approach

Next generation cathode materials have been developed at the bench scale by a number of researchers focusing on developing advanced lithium-ion battery materials. Process engineers will work with these researchers to gain an understanding of the materials and bench-scale processes used to make these materials and then scale–up and optimize the processes. Standard chemical engineering unit operations will be utilized to develop flexible systems that will enable scaling of a wide range of next generation high energy cathode materials.

Results

During Q1, it was reported that carbonate process optimization for the synthesis of $Li_{1.14}Mn_{0.57}Ni_{0.29}O_2$ on the 4L system was completed and work had begun on scaling the process to the 20L system. A primary issue identified on the 4L system was the fact that prior to reaching steady state, particles continued to grow past the optimal size forming a mixture of sized particles both larger and smaller than optimal, with a D50 particle size of 28.2 μm at steady state. (Figure IV - 238). A technique was identified and tested to overcome this issue to allow for continuous processing.
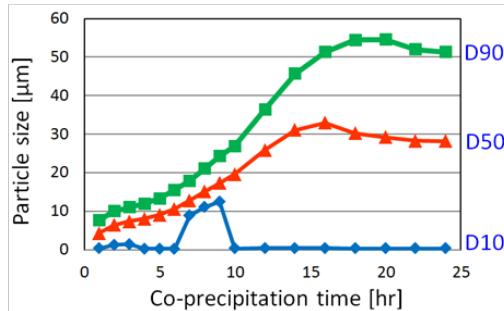

Figure IV - 238: Particle size distribution without growth control technology.

During Q2, the method for the prevention of plugging was revised to improve control of particle size,

distribution and morphology and was tested on the 20L system. Excellent control of particle size was obtained (Figure IV - 239) and a 1kg finished cathode material sample was generated (lot #2012-02-22) and delivered to the Materials Screening group for electrochemical evaluation. This material had a D50 particle size of 15.6 μm and a tap density of 1.36. Although we were able to obtain good coin cell results with this material, the particles showed signs of fracturing during pouch cell processing (Figure IV - 240). It is believed that this fracturing caused the material to show poor rate capability and was unable to handle a 5C or 3C HPPC test.
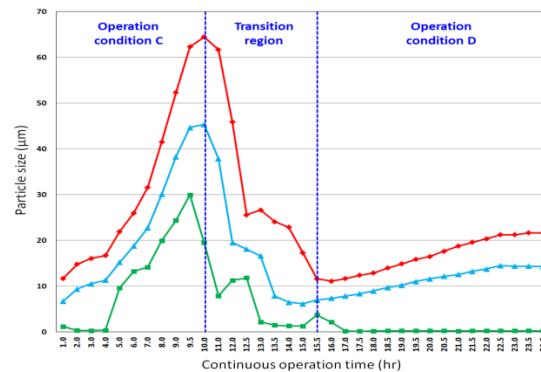

**Figure IV - 239:** Particle size distribution with growth control technology.
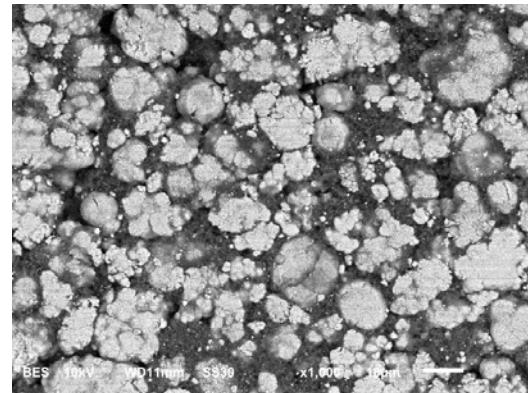
Figure IV - 240: Fractured cathode particles from calendaring from lot#2012-02-22.

During Q3, 5kg $Li_{1.39}Ni_{0.33}Mn_{0.67}O_y$ spherical precursor (#2012-07-09&11) with a narrow particle size distribution and smaller D50 particle size (7.8 μm) with a tap density of 1.49 was prepared to attempt to minimize fracturing during the calendar process. Coin cell result shows that cycle and C-rate performances are good (Figure IV - 241). 1C and 2C are 195 and 180mAh/g. C/3 is kept over 190mAh/g for 100 cycles. 10% capacity loss is occurred between 21 and 94 cycles.
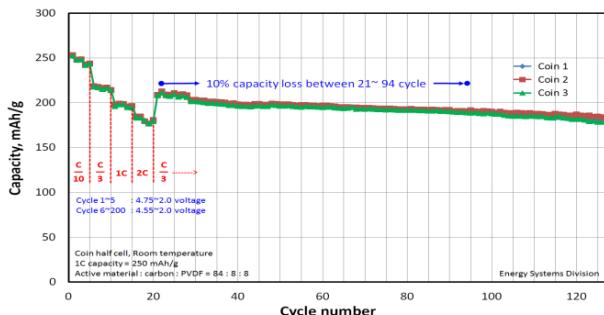
Figure IV - 241: Coin cell results from lot#2012-07-09&11.

During Q4, a 1kg sample of cathode material ($Li_{1.39}Ni_{0.33}Mn_{0.67}O_y$) was delivered to the Material Screening group for electrochemical validation from lot#2012-07-09&11 (Figure IV - 242). We were recently informed that this material also is fracturing (Figure IV - 243). We are still waiting on electrochemical test results, but we anticipate issues due to the cracking.
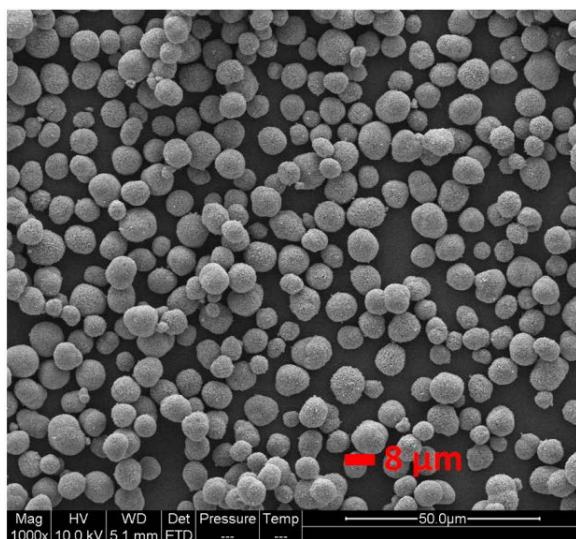

Figure IV - 242: 1kg lot #2012-07-09&11 delivered to Material Screening.
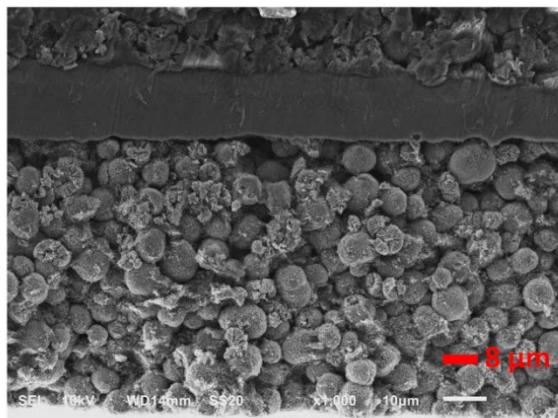

Figure IV - 243: Fractured cathode particles from calendaring from lot#2012-07-09&11.

At this time, we conducted an optimization study of the material's tap density. Various sized cathodes ($Li_{1.39}Ni_{0.33}Mn_{0.67}O_y$) were prepared by carbonate process in small quantity to evaluate the size effect on tap density. Tap density increases to 1.74g/ml when the particle size of cathode increases as shown in Figure IV - 244. To get higher tap density, 7.1μm cathode (sample 1) and 16.7μm cathode (sample 5) were mixed up at 2:8 ratio and the tap density of this mixture reaches to 1.89g/ml (8.6% increase). Figure IV - 245 shows that cycle performances are almost same independent of particle size. Maximum possible tap density of $Li_{1.39}Ni_{0.33}Mn_{0.67}O_y$ prepared by carbonate process is reported to be 1.8~2.0g/ml.

Figure IV - 244: Tap density optimization.
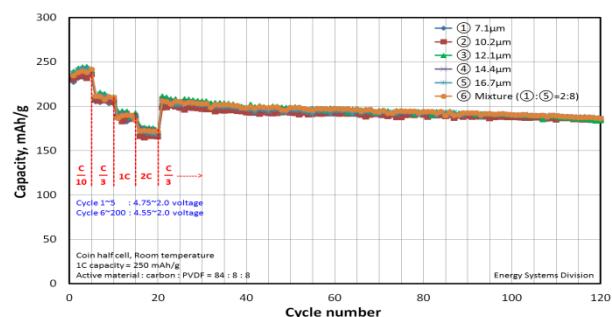
Figure IV - 245: Coin cell results after tap density optimization.

Carbonate Precursor Synthesis. An additional task that was started during Q4 was the synthesis of $MnCO_3$ and Li_2MnO_3 carbonate precursors of a specific particle size for use on a basic research project. The synthesis process technology we developed enables the generation of materials of a specific size distribution, something rather difficult to do on a small scale. We have synthesized 10 μm $MnCO_3$ precursor particles (Figure IV - 246) and are in the process of finishing the calcination of this material.
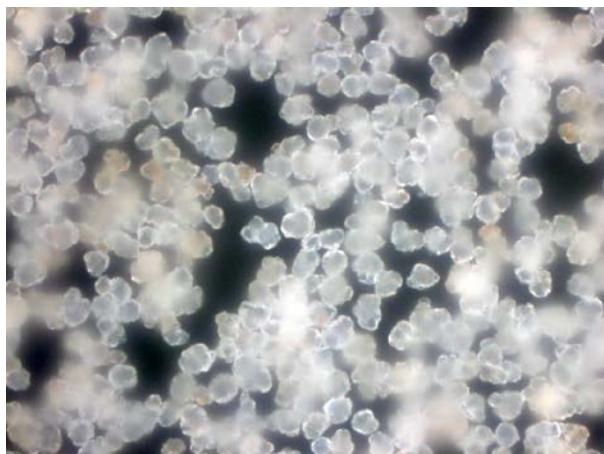
Figure IV - 246: Synthesized $MnCO_3$ precursors.

Relocation to the Materials Engineering Research Facility. Interm analytical labs were decommissioned and relocated to the Materials Engineering Research Facility (MERF). All cathode material analytical equipment is now housed in a single, dedicated analytical lab (Figure IV - 247). This laboratory is staffed by Gerald Jeka and Mike Kras. Mike also runs our newly established coin cell fabrication lab, enabling a far more rapid turnaround on making and testing coin cells, also located in the MERF. The MERF highbay will soon house the cathode material scale-up lab (Figure IV - 248). We have not decommissioned the intermediate laboratory at this time in order to complete the carbonate process scale up work on the first cathode material. We anticipate relocating this laboratory in January 2013.

Figure IV - 247: MERF Cathode Analytical Lab.

Figure IV - 248: MERF High bay, soon home to the Cathode Materials Scale-up Lab.

Conclusions and Future Directions

After the electrochemical validation of our optimized cathode material by the material screening group, we are concluding that the carbonate process has an inherent particle fracturing issue. We have also been informed that cathode material generated at the bench also demonstrates this issue. Commercial manufacturers have also hinted at this issue as well. Our initial attempts at preventing this fracturing by reducing particle size did not produce satisfactory results. Therefore, after discussions with our DOE sponsor, we have decided to attempt to make this cathode material using the hydroxide process for comparison. It is our understanding that material synthesized using the hydroxide process is far more resistant to cracking, although has a much lower tap density. We intend to synthesize the same cathode chemistry ($Li_{1.14}Mn_{0.57}Ni_{0.29}O_2$) using the hydroxide process and then attempt to optimize the tap density.

After we complete our comparison of the carbonate and hydroxide generated material we will then begin scaling a different chemistry developed by JPL ($Li_{1.2}Mn_{0.54}Ni_{0.13}Co_{0.13}O_2$) which has been developed and synthesized using the hydroxide process.

FY 2012 Publications/Presentations

1. 2012 DOE Annual Peer Review Meeting, May 14th-18th 2012, Washington DC. 4543
2. Patent is being prepared covering the method and apparatus for particle growth and size distribution control.

IV.E.1.2 Process Development and Scale-up of Advanced Electrolyte Materials (ANL)

Gregory K. Krumdick

Argonne National Laboratory
9700 South Cass Avenue
Argonne, IL 60439-4837
Phone: (630) 252-3952; Fax: (630) 252-1342
E-mail: gkrumdick@anl.gov

Collaborators:
Krzysztof (Kris) Pupek, Argonne National Laboratory
Trevor Dzwiniel, Argonne National Laboratory
Zhengcheng (John) Zhang, Argonne National Laboratory
Wenquan Lu, Argonne National Laboratory
Richard Jow, Army Research Laboratory

Start Date: June 2010
Projected End Date: September 2013

Objectives

The objective of this task is to conduct process engineering research for scale-up of new electrolyte and additive materials. Advanced electrolytes and additives are being developed to stabilize the interface of lithium-ion batteries by forming a very stable passivation film at the carbon anode. Stabilizing the interface has proven to be key in significantly improving the cycle and calendar life of lithium-ion batteries for HEV and PHEV applications. Up to this point, these advanced electrolytes and additives have only been synthesized in small batches. Scaling up the process involves modification of the bench-scale process chemistry to allow for the semi–continuous production of materials, development of a process engineering flow diagram, design of a mini-scale system layout, construction of the experimental system and experimental validation of the optimized process. The mini system will be assembled utilizing an existing synthesis reactor system. Electrolyte materials produced will be analyzed to confirm material properties and for quality assurance. The electrochemical properties of the material will be validated to confirm a performance match to the original materials.

Technical Barriers

Advanced electrolytes and additives have been synthesized in small batches using 1-5L vessels, which produce approximately 200mL of material. The bench-scale processes are labor-intensive and time-consuming.

Sufficient quantity of material cannot be generated for prototype testing, which is required prior to scaling the process to the next level. Therefore, pilot-scale facilities are required for battery materials scale-up research and development.

Technical Targets

- Scale-up 4-6 electrolyte materials in FY12.
- Relocate interim electrolyte scale-up lab to the Materials Engineering Research Facility (MERF).

Accomplishments

- Scale-up work has been completed on the following electrolyte materials:
  - LiDFOB
  - Lithium difluoro(oxalato)borate
  - ANL-1S1M3
  - 2,2-dimethyl-4,7,10,13-tetraoxa-2-silatetradecane
  - ANL-1NM2
  - 2,2-dimethyl-3,6,9-trioxa-2-siladecane
  - ARL-HFiPP
  - tris(1,1,1,3,3,3-hexafluoropropan-2-yl) phosphate
- Scale-up work has begun on the following electrolyte material:
  - ANL-RS21
- Interim electrolyte lab was relocated to two new labs in the MERF

✧   ✧   ✧   ✧   ✧

Introduction

Researchers in the battery materials programs across the DOE complex refer to scale up as synthesis of battery materials in gram quantities, and with time consuming, multiple small-scale runs. There is a need to develop scale-up processes for battery materials (primarily lithium-ion based batteries) to the kilogram and tens-of-kilograms quantities at DOE labs to support the transition of these technologies to industry. Currently, there is no systematic engineering research capability or program across the DOE complex or in industry to identify and resolve constraints to the development of cost-effective process technology for the high-volume manufacture of these advanced materials.

Approach

A formal approach for the scale-up of electrolyte materials has been defined (see Figure IV - 249). This approach starts with the initial discovery of a new electrolyte material and an initial electrochemical evaluation. This determines if the material is to be added to the inventory spreadsheet, ranked and prioritized. At this point, the scale-up process begins with the initial feasibility study, proof of concept testing, 1st stage scale-up and 2nd scale scale-up. Go/No go decisions are located after feasibility determination and electrochemical validation testing.
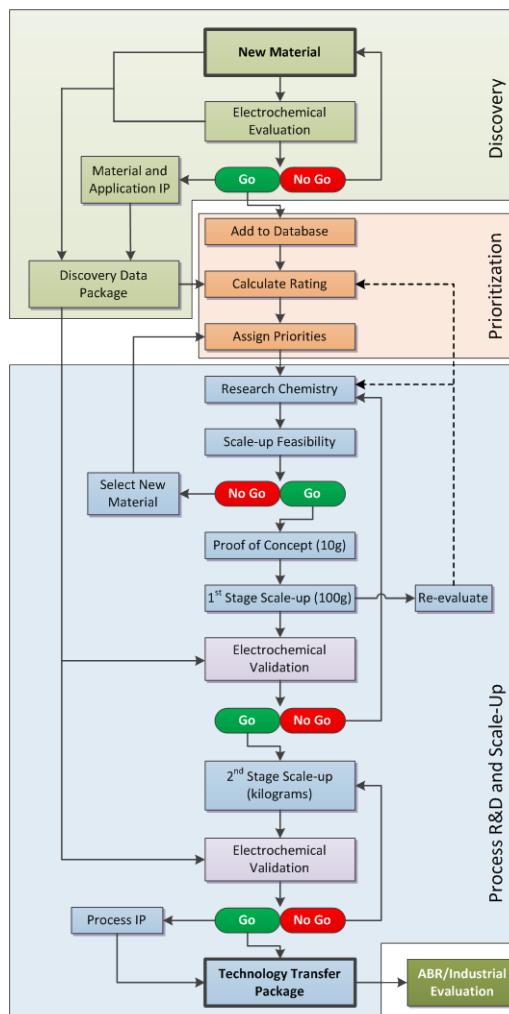

Figure IV - 249: Electrolyte Materials Process R&D Flowchart

For each material scaled, we will develop a scalable manufacturing process, analytical methods and quality control procedures. We will also prepare a "technology transfer package" which will include:

- Summary of the original process used by discovery researchers to synthesize the material.

- Summary of the scalable (revised) process suitable for large scale manufacturing.

- Detailed procedure of the revised process for material synthesis.

- Analytical data/Certificate of Analysis for the material (chemical identity and purity).

- The material impurity profile.

- Electrochemical performance test data.

- Preliminary estimates of production cost.

- MSDS for the material.

We will also make kilogram quantities of the material available for industrial evaluation, which has been fully characterized chemically and electrochemically.

Results

Wenquan Lu in the Materials Screening Group in the CSE division conducted the electrochemical validation of LiDFOB, 1S1M3 and HFiPP. 1NM2 is in the queue to be tested. Technology transfer packages have been prepared for all materials scaled. To date, we have provided 33 electrolyte material samples to interested companies and national labs.

NOTE: LiDFOB was synthesized (150 g) to provide material for researchers. Material is no longer commercially available.

Relocation to the Materials Engineering Research Facility. Intermediate laboratories were decommissioned and relocated to the Materials Engineering Research Facility. The Electrolyte Process R&D Laboratory (see Figure IV - 250) is equipped with organic synthesis equipment to develop and validate processes from gram to kilogram. The lab also includes analytical equipment for rapid in-lab analysis. The Process Scale-up Laboratory is equipped to scale processes from 1 to 50 kilograms (see Figure IV - 251).

Figure IV - 250: Electrolyte Materials Process R&D Laboratory.

Figure IV - 251: Electrolyte Materials Scale-up Laboratory.

Conclusions and Future Directions

Initially, scale-up work will continue on ANL-RS21 and soon begin on ARL-PFBP. Additional materials to scale will be added after discussions with the project sponsor. The scale-up of 4-6 electrolyte materials are targeted for FY13.

A list of milestones appears in Table IV - 15.

FY 2012 Publications/Presentations

1. 2012 DOE Annual Peer Review Meeting, May 14th-18th 2012, Washington DC.
2. Technology transfer packages were written for ANL-1S1M3, ANL-1NM2 and ARL-HFiPP
3. Patent was filed titled "METHOD FOR PRODUCING REDOX SHUTTLES" on May 2, 2012, Nonprovisional Patent Application Serial No. 13/462,012

Table IV - 15: List of Milestones – Process Development and Scale-Up of Advanced Electrolyte Materials.

MILESTONE	DATE
LiDFOB (Continued from FY11) - COMPLETED	
WP&C documentation approved	06/22/2011
Develop and validate scalable process chemistry (10g scale)	08/26/2011
First process scale-up (100g bench scale)	11/07/2011
150 g produced in a single batch, was purified and analyzed (produced for research purposes)	
1S1M3 (Continued from FY11) - COMPLETED	
Select CSE material to scale	01/04/2011
Assess scalability of CSE process	08/03/2011
WP&C documentation approved	02/22/2011
Develop and validate scalable process chemistry (10g scale)	09/02/2011
First process scale-up (100g bench scale)	11/04/2011
Second process scale-up (1000g pilot scale)	02/28/12
1,327 g produced in a single batch, purity 99.63%	
HFiPP - COMPLETED	
Assess scalability of disclosed process	10/07/2011
WP&C documentation approved	10/21/2011
Develop and validate scalable process chemistry (10g scale)	11/30/2011
First process scale-up (100g bench scale)	12/22/2011
Second process scale-up (1000g pilot scale)	01/27/2012
1,230 g produced in a single batch, purity 99.5%	
Relocation to Materials Engineering Research Facility - COMPLETED	
Decommission Interim Lab	04/06/2012
Transfer Equipment	April 2012
Electrolyte Process R&D Lab Operational	May 2012
Electrolyte Scale-up Lab Operational	July 2012
1NM2 - COMPLETED	
Assess scalability of disclosed process	7/20/12
WP&C documentation approved	8/1/12
Develop and validate scalable process chemistry (10g scale)	8/20/12
First process scale-up (100g bench scale)	9/17/12
Second process scale-up (10,000g pilot scale)	10/09/12
9,715 g produced in a single batch, purity >99.9%	
ANL-RS21 – In Progress	
Assess scalability of disclosed process	7/20/12
WP&C documentation approved	10/17/12
Develop and validate scalable process chemistry (10g scale)	In Progress

IV.E.2 Post-Test Diagnostics Facility

IV.E.2.1 Post-Test Diagnostic Activities (ANL)

Ira Bloom (Primary Contact), Nancy Dietz-Rago,
Javier Bareño

Argonne National Laboratory
9700 South Cass Avenue
Argonne, IL 60439
Phone: (630) 252-4516; Fax: (630) 252-4176
E-mail: ira.bloom@anl.gov

Start Date: April 2010
Projected End Date: Open

Objectives

- To accelerate the R&D cycle of DOE and industrial collaborators by developing and conducting standard procedures for post-test characterization of batteries in order to provide insight into physicochemical causes of performance degradation.

Technical Barriers

This project addresses the following technical barriers as described in the USABC goals [1, 2, 3]:

- Performance at ambient and sub-ambient temperatures.
- Calendar and cycle life.

Technical Targets

- EV: 5-y calendar life; 1,000 80% DOD DST cycles
- HEV: 15-year calendar life, 300,000 charge-sustaning cycles; EOL performance (min): 25 kW and 300 Wh
- PHEV: 15-year calendar life, 300,000 charge-sustaning cycles, 5,000 charge-depleting cycles; EOL performance (min): 45 kW and 300 Wh
- LEESS: 15-year calendar life, 300,00 charge-sustaining cycles; EOL performance (min): 20 kW and 56 Wh

Accomplishments

- A facility was built for the post-test examination of batteries and battery materials. The design of the facility allows most of the examinations to be performed under inert-atmosphere conditions. Safety reviews were written and standard operating procedures are still being developed. The facility

was fully operational in January 2012. Post-test examinations have begun.

✧ ✧ ✧ ✧ ✧

Introduction

Batteries are evaluated using standard tests and protocols which are transparent to technology [1, 2, 3]. The evaluation provides a lot of information about how battery performance changes with time under a given set of conditions. Post-test characterization of aged batteries can provide additional information regarding the cause of performance degradation which previously could only be inferred.

Approach

Post-test analysis consists of physical, spectroscopic, metallographic, and electrochemical characterization of battery components that have been harvested from aged cells. The aged cells have undergone standardized testing. The cells can come either from exploratory DOE programs, such as ABR and BATT, or from pre-competitive R&D programs managed by USABC and USDRIVE. The Post-Test Facility uses the experience and techniques developed in DOE's applied battery program in a standardized fashion.

Results

A summary of cells and materials examined during FY2011 is given in Table IV - 16. The techniques used are also included in the table.

Pouch cells from the ABR program, which were made by the Cell Fabrication Facility and tested in the EADL for cycle life, were examined to elucidate the possible causes of performance decline. These cells were based on NMC/graphite cell chemistry. After opening the cell in the inert-atmosphere glovebox, cell components were examined by many techniques to characterize changes in their morphology, phase distribution and surface and bulk chemistries.

Table IV - 16: Summary of cells and materials examined in the Post-Test Facility.

| System	Cell/Material	Quantity	Techniques used	Questions asked / answered
Li-ion (ABR)	Cycled cells and materials	15 75 materials for SEM only	XPS, FTIR, Raman, SEM/EDS, TGA	Cause of failure and nature of the materials
Li/Air	Cycled cells and materials	24	XPS, SEM/EDS	Is there irreversible formation of Li-O phases
Li/S	Cycled cells and materials	12	XPS, SEM/EDS	Possible formation of Li-S phases protective films on anode
Li-Ti-O	Cycled material	6	XPS, SEM/EDS	Oxidation state(s) of Ti
(Na/Mg) / V_2O_5	Cycled material	4	XPS	Intercalation vs. plating of active metal

Figure IV - 252 shows a typical pouch cell being unraveled. Changes in the separator and anode were seen. For example, white deposits were seen on the anode and dark deposits, on the separator.
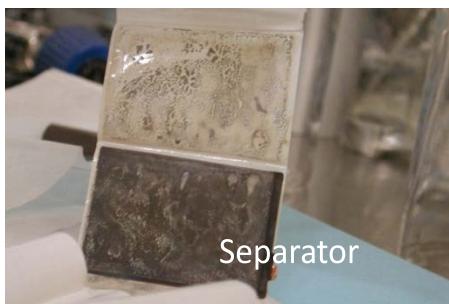
Figure IV - 252: A pouch cell being taken apart in the PTF.

Examination of a section of EMC-washed anode material before and after cycling showed the changes caused by cycling. Figure IV - 253 shows a SEM micrograph of the anode material from an uncycled anode. Here, the sharp edges of the graphite particles are clearly visible. With cycling, the graphite particles become covered by a precipitate, shown in Figure IV - 254, as nodule-like structures. Chemical analysis by EDS reveals that these nodules, most likely, consist of $LiPF_6$, which was the salt in the electrolyte, or $LiPF_6$- and/or electrolyte-reaction products.
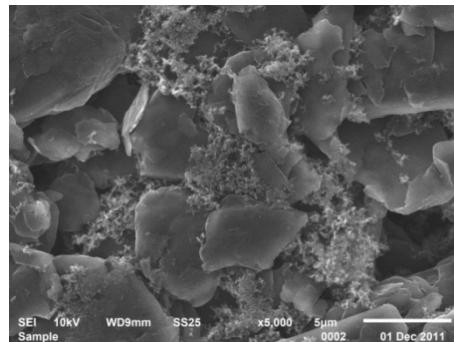
Figure IV - 253: SEM micrograph of a section of a pristine anode.
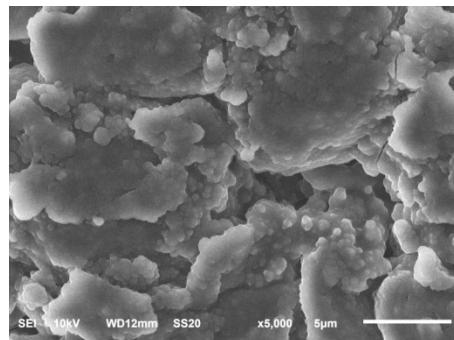
Figure IV - 254: SEM micrograph of a section of a cycled anode.

Continuing the examination to the separator shows the changes that occurred on this cell component. Figure IV - 255 shows a micrograph of the separator material before cycling. The pores in the material are clearly seen. With cycling, deposits on both the cathode and anode sides of the separator are seen, as shown in Figure IV - 256 and Figure IV - 257. EDS analyses indicate that the deposits consist of $LiPF_6$ or $LiPF_6$- and/or electrolyte-reaction products.
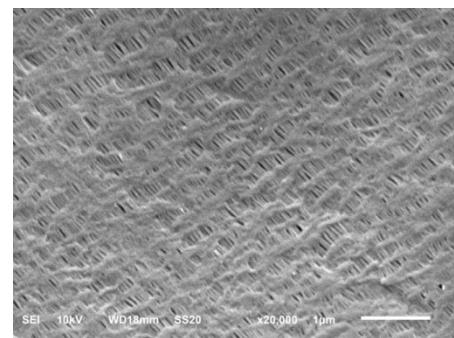
**Figure IV - 255:** SEM micrograph of Celgard separator before cycling.
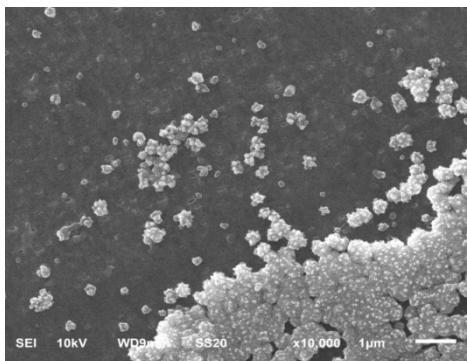
**Figure IV - 256:** SEM micrograph of the cathode side of the separator.
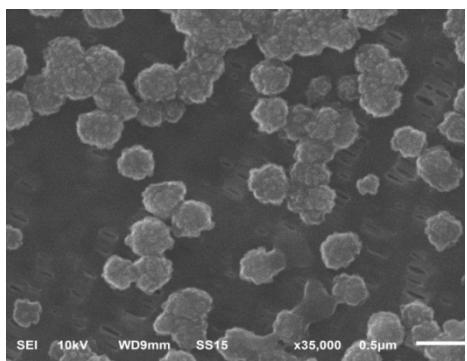
Figure IV - 257: SEM micrograph of the anode side of the separator.

Evidence from the XPS, shown in Figure IV - 258, is consistent with the presence of $LiPF_6$ reaction products in the SEI layer. Comparing the spectrum from the pristine anode to that from the aged material shows that there are changes in the structure and intensities of the F(1s) and O(1s) peaks. These peaks change in shape and intensity with cell cycling.
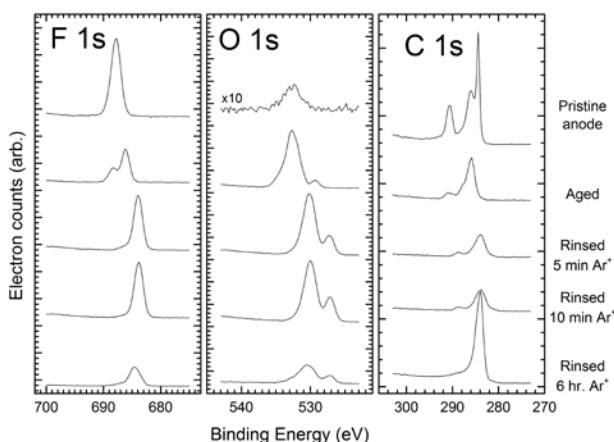

Figure IV - 258: XPS results from the anodes of ABR cells. With increased sputtering time, the F(1s) and O(1s) peaks decrease in intensity, indicating that these peaks are from surface layers, such as an SEI.

Conclusions and Future Directions

Post-test facility has been established at Argonne to support DOE and USABC projects. The facility is 100% operational now and is starting to generate the needed data to understand performance decline in lithium-ion cells. In the example above, performance decline was most likely due to the formation of electrolyte- and $LiPF_6$- and/or electrolyte-reaction products on the surface of anode and separator, thereby increasing cell resistance.

The next steps are as follows.

· Actively engage USABC and DOE battery contractors to help them understand the sources of performance decline.

· Collaborate with ABR, BATT and USABC programs.

References

1. FreedomCAR Battery Test Manual for Power-Assist Hybrid Electric Vehicles, DOE/ID-11069, October 2003.
2. FreedomCAR Battery Test Manual for Plug-In Hybrid Electric Vehicles, June 2010.
3. Electric Vehicle Battery Test Procedures Manual, Revision 2, January 1993.

List of Abbreviations

DOD: depth of discharge
DST: dynamic stress test profile
HEV: hybrid electric vehicles
PHEV: plug-in hybrid electric vehicles
EV: electric vehicles
LEESS: Low-Energy Energy Storage System
USABC: United States Advanced Battery Consortium (DOE, GM, Chrysler and Ford)
ABR: DOE's Advanced Battery Research Program
EADL: Electrochemical Analysis and Diagnostics Laboratory at Argonne
NMC: layered-layered cathode materials based on Li-Ni-Mn-Co-O phases
PTF: Post-Test Facility at Argonne
EMC: ethyl methyl carbonate, an electrolyte solvent
SEM: scanning-electron microscope
EDS: energy-dispersive x-ray (spectroscopy)
XPS: X-ray photoelectron spectroscopy
SEI: secondary electrolyte interphase

FY 2012 Publications/Presentations

1. DOE Annual Merit Review Presentation, May 2012.

IV.E.3 Battery Electrode and Cell Fabrication Facility

IV.E.3.1 Screening of Electrode Compositions and Cell Chemistries (ANL)

Wenquan Lu

Argonne National Laboratory
9700 South Cass Avenue
Argonne, IL 60439-4837
Phone: (630) 252-3704; Fax: (630) 972-4414
E-mail: luw@anl.gov

Collaborators:
Qingliu Wu (ANL)
Miguel Miranda (ANL)
Thomas K. Honaker-Schroeder (ANL)
Khadija Yassin-Lakhsassi (ANL)
Material scientists (ANL)
Bryant Polzin (ANL)
Andrew Jansen (ANL)
Jason Croy (ANL)
Kevin Gallagher (ANL)
Christopher Johnson (ANL)
Ilias Belharouak (ANL)
Dennis Dees (ANL)
Khalil Amine (ANL)
Gary Henriksen (ANL)
Cell Fabrication Facility (CFF-ANL)
Materials Engineering Research Facility (MERF)
Kang Xu (ARL)
Toda Kogyo (Japan)
ConocoPhillips (USA)
Energ2 (USA)
SWeNT (USA)
Superior Graphite (USA)
Cabot (USA)
Northwestern Univ. (USA)
Samsung (Korea)
Morgan AM&T (UK)
Daikin (Japan)
JSR (Japan)
ZEON (Japan)

Subcontractor:
Illinois Institute of Technology, Chicago, IL

Start Date: October 2008
End Date: September 2014

Objectives

The primary objective is to identify and evaluate low-cost materials and cell chemistries that can simultaneously meet the life, performance, and abuse tolerance goals for batteries used in PHEV applications.

A secondary objective is to enhance the understanding of the impact of advanced cell components on the electrochemical performance and safety of lithium-ion batteries.

Technical Barriers

An overwhelming number of materials are being marketed by vendors for lithium-ion batteries. It is a challenge to down-select and screen these materials effectively within the allocated scope of this project.

There are no commercially available high energy materials that can produce a battery capable of meeting the 40-mile all-electric-range (AER) within the weight and volume constraints established for PHEVs by DOE and the USABC. Identification of new high-energy electrode materials is the primary goal for this project.

Establishing the impact of formulation and processing on electrode performance for materials with a broad variation in chemical and physical properties is another major challenge.

Technical Targets

- Higher energy density materials identification and evaluation.
- Low cost cell components identification and characterization.
- Technical support to the Cell Fabrication Facility (CFF) and Materials Engineering Research Facility (MERF).

Accomplishments

- *Cathode materials*: Several **lithium manganese rich metal oxide (LMR-NMC) cathode materials** from Dr. I. Belharouak, Dr. J. Croy, and the MERF, were received and characterized. Different electrochemical properties were obtained for the range of LMR-NMC materials with various compositions. The screening results were transferred to the CFF. **$LiNi_{0.5}Mn_{1.5}O_4$**,

as a high energy and high power cathode material, was also investigated.

- In addition to high energy cathode materials, other cathode materials, such as $Li_{1+x}Ni_{0.5}Co_{0.2}Mn_{0.3}O_2$, $Li_{1+x}Ni_{1/3}Co_{1/3}Mn_{1/3}O_2$, and $LiMn_2O_4$ from various suppliers were also characterized for the CFF to build their material library.

- *Anode materials:* **Graphite** (Morgan AM&T), **hard carbon** (Energ2), and **$Li_4Ti_5O_{12}$** (Samsung and NEI) were received and screened at Argonne. The information was shared with material developers and the CFF.

- *Additives*: Several electrolyte additives were tested for LMR-NMC cathode and **LiDFOB** was found to improve the capacity retention. **Fluorinated ethylene carbonate (FEC)** was tested for Silicon based materials and better cycling performance was obtained.

- *Others*: Other cell components, such as binders, separators, carbon blacks and carbon nanotubes, were also characterized. The test results have been shared with the suppliers.

<div align="center">✧   ✧   ✧   ✧   ✧</div>

Introduction

High energy density electrode materials are required in order to achieve the 40-mile AER within the weight and volume constraints established by DOE and the USABC. One would need a combination of anode and cathode materials that provide 420mAh/g and 220mAh/g, respectively, as predicted by Argonne's battery design model, if one uses a 20% margin for energy fade over the life of the battery assuming an average cell voltage of 3.6 volts. Therefore, the search for new high energy density materials is the focus of this project.

In addition to high energy density electrode materials, other cell components continue to be evaluated to address the performance, safety, and cost issues.

Approach

The search for new high-energy materials includes new commercially available materials, as well as new high energy density materials under development. During the search and evaluation process, the cost issue is always considered, e.g. avoiding the rare elements, expensive precursors, and/or elaborate processing.

The selected electrode materials are evaluated in controlled conditions following established protocols. The commonly used parameters, such as pulse power and charge depleting (CD) capacity tests are derived from the "Battery Test Manual for Plug In Hybrid Electric Vehicle" (Mar. 2008) issued by Idaho National Laboratory. Depending on the portion of total cell energy that is

available for use during the CD discharge, the CD rate can vary from C/2 to C/3. Similarly, the pulse power rate could change from about 3C to 2C.

Coin cells (2032 size) are used for the initial screening studies. If promising results are obtained with coin cells, then larger laboratory cells such as the 32 cm² stainless steel planar test cell fixtures or simple single-stack pouch cells, are used. Preliminary accelerated aging studies are performed at 55 °C for promising materials to give a preliminary indication of life. Where appropriate, the thermal abuse response is studied using differential scanning calorimetry (DSC). Materials that show characteristics favorable for PHEV batteries are then recommended for more extensive life evaluation under the Cell Fabrication Facility.

In addition to electrode materials, other cell components, such as separators, binders, current collectors, etc., are secured and evaluated to establish their impact on electrochemical performance, thermal abuse, and cost. The test methods for different materials are separately defined.

Results

Composite-structure cathode materials. This year, composite-structure cathode materials are still our focus as cathode materials due to their high energy density. Several composite-structure cathode materials were received and investigated. One of composite-structure materials, $(Li_{1.7}Ni_{0.25}Mn_{0.75}O_{2+d})$ from Dr. I. Belharouak (ANL), will be discussed below as an example.

This composite electrode material was initially tested against lithium metal in the half cell configuration between 4.6V and 2.0V. The specific capacity was determined to be ~250mAh/g at the C/10 rate. The irreversible capacity loss (ICL) during the 1st cycle is about 22%. This material also showed good rate performance. There are still about 240mAh/g capacity at 1C rate. The cycle performance of a full cell is shown in Figure IV - 259. The applied voltage window for the graphite/composite full cell is between 4.55V and 2.0V. Good capacity retention was observed till 120 cycles.
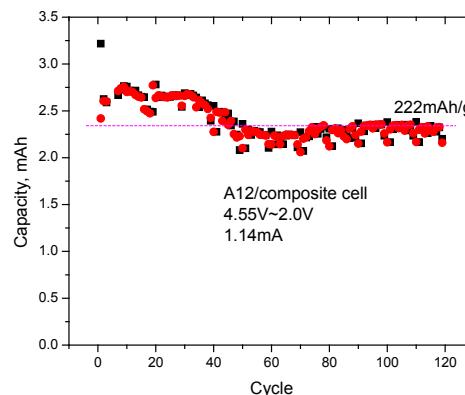

Figure IV - 259: Cycle performance of HE5050 full cell.

High Voltage Spinel (LiNi$_{0.5}$Mn$_{1.5}$O$_4$). Half cells using LiNi$_{1.5}$Mn$_{1.5}$O$_4$ (LNMO) has been investigated. The cells were cycled between 4.95V and 3.5V at C/10 rate (shown in Figure IV - 260). The 133 mAh/g specific capacity of LiNi$_{0.5}$Mn$_{1.5}$O$_4$ was obtained from the formation cycles with about 8% irreversible capacity losses. Compared to LiNi$_{0.8}$Co$_{0.15}$Al$_{0.05}$O$_2$ (NCA) and LMR-NMC, LNMO has less capacity and energy density. However, according to battery modeling work, the energy density of Graphite/LNMO cell system is comparable to NCA and LMR-NMC due to its high voltage and rate properties.
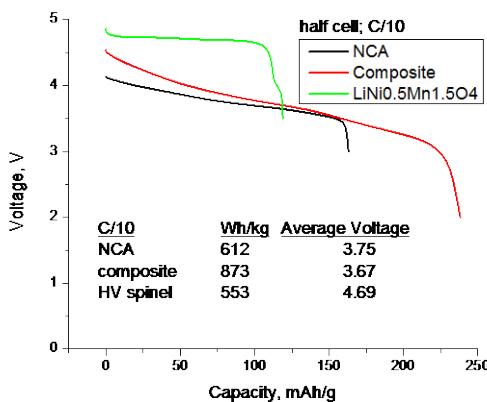

Figure IV - 260: Formation of LNMO half cell.

Graphite/LNMO full cells were also fabricated and tested. At a 1C rate, the cell can still deliver about 92% of its full capacity, indicating excellent rate and power performance. Good cycle performance was also obtained and is shown in Figure IV - 261. After more 70 cycles between 4.9V and 4.2V, only less than 5% capacity loss was observed. However, the coulombic efficiency (see inset) is consistently low compared to that of NCA cell system, which suggests possible electrolyte oxidation during the high voltage cycling. The novel electrolyte or additive for high voltage electrode should be developed to address this issue.
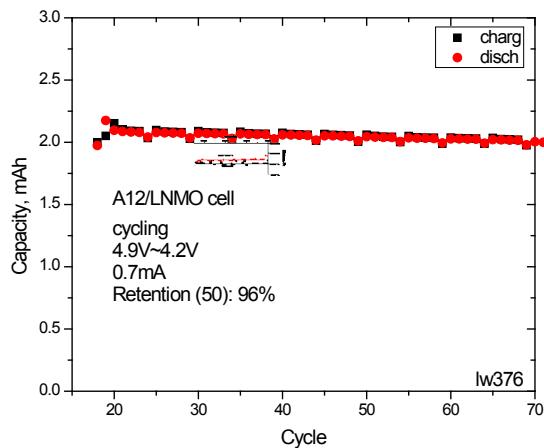

Figure IV - 261: Cycle performance of graphite/LNMO cell.

Additives for LMR-NMC. The effect of electrolyte solution with 2 wt.% LiDFOB on the electrochemical performance of graphite/LMR-NMC cells was investigated. A formation of different SEI films was observed during the initial formation process in the presence of additives. The utilization of LiDFOB dramatically enhanced the cyclability of graphite/ LMR-NMC cells with capacity retention of about 77% even after more than 200 cycles (Figure IV - 262).
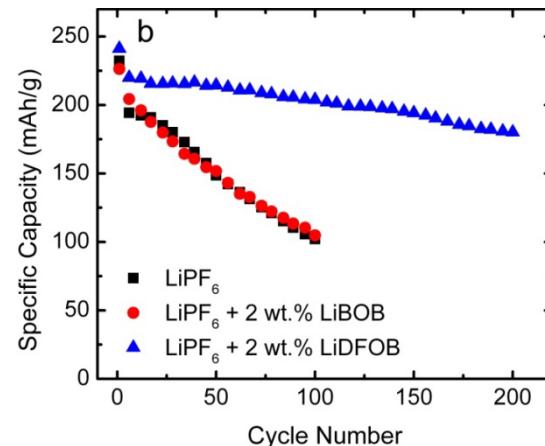

Figure IV - 262: Cycle performance of graphite/HE5050 cell with and without additives.

The analysis on the electrochemical behavior, SEM of cycled electrodes, and EIS suggested that the enhancement of cell performance could be ascribed to the thin and stable SEI films formed on the surface of anode in the presence of LiDFOB, which might prevent the lithium consumption during the cycling. The hypothesis of lithium consumption on the anode is investigated by testing the recovered electrodes from the cycled full cells. The voltages of all the recovered cathode half cells start from partially lithiated state. Furthermore, more charge capacity was obtained for the recovered LMR-NMC/Li half cell from the full cell with LiDFOB additive than those without additive. This strongly suggests that, more lithium was consumed and less lithium was available for the additive free full cells.

Additives for silicon anode. In addition to silicon's well-known volume expansion issue, another problem is that no stable SEI film is formed on the silicon surface, leading to lithium consumption and capacity fading. In this work, two additives were tested for the silicon based electrode, Lithium difluoro(oxalato)borate (LiDFOB) and fluorinated ethylene carbonate (FEC). 1.2M LiPF$_6$ EC/EMC (3/7) (Gen2) were used as the reference. Then, 2% LiDFOB and 10% FEC were added into Gen2 electrolyte, respectively.

After 3 formation cycles, we ran EIS on the electrodes and results are shown in Figure IV - 263. Clearly, very high impedance is found for the cell without any additive and least impedance was found for the cell with FEC as additive. FEC was found not only for this silicon material, but also other silicon based materials. The small

impedance of silicon cell with FEC can be attributed to the stable SEI.
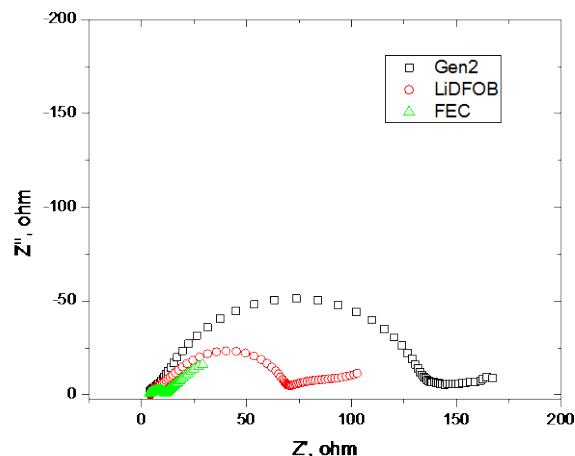
Figure IV - 263: EIS of Silicon half cell with and without additives.

The silicon electrode was coupled with both lithium metal and NCA electrodes. Very good cycling performance was obtained for the cell with FEC additive (shown in Figure IV - 264). There is only less than 20% capacity left after 70 cycles when Gen2 is used without any additive and no improvement is observed for LiDFOB additive. However, only 20% capacity loss was observed when 10% FEC was added into the Gen2 electrolyte.
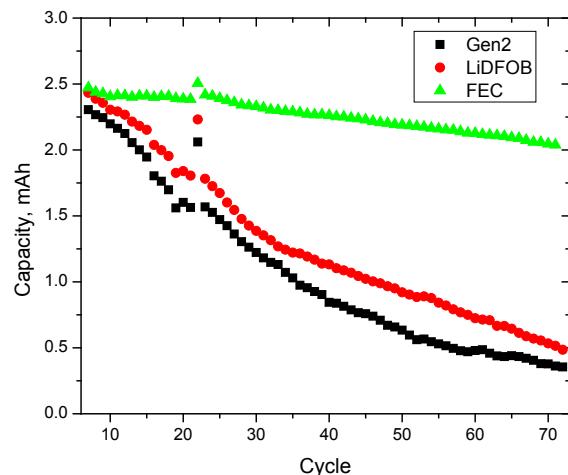

Figure IV - 264: Cycle performance of Silicon half cell with and without additives.

Due to space limitations, other materials, such as binders, separators, carbon blacks and carbon nanotubes, were also characterized. The test results have been shared with the suppliers.

Conclusions and Future Directions

Material screening results on one of composite cathode material developed at ANL confirmed that this type of material is still at the state of the art, whose performance can be further improved. Furthermore, its

cycle performance can be improved with the appropriate electrolyte and additives are used in the cell system. Other than composite material, another promising cathode material, high voltage spinel, was also characterized, which showed excellent rate and cycle performance. However, the relatively low coulombic efficiency suggests that a stable high voltage electrolyte is needed for this system.

This year, silicon electrode and additive effects on its electrochemical performance were investigated. It is found out that the conventional carbonate based electrolyte is not stable in the silicon-based electrode. FEC additive is very critical to making the silicon-based electrode work.

This project will be rolled into Cell Fabrication Facility (CFF) starting in FY 13. However, the focus of this project will remain on the identification and characterization of new high energy density cathode and anode materials. We will continue to work closely with CFF to support MERF and the modeling work.

FY 2012 Publications/Presentations

1. Numerous internal reports on material screening and external reports to material suppliers.
2. Effects of lithium difluoro(oxalate)borate on the performance of Li-rich composite cathode in Li-ion battery Qingliu Wu, Wenquan Lu, Miguel Miranda, Thomas K. Honaker-Schroeder, Khadija Yassin Lakhsassi, Dennis Dees, Electrochem. Comm., 24, 2012, 78-81.
3. Layered Na[Ni$_{1/3}$Fe$_{1/3}$Mn$_{1/3}$]O$_2$ Cathodes for Na-ion Battery Application, Donghan Kim, Eungje Lee, Michael Slater, Wenquan Lu, Shawn Rood, Christopher S. Johnson, Electrochem. Comm., 18, 2012, 66-69.
4. Overcharge Effect on Morphology and Structure of Carbon Electrodes for Lithium-Ion Batteries, Wenquan Lu, Carmen M. L´opez, Nathan Liu, John T. Vaughey, Andrew Jansen, and Dennis W. Dees, J. Electrochem. Soc., 159 (5) 2012, A566-A570.
5. Screen Electrode Materials & Cell Chemistries, W. Lu, 2012 DOE Annual Peer Review Meeting Presentation, May 14th-18th 2012, Washington DC.
6. Electrochemical and Thermal Studies of Fluorinated Electrolytes in Li-Ion Cell, A. Benmayza, V. Ramani, J. Prakash, and W. Lu, 220th ECS Meeting & Electrochemical Energy Summit in Boston, Massachusetts (October 9-14, 2011).

IV.E.3.2 Cell and Cell Component Activities (ANL)

Andrew N. Jansen
Argonne National Laboratory
9700 South Cass Avenue
Argonne, IL 60439-4837
Phone: (630) 252-4956; Fax: (630) 972-4461
E-mail: jansen@anl.gov

Collaborators:
Bryant Polzin, Argonne
Stephen Trask, Argonne
Dennis Dees, Argonne
Wenquan Lu, Argonne
Daniel Abraham, Argonne
Kevin Gallagher, Argonne
Joseph Kubal, Argonne
Materials Engineering Research Facility
    (MERF-Argonne)
Post-Test Facility (PTF-Argonne)
    Nancy Dietz

Start Date: October 2008
Projected End Date: September 2014

Objectives

- The objective of this work is to speed the evaluation of novel battery materials from the ABR and BATT programs, as well as from universities and the battery industry. The main objectives in FY12 were: 1) establish baseline data on electrode couples/systems, 2) evaluate new cell components, and 3) provide support to the battery research community in the form of standard electrodes and analytical cells.

Technical Barriers

- Newly developed battery materials for PHEVs need to be tested in limited batch size before larger scale industrial commitment.
- Validation tests are needed in cell formats with at least 0.4 Ah in capacity.
- Electrode designs must be developed that are appropriate for PHEV batteries.

Technical Targets

- Produce electrodes and cells based on high energy negative and positive active materials and test performance.
- Use electrochemical performance data and battery design modeling to design PHEV battery.

- Evaluate new scaled-up cathode materials and electrolytes developed by MERF.
- Establish an Electrode Library which is a collection of standardized electrodes (anodes and cathodes) that aid the battery research community.
- Continue to refine and improve upon the cell making process (pouch and 18650) as well as the data collection and analysis processes.

Accomplishments

- Optimized electrode slurry process using new high shear planetary mixer from Ross.
- Worked with the MERF facility at Argonne to evaluate materials as they are in the process of being scaled up.
- Completed one 18650 cell build to optimize cell construction process.
- Designed and fabricated baseline electrode sets to be used in high voltage electrolyte studies.
- Completed ten xx3450 pouch cell builds (8-24 pouches constructed and tested per build).
- Initiated electrolyte and additives studies.
- Completed nearly forty prototype pouch cells for advanced studies at research facilities including Advance Photon Source (Argonne) and Spallation Neutron Source (Oak Ridge).
- Completed eight pouch cells for destructive testing at Sandia National Laboratory.
- Completed eighteen xx3450 pouch cells in support of an NETL binder project.
- Supplied ~225 electrode sheets from the Electrode Library to industry, universities and other research laboratories.
- Teamed with the Post Test Facility to obtain essential analytical information on materials and tested cells.
- Collaborated with the Materials Validation, Modeling, and Diagnostics Efforts on optimizing cell design and electrode formulations.

✦   ✦   ✦   ✦   ✦

Introduction

Several new battery chemistries are being proposed for PHEV batteries that must be evaluated in cell formats that are larger than a few mAh in capacity. Cell builds are generally based on materials recommended by the ABR Screening subtask, many of which are novel materials developed in the ABR and BATT programs, but also

materials from industry and universities. The previous ATD program required cells designed for HEV applications, which used thin electrodes. The ABR Program has little experience with thicker electrodes that are now required for PHEV applications. The performance of these thicker electrodes must be determined and verified in cell builds using advanced battery materials. Once the influence of electrode thickness has been established, the many novel high-energy materials being developed world-wide will be explored in new cell builds.

Historically, cell builds have been carried out through subcontracts with battery developers to produce flexible or rigid cells per the ATD and ABR Program directions. This approach can occasionally result in delays due to lack of sufficient material quantities for the larger coating equipment or due to the battery developer's internal priorities taking precedence. Thus, it was decided that Argonne should develop its own in-house cell making capability.

Approach

Promising new exploratory materials are often developed in small coin cells, which may or may not scale up well in large PHEV battery designs. For this reason, pouch cells or rigid cells such as 18650s will be used for proofing of new battery materials in the capacity range of 0.4 to 2 Ah.

Pouch cells will be used for initial evaluations of long-term exploratory materials. Pouch cells are an efficient method of determining the stability of a cell system during calendar and cycle life aging. If the chemistry is not stable, it is likely that gassing will occur inside the cell. This will result in the pouch cell bulging or rupturing if the gassing is significant. More established materials and chemistries (or those that pass the pouch cell evaluation) will be used in rigid cells (e.g. 18650s).

Results

**Upgrade of Cell Fabrication Facility – Ross Mixer**. The ability to make cells with long cycle life and good electrochemical performance is dependent on making high quality electrodes. Key to this is the ability to make homogenously dispersed electrode slurries with intimate contact between active particles and conductive additives. To accomplish this step, a high energy/shear planetary mixer was purchased from Ross with a 2 liter chamber capacity (Figure IV - 265). This relatively small capacity size is ideal for the typical electrode builds made with the pilot scale coater, where supply of novel materials is often limited. Installation of this mixer was completed in October, 2011.
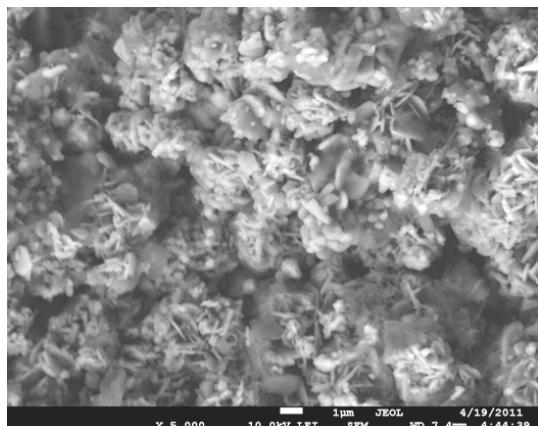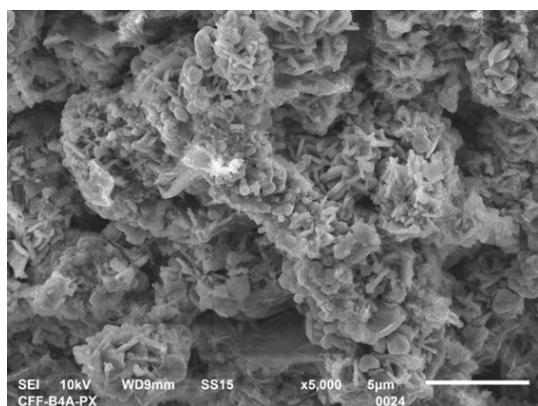

Figure IV - 265: High energy/shear planetary mixer from Ross with a 2 liter chamber capacity.

Numerous slurry batches were made using ConocoPhillips' A12 graphite and Toda's high energy cathode material HE5050 ($Li_{1.2}Ni_{0.15}Co_{0.10}Mn_{0.55}O_2$) to gain experience with the mixer and to optimize the mixing parameters and process steps. It was estimated that the minimum slurry volume is near 300 mL; below that amount resulted in insufficient mixing due to splatter from the high shear blade not fully engaging the slurry. Single-sided and double-sided electrodes were made with both anode and cathode slurries. Pouch cells (xx3450 format) were made using these electrodes.

Comparisons were made between the first pouch cell build, which relied on a smaller non-shear Thinky mixer, and the fourth cell build, which used the new Ross high-shear mixer. An SEM picture of the cathode cross-section from each cell build is shown in Figure IV - 266. Overall, both mixers were able to make slurries that coated well, but the Ross mixer appeared to distribute the carbon additive (Timcal Super P/ C45) more evenly around the Toda HE5050 particles. The electrochemical performance of the cell made with the Ross mixer was improved. A more detailed analysis is made in a latter section between Cell Builds 1 and 4, both of which used the same materials and composition.

a)   Cell Build 1 (Thinky mixer)

b)   Cell Build 4 (Ross mixer)

Figure IV - 266: SEM photos of electrodes based on Toda HE5050 high energy cathode materials made with 1) Thinky mixer, and 2) Ross mixer.

Evaluate materials from MERF scale-up of ABR's High Energy NM Cathode (2nd, 3rd, 8th & 13th Cell Builds). Of particular interest to the ABR Program is one of Argonne's advanced cathode materials under development. This material is a high-energy layered-layered LR-NMO cathode ($Li_{1.2}Ni_{0.3}Mn_{0.6}O_{2.1}$), and with the absence of cobalt metal, should result in a lower material cost. It was originally made by R&D staff at Argonne and referred to here as ABR1 cathode. Based on favorable results from the ABR Screening Task, the ABR1 cathode was selected to be the first material to be scaled up into kilogram quantities at Argonne's Materials Engineering Research Facility (MERF).

The MERF now has the capability to make tens of kilograms of advanced cathode materials in their 20 L reactor system. It made a 10 kg cathode batch of this high-energy LR-NMO cathode ($Li_{1.2}Ni_{0.3}Mn_{0.6}O_{2.1}$), referred to here as MERF-1. This material was validated in initial testing at the coin cell level. One kg of this batch was then delivered to CFF in early March of 2012. Single-sided and double-sided electrodes were made with this cathode in the CFF for further testing, after which a pouch cell build was conducted.

The initial slow discharge capacity of the MERF-1 cathode is impressive at 250 mAh/g, but the delivered capacity at higher rates is less than desired. The capacity faded significantly during cycle life testing. It is possible that this is due to non-uniformity of the particle morphology.

The MERF then adjusted their process conditions in an attempt to decrease the particle size and improve the uniformity, which should minimize the risk of particle cracking. A one kg batch of improved $Li_{1.2}Ni_{0.3}Mn_{0.6}O_{2.1}$ cathode was delivered to CFF in August of 2012, and is referred to as MERF-1B. This material first underwent validation at the MERF in coin cells. This material had much better uniformity with the desired smaller particle size. Single-sided and double-sided electrodes were then made with it in the CFF. The Post-Test Facility provided a SEM cross-section of the cathode electrode (Figure IV - 267) after calendering in the CFF.
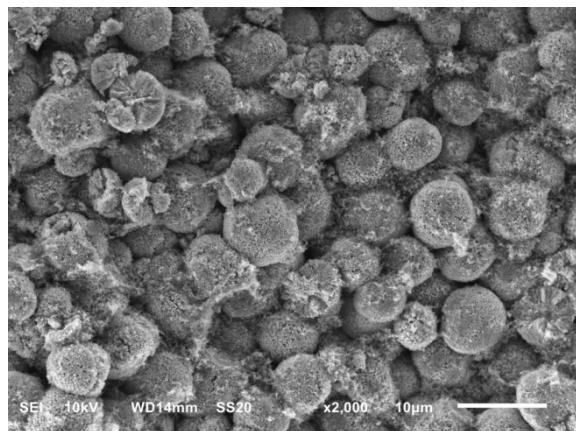

Figure IV - 267: SEM photos of electrode based on MERF-1B high energy cathode material. Note particle cracking from calendering process.

The MERF-1B cathode performed much better than the original MERF-1 cathode. A summary of its rate capability is shown in Figure IV - 268. However, its cycle life was not as long as the cell builds made using Toda HE5050 and some evidence of particle cracking was seen after calendering (see Figure IV - 267). Signs of particle fracturing during the calendering process were observed for the original cathode powders made by the ABR researchers. Little evidence of particle cracking was seen in electrodes made with Toda HE5050, which is made via a hydroxide process.
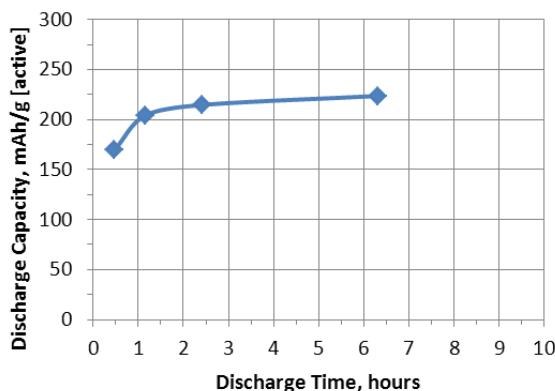
Figure IV - 268: Rate performance of MERF-1B high energy cathode material.

First cell build using 18650 cell making equipment. Effort was directed toward fabricating 18650 cells with commercially available materials and exploratory materials. It was anticipated that making 18650 cells would require significantly more material than pouch cell fabrication. For this reason, a commercial source was sought willing to supply openly at least 20 kg of advanced NCM material. Toda Kogyo agreed to supply Argonne with 40 kg of their NCM523 cathode ($Li_{1.1}(Ni_{0.5}Co_{0.2}Mn_{0.3})_{0.9}O_2$). This material arrived in March of 2012 and was shared with Sandia and Oak Ridge for their cell builds.

Enough double-sided electrodes were made to conduct a build with the 18650 format. A pouch cell build was performed first with these graphite and NCM523 electrodes to establish its rate capability and its cycle life. These pouch cells performed relatively well with 45% capacity loss over 900 cycles at the C/2 rate and 30°C. Better capacity retention is expected with optimization of the cathode electrode, addition of electrolyte additives, and lowering the upper voltage limit from 4.2 V to 4.1 V.

Delays were experienced due to problems in slitting consistent uniform edges. The electrodes tend to curve as they exit the slitter. Modifications were made to the slitter and to its operation to yield a straight cut. High-precision templates were also made to check the quality of the electrodes dimensions. These obstacles were overcome and the first small cell build in the 18650 format began in September of 2012.

Due to the concern of thermal runaway, the cells were started one at a time with a couple week spacing. As more experience (and confidence) is gained with 18650 fabrication, these time delays will be diminished. No thermal events were experienced so far with the few made and on test. The cycle data of the first 18650 cell is shown in Figure IV - 269. Its capacity is stable and is still under test at 30°C at the C/2 rate and upper voltage limit of 4.2 V. Reference performance tests are performed every 50 cycles. Direct comparisons will be made to the pouch cell builds.
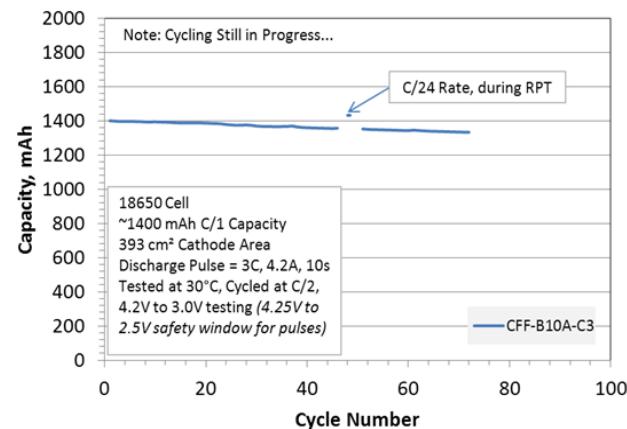

Figure IV - 269: Cycling data of cell from first 18650 cell build in Cell Fabrication Facility, ConocoPhillips A12 Graphite vs. Toda NCM523 cathode.

Cell Build Summary. Over thirteen full cell builds were performed in the CFF since it started operation in February of 2011. These builds consisted of numerous combinations of anodes and cathodes – each electrode system requiring several optimization steps to make a satisfactory electrode. A graphical summary of the prominent cell build systems is shown in Figure IV - 270. Several of these cell builds are discussed in the following sections. Note that no electrolyte additives were used in these cell builds, which was done so that a baseline could be established for each class of materials. Future cell builds with these materials will include additives and variations in electrode composition, formation process, and test conditions.
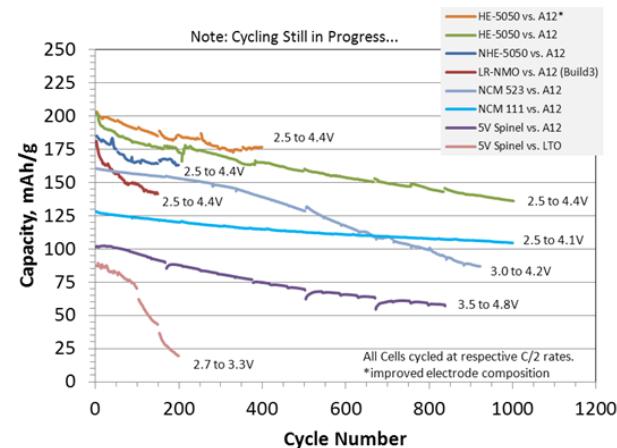
Figure IV - 270: Summary of the cycling data of prominent cell builds conducted in the CFF since February 2011.

High Energy NMC Cell Builds (1st, 4th, 9th, & 12th). Toda's high energy cathode material, HE5050 ($Li_{1.2}Ni_{0.15}Co_{0.10}Mn_{0.55}O_2$), was selected for the first positive electrode build and ConocoPhillips' (now Phillips 66) A12 graphite was selected for the first negative electrode build based on their screening results. The

selection of active materials to use was based chiefly on the criteria of high capacity and open availability.

In the first cell build, a small non-shear Thinky mixer was used to make the electrodes. Over a dozen pouch cell assemblies were made with these advanced electrodes and subjected to formation cycling and electrochemical performance characterization cycling. Once the Ross mixer was ready for operation, another cell build (Cell Build 4) was performed using electrodes made with the Ross mixer using the same composition as the Cell Build 1. After Cell Build 4, the Diagnostic effort made recommendations for the cathode composition that should help to minimize the impedance rise with cycling. These improvements were incorporated into Cell Build 9. Meanwhile, the latest version of HE5050 was received from Toda, which has a higher tap density than the previous version. Cell Build 12 was conducted with the new HE5050 using the same formulation as in Cell Build 9, without first going through the validation process. A summary of the electrode compositions is given in Table IV - 17.

After formation and characterization cycles were conducted, the pouch cells were placed on a cycle life profile, which consisted of repeated units of 40 cycles at C/2 rate followed by an HPPC test at the 5C discharge pulse. Based on earlier Diagnostic results, the upper voltage was limited to 4.4 V to enhance life. The cell data discussed here were tested at 30°C. Some accelerated aging tests are now being done at 55°C.

Table IV - 17: Summary of electrode composition for cell builds based on Toda HE5050 high energy cathode materials.

Component	Build Cathode Composition, %			
	1	4	9	12
HE5050	86	86	92	92
Solvay 5130 PVDF	8	8	4	4
Super P or C45	2	2	4	4
SFG6 Graphite	4	4	0	0
Mixer	Thinky	Ross	Ross	Ross

Component	Build Anode Composition, %			
	1	4	9	12
A12 Graphite	89.8	89.8	91.8	91.8
Kureha KF-9300 PVDF	6	6	6	6
Super P or C45	4	4	2	2
Oxalic Acid	0.17	0.17	0.17	0.17
Mixer	Thinky	Ross	Ross	Ross

A summary of the rate capability for the first four pouch cell builds using HE5050 cathodes is shown in Table IV - 18. Figure IV - 271 is a summary of the HPPC Discharge Pulse ASI evaluated at 50 % DOD over the life of a typical cell from each of these four cell builds. Significant improvements in rate and HPPC performance were seen between cell builds 1 and 4, which are chiefly attributed to the use of the Ross mixer. Further

improvements in performance were seen in Cell Build 9, which capitalized on the recommendations from the Diagnostic effort. However, Cell Build 12, which used the new version of HE5050 did not show improvement over Build 4. This shortcoming is attributed, at this stage of the analysis, to skipping the material validation and electrode optimization steps.

Table IV - 18: Summary of rate capability of cell builds based on Toda HE5050 high energy cathode materials.

| Rate	Capacity of Toda HE5050 Cell Builds (mAh/g of cathode)			
	1	4	9	12
2C			188	167
C	146	195	202	182
C/2	163	207	215	198
C/3	172	216	223	207
C/5	183	226	233	218
C/10		243	247	234
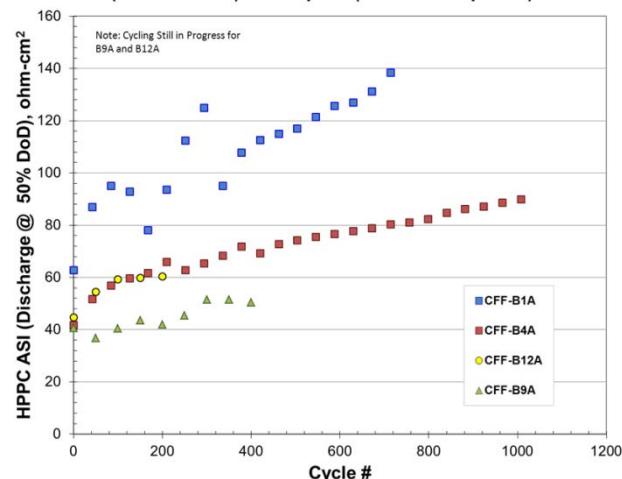
Figure IV - 271: HPPC impedance summary of cell builds based on Toda HE5050 high energy cathode materials vs. ConocoPhillips A12 graphite.

The high energy cathode results are shared with the Voltage Fade Effort to help in their studies. For instance, the voltage profiles are monitored for changes in their profile during cycling. Some voltage fade is observed in the voltage profile below 3.5 V (or 40 % DOD) as shown in Figure IV - 272. Note that the majority of the voltage fade probably occurred during the five formation cycles that take place before the rate analysis, and hence cannot be easily compared against the cycle 4 data shown in Figure IV - 272.
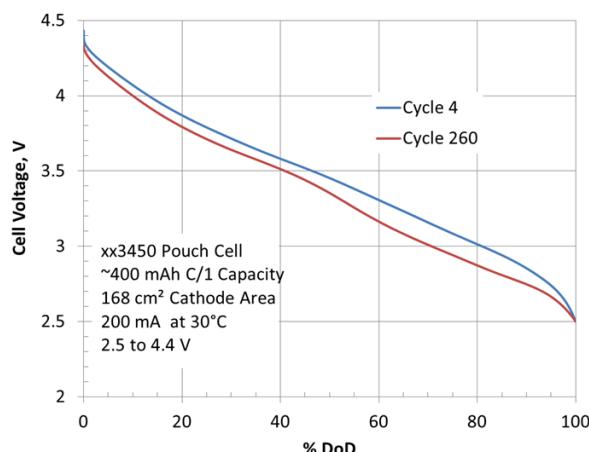
Figure IV - 272: Voltage profile change of ConocoPhillips A12 Graphite vs. Toda HE5050 (4th Cell Build).

Additional Cell Builds. In addition to the above high energy cathode cell builds, several more were conducted with traditional electrodes and non-traditional electrodes The traditional electrodes included commercial NCM523 and NCM111 cathodes. The non-traditional electrodes included $Li_4Ti_5O_{12}$ and the 5V $LiNi_{0.5}Mn_{1.5}O_4$ spinel. These electrodes and their combination of cell builds will not be discussed here in the interest of space, but a summary of their cycling performance is shown in Figure IV - 272 above.

Prototype Electrodes and Cells for Research Institutions. A secondary function of the CFF is to enable better science and research to be done on battery technology. This can be achieved by producing high quality electrodes for research use and by building specialized cells for non-conventional testing.

During the past year, the Electrode Library (EL) was created, which is a collection of anodes and cathodes that have been produced by the CFF. These electrodes were specifically designed so that the anodes and cathodes can be interchanged while maintaining and acceptable n:p ratio. By having these electrodes available to researchers, the quality of their data is improved and also allows the researcher to test their materials consistently against several materials. By having an "industrially" made electrode verses a handmade electrode, any variability is minimized. Currently, there are 6 anode and 8 cathode electrodes available. Electrodes will be continually added to the Electrode Library as more materials become available.

The CFF is also advancing research in batteries by producing specialized cells for non-conventional testing, which in FY12, have been done at national user facilities like the Advanced Photon Source (APS) at Argonne and the Spallation Neutron Source (SNS) at Oak Ridge National Laboratory. In these cases the crystal structures were analyzed *in situ* during electrochemical cycling. A conventional coin cell could not be used in these cases because the metal case of the coin cell absorbed or

reflected the X-rays or neutrons, which is much less of a problem for these specialized pouch cells. The CFF has completed close to 40 specialty pouch cells in the past year in which case most were used in *in situ* high energy diffraction studies, including XAS, XANES and EXAFS. These specialty pouch cells can be made with hand coated electrodes or electrodes from the Electrode Library, making possible a multitude of material combinations.

Both the Electrode Library collection and specialty pouch cell production have played, and will continue to play, an important role in the advancement of battery research. These two unique resources have been established in the past year and have had great success in supporting research. The Electrode Library has supplied ~225 electrodes to researchers along with 40 specialty pouch cells.

Conclusions and Future Directions

A Ross high energy/shear planetary mixer with a 2 liter chamber capacity was installed at the beginning of FY12. This relatively small capacity size proved to be ideal for the typical electrode builds made with the pilot scale coater, where supply of novel materials is often limited. The electrodes made with this mixer were shown to be homogenously dispersed with intimate contact between active particles and conductive additives.

A couple pouch cell builds were performed with two separate batches of scaled-up cathode material from the MERF. This material is a high-energy layered-layered NM cathode ($Li_{1.2}Ni_{0.3}Mn_{0.6}O_{2.1}$), originally developed by researchers in the ABR Program at Argonne. These cells showed good initial capacity but experienced capacity fade with cycling, which was attributed to particle cracking during the calendering process.

The 18650 cell build was successfully conducted at the end of FY12. Key to this success was in making consistent uniform electrodes, which enables proper winding. As expected, making 18650 cells required significantly more material than pouch cell fabrication. For this reason, a commercial source of NCM523 cathode was used for these trial cells.

Several pouch cell builds were conducted using Toda' high energy cathode material, HE5050, and Phillip 66's A12 graphite. Recommendations from the Diagnostic Effort and input from the Materials Validation Effort and the Post-Test Facility enabled significant advances in the cell performance. Several of these cells achieved 1,000 cycles with ~35 % capacity loss, while others are still on test.

Other pouch cell builds were conducted using LTO spinel anode, 5V LiNMO spinel cathode, NCM523 cathode, and NCM111 cathode. These electrodes serve as valuable baseline electrodes for high voltage electrolyte studies.

Numerous single-sided electrode samples were sent of all these chemistries to several outside research institutions and companies as part of the Electrode Library. Prototype pouch cells were also made to aid researchers at national user facilities like APS and SNS. This service will continue to grow by supplying more electrodes and specialty pouch cells in the next years.

For FY13, new generations of cathode materials based on LiNiMnO are anticipated from Argonne's Materials Engineering Research Facility. These cathode materials will be evaluated in pouch cell and 18650 cell formats made in the CFF. Priority will be given to high energy cathodes based on lithium manganese rich nickel cobalt manganese oxide (LMR-NCM).

As for anode materials, graphite will continue to be the baseline material to evaluate cathodes, but investigations of silicon composite electrodes will continue with an emphasis on identifying appropriate binders. In FY13, plans are to produce baseline pouch cell builds to assess the performance of four electrochemical couples: LMR-NCM and LNiMnO vs. graphite and silicon composites.

Variations in electrolyte additives, binders, and formation conditions will be explored, as well as methods to improve initial wetting before/during formation. Preliminary work by the Diagnostic effort on electrolyte additives have shown some encouraging results. Electrodes and cells made with these novel cathode materials (and other developmental electrode materials) will be distributed to ABR members and others as needed.

FY 2012 Publications/Presentations

1. Oral presentation at the DOE Vehicles Technology Program 2012 Annual Merit Review Meeting.
2. "High-Energy Electrode Investigation for Plug-in Hybrid Electric Vehicles", Wenquan Lu, Andrew Jansen, Dennis Dees, Paul Nelson, Nicholas R. Veselka, and Gary Henriksen, *J. Power Sources*, 196, 2011, 1537-1540.
3. "Overcharge Effect on Morphology and Structure of Carbon Electrodes for Lithium-Ion Batteries", Wenquan Lu, Carmen M. L´opez, Nathan Liu, John T. Vaughey, Andrew Jansen, and Dennis W. Dees, *Journal of the Electrochemical Society* 159(5), A566-A570 (2012).
4. "Positive Electrode Passivation by LiDFOB Electrolyte Additive in High-Capacity Lithium-ion Cells", Ye Zhu, Yan Li, Martin Bettge, and Daniel P. Abraham, accepted by the Journal of the Electrochemical Society.